

# Investigation of exciton properties in organic materials via many-body perturbation theory

J. Wehner

Copyright © 2019 by J. Wehner. All Rights Reserved.

Investigation of exciton properties in organic materials via many-body perturbation theory by J. Wehner.

Eindhoven: Technische Universiteit Eindhoven, 2019. Proefschrift.

printed by Gildeprint

A catalogue record is available from the Eindhoven University of Technology Library

ISBN 978-90-386-4744-9

# Investigation of exciton properties in organic materials via many-body perturbation theory

PROEFSCHRIFT

ter verkrijging van de graad van doctor aan de  
Technische Universiteit Eindhoven, op gezag van de  
rector magnificus prof.dr.ir. F.P.T. Baaijens, voor een  
commissie aangewezen door het College voor Promoties,  
in het openbaar te verdedigen op  
dinsdag 7 mei 2019 om 13:30 uur

door

Jens Wehner

geboren te Hannover, Duitsland

Dit proefschrift is goedgekeurd door de promotoren en de samenstelling van de promotiecommissie is als volgt:

voorzitter: prof.dr. J.J. Lukkien  
1e promotor: prof.dr.ir. B. Koren  
co-promotor: dr.Dipl.-Phys. B. Baumeier  
externe leden: prof.dr. K. Kremer (Johannes Gutenberg Universität Mainz)  
Prof.Dr. M. Rohlfing (Westfälische Wilhelms-Universität  
Münster)  
overige leden: prof.dr. M.A. Peletier  
prof.dr.ir. R.A.J. Janssen

Het onderzoek of ontwerp dat in dit proefschrift wordt beschreven is uitgevoerd in overeenstemming met de TU/e Gedragscode Wetenschapsbeoefening.

für Karl, Helga, Gerhard und Annchen



# Summary

## **Investigation of exciton properties in organic materials via many-body perturbation theory**

In this thesis the properties of bound electron-hole pairs, so called excitons, in organic materials are investigated using computer simulations. Central to the description of these molecular excitations are quantum mechanical methods to resolve the very short length scale phenomena, which largely determine the efficiency of molecular devices. To model the excitations the *GW*-BSE formalism is employed, a many-body perturbation theory approach, which is well suited to describe excitons in organic materials, as it accurately models the correlation and long range interaction between electrons.

To account for the influence of the environment on individual molecules in bulk and interface structures, a coupled quantum mechanical/molecular mechanics (QM/MM) framework using a polarizable environment is used here. This necessitated the implementation of density functional theory (DFT) to provide an accurate starting point for *GW*-BSE calculations, as well as improvements to speed and accuracy of the *GW*-BSE implementation itself. The combined DFT/*GW*-BSE formalism was successfully benchmarked for a set of small molecules. The QM/MM framework is then used to investigate charge transfer states inside a solvated DNA strand, highlighting the stabilization a polarizable environment provides to these bimolecular excitations. Building on the accurate description of excited states, a method to calculate electronic couplings for singlet and triplet states was developed and benchmarked against explicit dimer calculations. Furthermore, possible approximations for large systems were discussed. The electronic couplings in conjunction with classical electrostatics were then used to provide input for a set of coarse-grained rate equations, which allows to model exciton diffusion in DCV5T-ME(3,3), a crystalline

organic semiconductor. The inclusion of singlet radiative decay rates derived from *GW*-BSE results allows for an explicit treatment of exciton decay. Long range electronic couplings were classically treated using distributed charge representations of transition densities. The combination of rate models and atomic structure reduced to a directed graphs, which were solved using kinetic Monte Carlo simulations. The thesis concludes with an analysis of the exciton dynamics with regards to the impact of short and long ranged couplings as well as energetic disorder and the relevance of trap states on exciton diffusion length.



# Contents

Summary	vii
List of Figures	xiii
List of Tables	xvii
<b>1 Introduction</b>	<b>1</b>
<b>2 Organic electronics</b>	<b>7</b>
2.1 Organic semiconductors . . . . .	8
2.2 Organic solar cells . . . . .	10
2.3 Electronic excitations . . . . .	13
<b>3 Electronic structure theory</b>	<b>23</b>
3.1 The many electron system . . . . .	24
3.1.1 Non-interacting electrons . . . . .	28
3.1.2 Hartree-Fock and the variational principle . . . . .	30
3.2 Density functional theory . . . . .	34
3.2.1 Exchange-correlation functionals . . . . .	39
3.2.2 Basis functions . . . . .	40
3.2.3 Pseudo potentials . . . . .	43
3.3 Electronically excited states via <i>GW</i> -BSE . . . . .	46
3.3.1 One-particle-excitations . . . . .	46
3.3.2 Two-particle-excitations . . . . .	56
<b>4 Coarse-grained methods</b>	<b>63</b>
4.1 Molecular dynamics . . . . .	65

---

4.2	Rate models . . . . .	70
4.2.1	Excitation transfer reactions . . . . .	71
4.2.2	Partitioning of the system . . . . .	76
4.2.3	Site energies . . . . .	77
4.2.4	Reorganization energies . . . . .	84
4.2.5	Directed graphs . . . . .	85
<b>5</b>	<b>Numerical implementation of DFT/GW-BSE/MM in VOTCA</b>	<b>89</b>
5.1	Developing for VOTCA . . . . .	90
5.2	Density functional theory in a Gaussian basis . . . . .	92
5.3	GW-BSE in a Gaussian basis . . . . .	98
5.3.1	Single molecule data: Thiel set . . . . .	103
5.3.2	Comparison to experiment . . . . .	105
5.3.3	Optimal strategies for large-scale applications . . . . .	109
5.4	Quantum-classical QM/MM simulations . . . . .	113
5.4.1	Workflow and implementation . . . . .	114
5.4.2	Charge transfer excitations in aqueous DNA . . . . .	118
<b>6</b>	<b>Transfer integrals for exciton transport</b>	<b>131</b>
6.1	Excitonic coupling elements via GW-BSE-DIPRO . . . . .	133
6.2	Influence of intermolecular CT states . . . . .	136
6.2.1	Perturbation theory . . . . .	137
6.2.2	Reduction method . . . . .	138
6.3	Results . . . . .	139
6.3.1	Model pyrene dimers . . . . .	140
6.3.2	Optimizations for application to large scale morphologies . . . . .	149
6.4	Summary . . . . .	153
<b>7</b>	<b>Exciton dynamics in DCV5T</b>	<b>155</b>
7.1	Multiscale workflow . . . . .	156
7.2	Morphology . . . . .	159
7.3	Reorganization energies and polarization . . . . .	160
7.4	Site energies and lifetimes . . . . .	161
7.5	Electronic couplings . . . . .	165
7.6	Kinetic Monte-Carlo simulations . . . . .	168
<b>8</b>	<b>Conclusion and outlook</b>	<b>179</b>
<b>A</b>	<b>Appendix: Chemical structures</b>	<b>183</b>

**CONTENTS**

xi

---

<b>B Appendix: Thiel set data</b>	<b>187</b>
<b>C Appendix: DCV5T site energies</b>	<b>190</b>
<b>Bibliography</b>	<b>193</b>
<b>Acknowledgments</b>	<b>213</b>
<b>Curriculum Vitae</b>	<b>215</b>



# List of Figures

1.1	Improvements of solar cell efficiency from 1975 until 2017 . . . . .	6
2.1	Depiction of crystalline, semi-crystalline and amorphous organic materials. . . . .	8
2.2	Schematic representation of benzene (hydrogen not displayed), forming a conjugated system and corresponding DFT densities. . . . .	9
2.3	Depiction of electronic state localization and corresponding energy levels for different molecular arrangements. . . . .	11
2.4	Energy alignment of a donor-acceptor heterojunction and energy diagram of an organic solar cell under operating conditions . . . . .	12
2.5	Depiction of various processes in an organic solar cell. . . . .	14
2.6	Schematic definition of a hole in molecular excitations. . . . .	15
2.7	Depiction of different types of excitons. . . . .	16
2.8	Different excitations inside an organic molecule. . . . .	20
3.1	Adiabatic potential energy surfaces for the ground state and the first excited state of a two coordinate molecular system. . . . .	27
3.2	Energy levels for independent electrons. . . . .	30
3.3	Decomposition of a wave function into basis functions. . . . .	41
3.4	Pseudo potential and real potential and the corresponding wave functions. . . . .	45
3.5	Single particle Green's function for different time arguments. . . . .	48
3.6	Ground and excited states of a many-particle system. . . . .	48
3.7	Schematic representation of Hedin's equations for $G$ , $\Sigma$ , $W$ , $P$ , $\Gamma$ . . . . .	52
3.8	Many particle system and the Quasi-particle approximation . . . . .	53
3.9	Spectral function of the interacting system. . . . .	54

---

4.1	2,3 and 4 body bonded interaction potentials in classical forcefields.	66
4.2	Diabatic (black) and adiabatic (red dashed) potential energy surfaces along the reaction coordinate $\xi$ . . . . .	72
4.3	Partitioning scheme as employed in VOTCA . . . . .	77
4.4	Overview of the site energy calculation options in VOTCA. . . . .	79
4.5	Absorption and emission inside a molecule. . . . .	84
4.6	Molecular structure and the resulting directed graph. . . . .	86
4.7	KMC trajectory of an exciton . . . . .	87
5.1	Overview of the VOTCA suite of packages. . . . .	90
5.2	Software development workflow in VOTCA . . . . .	91
5.3	Convergence of the DFT total energy with the number of self-consistency iterations in methane. . . . .	93
5.4	DFT workflow as implemented in VOTCA-XTP. . . . .	97
5.5	GW-BSE workflow as implemented in VOTCA-XTP . . . . .	100
5.6	Influence of the self-consistency approach on HOMO-LUMO gaps and exciton-excitation energies in benzene. . . . .	102
5.7	Convergence of the quasi-particle HOMO-LUMO gap and the three lowest-energy singlet excitations of pyridine. . . . .	105
5.8	Comparison of calculated lowest singlet excitation energies with experimental data for the 28 small molecules in Thiel’s set. . . . .	106
5.9	Comparison of calculated lowest singlet excitation energies with the Theoretical Best Estimate for Thiel’s set . . . . .	110
5.10	Convergence of excitation levels in adenine with respect to unoccupied levels and the corresponding memory consumption . . . . .	110
5.11	Comparison of calculated lowest singlet excitation energies within the Tamm-Dancoff Approximation versus the full BSE for Thiel’s set	112
5.12	Schematic representation of DNA solvated in water. . . . .	115
5.13	QM/MM workflow as implemented in the VOTCA-XTP package. . . . .	116
5.14	DNA double strand sequence used in QM/MM simulation. . . . .	120
5.15	Density of states (DOS) for charge transfer (CT) excitations in aqDNA as obtained from dimers in vacuum and QM/MM embedded in a static background of point charges. . . . .	122
5.16	Comparison of CT excitation energies calculated in static and polarizable QM/MM setups with vacuum QM results. . . . .	123
5.17	Isosurfaces of excitation electron densities of the lowest energy adenine dimer . . . . .	124

---

5.18	Quasi-particle energy levels for HOMO-1, HOMO, LUMO, and LUMO+1 in base pair. . . . .	125
5.19	Effective charge transfer character in the CT excitations as a function of center-of-mass distance . . . . .	128
6.1	Illustration of the different pathways for exciton transfer between chromophores <i>A</i> and <i>B</i> . . . . .	132
6.2	Distance dependence of excitonic couplings for $S_1$ , $S_2$ , and $T_1$ excitations in an ideally $\pi$ -stacked pyrene dimer. . . . .	141
6.3	Rotational dependence of excitonic couplings for $S_1$ , $S_2$ , and $T_1$ excitations in a pyrene dimer. . . . .	143
6.4	Comparison of the distance and rotation dependence of effective excitonic couplings in the pyrene model dimers. . . . .	146
6.5	Comparison of the distance dependence of exciton transfer integrals in ideally $\pi$ -stacked dimers . . . . .	148
6.6	Comparison of the effect of different approximations on the distance dependence of triplet and singlet couplings in DCV5T . . . . .	151
6.7	Relative reduction of computation time of the <i>GW</i> -BSE calculation (excluding the DFT part) for the DCV5T singlet coupling. . . . .	152
7.1	Exciton diffusion workflow as implemented in the VOTCA-XTP package. . . . .	157
7.2	Exciton coupling for singlets and triplets. Schematic representation of the double cutoff used in VOTCA-XTP. . . . .	158
7.3	Crystal structure of DCV5T-Me(3,3) . . . . .	160
7.4	Distribution of decay times for singlet excitons in DCV5T . . . . .	163
7.5	<i>GW</i> corrected HOMO-LUMO gaps and excitation energies for DCV5T morphology . . . . .	164
7.6	Distribution of electronic couplings for singlets and triplets. . . . .	166
7.7	Distribution and correlation of electronic singlet couplings in the <i>GW</i> -BSE-DIPRO and TrEsp approximation. . . . .	168
7.8	Distribution of lifetimes for singlet exciton in DCV5T for a system without internal site energies. . . . .	173
7.9	Correlation between site energies and frequency of exciton decay for different snapshots without internal site energies. . . . .	176
7.10	Correlation between site energies and frequency of exciton decay for different snapshots with internal site energies. . . . .	177

8.1	CT and FE state energies at the DCV5T:C60 interface from <i>GW</i> -BSE calculations in a polarizable QM/MM environment. . . . .	181
C.1	Singlet site energy distributions. . . . .	191
C.2	Triplet site energy distributions. . . . .	192



# List of Tables

5.1	Total energies for methane ( $\text{CH}_4$ ), DCV2T and DCV5T, calculated with three different DFT implementations. . . . .	96
5.2	Comparison between singlet excitation energies for self-consistent $\text{evGW}$ and one-shot $G_0W_0$ using the PBE0 and PBE functionals . . .	108
6.1	Excitonic coupling elements $ J $ from Davydov splitting for $S_1$ , $S_2$ , and $T_1$ excitations in an ideally $\pi$ -stacked pyrene dimer. . . . .	144
6.2	Basis set dependence of the calculated transfer integrals $ J $ . . . . .	147
6.3	Effect of different computational parameters for DFT and $\text{GW-BSE}$ calculations on run times and exciton transfer integrals. . . . .	150
7.2	Standard deviation $\sigma$ for site energies . . . . .	162
7.7	Singlet diffusion lengths without internal site energies . . . . .	172
7.8	Singlet diffusion lengths with internal site energies . . . . .	172
7.9	Computational cost of Marcus rate input parameters for a system with $N$ sites . . . . .	174
B.1	Number of basis functions in the atomic orbital and RI basis for Thiel set. . . . .	188
B.2	Singlet excitation energies for Thiel set molecules. . . . .	189



# Chapter 1

## Introduction

The work behind this thesis was started to create a framework which allows to simulate electronic properties of organic semiconductors from only structural experimental data, whilst all other quantities are calculated from quantum mechanics. Such an approach has the potential to greatly aid experimental research on organic semiconductors by revealing the fundamental microscopic processes and linking them to experimentally available quantities. As we are facing global warming and the exhaustion of fossil fuels, more efficient photovoltaics are needed to ensure that the world's hunger for energy is stilled. In this chapter, I give a general overview over the current state of solar cell design and argue that solar cells based on organic semiconductors can greatly supplant the current energy mix.

In all photovoltaic cells sunlight is directly converted into electricity, using the following working principle: A semiconducting material absorbs photons which have energies larger than the energetic band gap of the semiconductor. This creates an exciton, a bound pair consisting of an electron and a hole. These excitons are then dissociated into free charges, which drift to the electrodes due to a built-in potential.

The efficiency of an (organic) solar cell is determined by three steps: 1) How many photons can the solar cell absorb and at which energy, 2) how many of these absorbed photons will be separated into electrons and holes, 3) how many of these electrons and holes make it to the electrodes and how much energy have they lost in the process. As only photons with energies above the band gap are absorbed,

designers of solar cells face the problem of either using high band gap materials, yielding a few high energy excitons or using a low band gap material which absorbs most of the solar spectrum yielding many excitons of only low energy. The power produced by a solar cell is proportional to the number of excitons times their energy. Given our solar spectrum this limits the maximum efficiency of an otherwise perfect single junction solar cell to 33.7% at an optimal band gap 1.34 eV, the so called Shockley-Queisser limit [1]. Even after the successful absorption of a photon, a multitude of loss mechanisms can annihilate the exciton or trap electrons or holes, thus further limiting the efficiency of the solar cell. As the band gap and also the losses are material and processing specific, a wide range of materials has been tried to find better solar cells.

In Fig. 1.1 the evolution of solar cell design since 1975 is shown. Most commercial solar cells today use crystalline silicon as the semiconducting material (blue lines in Fig. 1.1). Providing over 20% power conversion efficiency (PCE)<sup>1</sup> and little material degradation over their life span, they have been the workhorse of photovoltaics for the last 20 years. Unfortunately, the production of highly crystalline silicon is complicated and costly. Among the most promising replacements are currently perovskite solar cells (yellow dots), whose PCE has risen from 3.8% in 2009 to 22.7% in 2017 [2]. Although they are cheap to produce, they suffer from toxicity problems due to the lead inside the perovskite material [3] and from severe efficiency degradation in moist environments [4]. Competing developments are thin film cells, using strongly absorbing semiconductors like amorphous silicon or combinations of copper, indium, gallium, and selenide (CIGS cells), which are less energy consuming to produce, whilst being as efficient as crystalline silicon cells [5].

The top performing solar cells with efficiencies of up to 46% [6] are multi-junction solar cells, which absorb a broader range of the incident light by stacking multiple single-junction subcells with varying gaps. At the bottom end of the efficiency spectrum we find organic solar cells. In these cells the active layer is formed by highly light-absorbing molecules instead of an inorganic semiconductor. The remainder of this thesis will be about them.

These highly absorbing molecules are either polymers or small molecules, which like all organic materials are mostly composed of hydrogen, carbon, and nitrogen. These substances are abundantly available on earth. Cheap raw materials and the

---

<sup>1</sup>Power conversion efficiency is generated electric power/incident solar power (the solar power distributed over the solar spectrum, attenuated by the atmosphere.)

---

option to employ the whole arsenal of organic chemistry fabrication techniques reduces the production cost [7]. Polymer materials are usually deposited from liquid using ink printing, which allows the easy fabrication of large areas. Small molecules are typically deposited from vapor, requiring high vacuum conditions. In both cases though, fabrication can be performed below 400 K, which is much more energy efficient than the production of inorganic solar cells, where temperatures in excess of 1000 K are needed. The low processing temperature also allows to use polymer as substrates, allowing the creation of light, flexible solar cells [8]. Furthermore, the material properties can be altered by attaching different functional side groups, allowing application specific tuning (e.g., making them flexible or transparent at certain frequencies).

Such features make organic solar cells a promising addition to the range of solar cells with the potential for opening up new applications in architectural design, like solar cell coated facades or window pane solar cells, working in the ultraviolet range. To achieve full market penetration organic solar cells still have to overcome two challenges. First, the long term stability is still inferior to inorganic solar cells (2-3 years [9, 10] vs 20 years [11]) and secondly, power conversion efficiency still has to be improved, as the current record efficiency is only 15.7% [12]. Substantial improvements require a deeper understanding of the individual processes which lead to charge generation inside the organic solar cell and how they are influenced by the chemical structure.

Especially, establishing a clear link between chemical structures of the molecular building blocks, the resulting molecular arrangement upon processing, and finally the electronic properties would greatly aid the design of efficient organic solar cells. In Chapter 2 the current understanding of these dependencies and in particular charge generation and the role and properties of excitons in organic materials are described.

From a computational point of view, the description of electrons in molecules lies in the realm of quantum chemistry. Driven by exponential growth of computational power in the last 50 years and using the fundamental interactions between electrons and atomic nuclei, so-called *ab initio* methods can predict molecular properties without any experimental input besides the chemical composition. Since the Schrödinger equation, which describes the interaction between quantum mechanical particles, is fully known, one might assume that computational chemistry is now just a problem of throwing enough computational power at a chemical system. Unfortunately, the difficulty of solving the Schrödinger equation does not

increase proportionally to the size of the system, which is typically denoted as  $N$ . As an example, the most accurate approximate methods, which try to find the wave function of the system, scale as  $N^7$ , e.g., doubling of the system size requires a  $2^7 = 128$ -fold increase in computing power to finish in the same time. Thus simply increasing the computational power will in a reasonable time not allow us to access industrially relevant molecules with hundreds of electrons. Instead further approximations were introduced to capture the essential parts of the quantum mechanical interactions and treat smaller effects, e.g., electron correlation, approximately. In Chapter 3 we discuss two approaches, density functional theory (DFT) for ground state and  $GW$ -BSE for excited state calculations, which scale as  $N^3$  and  $N^5$ , respectively. Whereas DFT describes the ground state of an electron system, the  $GW$ -BSE approach models the electron and hole via Green's functions  $G$ , whose behavior is governed by the screened Coulomb potential  $W$  and whose interaction is described by the Bethe-Salpeter equation (BSE). These approaches allow us to study the chemical properties of technologically relevant molecules for organic photovoltaics applications.

While the simulation of electrons and excitons is already computationally expensive, the simulation of the combined motion of atomic nuclei and electrons is even more computationally demanding, as the methods mentioned earlier then have to be integrated over time. Unfortunately, the combined motion of nuclei and electrons is required for an explicit modeling of exciton dynamics, as will be shown in later chapters. Experimentally, the distance excitons traverse before dissociation or decay is roughly 10 nm [13]. A cube with the same side length, filled with organic molecules, contains of the order of 80000 atoms, which is far beyond the capabilities of *ab initio* methods, let alone time integration. Still, for smaller molecules and or smaller systems, the explicit simulation has already been performed using large supercomputers using partially parameterized quantum mechanical methods like Tight-Binding DFT [14].

In this thesis we focus instead on the development and application of a combination of two coarser, simpler computational chemistry methods to simulate the nuclear and electronic dynamics in a multiscale approach. First the atomistic structure of a large set of molecules, also called the *morphology*, is simulated using classical molecular dynamics (MD). In classical MD the atoms are approximated as classical point particles, which interact via potentials parameterized either from *ab initio* calculations or experimental results. Second we reintroduce the exciton into the simulation via a model, where exciton dynamics are described as a series of hops

---

from molecule to molecule. The individual hop is the result of *excitation transfer reaction*, which is quantified by a reaction rate. Each reaction rate depends on several factors: the chemical structure of the molecules, their relative positions and orientations and the chemical environment. The mathematical form of these rate equations, an explanation of the respective input parameters, as well as a concise treatment of molecular dynamics, can be found in Chapter 4.

The rate model formalism of excitation dynamics typically requires the calculation of thousands of quantities from *ab initio* methods, as each individual rate has to be determined independently. For this multiscale approach an efficient implementation of *ab initio* methods, namely DFT and *GW*-BSE is required. Their implementation inside the VOTCA-XTP software package is described in Chapter 5 with respective benchmarks. To accurately describe the electronic properties of a molecule inside a atomistic environment, we incorporate electrostatic and polarization effects of classical environments into *ab initio* calculations via a quantum mechanics/molecular mechanics (QM/MM) framework. The implementation and the application to a DNA strand in an aqueous environment are discussed towards the end of Chapter 5.

Among the input quantities for the rate model, the electronic coupling between two molecules, plays an eminent role, as it incorporates the effects of the relative molecular orientations and alignment. As the exciton is still a two-particle excitation, the transfer of an exciton from one molecule to another can proceed via various intermediate *charge transfer* (CT) states, where electron and hole reside on different molecules. All these pathways have to be accounted for in the electronic coupling to calculate the correct value of the excitation transfer rates. In Chapter 6 we develop an algorithm for the calculation of electronic couplings in the framework of *GW*-BSE. Additionally, we discuss approximations to reduce the computational footprint for large systems.

In Chapter 7 we employ the methods developed in previous chapters to a crystalline system of dicyanovinyl-substituted oligothiophene (DCV5T) molecules to simulate exciton transport. Taking exciton decay explicitly into account we discuss the influence of various approximations on the diffusion length of excitons and outline optimization strategies for efficient screening of exciton properties.

The thesis concludes with a summary and a discussion of further developments, which may increase the predictive power of multiscale simulations for the electronic properties of organic materials, in Chapter 8.

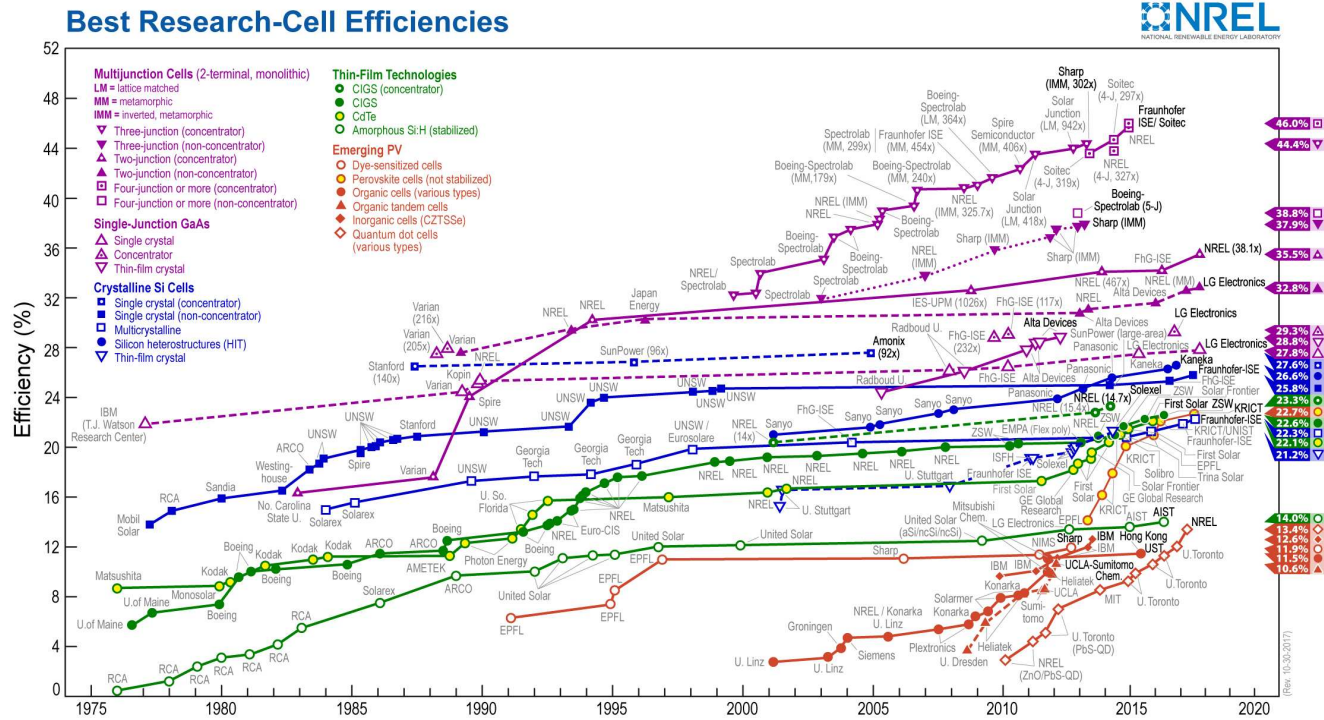


Figure 1.1: Improvements of solar cell efficiency from 1975 until 2017. Image is provided by the American National Renewable Energy Laboratory (NREL) at <http://www.nrel.gov/pv/assets/>.



## Chapter 2

# Organic electronics

Functional organic photovoltaic devices (OPVs) were first manufactured in labs in the 1980s, after the discovery of polymers with semi-conducting properties in the 1970s. In 2000 this discovery was rewarded with the Nobel prize in chemistry for Alan J. Heeger, Alan G. MacDiarmid and Hideki Shirakawa [15].

Since then organic solar cells have come a long way, reaching power conversion efficiencies of up to 15.7% [12]. Similarly organic light emitting diodes (OLEDs) and organic field effect transistors (OFETs) have reached commercialization. Responsible for this success are the unique properties of organic semiconductors. The combination of mechanical flexibility and chemical tuneability, combined with new production techniques, e.g., solution processing and spray coating [16] have opened new applications and markets for electronic materials.

In this chapter we discuss the chemical composition and molecular arrangement which are responsible for the unique properties but also limitations of organic semiconductors. We proceed by outlining how these properties influence the charge generation in organic solar cells. The step by step process from light absorption to the extraction of charges is described including loss mechanisms, which limit the efficiency of solar cells. At the end of the chapter we return to the exciton, whose creation by absorption of photons is the first step in the conversion of sunlight into electricity.

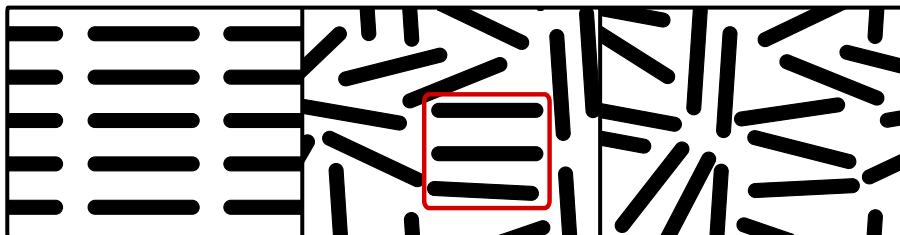


Figure 2.1: Depiction of crystalline, semi-crystalline and amorphous organic materials from left to right. Crystalline materials exhibit near perfect ordering, which periodically repeats. Amorphous materials are characterized by the absence of periodicity and long range order. Semi-crystalline materials mix crystalline (red box) with amorphous areas.

## 2.1 Organic semiconductors

Organic semiconductors are molecular solids. They consist of an arrangement of individual molecules, which agglomerate in a solid state. These molecules, mostly made up of carbon and hydrogen, are referred to as organic molecules. Carbon atoms can bind to up to four neighboring atoms, which allows them to form long chains, sheets and a near infinite variety of other structures and arrangements as building blocks for molecules. The different sizes and structures of these molecules agglomerate in a range of spatial arrangements, which can vary from perfectly crystalline, to semi-crystalline, or fully amorphous, as shown in Fig. 2.1.

Organic materials typically fall into either of two categories: small molecule and polymer materials. Polymers are larger molecules, which consist of chemically linked basic repeating units, the monomers. Polymers can contain thousands of atoms, whereas small molecules typically have less than a hundred atoms. Due to the size difference, different production methods are employed. Polymer based organic semiconductors like P3HT<sup>1</sup> [17] or P(NDI2OD-T2)<sup>2</sup> [18], are produced using solution processing techniques and subsequent solidification by solvent removal [19]. Small molecule based semiconductors, like DCV5T (see app. A) [20] or Alq3<sup>3</sup> [21] are typically produced via vapor deposition techniques [22].

<sup>1</sup>poly(3-hexylthiophene)

<sup>2</sup>poly[N,N'-bis(2-octyldodecyl)-1,4,5,8-naphthalenedicarboximide-2,6-diyl]-alt-5,5'-(2,2'-bithiophene)

<sup>3</sup>Tris (8-hydroxyquinoline)aluminum

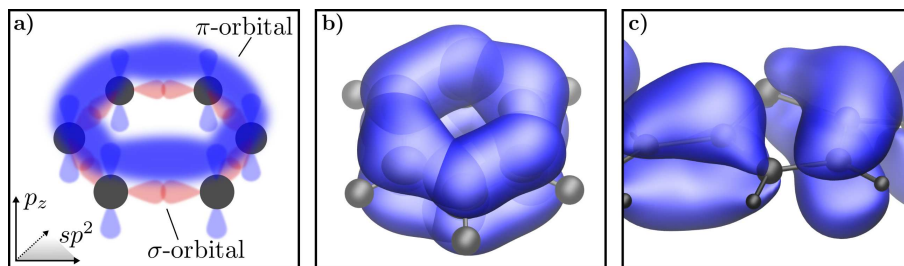


Figure 2.2: (a) Schematic representation of benzene, with hydrogen atoms removed, forming a conjugated system. The  $p_z$  orbitals form a delocalized electronic state. (b) DFT( explained in Chapter 3 density plot of the highest occupied molecular orbital (HOMO) of the benzene molecule. This is a superposition of the HOMO and HOMO-1, as the states are degenerate. (c) Conjugated system of a distorted molecule. The distortions lead to a localization of the electronic state.

What distinguishes organic semiconductors from other organic materials is simply their ability to conduct electrical charges. In contrast to most organic materials electrons in organic semiconductors are able to spread out over large parts of the molecule, which considerably eases the movement of electrons. This spreading out, or delocalization, happens because the molecules contain conjugated systems, where due to the chemical structure, electronic states extend over multiple atoms. Figure 2.2(a) shows a schematic view of the conjugated system in benzene. In this picture the carbon atoms in the ring bind to each other forming covalent  $\sigma$  bonds by overlapping the singly occupied atomic  $sp^2$  orbitals. This leaves a singly occupied  $p_z$  orbital for each atom sticking out of the plane of the ring. These orbitals overlap to form a delocalized occupied  $\pi$ -orbital and an unoccupied  $\pi^*$  orbital. The delocalization typically also leads to only a small energy gap between the  $\pi$  and  $\pi^*$  orbitals which is around 1–3 eV [23]. This gap is close to the average photon energy of sunlight, which leads to improved absorption in the visible range. Consequently, molecules with conjugated systems are often very good dyes and make excellent absorbers in organic solar cells.

Besides the electronic structure of the constituent molecules, the mutual interaction between molecules also influences the electronic properties of the organic semiconductor. The bonding, which causes the molecules to condensate into a solid, derives mostly from the *Van der Waals* interaction. Also known as dispersion interaction, it stems from the correlated fluctuations in the charge distributions of neighboring molecules, giving rise to an induced dipole-dipole interaction. In

addition to *Van der Waals* forces, electrostatic forces are very relevant for the mutual alignment of molecules, as will be discussed in Chapter 4. These interactions are typically an order of magnitude weaker than the covalent bonding inside the molecules. Thus the electronic structure of the individual molecules is only perturbed by the environment as depicted in Fig. 2.3(a,b). While the single molecule has a discrete spectrum of energy levels, an amorphous solid will show a distribution of states, because each molecule inside the solid experiences a different chemical environment, shifting the electronic state, as indicated in Fig. 2.3(b). At low temperatures and in perfectly ordered organic semiconductors narrow bands can emerge [24], as shown in Fig. 2.3(c).

The role of structural disorder and molecular interaction between molecules is a recurring theme in this thesis. Generally, the stronger the interaction between molecules, the more electronic states tend to delocalize and form bands. Strong interaction also leads to smaller vibrations, creating less thermal disorder at the same temperature. Consequently, weak interaction leads to more localization of the electronic states. Besides temperature, static disorder, created by mismatches in the crystalline structure, impurities or other defects also localize electronic states.

## 2.2 Organic solar cells

The excellent absorption properties of organic semiconductors motivate the construction of organic photovoltaic devices. The organic material absorbs the photons, which transfer their energy to the electrons during the absorption process. The electrons are promoted to an excited state across the HOMO-LUMO gap, as shown in Fig. 2.4(a). The gap is essential, as without it the electron can transfer back to the ground state via a series of intermediate states, using phonon emission, i.e., thermalization. Instead with the gap the electron has to lose the complete gap energy in one big chunk to return to the ground state, which is significantly less likely<sup>4</sup>.

In organic semiconductors the promoted electron is not free to move but bound to a hole, forming an electron-hole pair or exciton (see Fig. 2.4(a)). The exciton concept will be explained later in more detail. Important is that in order to convert an

---

<sup>4</sup>This does not mean, that enlarging the gap leads to longer decay times, as other decay mechanisms, e.g. radiative decay become more effective at larger gaps.

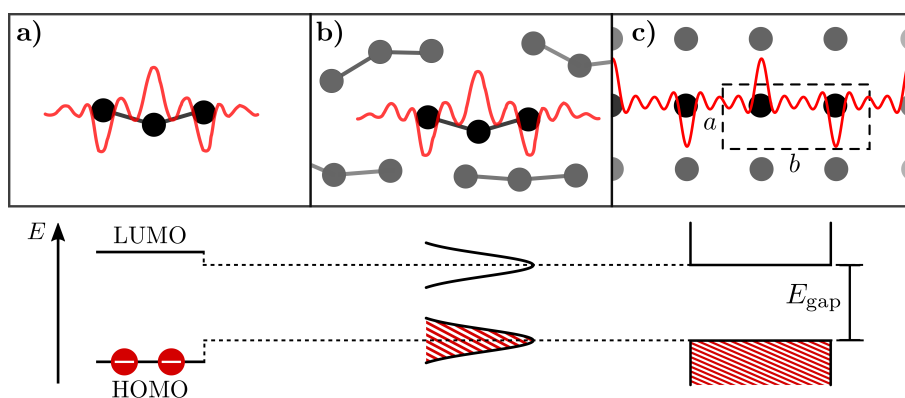


Figure 2.3: Depiction of electronic localization and corresponding energy levels for different molecular arrangements. (a) For a single organic molecule in vacuum the electronic state is localized on the molecule with exponential decay into the vacuum. The corresponding energy levels are discrete. The highest occupied molecular orbital (HOMO) is the highest occupied level and the lowest unoccupied molecular orbital (LUMO) is the first unoccupied level. (b) In organic semiconductors, due to structural and thermal disorder, the electronic states localize on individual molecules, with only small overlap with neighboring molecules. Due to the different environment of every molecule and the interaction between molecules, the discrete energy levels of each molecule create a smeared out distribution. (c) In crystalline semiconductors, the electronic states typically extend over the whole system, leading to formation of a band structure, with a bandgap of energy  $E_{\text{gap}}$  between occupied and unoccupied states.

exciton into free charges one has to overcome the exciton binding energy by providing a chemical environment in which it is energetically favorable for the exciton to split up. Although the exact mechanism is still subject of intense investigation, it was experimentally found that placing two different types of molecules with vastly different affinities to electrons and holes adjacent to each other can create such an energetically favorable situation. The energetic offset created at the interface between these two types of molecules, called donor and acceptor molecule, can greatly improve the dissociation of excitons [25]. In modern organic solar cells acceptor and donor molecules absorb photons, which are then split up at the interface and transported to the electrodes (see Fig. 2.4(a)). The energetic offset is typically denoted  $\Delta$  and is the energetic difference between the LUMO of the donor material and the LUMO of the acceptor material. For the design of an organic solar

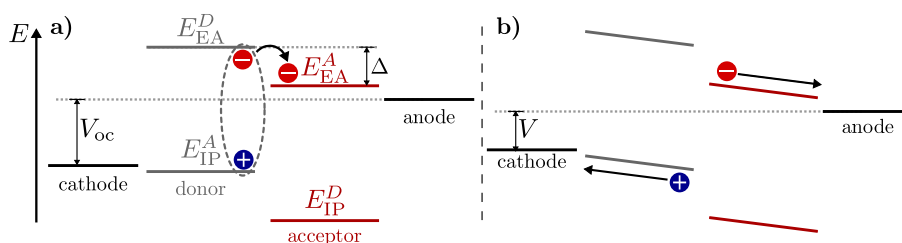


Figure 2.4: (a) Energy alignment of a donor-acceptor heterojunction, which splits excitons into free charge carriers via an energetic offset  $\Delta$ , producing an open-circuit voltage  $V_{oc}$ . (b) Energy diagram of an organic solar cell under operating conditions, producing drift currents of charge carriers towards the electrodes.

cell  $\Delta$  must be larger than the exciton binding energy to successfully split excitons but not too much larger than that, as the excess energy is wasted.

It has to be stressed that the exact energetics and kinetics of exciton dissociation are still not fully understood [26, 27]. The most widely accepted model of how the separation of the exciton into free electron and free hole actually proceeds, assumes that an intermediate step exists, the formation of a charge transfer state (CT) at the interface (see Fig. 2.5).

The efficiency of an organic solar cell critically depends on excitons reaching the interface and splitting up. As explained later in this chapter, excitons typically have a short lifespan and quickly decay back to the ground state [13, 28]<sup>5</sup>. The exciton, thus, has to be split up before it can decay. As the average distance an exciton moves before decaying is around 10 nm [13, 28], the absorber area must be close to the acceptor molecules. As the functional region thus is restricted to a thin strip along the donor-acceptor interface, increasing the efficiency of the solar cell demands maximizing the contact surface between both materials. Therefore, a finely interdispersed blend of acceptor and donor material providing a large interface area, called a heterojunction, is used. The structure of the heterojunction is critical for the efficiency of the organic solar cell, as all excitons which decay before reaching the donor-acceptor interface, do not contribute to the photo current. Better morphology control directed towards maximizing the exciton diffusion length is reported to increase power conversion efficiency by up to 30% [29].

<sup>5</sup>I mentioned earlier that the gap in an organic semiconductor protects against fast decay of excitons. This is true, as a gap blocks the fastest path to the ground state, but there are many other paths, hundreds of times slower, but still of the order of nanoseconds

After the dissociation the free charge carriers drift and diffuse towards the electrodes. The diffusion of charge carriers is driven by the concentration gradient inside the solar cell. The driving force behind the drift currents is the difference in work functions of the electrodes, which creates an internal electric field inside the solar cell (see Fig. 2.4(b)). At all stages of the free charge carrier generation, loss processes take place, which reverse the charge separation and lead to recombination and subsequent thermalization, as depicted in Fig. 2.5. To increase the efficiency of organic solar cells, it is paramount to suppress these loss mechanisms and increase the efficiency of the gain processes. In the next section we will focus on the first steps to generating electricity, the creation of an exciton and its diffusion to the donor-acceptor interface.

## 2.3 Electronic excitations

Calculating the electronic structure of a molecule with quantum mechanics yields a set of discrete set of energy values or energy levels the electrons can occupy. Each of these levels can be occupied by up to two electrons<sup>6</sup>. If all electrons occupy the energetically lowest state available to them, the molecule is in its ground state, as shown in Fig. 2.6.

If one of the electrons is stimulated by light or temperature and the right amount of energy is transferred to it, it may transition to a higher level, creating an excited state. Although this excitation is nothing more than a rearrangement of electrons, it is more intuitive to describe the excitation as a difference to the ground state. So the excitation has one electron more in an excited state and lacks one electron in the normally occupied states. This “lack” of electron is the aforementioned hole, which is charged positively with regards to the ground state (see Fig. 2.6). The negatively charged electron is attracted to the hole via the Coulomb interaction and consequently they form the already introduced bound electron-hole pair, or exciton in short. The bound exciton is lower in energy than electron and hole independently.

For electron-hole pairs the strength of the interaction strongly depends on the response of other electrons in the system. These electrons will agglomerate around

---

<sup>6</sup>This is only true within the single particle picture, but we gloss over this at the moment. See Chapter 3 for a more precise formulation.

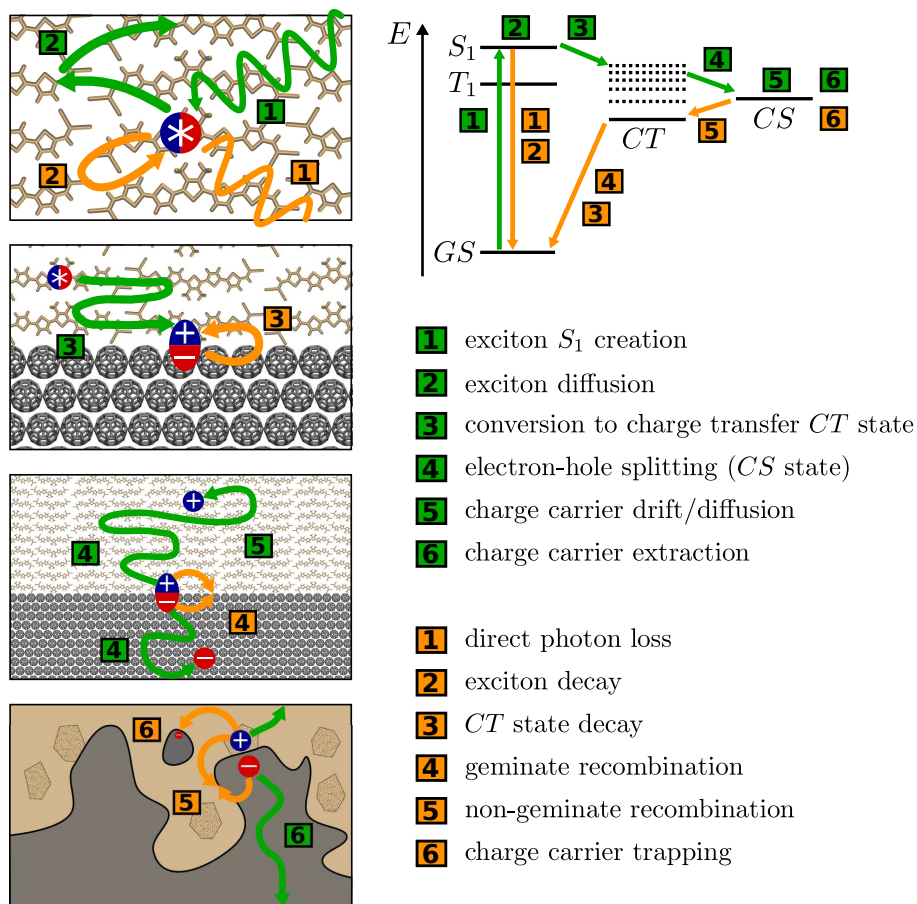


Figure 2.5: The creation of free charge carriers inside an organic solar cell, happens via intermediate stages and various length scales. Depicted are the various steps as well as the loss mechanism, which reduce the solar cell efficiency. On the right the energetic landscape of the respective processes is depicted.



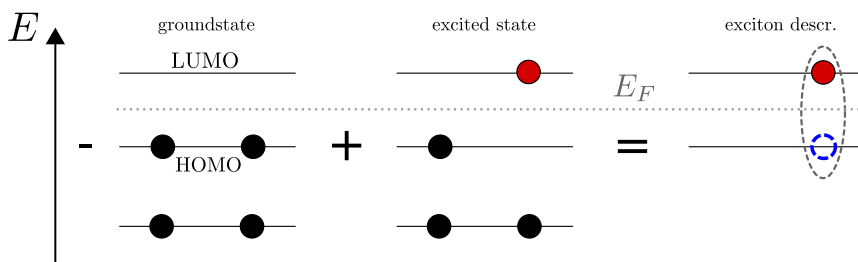


Figure 2.6: Depiction of the definition of a hole. In the ground state all levels from the bottom up are filled, i.e. below the Fermi energy  $E_F$ . Upon excitation an electron is promoted to a higher state. “Subtracting the ground state from this excited state configuration leaves a hole in the HOMO and an electron in the LUMO. Their interaction is caused by the rearrangement of all other electrons in response to this excitation (not shown).

the hole and so shield it from the excited electron, lowering the excitation binding energy (see Fig. 2.7). Depending on the availability of other electrons and their ability to relocate without incurring large energy penalties, excitons are either strongly bound, small, localized entities or extend over considerable distance. The material’s reaction to the exciton is approximately described by the dielectric constant  $\epsilon$  of the material.

Silicon, which in comparison to organic semiconductors has more free charge carriers, has a relative dielectric constant of 12 [30]. Consequently, in silicon the interaction between electron and hole is strongly screened. The exciton binding energy is 10 – 100 meV and thus excitons at room temperature can be easily split by thermal energy, which is of the order of 25 meV. Due to the strong screening the binding is weak and the exciton is delocalized over many unit cells. These delocalized excitons are called Wannier-Mott excitons.

In organic materials the relative dielectric constant is much lower,  $\epsilon = 3 - 4$  [23], thus the excitons are more tightly bound and localized. Binding energies are typically around 0.1 – 1 eV. These tightly bound excitons are called Frenkel excitons. Especially at interfaces another configuration is possible<sup>7</sup>, in which the electron is localized on one molecule and the hole on a neighboring molecule. These bimolecular states are the aforementioned charge-transfer (CT) states, which are assumed to play a major role in the dissociation of Frenkel excitations at donor-

<sup>7</sup>The energetic offset  $\Delta$  is important here, but the exact processes are still debated.

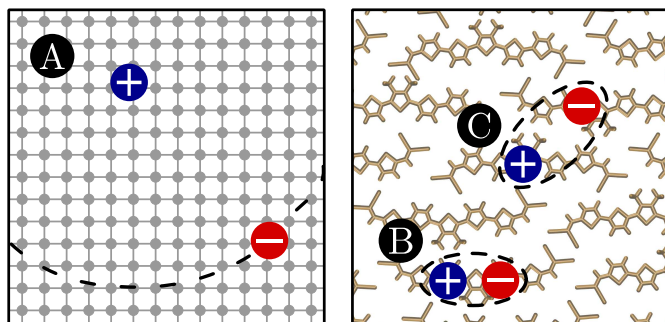


Figure 2.7: Depiction of different types of excitons. Depending on the dielectric constant, e.g. the screening of the electron-hole interaction, different localizations are observed. In inorganic semiconductors (A) free charges are available which screen the exciton well, leading to small binding energies  $< 0.1$  eV and delocalisation over many unit cells, creating Mott-Wannier excitons. In organic semiconductors (B/C) charge densities are low and the excitons are strongly bound (0.1 – 1 eV). The localized excitons are called Frenkel exciton (B). Due to the two-particle nature of the excitation, the electron and hole can also reside on neighboring molecules, forming charge transfer states (C).

acceptor interfaces.

Before we address which challenges organic solar cells thus face, let us briefly discuss the topic of exciton lifetimes.

Electron-hole pairs or excitons are mostly created by incident light, which promotes an electron to a higher state. Sometimes an exciton is created due to nuclear motion, i.e., thermal excitation. Thinking in terms of particles either a photon, the force mediating particle of the electro-magnetic field or a phonon, the collective excitation of atomic nuclei, is absorbed by the electron cloud and leads to the creation of an exciton.

Similarly, the two main channels for exciton decay are radiation of a photon and thermalization. In the former case light is emitted from the molecule. In the latter case the solar cell heats up a bit. Both cases are rather detrimental to the design of an efficient photovoltaic device, but which one is more prevalent?

To answer this question, we have to look at a quantum mechanical peculiarity, spin. All quantum mechanical particles have this additional degree of freedom, which separates them into two categories: those with fractional spin called fermions,

e.g., electrons, neutrons, and protons and those with integer spin, called bosons, of which the most prominent is the photon. Fermions are the building blocks of all matter and quantum mechanics dictates that two fermions cannot have exactly the same value for all of their quantum numbers, e.g., spin and energy. In the case of a quantum system which has discrete energy levels, e.g., the molecules we talked about before, each energy level can be occupied by two electrons. This is because electrons have a total spin  $s = \frac{1}{2}$ . Its projection on an arbitrary axis, usually the  $z$ -axis, can have two values  $s_z = \pm \frac{1}{2}$ , which are referred to as spin up (down) configurations. Each level can accommodate one electron with spin up and one with spin down. In heavier elements, the spin of individual electrons couples to the angular momentum via spin-orbit coupling. In this case the electronic states cannot be exactly distinguished by spin up or down configurations anymore, instead the total angular momentum has to be used to differentiate different states.

Let us consider the ground state of a molecule with all energy levels up to a certain level occupied with two electrons each. This ground state we will call  $|0\rangle$ . It has a total spin of 0 and is called closed shell, because all electrons are paired up. Some molecules (e.g.  $O_2$ ) and most atoms (non-noble gases) have unpaired electrons, but we ignore these cases for the moment.

If we create an exciton, i.e., promote an electron to a higher state, we have a set of possible combinations of spin states. Either the spin down electron or the spin up electron can be promoted to a higher level. If we also allow spins to flip we arrive at four distinct configurations. We describe these as arrows, with the first arrow being the spin of the electron and the second arrow indicating the spin of the hole. (Note that the spin of a hole is the inverse of the spin of an electron occupying that level.)

$$|\uparrow\uparrow\rangle, |\uparrow\downarrow\rangle, |\downarrow\uparrow\rangle, |\downarrow\downarrow\rangle \quad (2.1)$$

Without going into the details, the spins of the electron and the hole have to be added using the quantum mechanical rules for spin addition resulting in a total spin  $S$ [31]. Photons cannot change the total spin of a system, as shown later. Consequently, from an  $S = 0$  ground state, only transitions to other  $S = 0$  states are possible.

None of the four states in eq. 2.1 is a  $S = 0$  state<sup>8</sup>. Instead these states have to be linearly combined, which splits the four combinations into two subgroups. One

<sup>8</sup>This is again a consequence of the spin or more generally angular momentum addition [31].

state with total spin  $\mathfrak{S} = 0$  and three states with total spin  $\mathfrak{S} = 1$ , which are called singlets and triplets, respectively.

$$\underbrace{\frac{1}{\sqrt{2}}(|\downarrow\uparrow\rangle - |\uparrow\downarrow\rangle)}_{\mathfrak{S}=0 \text{ Singlet}} \quad \underbrace{|\uparrow\uparrow\rangle, |\downarrow\downarrow\rangle, \frac{1}{\sqrt{2}}(|\uparrow\downarrow\rangle + |\downarrow\uparrow\rangle)}_{\mathfrak{S}=1 \text{ Triplets}} \quad (2.2)$$

Triplet ( $T$ ) and singlet ( $S$ ) states have quite different electronic properties. To first order light absorption can only create singlets. The converse is also true, only singlets can, to first order, decay under emission of a photon, which is called *fluorescence*. Take a light wave, which can be mathematically modeled as a plane wave, with wave vector  $\mathbf{k}$  and energy  $E = \hbar|\mathbf{k}|$ , so its quantum mechanical operator  $\hat{A}$  is

$$\hat{A} = \exp(i\mathbf{k}\hat{\mathbf{r}}) \approx 1 + i\mathbf{k}\hat{\mathbf{r}}. \quad (2.3)$$

The latter approximation, also called “dipole approximation” holds if the wavelength of the light is much larger than the extension of the molecule. This is true for typical molecules (1 – 10 nm vs  $\lambda = 300 - 500$  nm).

The transition probability  $P_T$  between the ground state  $|0\rangle$  and the excited state  $|S\rangle$  is then proportional to the square of the transition dipole matrix element,  $\boldsymbol{\mu}_{Tr}$ .

$$P_T \propto |\langle 0|\hat{\mathbf{r}}|S\rangle|^2 = \boldsymbol{\mu}_{Tr}^2 \quad (2.4)$$

This equation explains that pure triplet states in the dipole approximation do not couple to photons (assuming a singlet ground state). A triplet state  $|T\rangle = |T_s\rangle|T_r\rangle$  is the product of a spin  $|T_s\rangle$  and space  $|T_r\rangle$  component. As  $\hat{\mathbf{r}}$  only acts on the space component, this leads to:

$$P_T \propto |\langle 0_r|\langle 0_s|\hat{\mathbf{r}}|T_r\rangle|T_s\rangle|^2 = |\langle 0_r|\hat{\mathbf{r}}|T_r\rangle|^2 \underbrace{|\langle 0_s|T_s\rangle|^2}_{=0} = 0. \quad (2.5)$$

Here, we assume that the ground state is a spin singlet state. Irrespective of the spatial part of the wave function, the spin components of the singlet ground state and triplet excited state are orthogonal to each other.

To compare the coupling of different states to the electromagnetic field, the transition dipole is normalized with the excitation energy of the state,  $\Omega_S$ , leading to oscillator strength  $f$ :

$$f = \frac{2}{3} \mu_{Tr}^2 \Omega_S. \quad (2.6)$$

$f$  can be interpreted as the ratio of the quantum mechanical transition rate to the classical absorption rate of an electron at the same energy. Not all singlets have large transition dipoles, so singlets fall into either of two categories: dark ( $f \approx 0$ ) and bright ( $f > 0$ ). As only bright singlet states can be created via light absorption, how can triplets or dark singlets be created? As shown in Fig. 2.8 a range of other transitions can occur inside a molecule.

- Eq. 2.3 is only the first order expansion of the electromagnetic field. Electric quadrupole and magnetic dipole interaction allow dark singlets to be created. These interactions are orders of magnitude smaller and thus do not dominate the spectrum when bright singlets exist.
- The nuclear vibrations also known as phonons couple with the electrons, as will be described in more detail in the next chapters. These phonons occasionally “knock” an electron into a higher excited state of the same spin. The reverse process of converting an electronic excitation into a lower excited or ground state plus a vibration is referred to as *internal conversion*.
- Separating the electronic states into  $\mathfrak{S} = 0$  singlet and  $\mathfrak{S} = 1$  triplet is only approximately true. Spin-orbit coupling, which is most pronounced in heavy atoms, couples the electron angular momentum  $L$  to its spin. Thus both are no longer good quantum numbers and do not describe the electronic states properly. Instead the total angular momentum  $J = \mathfrak{S} + L$  has to be used. The coupling between singlets and triplets is not strong in organic molecules, as they typically only contain light elements. However, even the small effect allow triplets to turn into singlets, which is referred to as an *intersystem crossing*. The intersystem crossing from  $T_1$  to the ground state under emission of a photon is also called phosphorescence.

As already mentioned earlier the mechanisms of how excitons reach the heterojunction and how they split up (see Fig. 2.5) is not fully understood. However, it is clear that for an efficient solar cell, excitons have to get to the heterojunction before decaying. Singlet lifetimes are typically on the order of 0.5 ns. Triplets

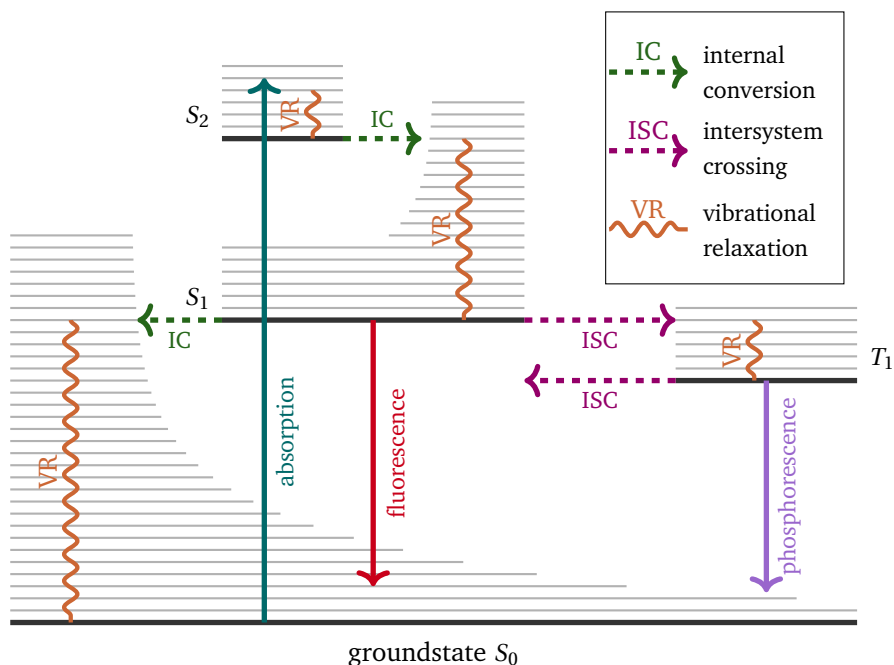


Figure 2.8: Different excitations inside an organic molecule. The vibrational levels on top of the electronic excitation are depicted in gray. (Adapted from [32])

lifetimes due to the spin-forbidden transition to the ground state are usually 6 orders of magnitude larger, as lightweight organic compounds have only very small spin-orbit coupling [13]. Triplets seem to be a much better suited to transfer the absorbed photon energy to the interface due to their longer lifetime, but they have two problems. Firstly, triplet excitons cannot be generated by light absorption (see eq. 2.5), which requires intersystem crossings. Secondly, triplets move slower than singlets as will be discussed below and in Chapter 6.

In organic semiconductors exciton movement is often described as a hopping from one molecule to the next [14, 33–35]. This is a result of the localization of electronic states in organic semiconductors (see Fig. 2.3), with only weak coupling to neighboring molecules. This coupling, which we will describe in detail in Chapter 6, is different for singlets and triplets. Triplets can only hop to their next neighbors, as the coupling is mediated by molecular overlap [36, 37] and thus exponentially decays with distance. Singlets can hop up to 1-5 nm [38, 39], as their

coupling is mediated by exchange of a virtual photon with distant molecules.

In the following chapter we will first develop the quantum mechanical framework for calculation ground- and excited state properties. Afterwards we will look at the hopping models, which allow us to quantify and finally simulate exciton transfer.





## Chapter 3

# Electronic structure theory

Over the last 60 years computer simulations have become increasingly useful to predict properties of material compounds, such as molecular geometries and spectra, and to gain insight into processes on length and time scales experiments cannot resolve. This chapter will give an overview of the most important methods to predict properties of organic materials. The list of methods is nowhere near complete so many interesting approaches are not included. I chose to mainly explain methods which were used in this thesis.

The chapter is divided into two sections. First we will deal with quantum mechanical methods, which require no additional input besides the geometric structure to provide accurate information about the electronic structure of the molecule in question. The most popular of these ab initio methods is Density Functional Theory or DFT. DFT is arguably is not a fully ab initio method, because parts of the electron-electron interaction are captured by the exchange correlation functional, whose exact form is not known. Instead one of many approximations of the exchange correlation functional has to be chosen. Nonetheless, because of its relative ease of use and good balance between speed and accuracy, it has become the dominant technique to access ground state properties. Its use has become so widespread and the insights into physics, chemistry, and biology it generated so important, that in 1998 one of its inventors, Walter Kohn, received a Nobel prize for it [40].

While DFT produces very accurate ground state properties provided the right functional is chosen, it fails to predict accurate band gaps and excited state properties

for nearly all materials [41]<sup>1</sup>. Without going into the details of why DFT fails, we introduce a more advanced method, the *GW* and Bethe Salpeter Equation method (*GW*-BSE) in the second part of this chapter. *GW*-BSE is a Green's function based approach, which originates from condensed matter physics but is now used to calculate excited state properties in molecular systems. A more in-depth treatment of ab initio methods, DFT and *GW*-BSE, can be found in [42–46].

### 3.1 The many electron system

A molecule consists of  $N$  electrons at positions  $\mathbf{r}$ , and  $M$  nuclei at positions  $\mathfrak{R}$ . Here we use the following notation: a Fraktur quantity represents a whole set of values, e.g.,  $\mathbf{r} = \{\mathbf{r}_1, \mathbf{r}_2, \dots, \mathbf{r}_N\}$ .

The non-relativistic Hamiltonian of the system then reads

$$\hat{\mathcal{H}} = \hat{T}_{\text{el}} + \hat{T}_{\text{nuc}} + \hat{V}_{\text{nuc-nuc}} + \hat{V}_{\text{el}} + \hat{V}_{\text{nuc-el}} \quad (3.1)$$

with  $\hat{T}_{\text{el}}$  and  $\hat{T}_{\text{nuc}}$  as the kinetic energy operators of electrons and nuclei,  $\hat{V}_{\text{nuc-nuc}}$  and  $\hat{V}_{\text{el-el}}$  as the nuclei-nuclei and electron-electron interaction operator, respectively, and finally  $\hat{V}_{\text{nuc-el}}$  the nuclei-electron interaction. The individual terms read:

$$\hat{T}_{\text{el}} = \sum_i \frac{\hat{\mathbf{p}}_i^2}{2m_e} \quad (3.2)$$

$$\hat{T}_{\text{nuc}} = \sum_K \frac{\hat{\mathbf{p}}_K^2}{2M_K} \quad (3.3)$$

$$\hat{V}_{\text{nuc-nuc}} = \frac{1}{2} \sum_{K \neq L} \frac{Z_L Z_K e^2}{|\mathbf{R}_L - \mathbf{R}_K|} \quad (3.4)$$

$$\hat{V}_{\text{el-el}} = \frac{1}{2} \sum_{i \neq j} \frac{e^2}{|\mathbf{r}_i - \mathbf{r}_j|} \quad (3.5)$$

$$\hat{V}_{\text{nuc-el}} = - \sum_{i,K} \frac{Z_K e^2}{|\mathbf{r}_i - \mathbf{R}_K|}. \quad (3.6)$$

---

<sup>1</sup>DFT results vs experiment: silicon 0.56 eV vs 1.17 eV; carbon 4.1 eV vs 5.5 eV. So the error is about 20-40 times the thermal energy at room temperature (25 meV)

$\hat{\mathbf{p}}_i$  ( $\hat{\mathbf{P}}_K$ ) is the momentum operator of an electron (nucleus), with  $m_e$  ( $M_k$ ) the corresponding mass and  $e$  ( $Z_k e$ ) the corresponding charge<sup>2</sup>.

The time evolution of the nuclear and electron dynamics is governed by the Schrödinger equation

$$\hat{\mathcal{H}}\Psi(\mathbf{r}, \sigma, \mathfrak{R}, t) = i \frac{\partial}{\partial t} \Psi(\mathbf{r}, \sigma, \mathfrak{R}, t), \quad (3.7)$$

where  $\Psi(\mathbf{r}, \sigma, \mathfrak{R}, t)$  is the wave function of the system. Here,  $\sigma$  denotes the spin variable and is only listed for completeness, as the Hamiltonian above does not explicitly depend on spin. The spin is only needed for the correct particle statistics, which we will cover later and otherwise neglect from now on<sup>3</sup>. Furthermore,  $\mathcal{H}$  does not explicitly depend on  $t$ , so eq. 3.7 is separable into a spatial( $\Psi_s$ ) and temporal part( $\Psi_t$ ):

$$\Psi(\mathbf{r}, \sigma, \mathfrak{R}, t) = \Psi_s(\mathbf{r}, \sigma, \mathfrak{R}) \Psi_t(t), \quad (3.8)$$

with  $\Psi_t(t) = \exp(-iEt)$  and  $\mathcal{H}\Psi_s(\mathbf{r}, \sigma, \mathfrak{R}) = E\Psi_s(\mathbf{r}, \sigma, \mathfrak{R})$ .

Unfortunately the Schrödinger equation can only be solved analytically for a few special cases, in particular for  $N = 1$  and  $M = 1$ , i.e., the hydrogen atom. For larger and technologically relevant systems, these equations become impossible to solve even with the help of large computers.

We will now outline possible approximations, which simplify the problem and make calculations of larger and more relevant systems feasible. We know that nuclei are about three orders of magnitude heavier than electrons. Electrons can thus react nearly instantaneously to the movement of the heavy nuclei. If we keep the nuclei fixed, the system would be governed by an electronic Schrödinger equation, in which the nuclear coordinates  $\mathfrak{R}$  enter the electronic part of the Hamiltonian only as a parameter, which is denoted by the semi-colon in the function argument:

$$\hat{H}_{\text{el}}\psi_a(\mathbf{r}; \mathfrak{R}) = E_a(\mathfrak{R})\psi_a(\mathbf{r}; \mathfrak{R}). \quad (3.9)$$

The energies  $E_a$  and wave functions  $\psi_a$  are called adiabatic energies and wave functions, with  $\hat{H}_{\text{el}} = \hat{T}_{\text{el}} + \hat{V}_{\text{el-el}} + \hat{V}_{\text{nuc-el}}$ . The whole set of adiabatic wave functions

<sup>2</sup>We will use atomic units from here on:  $m_e \equiv 1$ ,  $e \equiv 1$ ,  $\hbar \equiv 1$ ,  $1/4\pi\epsilon_0 \equiv 1$ .

<sup>3</sup>For heavy atoms the spin couples with the angular momentum due to relativistic effects, which we neglect here as well.

forms the complete adiabatic electronic basis, which can be used to expand the full wave function in eq. 3.7 according to

$$\Psi(\mathbf{r}, \mathfrak{R}) = \sum_a \Lambda_a(\mathfrak{R}) \psi_a(\mathbf{r}; \mathfrak{R}), \quad (3.10)$$

where  $\Lambda_a$  represent the nuclear wave functions belonging to the electronic configuration  $\psi_a(\mathbf{r}; \mathfrak{R})$ . Inserting eq. 3.10 into eq. 3.7 and using the electronic Schrödinger equation (eq. 3.9) and the real space representation of the nuclear momentum operator  $\hat{\mathbf{P}}_K = -i\nabla_K$ , we arrive at an equation for each  $\Lambda_a$ :

$$\hat{H}_{\text{nuc}}^a(\mathfrak{R}) \Lambda_a(\mathfrak{R}) + \sum_{b \neq a} \Theta^{ab} \Lambda_b(\mathfrak{R}) = i \frac{\partial}{\partial t} \Lambda_a(\mathfrak{R}), \quad (3.11)$$

where we have introduced the nuclear Hamiltonian  $\hat{H}_{\text{nuc}}^a(\mathfrak{R})$ :

$$\hat{H}_{\text{nuc}}^a(\mathfrak{R}) = \hat{T}_{\text{nuc}} + \underbrace{\hat{V}_{\text{nuc-nuc}} + E_a(\mathfrak{R}) + \hat{\Theta}^{aa}}_{U^a(\mathfrak{R})} \quad (3.12)$$

and the non-adiabacity operator:

$$\hat{\Theta}^{ab} = \langle \Lambda_a(\mathfrak{R}) | \hat{T}_{\text{nuc}} | \Lambda_b(\mathfrak{R}) \rangle + \sum_{K=1}^M \frac{1}{M_K} \langle \Lambda_a(\mathfrak{R}) | \hat{\mathbf{P}}_K | \Lambda_b(\mathfrak{R}) \rangle \hat{\mathbf{P}}_K, \quad (3.13)$$

which operates on  $\Lambda_b(\mathfrak{R})$  and thus couples the equations of motion for different nuclear states. Integrals over electronic degrees of motion are abbreviated by

$$\langle \Lambda_a(\mathfrak{R}) | \hat{O} | \Lambda_b(\mathfrak{R}) \rangle = \int d\mathbf{r} \psi_a(\mathbf{r}; \mathfrak{R}) \hat{O} \psi_b(\mathbf{r}; \mathfrak{R}). \quad (3.14)$$

Eq. 3.11 can now be interpreted as follows: The nuclear coordinates are propagated by the nuclear Hamiltonian operator  $\hat{H}_{\text{nuc}}^a(\mathfrak{R})$ , as long as the electrons remain in the adiabatic state  $\psi_a$ . The nuclei thus move in the effective adiabatic potential  $U^a(\mathfrak{R})$ . This potential geometrically represents a surface in the space of nuclear coordinates, called the adiabatic potential energy surface (PES). The non-adiabacity operator occasionally triggers the nuclei to transition from one adiabatic state  $\psi_a$  to another adiabatic state  $\psi_b$ . These transitions correspond to the vibrational relaxation and excitation mentioned in sec. 2.3 (also see Fig. 2.8).

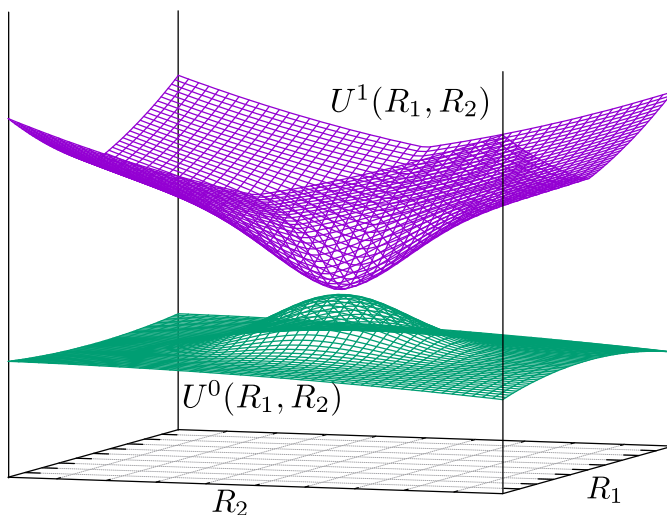


Figure 3.1: Adiabatic potential energy surfaces for the ground state and the first excited state of a two coordinate molecular system. In the center they approach each other, so that the adiabatic approximation is no longer valid to describe the dynamics.

Actually solving for the equation of motion of the nuclei requires the determination of every  $\psi_a$  and  $U_a(\mathfrak{R})$  for every nuclear configuration  $\mathfrak{R}$  by solving eq. 3.9. How to determine these quantities will be described later in this chapter. There we will see in detail why even for a handful of atoms the calculation of the full set of PESs is plainly impossible with any degree of accuracy. Fortunately, for many systems the full set of PESs is not required. For many chemical systems the ratio between the energy spacing of different PESs  $\langle \Delta E \rangle_{\text{el}}$  and the vibrational energy of the nuclei  $\omega_{\text{nuc}}$  can be estimated as

$$\frac{\langle \Delta E \rangle_{\text{el}}}{\omega_{\text{nuc}}} \approx \sqrt{\frac{M}{m_e}}. \quad (3.15)$$

As nuclei are roughly 1000 times heavier than electrons, the electronic separation is 1-2 orders of magnitude larger than the vibrational energy of the nuclei, making transitions between PESs extremely unlikely, i.e., the off-diagonal elements of the non-adiabacity operator can be neglected. This is known as the adiabatic approximation, which only requires the calculation of a single PES. It only breaks down if two PES come very close to each other for some nuclear configuration  $\mathfrak{R}$ . This is

exactly the case for exciton dynamics in organic materials and will be explained in more detail in Chapter 4.

If we completely neglect the non-adiabaticity operator we arrive at the Born-Oppenheimer approximation. We can write the complete wave function  $\Psi$  as a product of electronic and nuclear wave functions:

$$\Psi_{aM}(\mathbf{r}, \mathfrak{R}) = \psi_a(\mathbf{r}; \mathfrak{R}) \Lambda_{aM}(\mathfrak{R}), \quad (3.16)$$

where  $a$  denotes the electronic and  $M$  the vibrational level of the nuclei. Accordingly, eq. 3.11 reduces to:

$$[\hat{T}_{\text{nuc}} + U^a(\mathfrak{R})] \Lambda_a(\mathfrak{R}) = i \frac{\partial}{\partial t} \Lambda_a(\mathfrak{R}). \quad (3.17)$$

At higher temperatures and for heavier elements we can use the Ehrenfest theorem to transform eq. 3.17 into a classical equation of motion for the nuclei, which move on the ground state PES  $U^0$ :

$$M_K \frac{\partial^2 \mathbf{R}_K}{\partial t^2} = -\nabla_K U^0(\mathfrak{R}). \quad (3.18)$$

We will come back to this equation in sec. 4.1 and focus for now on the electronic Schrödinger equation (eq. 3.9) and the corresponding Hamiltonian

$$\hat{H}_{\text{el}} = \sum_i \frac{\hat{\mathbf{p}}^2}{2} - \sum_{i,K} \frac{Z_K}{|\mathbf{r}_i - \mathbf{R}_K|} + \frac{1}{2} \sum_{i \neq j} \frac{1}{|\mathbf{r}_i - \mathbf{r}_j|}. \quad (3.19)$$

### 3.1.1 Non-interacting electrons

The hardest part to deal with is the electron-electron interaction because the dynamics of each electron are influenced by the dynamics of every other electron. Consequently, each of these interactions between quantum mechanical particles has to be taken into account, which is computationally impossible even for the smallest of systems. If instead the electrons did not interact, each electron would move independently in a static potential generated by the nuclei. Let us assume this simplistic case first and neglect the electron-electron interaction. The Hamiltonian then reduces to a sum of single-particle Hamiltonians  $\hat{h}$ :

$$\hat{H}_{\text{el}} = \sum_i \frac{\hat{\mathbf{p}}_i^2}{2} - \sum_i \sum_K \frac{Z_K}{|\mathbf{r}_i - \mathbf{R}_K|} = \sum_I \left[ \frac{\hat{\mathbf{p}}^2}{2} - \sum_K \frac{Z_K}{|\mathbf{r}_i - \mathbf{R}_K|} \right] = \sum_i \hat{h}_i, \quad (3.20)$$

with:

$$\hat{h}_i = \frac{\hat{\mathbf{p}}_i^2}{2} - \sum_K \frac{Z_K}{|\mathbf{r}_i - \mathbf{R}_K|}. \quad (3.21)$$

This allows to solve each single particle problem independently,  $\hat{h}_i \phi_i = \varepsilon_i \phi_i$ , where  $\phi_i$  is a single particle wave function and  $\varepsilon_i$  the corresponding single particle energy. As the electrons are non-interacting, the Hamiltonian of electron  $i$  does not contain any interaction-term with electron  $j$ , thus  $\hat{h}_i \phi_j = 0$ . The exact wave function of the non-interacting Hamiltonian (eq. 3.20) is then simply the product of these single-particle wave functions, the *Hartree* wave function:

$$\psi^{\text{H}}(\mathbf{r}) = \prod_i \phi_i(\mathbf{r}_i). \quad (3.22)$$

The Hartree wave function is not physical because any fermionic wave function  $\Phi^{\text{F}}$  has to be anti-symmetrical with respect to particle exchange due to the Pauli principle:

$$\Phi^{\text{F}}(\mathbf{r}_1, \mathbf{r}_2, \dots, \mathbf{r}_k, \mathbf{r}_l, \dots, \mathbf{r}_N) = -\Phi^{\text{F}}(\mathbf{r}_1, \mathbf{r}_2, \dots, \mathbf{r}_l, \mathbf{r}_k, \dots, \mathbf{r}_N). \quad (3.23)$$

Anti-symmetrizing  $\psi^{\text{H}}$  yields the Hartree-Fock wave function (HF-wf)  $\psi^{\text{HF}}(\mathbf{r})$ :

$$\psi^{\text{HF}}(\mathbf{r}) = \frac{1}{\sqrt{N!}} \sum_{\text{perm}} pP \left[ \psi^{\text{H}}(\mathbf{r}) \right], \quad (3.24)$$

where the sum runs over all possible permutations of the ensemble of electron coordinates  $\mathbf{r}$  in  $\psi^{\text{H}}(\mathbf{r})$ .  $P$  is the operator which permutes the electrons and  $p$  is signature of the permutation<sup>4</sup>.

The mathematical structure of  $\psi^{\text{HF}}(\mathbf{r})$  allows to write it as a determinant over the matrix of single particle wave functions  $\phi_i(\mathbf{r}_i)$ . Thus, the Hartree-Fock wave function is also called a Slater determinant.

<sup>4</sup>The signature of a permutation is +1, if an even number of pair exchanges is required to achieve a given permutation and -1 otherwise.

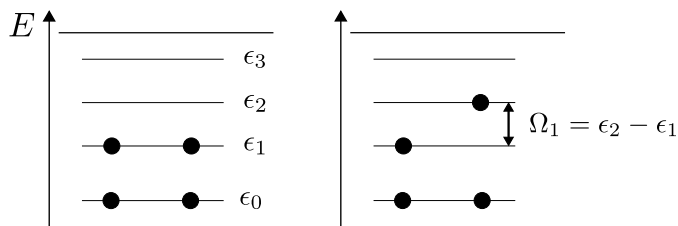


Figure 3.2: Energy levels for independent electrons. In the independent particle picture the particles just fill in the single particle levels. Excitation energies are simply differences between energy levels.

For a two-level system with states  $\phi_1$  and  $\phi_2$  the Hartree-Fock wave function is given by

$$\begin{aligned} \psi^{\text{HF}}(\mathbf{r}_1, \mathbf{r}_2) &= \frac{1}{\sqrt{2}}(\phi_1(\mathbf{r}_1)\phi_2(\mathbf{r}_2) - \phi_2(\mathbf{r}_1)\phi_1(\mathbf{r}_2)) \\ &= \frac{1}{\sqrt{2}} \begin{vmatrix} \phi_1(\mathbf{r}_1) & \phi_2(\mathbf{r}_1) \\ \phi_1(\mathbf{r}_2) & \phi_2(\mathbf{r}_2) \end{vmatrix}, \end{aligned}$$

where  $|\dots|$  is the determinant of the matrix.

Each single particle orbital can be occupied by two electrons due to the spin and the total energy is simply the sum of the single particle energies. A convenient advantage of the non-interacting particle picture is that the energy levels are only determined by the nuclear interaction and do not depend on the position of the electrons relative to each other. Therefore, we can move electrons from one energy level to another without changing these levels. After the introduction of the electron-electron interaction this will no longer be the case.

### 3.1.2 Hartree-Fock and the variational principle

Now we have solved the non-interacting system of electrons, but does this help with the interacting system? Let us assume we had the ground state solution  $\Psi_0$  to eq. 3.19 and the corresponding energy eigenvalue  $E_0$ . In quantum mechanics any energy calculated using  $\hat{H}_{\text{el}}$  (eq. 3.19) and a trial wave function  $\Psi_{\text{trial}}$  is larger than or in the case we hit the exact solution equal to  $E_0$ :



$$\langle \Psi_{\text{trial}} | \hat{H}_{\text{el}} | \Psi_{\text{trial}} \rangle \geq E_0. \quad (3.25)$$

This is also known as the variational principle of quantum mechanics<sup>5</sup>. So we only have to calculate a “good” trial wave function and can then get as close as necessary to the real ground state energy  $E_0$ . Unfortunately, the space of possible functions is extremely large and so it is important to find a good approximation which captures the necessary physics but is also numerically convenient. The independent electron solutions are just such a basis.

So the next step is to introduce the electron-electron interaction. We use the Hartree-Fock wave function as a guess and insert it into the full Hamiltonian  $\hat{H}_{\text{el}}$ . For the rest of this section we will drop the HF label from  $\psi(\mathbf{r})$ . Furthermore, we are mainly interested in finite system for which  $\psi(\mathbf{r})$  can be chosen to be real, we thus drop the complex conjugation for the rest of the chapter, i.e.,

$$\langle \psi(\mathbf{r}) | \hat{H}_{\text{el}} | \psi(\mathbf{r}) \rangle = \int d\mathbf{r} \psi(\mathbf{r}) \hat{H}_{\text{el}} \psi(\mathbf{r}). \quad (3.26)$$

Using definitions eq. 3.24 and eq. 3.19, this leads to:

$$\langle \psi(\mathbf{r}) | \hat{H}_{\text{el}} | \psi(\mathbf{r}) \rangle = \sum_i^N h_i + \frac{1}{2} \sum_{i,j}^N (\phi_i \phi_i | \phi_j \phi_j) - (\phi_i \phi_j | \phi_j \phi_i) \quad (3.27)$$

with:

$$h_i = \langle \phi_i | \hat{h}_i | \phi_i \rangle \quad (3.28)$$

$$(\phi_i \phi_i | \phi_j \phi_j) = \iint d^3\mathbf{r} d^3\mathbf{r}' |\phi_i(\mathbf{r})|^2 \frac{1}{|\mathbf{r} - \mathbf{r}'|} |\phi_j(\mathbf{r}')|^2 \quad (3.29)$$

$$(\phi_i \phi_j | \phi_j \phi_i) = \iint d^3\mathbf{r} d^3\mathbf{r}' \phi_i(\mathbf{r}) \phi_i(\mathbf{r}') \frac{1}{|\mathbf{r} - \mathbf{r}'|} \phi_j(\mathbf{r}) \phi_j(\mathbf{r}'). \quad (3.30)$$

The first term is again only the single particle energies' contribution. The second term can be interpreted as a simple classical electrostatic energy of a charge density

$$n(\mathbf{r}) = \sum_i^N \phi_i(\mathbf{r})^2. \quad (3.31)$$

<sup>5</sup>As we assume that  $\langle \Psi_{\text{trial}} | \Psi_{\text{trial}} \rangle = 1$ , the term on the left hand side is just the Rayleigh quotient, as  $\hat{H}_{\text{el}}$  is hermitian.

This term usually is called *Coulomb* or *Hartree* energy. The last term has no simple interpretation, as there is no classical analogue. It is called *exchange* energy, as the term originates from the fact that the HF-wave function is constructed to be anti-symmetric under particle-exchange. Note that for  $i = j$  both terms cancel each other exactly, so that a single particle does not interact with itself.

We can now seek one-particle functions that minimize  $\langle \psi(\mathbf{r}) | \hat{H}_{\text{el}} | \psi(\mathbf{r}) \rangle$ . Variation of the total energy with respect to these functions is expressed via a set of functional derivatives and yields a set of  $N$  equations:

$$\frac{\delta \langle \psi(\mathbf{r}) | \hat{H}_{\text{el}} | \psi(\mathbf{r}) \rangle}{\delta \phi_i} = 0. \quad (3.32)$$

Explicitly the functional derivative yields a system of equations for the single-particle wave functions, the *Hartree-Fock equations*:

$$[\hat{h}_i + V_{\text{H}} + V_{\text{x}}] \phi_i = \epsilon_i^{\text{HF}} \phi_i \quad (3.33)$$

with  $V_{\text{H}}$  the Hartree potential:

$$V_{\text{H}} = \int d^3 \mathbf{r}' \sum_j^N |\phi_j(\mathbf{r}')|^2 \frac{1}{|\mathbf{r} - \mathbf{r}'|} = \int d^3 \mathbf{r}' \frac{n(\mathbf{r}')}{|\mathbf{r} - \mathbf{r}'|} \quad (3.34)$$

and  $V_{\text{x}}$  the exchange-potential defined as:

$$V_{\text{x}} \phi_i(\mathbf{r}) = \sum_j^N \int d^3 \mathbf{r}' \phi_j(\mathbf{r}') \frac{1}{|\mathbf{r} - \mathbf{r}'|} \phi_i(\mathbf{r}') \phi_j(\mathbf{r}). \quad (3.35)$$

The solution to equation eq. 3.33 then yields the independent electron energies  $\epsilon_i^{\text{HF}}$ , but due to eq. 3.34 and eq. 3.35 the solution is not straightforward:

1. Solving eq. 3.33 yields a set  $\phi_i$  but as an input also requires the set of  $\phi_i$ . So this equation has to be solved self-consistently, which means an initial guess for the  $\phi_i$ ,  $\phi_i^{(0)}$  has to be given. Solving eq. 3.33 with  $\phi_i^{(0)}$  inserted on the left, results in a new set of  $\phi_i^{(1)}$ , which are inserted into eq. 3.33 again. This is repeated until after  $n$  iterations, the difference between  $\phi_i^{(n-1)}$  and  $\phi_i^{(n)}$  vanishes and thus the solution  $\phi_i^{(n)}$  is self-consistent within numerical limits.

2. The  $V_x$  (eq. 3.35) operator is non-local. Its value depends on  $\phi_i$  at all coordinates  $\mathbf{r}'$  due to the spatial integration. So  $V_x$  does act on  $\phi_i$  but requires the value of it at every point in space, not just at  $\mathbf{r}$ .
3. The operators  $V_H$  and  $V_x$  sum over all electrons, so the individual electron does not see all the individual contributions of the other electrons but only their averaged (often called mean field) potential. Thus the Hartree-Fock approximation is called a mean-field theory.
4. In addition to the last point, the wave function in eq. 3.24 is a single determinant wave function. Being a single Slater determinant and not a linear combination of determinants has two consequences. First HF cannot model dissociation of molecules into smaller molecules, because it would have to distribute the electrons equally on both molecules [47, 48]. A one determinant approach cannot do this. For these cases multi reference methods have to be used (e.g. Multi-configurational self-consistent field theory[49]). Secondly, using a linear combination of determinants as the starting wave function  $\psi$ , actually introduces “correlation” between electrons:

$$\psi = \psi^{\text{HF}} + \sum_i \psi_i + \sum_{i \neq j} \psi_{ij} \dots, \quad (3.36)$$

with  $\{\psi_i\}$  being the set of all singly excited Slater determinants and  $\{\psi_{ij}\}$  being the set of all doubly excited Slater determinants<sup>6</sup>. Inclusion of independent electron excited states, provides the approximate wave function the mathematical flexibility to model the individual response of one electron to another. So the inclusion of independent electron excited states equates to the inclusion of correlation effects, but at the cost of making the calculation exponentially more costly. A number of methods approximate this expansion to capture most of the correlation effects at reduced cost (Coupled cluster [50], Configuration interaction [51], Møller-Plesset perturbation theory [52]).

The effects of correlation and the associated correlation energy are thus the hardest part to accurately model in quantum mechanical simulations. The definition of correlation itself is a bit circular. Exchange interaction certainly is a correlation

---

<sup>6</sup>The ground state determinant is  $|\phi_1(\mathbf{r}_1)\phi_2(\mathbf{r}_2)\cdots\phi_i(\mathbf{r}_i)\cdots\phi_N(\mathbf{r}_N)|$ , with  $N$  the number of electrons. A singly excited determinant, with excited state  $j$ ,  $j > N$ , has a single particle excited state of electron  $i$  yielding  $|\phi_1(\mathbf{r}_1)\phi_2(\mathbf{r}_2)\cdots\phi_j(\mathbf{r}_i)\cdots\phi_N(\mathbf{r}_N)|$ .

effect between electrons of the same spin, but correlation is defined as the difference between the best possible HF result and the exact result. Typically, correlation energies are quite small in comparison to the total energy of the system. Unfortunately, the energy differences between different molecular structures or different chemical environments are of the same order of magnitude or even smaller. Despite the small absolute contribution correlation effects may have a large impact on chemical properties. In the next section we discuss a different approach to approximately handle correlation effects at low computational cost.

## 3.2 Density functional theory

In the last section we introduced the electronic wave function of an  $N$ -electron system,  $\psi(\mathbf{r}_1, \mathbf{r}_2, \dots, \mathbf{r}_N)$ , which depends on  $3N$  coordinates and is difficult to model mathematically. Even worse, it is not an observable of the physical system. We can measure the electron density  $n$ , which is related to  $\psi$  via

$$n(\mathbf{r}_1) = N \int d^3\mathbf{r}_2 \dots d^3\mathbf{r}_N |\psi(\mathbf{r}_1, \mathbf{r}_2, \dots, \mathbf{r}_N)|^2. \quad (3.37)$$

This is a simple quantity as it only depends on one position alone. To be coherent with literature we will drop the index on  $\mathbf{r}_1$  now and instead only write  $\mathbf{r}$ , which only refers to one position. The electron density describes how the electrons arrange themselves in a molecule. They will certainly do so to minimize the total energy of the system. So it is not unreasonable to assume that the total energy of the system is a functional of the electron density. It turns out you actually can write the total energy as a functional of the electron density, which naturally led to the name Density functional theory or in short DFT.

The inventors of DFT, Hohenberg and Kohn, proved that the total energy is a functional of the density,  $E_{\text{tot}}[n]$ , and furthermore that the approach is even variational [53]. The correct electron density will yield the lowest total energy  $E_{\text{tot}}$ :

$$E_{\text{tot}}[n] \geq E_{\text{tot}}[n_0] \equiv E_0, \quad (3.38)$$

where  $E_0$  is the energy of the ground state and  $n_0$  the corresponding ground state density. This furthermore means that at the ground state the functional derivative of  $E_{\text{tot}}$  with respect to the density must be zero:

$$\left. \frac{\delta E_{\text{tot}}[n]}{\delta n} \right|_{n=n_0} = 0. \quad (3.39)$$

This allows you to actually find  $n_0$  and consequently  $E_0$ . The challenge here is to find an explicit form for  $E_{\text{tot}}[n]$

$$E_{\text{tot}}[n] = E_{\text{nuc-el}}[n] + T_{\text{el}}[n] + E_{\text{el-el}}[n] + E_{\text{xc}}[n]. \quad (3.40)$$

Only  $E_{\text{nuc-el}}[n]$  explicitly depends on the nuclear coordinates and charges, whereas all other terms solely describe electron behavior and are thus chemistry independent. The functional form of the classical electrostatic contributions  $E_{\text{el-el}}$  and  $E_{\text{nuc-el}}$  are well known:

$$E_{\text{el-el}}[n] = \frac{1}{2} \iint d^3\mathbf{r} d^3\mathbf{r}' \frac{n(\mathbf{r})n(\mathbf{r}')}{|\mathbf{r}-\mathbf{r}'|} \quad (3.41)$$

$$E_{\text{nuc-el}}[n] = \int d^3\mathbf{r} \hat{V}_{\text{nuc-el}}(\mathbf{r})n(\mathbf{r}), \quad (3.42)$$

where  $\hat{V}_{\text{nuc-el}}$  is the nuclear potential defined in eq. 3.6. Nobody knows how to exactly calculate the kinetic energy from the electron density and so the exact functional form of  $T_{\text{el}}[n]$  is unknown. The same holds for the exchange-correlation functional  $E_{\text{xc}}[n]$ . A first approximation to  $T_{\text{el}}[n]$  is the Thomas-Fermi functional [54]:

$$T_{\text{el}}^{\text{TF}}[n] = \frac{3}{10} \left( \frac{3}{8\pi} \right)^{2/3} \int d^3\mathbf{r} n(\mathbf{r})^{5/3}. \quad (3.43)$$

Combining it with an  $E_{\text{xc}}[n]$  functional leads to orbital-free DFT. It offers a very simple and cheap way to arrive at an electron density but unfortunately it can neither predict the shell structure of individual atoms nor does it predict even simple molecules to be stable [55]. This failure directly derives from the failure of purely density dependent functionals as the Thomas Fermi functional.

To better approximate the real kinetic energy functional, a different approach was devised by Kohn and Sham [56]. They postulated that as the electron density is the fundamental quantity, the real wave function is important but instead a factious

wave function can be used, as long as it produces the same density. So they imagined this density not coming from the real complicated  $N$ -electron wave function  $\psi$  but from a system of non-interacting fermions:

$$n(\mathbf{r}) = \sum_{i=1}^N \phi_i^{\text{KS}}(\mathbf{r})^2, \quad (3.44)$$

where the  $\phi_i^{\text{KS}}$  are the single particle wave functions for the non-interacting fermions, also called Kohn-Sham (KS) wave functions. This allows us to use the formalism of non-interacting particles, which we developed earlier. As before we drop the KS label and reintroduce it at the end of the section. We can now rewrite eq. 3.40 as

$$E_{\text{tot}}[n] = T_{\text{el}}^{\text{KS}}[n] + \int d^3\mathbf{r} \hat{V}_{\text{nuc-el}}(\mathbf{r})n(\mathbf{r}) + \frac{1}{2} \iint d^3\mathbf{r} d^3\mathbf{r}' \frac{n(\mathbf{r})n(\mathbf{r}')}{|\mathbf{r}-\mathbf{r}'|} + \underbrace{E_{\text{xc}}}_{E_{\text{xc}}[n] + (T_{\text{el}}[n] - T_{\text{el}}^{\text{KS}}[n])} \quad (3.45)$$

As  $\tilde{E}_{\text{xc}}$  can only be approximated anyway, the distinction between  $\tilde{E}_{\text{xc}}$  and  $E_{\text{xc}}$  is commonly ignored. One should still be aware though that the kinetic energies can differ significantly if there is not at least some similarity between the KS-system and the real system.

We first ignore the issue of  $E_{\text{xc}}$  and derive an equation for  $\phi_i^{\text{KS}}$ , from which  $n$  and then  $E_0$  can be calculated. Eq. 3.39 says that we have to find a stationary point of the energy with respect to density. Unfortunately, the kinetic energy is a function of  $\phi_i$ , so instead we vary the set of  $\phi_i$ , i.e.,

$$\frac{\delta E_{\text{tot}}}{\delta \phi_i} = 0. \quad (3.46)$$

So we have a set of equations, one for every  $\phi_i$ . We cannot vary the  $\phi_i$  freely but have to modify them in a way which forces them to remain orthonormal to each other

$$\int d^3\mathbf{r} \phi_i(\mathbf{r})\phi_j(\mathbf{r}) = \delta_{ij}, \quad (3.47)$$

where  $\delta_{ij}$  is the Kronecker-symbol. This is a constrained optimization, which is mathematically implemented by adding Lagrange multipliers  $\epsilon_{ij}$ , which enforce the orthonormality constraint according to

$$\frac{\delta}{\delta\phi_i} \left[ E_{\text{tot}}[n] - \sum_{j,k} \epsilon_{jk} \left( \int d^3\mathbf{r} \phi_k \phi_j - \delta_{jk} \right) \right] = 0. \quad (3.48)$$

Inserting equation eq. 3.45 into eq. 3.48 yields:

$$\begin{aligned} 0 &= \frac{\delta}{\delta\phi_i} \left[ E_{\text{tot}} - \sum_{j,k} \epsilon_{jk} \left( \int d^3\mathbf{r} \phi_k \phi_j - \delta_{jk} \right) \right] \quad (3.49) \\ &= \frac{\delta}{\delta\phi_i} E_{\text{tot}} - 2 \sum_j \epsilon_{i,j} \phi_j + 0 \\ 2 \sum_j \epsilon_{i,j} \phi_j &= \frac{\delta}{\delta\phi_i} \left[ T_{\text{el}}^{\text{KS}}[n] + \int d^3\mathbf{r} \hat{V}_{\text{nuc-el}}(\mathbf{r}) n(\mathbf{r}) + \frac{1}{2} \iint d^3\mathbf{r} d^3\mathbf{r}' \frac{n(\mathbf{r})n(\mathbf{r}')}{|\mathbf{r}-\mathbf{r}'|} + E_{\text{xc}} \right] \\ &= \frac{\delta}{\delta\phi_i} T_{\text{el}}^{\text{KS}}[n] + \frac{\delta}{\delta n} \left[ \int d^3\mathbf{r} \hat{V}_{\text{nuc-el}}(\mathbf{r}) n(\mathbf{r}) + \frac{1}{2} \iint d^3\mathbf{r} d^3\mathbf{r}' \frac{n(\mathbf{r})n(\mathbf{r}')}{|\mathbf{r}-\mathbf{r}'|} + E_{\text{xc}} \right] \frac{\partial n}{\partial\phi_i} \\ &= \frac{\delta}{\delta\phi_i} T_{\text{el}}^{\text{KS}}[n] + \left[ \hat{V}_{\text{nuc-el}} + \underbrace{\int d^3\mathbf{r}' \frac{n(\mathbf{r}')}{|\mathbf{r}-\mathbf{r}'|}}_{=V_H} + V_{\text{xc}} \right] \frac{\partial n}{\partial\phi_i}. \quad (3.50) \end{aligned}$$

We simply defined  $\frac{\delta E_{\text{xc}}[n]}{\delta n} = V_{\text{xc}}$  to be the exchange-correlation potential,  $V_{\text{xc}}$ , used the definition of  $V_H$  and used the chain rule in the third step.

Using

$$\frac{\partial n}{\partial\phi_i} = \frac{\partial \sum_j \phi_j^2}{\partial\phi_i} = 2 \sum_j \epsilon_{ij} \phi_j \quad (3.51)$$

we arrive at

$$\frac{\delta}{\delta\phi_i} T_{\text{el}}^{\text{KS}}[n] + [\hat{V}_{\text{nuc-el}} + V_H + V_{\text{xc}}] 2\phi_i = 2 \sum_j \epsilon_{ij} \phi_j. \quad (3.52)$$

We focus on the derivative of the kinetic energy, which for a non interacting system is defined as:

$$T_{\text{el}}^{\text{KS}}[n] = -\frac{1}{2} \sum_i \int d^3\mathbf{r} \phi_i \nabla^2 \phi_i. \quad (3.53)$$

$$\frac{\delta T_{\text{el}}^{\text{KS}}[n]}{\delta \phi_i} = -\frac{1}{2} \frac{\delta}{\delta \phi_i} \sum_j \int d^3 \mathbf{r} \phi_j \nabla^2 \phi_j \quad (3.54)$$

$$= -\frac{1}{2} \sum_j \left( \delta_{ij} \nabla^2 \phi_j + \nabla^2 \phi_j \delta_{ij} + \underbrace{\text{surface terms}}_{=0} \right) \quad (3.55)$$

$$= -\frac{2}{2} \nabla^2 \phi_i \quad (3.56)$$

Inserting the result into eq. 3.53 and dividing by 2, we arrive at

$$\underbrace{\left[ -\frac{1}{2} \nabla^2 + \hat{V}_{\text{nuc-el}} + V_{\text{H}}[n] + V_{\text{xc}}[n] \right]}_{\hat{H}^{\text{DFT}}[n]} \phi_i = \sum_j \epsilon_{ij} \phi_j. \quad (3.57)$$

As the total electron density is invariant under rotation of the  $\phi_i$ , we choose a set of  $\phi_i$ , which diagonalize  $\epsilon_{ij}$  and denote them as  $\phi_i^{\text{KS}}$ , leading to

$$\hat{H}^{\text{DFT}}[n] \phi_i^{\text{KS}}(\mathbf{r}) = \epsilon_i^{\text{KS}} \phi_i^{\text{KS}}(\mathbf{r}). \quad (3.58)$$

This resembles a Schrödinger equation of the full system but it is not. It describes a fictional system of non-interacting particles, whose density is identical to the density of the real system.

The Kohn-Sham energies  $\epsilon_i^{\text{KS}}$  are not physical energies, they are simply Lagrange parameters to enforce orthogonality of the Kohn-Sham orbitals.  $\phi_i^{\text{KS}}$  in eq. 3.58 depends on  $n$ , which in turn depends on  $\phi_i^{\text{KS}}$ . Thus the problem of self-consistency as discussed for the Hartree-Fock approach appears again. Eq. 3.58 also resembles the Hartree-Fock equation (eq. 3.33), but there are important differences. Hartree-Fock is an approximate theory, as it uses a product of single particle wave functions to model the exact wave function, but can be solved exactly. In contrast, DFT is an exact theory, where the exchange correlation potential  $V_{\text{xc}}$  encapsulates all the effects of many-particle quantum mechanics. Its exact form is unknown and, though, in principle DFT is an exact theory, approximations to  $V_{\text{xc}}$  have to be used, which we will discuss in the next section.



### 3.2.1 Exchange-correlation functionals

In density functional theory all the many-body complications are buried in the exchange-correlation functional  $V_{xc}$ . Unfortunately, the exact form of  $V_{xc}$  is not known and thus it has to be approximated. Nowadays, a large zoo of exchange correlation functionals exist, which can produce very different results. Most functionals in use today are either fitted to reproduce experimental or wave function method data e.g. B3LYP [57, 58] or interpolate between limiting cases, where the result for the exact  $V_{xc}$  is known e.g. PBE [59].

The first and simplest approximation ignores the impact of the external potential and takes the exchange and the correlation part from the homogeneous electron gas and assumes that it is also locally valid for a spatially varying density  $n(\mathbf{r})$ . In this approximation  $V_{xc}$  only depends on the local density and thus is known as the Local Density Approximation or LDA. LDA yields poor thermochemistry data for most molecules and other systems with strongly varying electron density [60].

To improve on the LDA,  $V_{xc}$  is assumed to not only depend on  $n(\mathbf{r})$  but also on the density gradient  $|\nabla n(\mathbf{r})|$ . This is known as the Generalized Gradient Approximation. Functionals belonging to this group are commonly denoted as GGAs. An often used example is PBE [59], which significantly improves on LDA for most systems. The inclusion of  $|\nabla n(\mathbf{r})|$  takes the immediate vicinity around  $\mathbf{r}$  into account. Consequently these functionals are also referred to as semi-local.

As the exact exchange-correlation functional is known to be non-local, many functionals mix the GGAs with some portion of exact Hartree Fock exchange  $V_x^{HF}$  (see eq. 3.35)[61]

$$V_{xc} = V_c^{GGA} + \alpha^m V_x^{HF} + (1 - \alpha^m) V_x^{GGA}, \quad (3.59)$$

with  $\alpha^m$  ranging from 0.2 to 0.5 for most functionals. The most prominent examples are B3LYP ( $\alpha^m = 0.2$ ) and PBE0 ( $\alpha^m = 0.25$ ) [62], which yield improved results for thermo chemistry, geometries and energies, especially for molecular systems.

A critical shortfall of the approximate  $V_{cc}$  functionals is the wrong long-range behavior, as the real  $V_{cc}$  is known to decay as  $1/r$ , whereas GGAs in the asymptotic limit fall off proportional to the density as  $\propto \exp(-r)$  and hybrid functionals fall off as  $\alpha^m/r$ . This is especially problematic for the treatment of spatially separated charge transfer states, which are ubiquitous in organic electronic systems [63].

Range-separated functionals can partially overcome this weakness. Here  $a^m$  is replaced by a range dependent cutoff function  $c(\mathbf{r})$ , typically  $c(\mathbf{r}) = \text{erf}(\mu|\mathbf{r}|)$ , with  $\text{erf}$  the error function and  $\mu$  as a cutoff parameter. Thus at short ranges, DFT exchange is used, whereas at long separations only exact Hartree Fock exchange is used, giving the correct asymptotic behavior. Although this approach alleviates the DFT problems with charge transfer states, transferability and generality of these functionals is limited. Often the parameter  $\mu$  is optimized for a specific system to agree with quantum chemistry or experimental results, reducing the predictive capabilities of DFT [64].

Due to the approximate treatment of correlation effects in current exchange-correlation functionals, dispersive interaction between molecules is not modeled. There is a number of solutions to this problem from empirical forcefields [65] or introducing correlation effects from higher order wave function methods [66, 67]. Despite all these problems, DFT offers excellent results for a wide variety of systems, as the application range and validity of the common functionals is well-established [64, 68–70].

### 3.2.2 Basis functions

In the beginning of the chapter we mentioned optimizing single-particle wave functions,  $\phi_i(\mathbf{r})$ . But what exactly do we optimize? This question is intimately related with the task of representing  $\phi(\mathbf{r})$  on a computer efficiently. As  $\phi_i(\mathbf{r})$  has a certain value at every point and consequently, infinitely many points, an exact representation is impossible. Instead  $\phi(\mathbf{r})$  is expanded in some finite basis with  $M$  basis functions  $\chi_m(\mathbf{r})$  and expansion coefficients  $X_{im}$

$$\phi_i(\mathbf{r}) = \sum_{j=1}^M X_{ij} \chi_j(\mathbf{r}). \quad (3.60)$$

If we insert this into eq. 3.58 and multiply from the left with  $\chi_k(\mathbf{r})$ , we arrive at

$$\sum_{j=1}^M \underbrace{\langle \chi_k | \hat{H}^{\text{DFT}} | \chi_j \rangle}_{\mathbf{E}_{kj}} X_{ij} = \sum_{j=1}^M \underbrace{\langle \chi_k | \chi_j \rangle}_{\mathbf{S}_{kj}} X_{ij} \epsilon_i. \quad (3.61)$$

The expectation value of the DFT Hamiltonian and the basis functions is typically called the *Fock-Matrix*  $\mathbf{E}$ , whereas the overlap between basis functions  $\langle \chi_k | \chi_j \rangle$  is

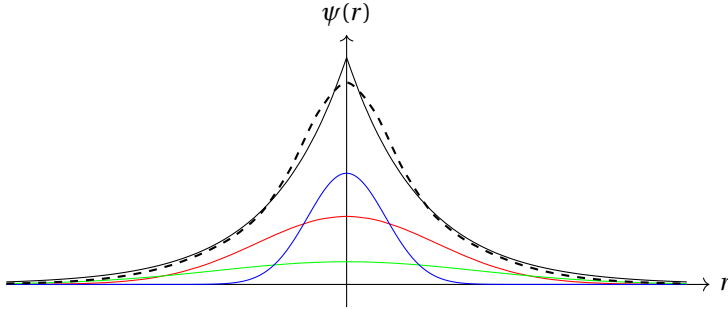


Figure 3.3: Decomposition of a wave function into basis functions. To approximate the real wave function (black line) a linear combination of Gaussian basis functions can be used. A linear combination of Gaussians with different decay coefficients yields an approximation but fails to capture the cusp at  $r = 0$  and the correct exponential decay.

called the *overlap matrix*  $\underline{\mathbf{S}}$ .

In matrix notation this reduces to:

$$\underline{\mathbf{F}}\underline{\mathbf{X}}_i = \epsilon_i \underline{\mathbf{S}}\underline{\mathbf{X}}_i. \quad (3.62)$$

The electron density, defined before in eq. 3.44, can then be rewritten as:

$$n(\mathbf{r}) = \sum_{i=1}^N |\phi_i(\mathbf{r})|^2 = \sum_{i=1}^N \sum_{j=1}^M X_{ij} \chi_j(\mathbf{r}) \sum_{k=0}^M X_{ik} \chi_k(\mathbf{r}) = \sum_{jk} \underline{\mathbf{D}}_{kj} \chi_j(\mathbf{r}) \chi_k(\mathbf{r}). \quad (3.63)$$

Here we introduce  $\underline{\mathbf{D}}$ , the *density matrix*:

$$\underline{\mathbf{D}}_{kj} = \sum_{i=1}^N X_{ik} X_{ij}, \quad (3.64)$$

which is the representation of electron density in the basis of Kohn-Sham orbitals.

Which kind of basis function should you choose? On the one hand basis functions should be as close as possible to  $\phi(\mathbf{r})$ , as it allows to keep the number of basis functions  $M$  small, which reduces matrix sizes and computational effort. On the other hand integrals over basis functions like  $\langle \chi_k | \hat{H}^{\text{DFT}} | \chi_j \rangle$  should be easy to

calculate. A third consideration is how to approach the limit of an exact basis. Preferably increasing the number of basis functions  $M$  should converge results towards the limit of a complete basis. This is not necessarily true for non-orthogonal basis sets, where  $\langle \chi_k | \chi_j \rangle \neq \delta_{kj}$ . Adding more functions to a non-orthogonal basis can lead to linear dependencies and finally numerical problems. All basis sets are different compromises between these considerations. A few options for finite, i.e., non-periodic, systems will be presented below.

1. Numerical orbitals represent  $\phi(\mathbf{r})$  as a large array of  $\phi(\mathbf{r}_i)$  for many  $\mathbf{r}_i$ . This allows for great flexibility, but integrals over operators require numerical integration and thus are rather slow. As the value of  $\phi$  at every grid point  $\mathbf{r}_i$  could be varied, the number of optimization parameters is extremely large. Instead groups of grid points with fixed ratios are used and only the coefficients for these groups are optimized.
2. For molecular systems using linear combinations of solutions to the hydrogen atom, so called Slater Type Orbitals or STOs are useful. They, as the real wave function, decay as  $\exp(-|\mathbf{r}|)$  and have cusps at the atomic nuclei. Their functional form is  $\chi(\mathbf{r}) = N_{l,\alpha} Y_{lm}(v, \phi) |\mathbf{r}|^l \exp(-\alpha|\mathbf{r}|)$ , with normalization constant  $N_{l,\alpha}$  and spherical harmonic  $Y_{lm}(v, \phi)$ <sup>7</sup>. The exponential form does not lead to easy evaluation of integrals, as all integrals of basis functions with operators have to be evaluated numerically. Due to their similarity to the orbitals of the hydrogen atom, these functions are also named as  $s, p, d, f, \dots$  depending on the value of  $l$  (0,1,2,3...). All functions with the same  $l$  and  $\alpha$  are collectively referred to as a shell. A big disadvantage of STOs is, that they do not form an orthogonal basis. So adding more basis functions does not guarantee convergence towards the infinite basis limit controlled by a single parameter. Instead individual sets of basis functions for each element were created by hand. These basis sets differ in size and composition and are benchmarked to yield results up to a given accuracy.
3. A less accurate but much faster alternative to STOs is to use Gaussian Type Orbitals or GTOs. Their functional form  $\chi(\mathbf{r}) = N_{l,\alpha} Y_{lm}(v, \phi) r^l \exp(-\alpha r^2)$  allows all but the  $V_{cc}$  matrix elements to be evaluated analytically, accelerating calculations massively[71]. As they do not really resemble real molecular orbitals, linear combinations of GTOs are used to approximate one STO. These

---

<sup>7</sup> $\phi$  here simply denotes an angle not any sort of wave function.

are called contractions:

$$\chi(\mathbf{r}) = \sum_i c_i N_{l,\alpha_i} Y_{lm} |\mathbf{r}|^l \exp(-\alpha_i |\mathbf{r}|^2) \quad (3.65)$$

with fixed contraction coefficients  $c_i$ . Due to the contractions, GTO implementations have to evaluate many more integrals than STO codes but even then GTO evaluation is still much faster than numerical integration over STOs. Unfortunately, GTOs are neither able to simulate the cusp at the nuclei positions nor the correct exponential asymptotic decay of the wave function (see Fig. 3.3). Otherwise they share all the same advantages and disadvantages of STOs and, especially, due to the speed advantage over STOs a large library of basis sets exists. A widely used example is the def2-svp basis set [72], which for carbon has: 3 contracted  $s$ -shells, 2 contracted  $p$ -shells and 1 simple  $d$ -shell for a total of  $3 \cdot 1 + 2 \cdot 3 + 1 \cdot 5 = 14$  variable coefficients. The functions of the  $d$ -shell are referred to as polarization functions, as they are not needed for the isolated atom, but add more degrees of freedom to allow the electron cloud to be polarized in a molecular environment.

Basis sets enable us to express the quantum mechanical equations of infinite dimensions, as a finite dimensional matrix equations. We want these basis sets to be as complete as possible but also as small as possible to reduce the computational cost. One approach, described in the next section, is to reduce the number of electrons taken explicitly into account, which cuts the number of basis functions needed for a specific accuracy.

### 3.2.3 Pseudo potentials

The properties of most molecules and solid state systems are governed by the outer shell electrons, also referred to as valence electrons. The core electrons are typically energetically separated by multiple eV from the valence electrons and hardly contribute to the chemical properties: in carbon the Kohn-Sham energies of the  $1s$  core electrons are separated by about 260 eV<sup>8</sup> from the valence  $2s$  electrons. Despite hardly contributing to the chemical properties, the description of the spatially localized core electrons requires many additional basis functions. Especially the valence electron states oscillate rapidly in the core region because they have to be orthogonal to the core states (see Fig. 3.4). To reduce the computational cost, the

<sup>8</sup>single atom, ORCA-PBE/def2-svp  $\epsilon_0 = -273.1191$  eV and  $\epsilon_1 = -13.0731$  eV

core electrons and the nucleus are replaced by a pseudo potential, which is much smoother in the core region, typically defined by a cutoff  $r_c$ . Outside the cutoff the pseudo potential exactly reproduces the combined behavior of the nucleus and the core electrons.

Pseudo potentials require that we can energetically separate the electronic states  $|\phi\rangle$  into valence  $|\phi^v\rangle$  and core states  $|\phi_n^c\rangle$

$$|\phi\rangle = |\phi^v\rangle + \sum_n a_n |\phi_n^c\rangle. \quad (3.66)$$

As  $|\phi^v\rangle$  must be orthogonal to all core states, the  $a_n$  coefficients are fixed via:

$$\langle \phi_n^c | \phi \rangle = \langle \phi_n^c | \phi^v \rangle + a_n = 0. \quad (3.67)$$

For  $|\phi\rangle$  we then find:

$$|\phi\rangle = |\phi^v\rangle - \sum_n |\phi_n^c\rangle \langle \phi_n^c | \phi^v \rangle. \quad (3.68)$$

Inserting eq. 3.68 into the electronic Schrödinger equation (see eq. 3.9)  $\hat{H}_{\text{el}}|\phi\rangle = E|\phi\rangle$  and assuming that the core state problem can be solved, e.g.  $\hat{H}_{\text{el}}|\phi_n^c\rangle = E_n^c|\phi_n^c\rangle$  leads to:

$$\hat{H}_{\text{el}}|\phi^v\rangle - \sum_n E_n^c |\phi_n^c\rangle \langle \phi_n^c | \phi^v \rangle = E \left( |\phi^v\rangle - \sum_n |\phi_n^c\rangle \langle \phi_n^c | \phi^v \rangle \right), \quad (3.69)$$

which can be rearranged to give an effective Schrödinger equation for the valence states with a non-local pseudo potential.

$$[\hat{H}_{\text{el}} + \underbrace{\sum_n (E - E_n^c) |\phi_n^c\rangle \langle \phi_n^c|}_{\hat{V}_{\text{pseudo}}}] |\phi^v\rangle = E |\phi^v\rangle. \quad (3.70)$$

$\hat{V}_{\text{pseudo}}$  depends on  $E$  but if  $(E - E_n^c)$  is large, e.g. core and valence levels are well separated, then replacing  $E$  by the atomic valence energy for  $|\phi^v\rangle$  is a reasonable approximation. To increase the transferability of the pseudo potential  $E$  is chosen in order to obtain the same scattering properties for the all-electron and the pseudo

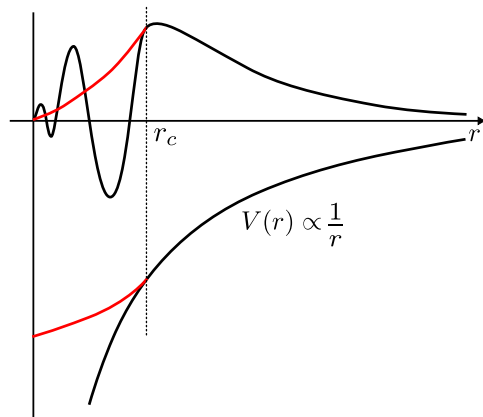


Figure 3.4: Pseudo potential and real potential and the corresponding wave functions. The pseudo potential (lower red line) is constructed to avoid the singularity at  $r = 0$  (black line) of the Coulomb potential. Omission of core states leads to a much smoother wave function (upper red line). Beyond the cutoff  $r_c$  the all-electron wave function (upper black line) and the pseudo wave function agree.

potential case. This requires the radial part  $R_l^{\text{all}}$  and  $R_l^{\text{pseudo}}$  for an atomic all-electron and pseudo potential calculation at given angular momentum  $l$  to fulfill:

$$\int_0^{r_c} r^2 R_l^{\text{all}}(r) dr = \int_0^{r_c} r^2 R_l^{\text{pseudo}}(r) dr. \quad (3.71)$$

Pseudo potentials which fulfill this condition are called norm-conserving.

Pseudo potentials greatly reduce the number of basis functions needed to describe a molecule within a given accuracy, especially for heavy elements with hundreds of core electrons. Furthermore, as the pseudo potential is typically constructed from an atomic all-electron calculation of the element in question, relativistic core-corrections can be incorporated without having to modify the rest of the DFT procedure. Despite these advantages, pseudo potentials introduce a lot of additional parameters into the calculation. These approximations can reduce the accuracy of a calculation, as the separation into valence and core orbitals, the reference all-electron calculation for the construction and the choice of the cutoff  $r_c$  limit the transferability of the pseudo potential from one chemical environment to another. The ambiguity in the construction lead to the creation of a zoo of pseudo potentials, all optimized towards different objectives.

### 3.3 Electronically excited states via *GW*-BSE

Whereas density functional theory has done an excellent job at calculating ground state properties even of larger systems, excited state properties are still very much harder to compute. *GW*-BSE describes the behavior of electron- and hole-like excitations on the ground state electron configuration. Originally more rooted in the solid-state community, it has recently received increasing attention from several groups for the treatment of electronically excited states of molecular systems [73–76]. It can in contrast to time dependent density functional theory (TDDFT) describe localized (Frenkel) and bimolecular charge transfer (CT) excitons on an equal footing [75, 77, 78] because it correctly accounts for long and short ranged interaction. Its computational footprint is close to that of TDDFT but avoids the weaknesses of the exchange correlation functional. For molecules using efficient localized orbital based implementations *GW*-BSE can be readily applied to molecules or clusters of molecules of technological relevance [79–81].

Before we recapitulate the major concept behind *GW*-BSE, let us emphasize that to keep the notation simple we restrict the discussion to the following case. We consider a closed shell system, with a total spin of 0, allowing us to neglect spin, as we did in the previous paragraph. Furthermore we again work in the Born-Oppenheimer approximation: the geometry of the molecule is fixed, the electron-phonon interaction and with it satellite peaks and geometry reorganization are not taken into account.

#### 3.3.1 One-particle-excitations

*GW*-BSE builds on Green's function theory of many-particle systems. As a starting point we go back to the electronic Hamiltonian  $\hat{H}_{el}$  (eq. 3.19) and rewrite it in second quantization,

$$\hat{H}_{el} = \int d^3\mathbf{r} \hat{\phi}^\dagger(\mathbf{r}) h(\mathbf{r}) \hat{\phi}(\mathbf{r}) + \frac{1}{2} \iint d^3\mathbf{r} d^3\mathbf{r}' \hat{\phi}^\dagger(\mathbf{r}) \hat{\phi}^\dagger(\mathbf{r}') v(\mathbf{r}, \mathbf{r}') \hat{\phi}(\mathbf{r}) \hat{\phi}(\mathbf{r}'), \quad (3.72)$$

with  $h(\mathbf{r})$  the single particle Hamiltonian operator in real space, defined in eq. 3.21, and  $v(\mathbf{r}, \mathbf{r}') = |\mathbf{r} - \mathbf{r}'|^{-1}$ .  $\hat{\phi}^\dagger$  ( $\hat{\phi}$ ) is the single particle electron creation (annihilation) operators for the single particle wave function:



$$\hat{\phi}^\dagger(\mathbf{r}) = \sum_i \phi_i(\mathbf{r}) \hat{a}_i^\dagger. \quad (3.73)$$

The one-particle Green's function  $G_1$  then is:

$$G_1(\mathbf{r}t, \mathbf{r}'t') = -i \langle n, 0 | \hat{T} \left[ \hat{\phi}(\mathbf{r}t) \hat{\phi}^\dagger(\mathbf{r}'t') \right] | n, 0 \rangle, \quad (3.74)$$

with  $|n, s\rangle$  being the  $n$ -electron  $s$ -th excited state of the system with Hamiltonian  $\hat{H}_{\text{el}}$ :

$$\hat{H}_{\text{el}} |n, 0\rangle = E_{n,0} |n, 0\rangle, \quad \hat{H}_{\text{el}} |n+1, s\rangle = E_{n+1,s} |n+1, s\rangle. \quad (3.75)$$

$\hat{T}$  is the fermionic time ordering operator, which with the help of the Heaviside function,  $\Theta(t-t')$ , can be written as:

$$\hat{T} \left[ \hat{\phi}(\mathbf{r}t) \hat{\phi}^\dagger(\mathbf{r}'t') \right] = \Theta(t-t') \hat{\phi}(\mathbf{r}t) \hat{\phi}^\dagger(\mathbf{r}'t') - \Theta(t'-t) \hat{\phi}(\mathbf{r}'t') \hat{\phi}^\dagger(\mathbf{r}t), \quad (3.76)$$

where  $\hat{\phi}^\dagger(\mathbf{r}t)$  ( $\hat{\phi}(\mathbf{r}t)$ ) is a single particle electron creation (annihilation) operator in the Heisenberg picture, i.e.,  $\hat{\phi}(\mathbf{r}t) = \exp(i\hat{H}t) \hat{\phi}(\mathbf{r}) \exp(-i\hat{H}t)$ .

The 1-particle Green's function describes single particle-like excitation processes in which an electron is added to ( $n \rightarrow n+1$ ) (or removed from ( $n \rightarrow n-1$ )) the system, propagated from  $t$  to  $t'$  and then removed (added) as schematically shown in Fig. 3.5. The process of removing or adding an additional electron corresponds to the experimental photo emission or inverse photo emission effect, respectively (see Fig. 3.6). Note that the single particles we insert into the many body system are not eigenstates of  $\hat{H}_{\text{el}}$ , so they do not have an eigenenergy. When they are propagated in time the inserted particles will spread out until they are completely delocalized. If the delocalization happens slowly we can describe the evolution of the whole many body system as the evolution of one particle with finite lifetime, or a complex energy. The lifetime then will depend on the "how much" the many body system deviates from the independent particle picture, i.e., how strong correlation is.

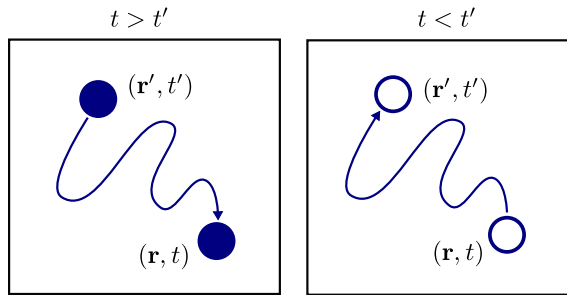


Figure 3.5: Single particle Green's function for different time arguments. (a) For  $t > t'$  create electron at  $(\mathbf{r}', t')$ , propagate and then annihilate at  $(\mathbf{r}, t)$ . (b) For  $t' > t$  annihilate electron (create hole) at  $(\mathbf{r}, t)$ , propagate and then create electron (annihilate hole) at  $(\mathbf{r}', t')$ .

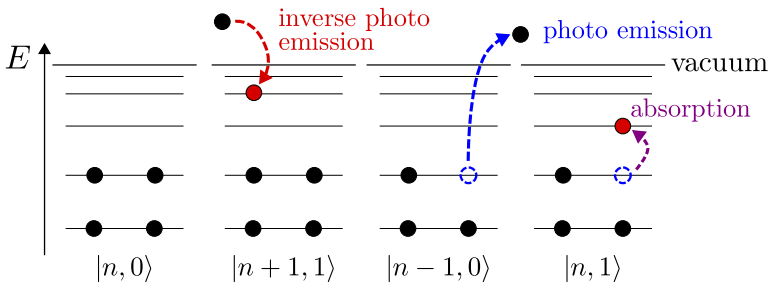


Figure 3.6: Ground state and excited states of a many-particle system. The inverse photo emission adds an outside electron to the system. The properties of that additional electron are described by  $G_1$  for  $t > t'$ . Photo emission removes one electron from the system and creates a hole, which is described by  $G_1$  for  $t' > t$ . The excitation of an electron to a higher state is a two-particle process, creation of an electron and a hole requires a 2-particle Green's function.

Excitation energies can be calculated from:

$$\begin{aligned}
\langle n, 0 | \hat{\phi}(\mathbf{r}t) | n+1, s \rangle &= \langle n, 0 | \exp(i\hat{H}t) \hat{\phi}(\mathbf{r}) \exp(-i\hat{H}t) | n+1, s \rangle \\
&= \langle n, 0 | \exp(iE_{n,0}t) \hat{\phi}(\mathbf{r}) \exp(-iE_{n+1,s}t) | n+1, s \rangle \\
&= \underbrace{\langle n, 0 | \hat{\phi}(\mathbf{r}) | n+1, s \rangle}_{f_s(\mathbf{r})} \exp \left[ -i \underbrace{(E_{n+1,s} - E_{n,0})}_{\varepsilon_s} t \right]. \quad (3.77)
\end{aligned}$$

A useful representation of  $G_1$  can be derived from eq. 3.74, where we assume  $t > t'$  for simplicity:

$$\begin{aligned}
G_1(\mathbf{r}t, \mathbf{r}'t') &= -i \langle n, 0 | \hat{\phi}(\mathbf{r}t) \hat{\phi}^\dagger(\mathbf{r}'t') | n, 0 \rangle \\
&= -i \langle n, 0 | \exp(i\hat{H}t) \hat{\phi}(\mathbf{r}) \exp(-i\hat{H}t) \exp(i\hat{H}t') \hat{\phi}^\dagger(\mathbf{r}') \exp(-i\hat{H}t') | n, 0 \rangle \\
&= -i \langle n, 0 | \hat{\phi}(\mathbf{r}) \exp[-i(\hat{H} - E_{n,0})(t - t')] \hat{\phi}^\dagger(\mathbf{r}') | n, 0 \rangle \\
&= -i \sum_s f_s(\mathbf{r}) f_s^*(\mathbf{r}') \exp[-i(E_{n+1,s} - E_{n,0})(t - t')]. \quad (3.78)
\end{aligned}$$

In the last line we used the identity  $\sum_s |n+1, s\rangle \langle n+1, s| = \hat{1}$  and eq. 3.77. Switching from the time to the frequency domain via Fourier transformation  $(t - t') \rightarrow \omega$  leads to

$$G_1(\mathbf{r}, \mathbf{r}', \omega) = \sum_s \frac{f_s(\mathbf{r}) f_s^*(\mathbf{r}')}{\omega - \varepsilon_s - i\eta}, \quad (3.79)$$

where we introduced a small imaginary part  $\eta$  to ensure convergence of the Fourier transform. Eq. 3.79 is the spectral representation of the Green's function.

From the equation of motion of the field operators in the Heisenberg picture,

$$i \frac{\partial}{\partial t} \hat{\phi}(\mathbf{r}, t) = [\hat{\phi}(\mathbf{r}, t), \hat{H}], \quad (3.80)$$

we can derive an equation of motion for the Green's function  $G_1$ :

$$\left[ \frac{\partial}{\partial t} - \hat{h} \right] G_1(\mathbf{r}t, \mathbf{r}'t') + i \int d^3\mathbf{r}'' v(\mathbf{r}, \mathbf{r}'') G_2(\mathbf{r}''t, \mathbf{r}'t', \mathbf{r}'t', \mathbf{r}t) = \delta(\mathbf{r} - \mathbf{r}') \delta(t - t'), \quad (3.81)$$

where  $G_2(\mathbf{r}''t, \mathbf{r}'t', \mathbf{r}t)$  is the two-particle Green's function

$$G_2(1, 2, 3, 4) = i^2 \langle n, 0 | \hat{T} \left[ \hat{\phi}(1) \hat{\phi}(3) \hat{\phi}^\dagger(4) \hat{\phi}^\dagger(2) \right] | n, 0 \rangle. \quad (3.82)$$

To simplify the notation we combine the time and space variables into a single variable  $(\mathbf{r}_1, t_1 \equiv 1)$ . So the equation of motion for the 1-particle Green's function contains a 2-particle Green's function. This continues for higher order Green's functions as well and leads to an infinite system of equations. To arrive at a closed system of equations we introduce the self-energy  $\Sigma(\mathbf{r}t, \mathbf{r}''t'')$  via

$$i \int d^3 \mathbf{r}'' v(\mathbf{r}', \mathbf{r}'') G_2(\mathbf{r}''t, \mathbf{r}'t', \mathbf{r}t) = - \int d^3 \mathbf{r}'' dt'' \Sigma(\mathbf{r}t, \mathbf{r}''t'') G_1(\mathbf{r}''t'', \mathbf{r}t). \quad (3.83)$$

This simplifies eq. 3.81 to:

$$\left[ \frac{\partial}{\partial t} - \hat{h} \right] G_1(\mathbf{r}t, \mathbf{r}'t') - \int d^3 \mathbf{r}'' dt'' \Sigma(\mathbf{r}t, \mathbf{r}''t'') G_1(\mathbf{r}''t'', \mathbf{r}t) = \delta(\mathbf{r} - \mathbf{r}') \delta(t - t'). \quad (3.84)$$

The task is now to find the self-energy operator, which is a highly complicated object, being non-local and non-hermitian. Before we continue, the independent particle contribution has to be addressed. Although in the derivation we used non-interacting particles with  $\hat{h} = V_{\text{kin}} + V_{\text{ext}}$ , in most practical applications better starting points are used, either Hartree, Hartree-Fock, or even Kohn-Sham particles. This modifies the definition of  $\Sigma$  accordingly. We will use the most common formulation with  $\hat{h}_0 = \hat{h} + \hat{V}_H$ , which yields  $\Sigma_H = \Sigma - \hat{V}_H$ . For the ease of notation we will drop the subscript immediately.

Without derivation the self-energy can now be obtained from a closed set of coupled equations [45]:

$$G_1(1,2) = G_0(1,2) + \int d34 G_0(1,3)\Sigma(3,4)G_1(4,2) \quad (3.85)$$

$$\Sigma(1,2) = i \int d34 G_1(1,3)W(1,4)\Gamma(4,2,3) \quad (3.86)$$

$$\Gamma(1,2,3) = \delta(1,2)\delta(1,3) + \int d4567 \frac{\delta\Sigma(1,2)}{\delta G_1(4,5)} G_1(4,6)G_1(5,7)\Gamma(6,7,3) \quad (3.87)$$

$$P(1,2) = -i \int d34 G_1(1,3)G_1(4,1)\Gamma(3,4,2) \quad (3.88)$$

$$W(1,2) = v(1,2) + \int d34 v(1,3)P(3,4)W(4,2). \quad (3.89)$$

Here  $G_0$  is the non-interacting Green's function,  $\Gamma$  the vertex correction,  $P$  the polarizability,  $W$  the screened Coulomb interaction and  $v$  the Coulomb interaction. Inverting equation eq. 3.89 for  $W$  leads to another common form:

$$\varepsilon(1,2) = \delta(1,2) - \int d3 v(1,3)P(3,2) \quad (3.90)$$

$$W(1,2) = \int d3 \varepsilon^{-1}(1,3)v(3,2), \quad (3.91)$$

where we defined  $\varepsilon$  as the microscopic dielectric function and its inverse as

$$\int d2 \varepsilon(1,2)\varepsilon^{-1}(2,3) = \delta(1,3). \quad (3.92)$$

Evaluating this system of coupled equations poses severe computational problems, especially the calculation of the derivative with respect to  $G$  in  $\Gamma$  (eq. 3.87). The *GW* approximation reduces the vertex correction to

$$\Gamma(1,2,3) = \delta(1,2)\delta(1,3). \quad (3.93)$$

Eq. 3.85 to eq. 3.89 thus simplify.

$$\Sigma(1,2) = iG_1(1,2)W(1,2) \quad (3.94)$$

$$P(1,2) = -iG_1(1,2)G_1(2,1) \quad (3.95)$$

$$\varepsilon(1,2) = \delta(1,2) - \int d3 v(1,3)P(3,2) \quad (3.96)$$

$$W(1,2) = \int d3 \varepsilon^{-1}(1,3)v(3,2) \quad (3.97)$$

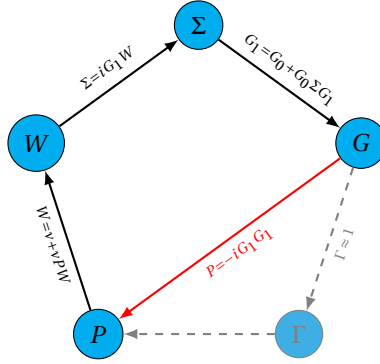


Figure 3.7: Schematic representation of Hedin's equations for  $G$ ,  $\Sigma$ ,  $W$ ,  $P$ ,  $\Gamma$

The  $GW$  approximation is not a formal perturbation expansion, but it makes physical sense to expand the self-energy in  $W$  and not in  $v$ , as the screened interaction is much more docile at long range. Furthermore, the approximation conserves particle number. The dielectric function is reduced to Random Phase Approximation (RPA) screening, i.e., the other electrons react to the excitation as if they were non-interacting.

To proceed we express  $G_1$  in its spectral representation, where to facilitate the next steps we extend  $\omega$  from a real to a complex quantity  $z \in \mathbb{C}$ :

$$G_1(\mathbf{r}, \mathbf{r}', z) = \sum_i \frac{\psi_i(\mathbf{r}, z) \bar{\psi}_i(\mathbf{r}', z)}{z - E_i(z)}, \quad (3.98)$$

where  $\psi_i(\mathbf{r}, z)$  ( $\bar{\psi}_i(\mathbf{r}', z)$ ) are the right (left) eigenvectors of the non-Hermitian operator  $\hat{H} = \hat{h}_0 + \Sigma(\mathbf{r}, \mathbf{r}', z)$  and  $E_i(z)$  the corresponding eigenvalues. Inserting eq. 3.98 into the frequency representation of eq. 3.84 leads to

$$\hat{h}_0 \psi_i(\mathbf{r}, z) + \int d^3 \mathbf{r}' \Sigma(\mathbf{r}, \mathbf{r}', z) \psi_i(\mathbf{r}', z) = E_i(z) \psi_i(\mathbf{r}, z). \quad (3.99)$$

One of the large problems in solving eq. 3.99 is the frequency dependence of  $\Sigma(z)$ . To solve it we have to evaluate  $\Sigma$  at all frequencies  $\omega$ . We now assume that the low-lying excitations can be described via quasi-particles with complex energies  $\varepsilon_i^{\text{qp}}$ . The particle-like excitations have energies, corresponding to the poles of  $G_1$  (eq. 3.98), i.e.:

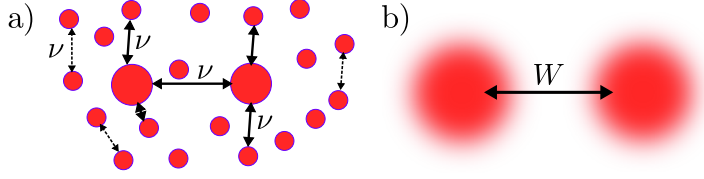


Figure 3.8: The many-particle system of interacting particles (a) is approximated by Quasi-particles (b), which take the screening due to the other particles into account by using the screened interaction  $W = \epsilon^{-1}\nu$  instead of the Coulomb interaction  $\nu$ . Neglecting the dashed interactions in (a) corresponds to RPA screening in (b)

$$\omega - E_i(z) = 0 \Rightarrow \epsilon_i^{\text{QP}} - E_i(\epsilon_i^{\text{QP}}) = 0. \quad (3.100)$$

Inserting this into eq. 3.99, using  $\Sigma = iGW$  and returning to the bra-ket notation we arrive at:

$$\left[ \hat{h}_0 + \Sigma(\epsilon_i^{\text{QP}}) \right] |\phi_i^{\text{QP}}\rangle = \epsilon_i^{\text{QP}} |\phi_i^{\text{QP}}\rangle, \quad (3.101)$$

where  $\langle \mathbf{r} | \phi_i^{\text{QP}} \rangle = \psi_i(\mathbf{r}, z = \epsilon_i^{\text{QP}})$ . We now use 'QP' instead of 'qp' as the state label to indicate the use of the  $GW$  approximation for  $\Sigma$ .

Returning to quasi-particles, it has to be pointed out that these are not real particles but mathematical constructs which allow us to reduce the many-particle problem to a single particle one. The quasi-particles interact not via the Coulomb interaction  $\nu$  but via the screened Coulomb interaction  $W$ , as each quasi-particle can be thought of as a real particle and a cloud of screening particles (see Fig. 3.8). This approximation only holds if the quasi-particles are in some sense “close” to the real particles, so they have to have long lifetimes, i.e., the imaginary part of the self-energy is small ( $\Im \Sigma_{ii} \rightarrow 0$ ) and correlation should be small. If we look at the spectral function  $A(\omega)$  of  $G_1$  (Fig. 3.9), which is defined as:

$$A(\mathbf{r}, \mathbf{r}', \omega) = -\frac{1}{\pi} \Im(G_1(\mathbf{r}, \mathbf{r}', \omega)) \text{sgn}(\omega - \mu), \quad (3.102)$$

where  $\mu$  is the chemical potential and  $\text{sgn}(\omega)$  the signum function, we see that the full spectral function decomposes into a coherent and incoherent part. The coherent part is centered around  $\epsilon^{GW}$ , which is shifted from the non-interacting energy  $\epsilon_0$  by  $\Re(\Sigma(\epsilon^{GW}))$ , with a spectral broadening proportional to  $\Im(\Sigma(\epsilon^{GW}))$ . The

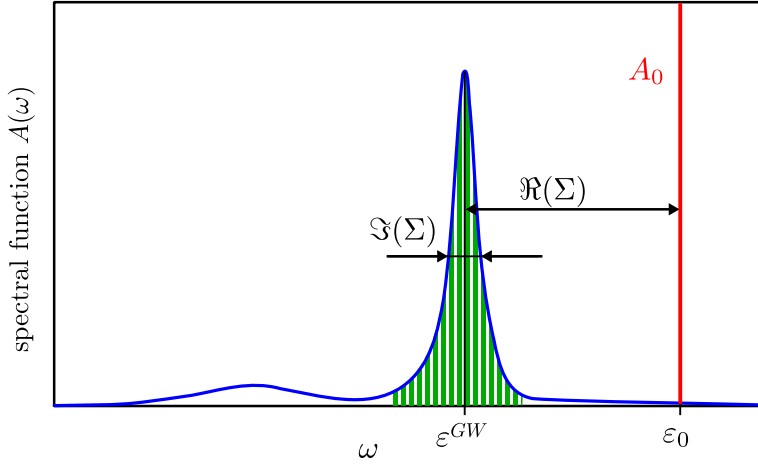


Figure 3.9: Spectral function of an infinite system, the spectral function becomes a continuous function, depicted in blue. The line  $A_0$  corresponds to the non-interacting system with excitation energy  $\epsilon_0$ . The quasi-particle approximation neglects all structure outside the peak at  $\epsilon^{GW}$  and describes it via a Lorentzian peak of  $\text{FWHM} = \Im(\Sigma)$ .

incoherent part may include satellite peaks but is neglected in the Quasi-particle approximation.

How do we start solving eq. 3.94-eq. 3.97 and then eq. 3.101? First,  $G_0$  is approximated by the Green's function of Kohn-Sham orbitals  $\phi^{KS}$  from a preceding DFT calculation. Although strictly Kohn-Sham orbitals carry no physical meaning, they are empirically found to often resemble quasi-particle states, as they already carry some, although approximate correlation corrections from the exchange-correlation functional:

$$G_0(\mathbf{r}, \mathbf{r}', \omega) = \sum_i \frac{\phi_i^{KS}(\mathbf{r}) \phi_i^{KS}(\mathbf{r}')}{\omega - \epsilon_i^{KS} \pm i\eta} \quad (3.103)$$

From there we calculate  $\Sigma$  via eq. 3.94-eq. 3.97. As mentioned earlier  $\hat{h}_0 = \hat{h} + \hat{V}_H \approx \hat{h}_0^{\text{DFT}} = \hat{H}^{\text{DFT}} - \hat{V}_{xc}$ , so we have to subtract  $V_{xc}$  from  $\Sigma$  via

$$\left[ \hat{H}^{\text{DFT}} + \Sigma(\epsilon_i^{QP}) - \hat{V}_{xc} \right] |\phi_i^{QP}\rangle = \epsilon_i^{QP} |\phi_i^{QP}\rangle, \quad (3.104)$$



Using the assumption that Kohn-Sham states actually approximate the  $GW$  quasi-particle states well,

$$|\phi_i^{QP}\rangle \approx |\phi_i^{KS}\rangle, \quad (3.105)$$

we can write eq. 3.104 with help of eq. 3.105 as:

$$\varepsilon_i^{GW} - \varepsilon_i^{KS} = \langle \phi_i^{KS} | \Sigma(\varepsilon_i^{GW}) - \hat{V}_{xc} | \phi_i^{KS} \rangle, \quad (3.106)$$

where we introduce  $\varepsilon_i^{GW}$  as  $\langle \phi_i^{KS} | \Sigma(\varepsilon_i^{GW}) | \phi_i^{KS} \rangle$ , as the  $GW$  corrected KS-state energies<sup>9</sup>. Now we can approximate  $\Sigma(\varepsilon_i^{GW}) \approx \Sigma(\varepsilon_i^{KS})$ . This approach is typically denoted as  $G_0W_0$ . Instead we can also insert the energies from a  $G_0W_0$  calculation back into  $\Sigma$  and iterate until  $\varepsilon_i^{GW}$  are converged. This is commonly denoted as  $GW_0$ . The  $\varepsilon_i^{GW}$  can then be used to calculate a new  $W$ , e.g.  $\Sigma = G(\varepsilon_i^{GW})W(\varepsilon_i^{GW})$  and iterated until convergence. Self-consistency of  $\varepsilon_i^{GW}$  in  $G$  and  $W$  is known as  $evGW$  [82]. More details on this can be found in Chapter 5.

Eq. 3.105 holds, if the off-diagonal elements of  $\Sigma(\varepsilon_i^{GW})$  are small. Otherwise, we have to expand the quasi-particle states in Kohn-Sham states,  $|\phi_j^{KS}\rangle$ :

$$|\phi_i^{QP}\rangle = \sum_j C_{ij} |\phi_j^{KS}\rangle \quad (3.107)$$

and explicitly solve eq. 3.101. As  $\Sigma$  is still non-Hermitian in this case, it is typically approximated by:

$$\langle \phi_i^{QP} | \Sigma | \phi_j^{QP} \rangle = \frac{1}{2} \left[ \langle \phi_i^{QP} | \Sigma(\varepsilon_i^{QP}) | \phi_j^{QP} \rangle + \langle \phi_j^{QP} | \Sigma(\varepsilon_j^{QP}) | \phi_i^{QP} \rangle \right] \quad (3.108)$$

as outlined by Faleev et al [83].

Although the  $GW$  framework is excellent for single particle excitations, like individual electrons and holes it cannot simulate excitons. Due to the neglect of the vertex correction according to eq. 3.93, quasi-particle quasi-particle interaction is not included in the  $GW$  approximation. Thus the simulation of excitons requires another approach for the description of the electron-hole interaction.

<sup>9</sup>To iterate, three different excited state energies have appeared so far:  $\varepsilon^{GW}$ :  $GW$  corrected energies for KS levels.  $\varepsilon^{QP}$ : quasi particle energies in the  $GW$  approximation.  $\varepsilon^{QP}$ : quasi particle energy including vertex corrections.

### 3.3.2 Two-particle-excitations

Whereas single particle-excitations can be accurately modeled via single-particle Green's functions, as demonstrated in the last section, this approach fails for charge neutral excitations. The quantity, which defines these excitations is the already introduced dielectric function  $\epsilon(\omega)$  in eq. 3.90. It describes the reaction of the system to small perturbations, e.g., incident light. These are typically charge displacements respective to the ground state, which can be interpreted as an electron-hole pair. Although we have calculated  $\epsilon(\omega)$ , we did so in the *GW* approximation, in which the vertex correction  $\Gamma$  was neglected. Without the vertex correction the screening reduces to the RPA, which is the screening of independent particles. So the *GW* via the RPA throws away the quasi-particle interaction we are looking for. We could reintroduce the vertex correction, but as said in the last section the whole set of Hedin's equations, eq. 3.85-eq. 3.89, would have to be iterated, as a simple expansion of  $P$  would depend on higher order polarization functions. Additionally, the form of the vertex correction makes a numerical treatment very difficult [84, 85].

Instead we will expand the two point Green's functions to four point quantities to rigorously describe electron-hole interactions of the kind  $|n, 0\rangle \rightarrow |n, S\rangle$ , which do not change the number of electrons in the system.

A natural quantity to start from is the two-particle correlation function, which allows to model the correlated motion of electron and hole

$$L(12, 1'2') = -G_2(12, 1'2') + G_1(12)G_1(1'2'), \quad (3.109)$$

where the second term represents the independent movement of electron and hole as a product of single particle Green's functions and the first term,  $G_2$ , is the two-particle Green's function the correlation. It can be found using a Dyson-like equation for  $L$ , the *Bethe-Salpeter-Equation* (BSE), which reads

$$L(12, 1'2') = L_0(12, 1'2') + \int d3456 L_0(14, 1'3)K(35, 46)L(62, 52'), \quad (3.110)$$

with  $L(12, 1'2')$  the two-particle Green's function for electron and hole,  $K(35, 46)$  the interaction kernel, explained below, and  $L_0(12, 1'2') = G_1(1, 1')G_1(2, 2')$  is the two-particle non-interacting Green's function.

As optical excitations involve the simultaneous creation and annihilation of quasi-particles we can reduce the four time variables to two. Furthermore, as in the previous paragraph we assume a Hamiltonian without an explicit time dependence, so  $L(12,1'2')$  can be reduced to  $L(12,1'2',\omega)$ , with the indices only representing position.

The Kernel  $K$  is given by the functional derivative of the full self-energy with respect to non-interacting Quasi-particles<sup>10</sup>:

$$K(35,46) = \frac{\delta[\Sigma(3,4) + V_H]}{\delta G_1(6,5)}, \quad (3.111)$$

using the  $GW$  approximation  $\Sigma = iGW$  and assuming  $\delta W/\delta G_1 \approx 0$ , i.e. the screening is not influenced by the excitation, we arrive at:

$$\begin{aligned} K(35,46) &= -i\delta(3,4)\delta(5,6)\nu(3,6) + i\delta(3,6)\delta(4,5)W(3,4) \\ &= K^x(35,46) + K^d(35,46). \end{aligned} \quad (3.112)$$

$K^d$  is normally called the *direct interaction* and originates from the screened interaction  $W$  between electron and hole and is responsible for the binding in the electron hole pair.  $K^x$  originates from the unscreened interaction  $\nu$  and is responsible for the singlet-triplet splitting. It is normally denoted *exchange interaction*.

$L_0$  can now be written as a combination of independent quasi-particles excitations, which in position space yields:

$$L_0(\mathbf{r}_1, \mathbf{r}_2, \mathbf{r}'_1, \mathbf{r}'_2, \omega) = i \sum_{v,c} \left[ \frac{\phi_c(\mathbf{r}_1)\phi_v(\mathbf{r}_2)\overline{\phi_v^*(\mathbf{r}'_1)}\phi_c^*(\mathbf{r}'_2)}{\omega - (\varepsilon_c - \varepsilon_v) + i\eta} - \frac{\phi_v(\mathbf{r}_1)\phi_c(\mathbf{r}_2)\phi_c^*(\mathbf{r}'_1)\overline{\phi_v^*(\mathbf{r}'_2)}}{\omega + (\varepsilon_c - \varepsilon_v) - i\eta} \right] \quad (3.113)$$

where  $c$  runs over all occupied hole states and  $v$  over all empty electron states. This suggests a basis of product states of single-particle wave functions  $\chi^{ex}$ :

$$\chi^{ex}(\mathbf{r}_1, \mathbf{r}_2) = \sum_{n_1, n_2} \phi_{n_1}(\mathbf{r}_1)\phi_{n_2}^*(\mathbf{r}_2), \quad (3.114)$$

<sup>10</sup>As the particles are non-interacting,  $V_H$  has to be explicitly included.

allowing us to rewrite eq. 3.110 as a matrix equation:

$$\underline{\mathbf{L}}(\omega) = \underline{\mathbf{L}}_0(\omega) + \underline{\mathbf{L}}_0(\omega)\underline{\mathbf{K}}(\omega)\underline{\mathbf{L}}(\omega). \quad (3.115)$$

Multiplying with  $-i$  and transforming  $L_0(\mathbf{r}_1, \mathbf{r}_2, \mathbf{r}'_1, \mathbf{r}'_2, \omega)$  to  $L_0^{n_1, n_2, n_3, n_4}(\omega)$  yields:

$$-iL_0^{n_1, n_2, n_3, n_4}(\omega) = \sum_{v,c} \frac{\delta_{n_1 c} \delta_{n_2 v} \delta_{n_3 c} \delta_{n_4 v}}{\omega + (\varepsilon_c - \varepsilon_v) - i\eta} - \frac{\delta_{n_1 c} \delta_{n_2 v} \delta_{n_3 c} \delta_{n_4 v}}{\omega - (\varepsilon_v - \varepsilon_c) + i\eta} \quad (3.116)$$

So in this basis  $-iL_0^{n_1, n_2, n_3, n_4}(\omega)$  is diagonal  $n_1 = n_3$ ,  $n_2 = n_4$ . Furthermore, only transitions from occupied  $\rightarrow$  unoccupied and unoccupied  $\rightarrow$  occupied carry a weight. In the matrix representation:

$$-i\underline{\mathbf{L}}_0(\omega) = \begin{array}{c} n_1 n_2 \backslash n_3 n_4 \\ \begin{array}{cc} vv & cc \\ cc & vv \\ vc & cv \\ cv & vc \end{array} \end{array} \begin{pmatrix} vv & cc & vc & cv \\ 0 & 0 & 0 & 0 \\ 0 & 0 & 0 & 0 \\ 0 & 0 & \frac{1}{\Delta\varepsilon_{n_2 n_1} - \omega} & 0 \\ 0 & 0 & 0 & \frac{-1}{\Delta\varepsilon_{n_2 n_1} - \omega} \end{pmatrix}, \quad (3.117)$$

where  $\Delta\varepsilon_{n_2 n_1} = \varepsilon_{n_2} - \varepsilon_{n_1}$ . Now we can rewrite  $-iL_0^{n_1, n_2, n_3, n_4}(\omega)$  using occupation factors  $f_i$  ( $f_v = 1$ ,  $f_c = 0$ ):

$$-iL_0^{n_1, n_2, n_3, n_4}(\omega) = \frac{f_{n_2} f_{n_1} \delta(n_1, n_3) \delta(n_2, n_4)}{\Delta\varepsilon_{n_2 n_1} - \omega}. \quad (3.118)$$

This allows us to introduce an occupation matrix  $\underline{\mathbf{F}}$ , with components:

$$F^{n_1, n_2, n_3, n_4} = f_{n_2} f_{n_1} \delta(n_1, n_3) \delta(n_2, n_4). \quad (3.119)$$

We now restrict the further derivation of  $L_0$  to the physically meaningful subspace  $(vc)(cv)$  belonging to occupied  $\rightarrow$  unoccupied and unoccupied  $\rightarrow$  occupied transitions

$$\underline{\mathbf{L}}_0 = \tilde{\underline{\mathbf{L}}}_0 \underline{\mathbf{F}} \text{ with } \underline{\mathbf{F}} = \begin{pmatrix} \underbrace{f_2 - f_1}_{=-1} & 0 \\ 0 & \underbrace{f_2 - f_1}_{=1} \end{pmatrix}. \quad (3.120)$$

So we can solve eq. 3.115 for  $\underline{L}$ :

$$-i\underline{L}(\omega) = [-i\underline{L}_0^{-1}(\omega) - i\underline{F}\underline{K}(\omega)]^{-1}. \quad (3.121)$$

As  $-i\underline{L}_0^{-1}(\omega)$  is diagonal the inverse is readily calculated:

$$-i\underline{L}_0^{-1}(\omega) = \begin{pmatrix} \Delta\varepsilon_{n_2 n_1} - \omega & 0 \\ 0 & \Delta\varepsilon_{n_2 n_1} - \omega \end{pmatrix}. \quad (3.122)$$

This allows us to single out the frequency dependence:

$$-i\underline{L}_0^{-1}(\omega) = \begin{pmatrix} \Delta\varepsilon_{n_2 n_1} & 0 \\ 0 & \Delta\varepsilon_{n_2 n_1} \end{pmatrix} - \omega \begin{pmatrix} 1 & 0 \\ 0 & 1 \end{pmatrix}, \quad (3.123)$$

which enables us to rewrite the denominator introducing an effective two-particle Hamiltonian  $H^{\text{BSE}}$ :

$$\begin{aligned} \underline{\mathbf{H}}^{\text{BSE}} &= \begin{pmatrix} \Delta\varepsilon_{n_2 n_1} & 0 \\ 0 & \Delta\varepsilon_{n_2 n_1} \end{pmatrix} - i\underline{F}\underline{K}(\omega) \\ &= \begin{pmatrix} \Delta\varepsilon_{n_2 n_1} & 0 \\ 0 & \Delta\varepsilon_{n_2 n_1} \end{pmatrix} + i \begin{pmatrix} K_{vc, v'c'} & K_{vc, c'v'} \\ -K_{cv, v'c'} & -K_{cv, c'v'} \end{pmatrix} \end{aligned} \quad (3.124)$$

This Hamiltonian is in general non-Hermitian and is typically labeled:

$$\underline{\mathbf{H}}^{\text{BSE}} = \begin{pmatrix} H^{\text{res}} & K \\ -K & -H^{\text{res}} \end{pmatrix} \quad (3.125)$$

The *resonant* part  $H^{\text{res}}$  treats transitions between occupied and unoccupied states, whereas  $-H^{\text{res}}$  is also called *anti-resonant* part and describes unoccupied to occupied transitions with negative frequencies.  $K$  couples these resonant and anti-resonant transitions. As in sec. 3.3.1, we now do not try to solve eq. 3.121, as it involves inverting a four index quantity for every  $\omega$ . Instead we can use the spectral representation of  $L(\omega)$ :

$$-i\underline{L}(\omega) = (\underline{\mathbf{H}}^{\text{BSE}} - \omega)^{-1} = \sum_S \frac{|\bar{\chi}_S\rangle\langle\chi_S|}{\Omega_S - \omega} \quad (3.126)$$

and find the eigenvalues to the anti-Hermitian eigenvalue problem:

$$\underline{\mathbf{H}}^{\text{BSE}}|\chi_S\rangle = \Omega_S|\chi_S\rangle, \quad (3.127)$$

which using eq. 3.125 is typically written as:

$$\begin{pmatrix} H^{\text{res}} & K \\ -K & -H^{\text{res}} \end{pmatrix} \begin{pmatrix} A^S \\ B^S \end{pmatrix} = \Omega_S \begin{pmatrix} A^S \\ B^S \end{pmatrix}, \quad (3.128)$$

with:

$$\langle \mathbf{r}_1, \mathbf{r}_2 | \chi_S \rangle = \chi_S(\mathbf{r}_1, \mathbf{r}_2) = A_{vc}^S \phi_c(\mathbf{r}_1) \phi_v^*(\mathbf{r}_2) + B_{vc}^S \phi_v(\mathbf{r}_1) \phi_c^*(\mathbf{r}_2). \quad (3.129)$$

For many systems the off-diagonal blocks  $K$  in eq. 3.128 are small and can be neglected. This leads to the Tamm-Dancoff approximation (TDA) [46]:

$$H^{\text{res}} A_{\text{TDA}}^S = \Omega_S^{\text{TDA}} A_{\text{TDA}}^S \quad (3.130)$$

and the resulting electron-hole amplitude:

$$\chi_S^{\text{TDA}}(\mathbf{r}_1, \mathbf{r}_2) = \sum_{vc} A_{vc, \text{TDA}}^S \phi_c(\mathbf{r}_1) \phi_v^*(\mathbf{r}_2) \quad (3.131)$$

This approximation halves the size of the the BSE matrix<sup>11</sup>. Additionally it helps to reduce triplet instabilities [86], but especially for small molecules the error due to the neglect of the anti-resonant parts can be quite significant [87].

Explicitly,  $H^{\text{res}}$  and  $K$  are given by:

$$H_{vc, v'c'}^{\text{res}}(\omega) = D_{vc, v'c'} + H_{vc, v'c'}^x + H_{vc, v'c'}^d \quad (3.132)$$

$$K_{cv, v'c'}(\omega) = H_{cv, v'c'}^x + H_{cv, v'c'}^d. \quad (3.133)$$

<sup>11</sup>Although the full matrix has size  $2N \times 2N$ , due to its anti-Hermitian structure, the problem can be recast into problem of the two matrices  $\underline{\mathbf{H}}^{\text{res}} - \underline{\mathbf{K}}$  and  $\underline{\mathbf{H}}^{\text{res}} + \underline{\mathbf{K}}$

In the basis of non-interacting quasi-particle states the respective matrix elements are:

$$D_{\nu c, \nu' c'} = (\varepsilon_\nu - \varepsilon_c) \delta_{\nu \nu'} \delta_{c c'} \quad (3.134)$$

$$H_{\nu c, \nu' c'}^x = \int d^3 \mathbf{r} d^3 \mathbf{r}' \phi_c^*(\mathbf{r}) \phi_\nu(\mathbf{r}) v(\mathbf{r}, \mathbf{r}') \phi_{c'}(\mathbf{r}') \phi_{\nu'}^*(\mathbf{r}') \quad (3.135)$$

$$H_{\nu c, \nu' c'}^d = \int d^3 \mathbf{r} d^3 \mathbf{r}' \phi_c^*(\mathbf{r}) \phi_{c'}(\mathbf{r}) \phi_\nu(\mathbf{r}') \phi_{\nu'}^*(\mathbf{r}') W(\mathbf{r}, \mathbf{r}', \omega = 0). \quad (3.136)$$

Here we assume, that the dynamic properties of  $W(\omega)$  are negligible and use the static approximation, which reduces the computational cost significantly by not demanding self-consistency. This is only valid if  $\Omega_S - (\varepsilon_c - \varepsilon_\nu) \ll \omega_l$ , where  $\omega_l$  is the plasmon frequency, which determines the screening properties.

The spin structure of the BSE solutions depends on the spin-orbit coupling. If the ground state is a spin singlet state and spin-orbit coupling is small, the Hilbert space of the electron-hole pairs has four distinct subspaces:

$$|\uparrow\uparrow\rangle, |\downarrow\downarrow\rangle, |\uparrow\downarrow\rangle, |\downarrow\uparrow\rangle,$$

where the first arrow indicates the spin of the electron and the second arrow the spin of the hole. Most of matrix elements eq. 3.134-3.136 between these subspaces are zero<sup>12</sup>

$$H^{\text{BSE}} = \begin{pmatrix} D + H^x + H^d & 0 & 0 & H^x \\ 0 & D + H^d & 0 & 0 \\ 0 & 0 & D + H^d & 0 \\ H^x & 0 & 0 & D + H^x + H^d \end{pmatrix} \begin{matrix} |\uparrow\downarrow\rangle \\ |\uparrow\uparrow\rangle \\ |\downarrow\downarrow\rangle \\ |\downarrow\uparrow\rangle \end{matrix} \quad (3.137)$$

This Hamiltonian can be diagonalized, yielding

$$\underbrace{|\uparrow\uparrow\rangle, |\downarrow\downarrow\rangle, \frac{1}{\sqrt{2}}(|\downarrow\uparrow\rangle + |\uparrow\downarrow\rangle)}_{S=1 \text{ Triplets}}, \quad \underbrace{\frac{1}{\sqrt{2}}(|\downarrow\uparrow\rangle - |\uparrow\downarrow\rangle)}_{S=0 \text{ Singlet}}.$$

This allows to solve the BSE equation separately for both spin types.  $H^x$  vanishes for spin-triplet solutions, whereas it is non-zero and typically repulsive for singlets. The exchange interaction is thus responsible for the singlet-triplet energy splitting.

<sup>12</sup>A spin of  $\downarrow$  for a hole corresponds to  $\uparrow$  of an electron, that could be there. This yields  $\langle \uparrow_e | \downarrow_h \rangle = 1$  and  $\langle \uparrow_e | \uparrow_h \rangle = 0$

$$H_{\text{singlet}}^{\text{BSE}} = D + H^d + 2H^x \quad (3.138)$$

$$H_{\text{triplet}}^{\text{BSE}} = D + H^d \quad (3.139)$$

If spin-orbit coupling is large, the matrices no longer decouple and instead the BSE Hamiltonian must be evaluated using the full spin structure, which increases the size of the Hamiltonian by a factor of four. More complex spin contributions also arise for open shell systems, where the ground state is not a singlet.

With the solution of the BSE eigenvalue equation, we arrive at exciton excitation energies and oscillator strengths, which are two important quantities we introduced in the last chapter. In the next chapter we will discuss more approximate methods, which allow us to deal with systems, which are too large to handle with *GW*-BSE or even DFT. The actual implementation of DFT and *GW*-BSE in the software package VOTCA-XTP will be discussed in Chapter 5.



## Chapter 4

# Coarse-grained methods

Although quantum mechanical methods have pushed the envelope of accessible system size further and further due to algorithmic and hardware developments, their practical applicability is still limited to at maximum a few thousand atoms [88]<sup>1</sup>. In order to treat larger systems, degrees of freedom have to be grouped together, which is generically called coarse graining. Which degrees of freedom to group together and which to keep separate essentially depends on the property of interest. In the following section we will look at two different strategies, *molecular dynamics* and *rate models*, which help to answer very different questions. This chapter covers the all the non-quantum methods employed in this thesis.

A simple way to reduce the degrees of freedom in a molecular system is to neglect the explicit dynamics of electrons if one is only interested in structural or morphological features. Instead their effects are incorporated into an effective potential for interatomic interaction. The collection of these interatomic interactions is typically called a *force field*. Elimination of electrons reduces the degrees of freedom by a factor of 10-100. If electronic degrees of freedom are not explicitly of interest, and good force fields exist, this is a viable approach. Additionally, atoms are much heavier than individual electrons and can thus often be treated classically. Integrating the classical equations of motion for atoms is called *classical* molecular dynamics and is summarized in some detail in the following. However, often systems of in-

---

<sup>1</sup>A DFT calculation with BigDFT, a linear scaling implementation of DFT has achieved 15000 water molecules on 9600 cores running for 25 minutes.

terest, e.g., large polymers, proteins, or cell walls, are still larger than what can realistically be handled by such atomistic molecular dynamics. A widespread approach is then to group neighboring atoms into one effective particle, called a bead. This reduces molecules of hundreds of atoms to a handful of beads, which interact via an effective potential, which mimics important effects of the underlying atoms. This approach is what is most commonly understood as *coarse graining*. Coarse graining on the atomistic and higher level is, however, not part of this thesis.

What do you do, if the electronic states are still of interest but the system is beyond the size of quantum mechanical methods. System specific strategies have to be employed. For highly ordered crystalline systems the electronic structure can be calculated from a single unit cell. To derive the transport properties from the electronic structure then only requires additional knowledge of scattering sources, such as phonons or defects, which can also be extracted from calculations on super cells. Although small defect densities still require large supercells to reduce defect-defect interaction, in general periodicity helps to reduce the computational cost.

Although some organic molecules form crystals and sometimes even exhibit narrow electronic bands [89], most organic semiconductors are rather disordered, as molecules are only weakly bound to each other at room temperature. Consequently, thermal fluctuations are not just a small perturbation but have a large influence on the local ordering [90]. This and the static disorder, inherent to many, especially amorphous, organic materials localizes the wave functions to individual molecules with only small overlap to neighboring molecules (see Fig. 2.3).

Aiming at the understanding of electron dynamics, this allows us to focus on isolated molecules and introduce interactions with the neighboring molecules as small perturbations. Excitons or charge carriers are thus mostly confined to individual molecular units and move only in rare, often phonon/temperature assisted, hops to neighboring molecules. Localization enables us to describe each molecule as a single site, where the population of each site is connected to neighboring site populations by a certain transition rate. The evolution of site populations and consequently the exciton movement can then be calculated via kinetic Monte Carlo, after all the input parameters for the rates are calculated from the molecular properties.

For more information on the topics in this chapter see [43, 91, 92].

## 4.1 Molecular dynamics

As mentioned above, classical molecular dynamics uses atoms as the principle entities. The interatomic potential between  $N$  atoms  $U(1,2,\dots,N)$ , in general, is a very complicated quantity, as it has to incorporate all the nuclear and electronic contributions to the interaction between atoms. Due to the difficulty of calculating such a high dimensional quantity, the interatomic potential is instead expanded in  $n$ -body interactions:

$$U(1,2,3,\dots,N) \approx \sum_{i<j}^N V_{ij} + \sum_{ijk} V_{ijk} + \sum_{ijkl} V_{ijkl} + \dots, \quad (4.1)$$

where the expansion is typically truncated at  $n < 5$ . The two-body interaction usually is the largest contribution to  $U(1,2,\dots,N)$ .

The challenge is to find expression for these potentials, which reproduce the real dynamics as well as possible and are easy to calculate at the same time. These sometimes conflicting requirements led to a large zoo of different functional forms and parameters for these interaction potentials. In the following a short summary of the most common forms is given.

For the simulation of molecular materials interaction potentials fall into one of two categories:

- *bonded potentials* comprise 2, 3, 4 body interactions between bonded atoms. Their purpose is to keep individual molecules close to the quantum mechanically or experimentally predicted shape by reproducing the covalent interaction inside the molecule.
- *non-bonded potentials* describe the interaction between different molecules and spatially separated areas in large molecules itself.

The *bonded potentials* typically consist of three different terms, as shown in Fig. 4.1:

1. The bond stretching potential, often harmonic, which enforces fluctuations around correct interatomic distance  $r_{ij}^0$ .

$$V_{ij} = \frac{1}{2} k_{ij} (r_{ij} - r_{ij}^0)^2. \quad (4.2)$$

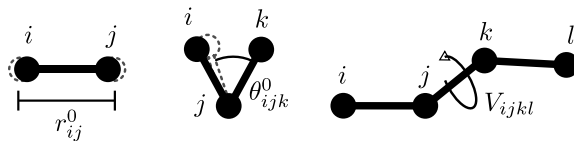


Figure 4.1: 2,3 and 4 body bonded interaction potentials in classical forcefields. These are bond stretching, bond angle and dihedral potential.

2. The bond angle potential for a triplet of atoms ( $i-j-k$ ), allows for harmonic fluctuations around the equilibrium angle  $\theta_{ijk}^0$

$$V_{ijk} = \frac{1}{2} k_{ijk}^{\theta} (\theta_{ijk} - \theta_{ijk}^0)^2. \quad (4.3)$$

3. The dihedral potential, which describes torsion of the molecule. A common form is the Ryckaert-Bellemans potential given as:

$$V_{ijkl} = \sum_{n=0}^5 C_n \cos^n(\phi), \quad (4.4)$$

where  $\phi = \psi - \pi$  is the dihedral angle and  $C_n$  the force constants. The potential here is periodic and thus allows for rotation around the bond. Dihedral potentials which allow for this are called *proper dihedral*, whereas also simple harmonic dihedrals are used, which do not allow for a full rotation and are typically referred to as *improper dihedrals*. They are mainly used to keep planar groups planar.

The two major *non-bonded potentials* are:

- The Coulomb interaction for atoms  $i, j$  carrying charges  $q_i, q_j$  is given by Coulomb's law:

$$V_{ij}^C = \frac{q_i q_j}{r_{ij}}, \quad (4.5)$$

with  $r_{ij}$  the interatomic distance.

- The dispersion interaction, which accounts for the correlated motion or mutual polarization of the electron clouds of atoms  $i$  and  $j$ , is classically described via an attractive  $r_{ij}^{-6}$  law. To model the quantum mechanical Pauli repulsion between the clouds a repulsive  $r_{ij}^{-12}$  is added. Whereas the functional

form of the dispersion term has a clear physical justification, the repulsion term is chosen for computational simplicity, as  $r_{ij}^6$  has only to be squared to arrive at  $r_{ij}^{12}$ . Both terms together are called the *Lennard-Jones potential*:

$$V_{ij}^{\text{LJ}} = 4\varepsilon_{ij} \left[ \left( \frac{\sigma_{ij}}{r_{ij}} \right)^{12} + \left( \frac{\sigma_{ij}}{r_{ij}} \right)^6 \right]. \quad (4.6)$$

In contrast to the Coulomb potential, which is strictly a two-body potential, the dispersive interaction is not. A third atom in the vicinity of atoms  $i$  and  $j$  will change the polarization response as well as the quantum mechanical repulsion between atoms  $i$  and  $j$ . As this effect requires advanced quantum mechanical calculations, it is neglected in nearly all computations and the dispersion is instead evaluate as the two-body Lennard-Jones potential.

The set of parameters  $q_i, \varepsilon_{ij}, \sigma_{ij}, k_{ij}, k_{ijk}, C_n$ , besides the functional form of the potential, determine the forces acting on the atoms and are called the *force field*. For a system of a few distinct elements these can already number hundreds of parameters. As even atoms of the same element, situated in different chemical environments, may require different sets of parameters, the number of parameters increases even more. Many force fields use combination rules of the type  $\sigma_{ij} = \sqrt{\sigma_{ii} \cdot \sigma_{jj}}$  to reduce the number of free parameters, but the remaining parameters have to be either fitted to experimental or quantum chemistry data. As the fitting is quite ambiguous, a huge variety of different force fields exists, which all have different areas of application and validity.

Although molecular dynamics simulations can treat millions of atoms, it is nowhere near macroscopic scale. Even a cluster of a million atoms still has still

$$N_{\text{edge}} = \sqrt[3]{N} \rightarrow \frac{N_{\text{surface}}}{N_{\text{bulk}}} \approx \frac{N_{\text{edge}}^2}{N_{\text{edge}}^3} = N^{-1/3} \stackrel{N=10^6}{=} 1\% \quad (4.7)$$

of the atoms directly at the surface. If a bulk material has to be simulated, a common strategy to reduce the surface effects is to introduce periodic boundary conditions. A particle located at  $x, y, z$  in a cubic<sup>2</sup> simulation box of length  $L$  thus is copied to all  $x + n_x L, y + n_y L, z + n_z L$  with  $n_x, n_y, n_z \in \mathbb{Z}$ . The downside of this approach is the introduction of an artificial periodicity with period  $L$  and the

<sup>2</sup>Chosen for simplicity: most MD packages offer cubic, orthogonal, or even trigonal simulation boxes

interaction distance between molecules has to be restricted to  $r_c = L/2$  to avoid self-interaction between mirror images of the same particle.

Once you have chosen a force field and the appropriate boundary conditions, the force  $\mathbf{F}_i$  acting on each atom can be calculated according to

$$\mathbf{F}_i = -\frac{\partial U}{\partial \mathbf{r}_i}, \quad (4.8)$$

which allows to solve the classical equations of motion

$$\frac{d\mathbf{r}_i}{dt} = \mathbf{v}_i; \quad \frac{d\mathbf{v}_i}{dt} = \frac{\mathbf{F}_i}{m_i}, \quad (4.9)$$

where  $m_i$  is the mass of the atom  $i$  and  $\mathbf{v}_i$  its velocity. From the velocities of the system the kinetic energy  $E_{\text{kin}}$  at time  $t$  can be calculated as

$$E_{\text{kin}}(t) = \frac{1}{2} \sum_i m_i \mathbf{v}_i^2. \quad (4.10)$$

This opens an avenue to calculate the instantaneous, absolute temperature  $T$  of the system, as the kinetic energy is related to  $T$  as  $\frac{1}{2} N_f k_B T = E_{\text{kin}}$ , where  $k_B$  is Boltzmann constant and  $N_f$  are the degrees of freedom of the system. They comprise the  $3N$  translational degrees of freedom of each atom minus the center of mass translation. If periodic boundary conditions are not applied three additional degrees of freedom for the rigid rotations of the whole system have to be subtracted. The same holds for any additional constraints placed on the system.

As eq. 4.9 cannot be analytically integrated for more than two bodies, a numerical integration scheme with a discrete time step  $\Delta t$  is used. One commonly used algorithm to update positions and velocities is the *velocity Verlet* [93] integration:

$$\mathbf{r}(t + \Delta t) = \mathbf{r}(t) + \Delta t \mathbf{v} + \frac{\Delta t^2}{2m} \mathbf{F}(t) \quad (4.11)$$

$$\mathbf{v}(t + \Delta t) = \mathbf{v}(t) + \frac{\Delta t}{2m} [\mathbf{F}(t) + \mathbf{F}(t + \Delta t)], \quad (4.12)$$

where we dropped the atom index  $i$  for clarity. Other integration schemes like the *leap-frog* algorithm are also feasible, as long as they are symplectic and time-reversible. Symplectic integrators conserve the phase space volume of a system and thus the calculated energy remains close to exact solution for arbitrary many

integration steps. So these integrators avoid a drift of the total energy due to the discrete time step [94]. Time-reversibility allows to integrate backwards from a system at  $t = n\Delta t$  to  $t = t_0$  by simply changing the sign of the time step from  $\Delta t$  to  $-\Delta t$  and arrive at exactly the initial structure at  $t = t_0$ . Although these properties help to keep the integration stable, the non-linear form of the interaction potential and floating point arithmetic of computers lead to numerical instabilities, if the time step is not small enough. Typically  $\Delta t$  is chosen to be ten times smaller than the smallest oscillation period in the system. For systems containing hydrogen, these are typically the hydrogen bond vibrations ( $\omega_{\text{H}} \approx 10^{-14}$  Hz[95]), so the time step is often chosen as  $\Delta t = 1$  fs.

As the symplectic integrators conserve the total energy, molecular dynamics simulation are conceptually performed in the micro canonical, or  $NVE$ , ensemble (constant particle number  $N$ , constant volume  $V$  and constant energy  $E$ ). Experiments are typically performed in the  $NVT$  or canonical ensemble. Although all ensembles lead to the same result in the thermodynamic limit, meaning infinite system size, numerical calculations require small systems. Thus, thermostats are required to drive the system to the target temperature  $T_0$ .

The simplest thermostat, known as *velocity rescaling*, rescales all velocities by a factor  $\lambda = \sqrt{T_0/T(t)}$ . This approach can transfer heat in each time step but does not sample the canonical ensemble (i.e., the velocities are not Boltzmann-distributed after rescaling). This can be remedied by using stochastic velocity rescaling, where the target kinetic energy in each rescaling step is drawn from a canonical distribution [96].

A more gentle approach uses weak coupling to an external heat bath with the target temperature  $T_0$ . The *Berendsen thermostat* [97] slowly corrects the system temperature by rescaling all velocities according with

$$\lambda = \left[ 1 + \frac{\Delta t}{\tau} \left( \frac{T_0}{T(t)} - 1 \right) \right]^{1/2}. \quad (4.13)$$

This allows the temperature to fluctuate but it is exponentially dampened towards  $T_0$ , with the damping determined by the coupling to the external bath  $\tau$ . Due to the temperature rescaling the Berendsen thermostat still does not sample the canonical ensemble. An example of a non-stochastic thermostat, which correctly adjust the temperature to produce a canonical ensemble, is the Nosé-Hoover thermostat. It adds a heat bath coordinate to the equations of motion [98], leading to a much

slower oscillatory dampening of the temperature fluctuations. A more extensive review of thermostats can be found in [99]. In the same vein as temperature, pressure can be adjusted via barostats leading to the  $NpT$  ensemble [97, 100].

Despite the limitations of molecular dynamics for the simulation of electronic properties of organic materials due to neglecting the explicit electronic degrees of freedom, it has proven crucial for the larger scale simulation of interfaces and amorphous molecular structures. The reliance on a parameterized force field is probably the greatest weakness, as it limits transferability to new molecules and introduces additional arbitrariness into the simulation. This can be remedied in principle by employing *ab initio molecular dynamics*. Here the nuclear motion is classically described, while interatomic forces are explicitly calculated by the solution of the electronic Schrödinger equation. There are different schemes to achieve this coupling, e.g., Carr Parrinello [101] or Ehrenfest dynamics [43]. Although these methods constitute the most complete approach to simulating disordered matter, they are also by far the most expensive computationally.

To accurately model disorder in organic electronic systems, large system sizes are required [102], which necessitates classical molecular dynamics simulations or alternatively, Monte-Carlo simulations [103]. Both approaches conventionally do not treat electrons explicitly. How to extract approximate electronic dynamics from morphologies by using rate models is explained in the next section.

## 4.2 Rate models

As discussed before, the electronic properties of organic semiconductors are influenced by processes on many different length and timescales, which span many orders of magnitude. Thus a multi scale approach is needed, which can capture the important contributions at each level, but allows us to integrate out or collect less important contributions in effective quantities. The large difference between inter- and intra-molecular interaction strengths indicate a possible approach. Excitations are localized on individual molecules, which only interact weakly with each other. The weak interaction also leads to dynamics where excitations remain on one site for a comparably long time and only move infrequently from molecule to molecule, assisted by thermal motion. This sparsity of transition events allows us to define transition rates for the movement from one site to another. These rates obviously incorporate the effects of the underlying electronic and nuclear arrangements, e.g.,



fast intramolecular nuclear/thermal vibrations, relative molecular arrangement, or electrostatic environment. Nuclear vibrations, especially, critically influence excitation transport. High frequency oscillations provide the energy required for excitation hopping, whereas the slower molecular rearrangement is basically frozen on the time scales of excitation transfer and only contributes by increasing the static disorder. This separation into fast and slow degrees allows the fast electronic processes to happen on a mesoscopically frozen morphology, which thus can be computed beforehand using molecular dynamics.

In this section we will briefly outline how rate models arise from the coupled nuclear and electronic motion via the introduction of diabatic states. Afterwards we will outline how the input quantities for the appropriate rate model can be calculated using classical and quantum mechanical models. The chapter concludes with an outline of the kinetic Monte-Carlo algorithm which allows us to extract transport properties from rate models.

### 4.2.1 Excitation transfer reactions

The basic process of all rate models is the excitation transfer reaction from a donor molecule  $A$  to an acceptor molecule  $B$ :



where  $A^*$  denotes a molecule  $A$  in its excited state. The excitation can either be a single particle excitation, such as a hole or electron, or a two-particle excitation, like a singlet or triplet exciton. For the two molecule system we introduce the adiabatic states  $|0\rangle$  and  $|1\rangle$ , which depend on the set of nuclear coordinates,  $\mathbf{R}$ , as discussed in Chapter 3. Instead of this multidimensional space, we focus on the one-dimensional reaction coordinate  $\xi$ , which is some linear combination of all nuclear coordinates. The ground state and first excited state adiabatic potential energy surfaces are plotted as red dashed lines in Fig. 4.2. For a given molecular arrangement, denoted  $\xi_A$ , the excitation localizes on molecule  $A$  and for  $\xi_B$  on molecule  $B$ . Expanded in the adiabatic states, the full Hamiltonian of the dimer complex can be expressed as

$$\mathcal{H}^{AB} = \sum_{i=0,1} \hat{H}_{\text{nuc}}^i(\xi) |i\rangle\langle i| + \hat{\Theta}^{01}(\xi) |0\rangle\langle 1| + \hat{\Theta}^{10}(\xi) |1\rangle\langle 0|. \quad (4.15)$$

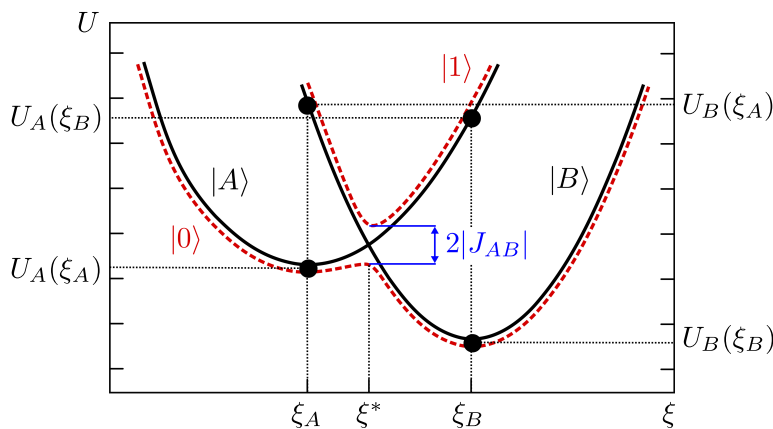


Figure 4.2: Diabatic (black) and adiabatic (red dashed) potential energy surfaces along the reaction coordinate  $\xi$ . Whereas the adiabatic surfaces do not cross, but change character, the diabatic states retain their chemical character but cross. The electronic coupling  $J_{AB}$  can be read of as half the energetic separation between  $|0\rangle$  and  $|1\rangle$  at  $\xi^*$ .

Transitions between these states are mediated by the matrix elements  $\hat{\Theta}^{01}$  and  $\hat{\Theta}^{10}$  of the *non-adiabicity* operator<sup>3</sup>  $\hat{\Theta}^{ij}$ . If the system is in either state  $|0\rangle$  or  $|1\rangle$  the nuclear dynamics are governed by:

$$\hat{H}_{\text{nuc}}^{0/1}(\xi) = \hat{T}_{\text{nuc}} + \underbrace{\hat{V}_{\text{nuc-nuc}} + \hat{\Theta}^{0/1}(\xi) + E_{\text{el}}^{0/1}(\xi)}_{=U^{0/1}(\xi)}. \quad (4.16)$$

In the case of a delocalized system, the electronic excitation is well described by  $|0\rangle$  and the nuclear motion will be governed by  $\hat{H}^0$  from eq. 4.16. This situation corresponds to a large split of the adiabatic energy surfaces ( $J_{AB}$  in Fig. 4.2).

If the electronic excitation is strongly localized on molecule  $A$ ,  $|0\rangle$  alone would describe it poorly. Instead a mixture of adiabatic states is needed to describe the localized state, i.e. something along the state  $|A\rangle$ . Describing this localized state in terms of  $|0\rangle$  and  $|1\rangle$  is difficult, as they couple via the *non-adiabicity* operator. To ease the calculation we introduce a localized electronic basis, known as the *diabatic basis*.

<sup>3</sup>Here we use the indices  $i, j$  for summing over adiabatic states instead of  $a, b$  as in Chapter 3 to avoid confusion with diabatic states  $|A\rangle$  and  $|B\rangle$ .

The diabatic states  $|A\rangle$ ,  $|B\rangle$  are related to the adiabatic basis  $|0\rangle, |1\rangle$  via a basis transformation:

$$\begin{pmatrix} |A(\xi_0)\rangle \\ |B(\xi_0)\rangle \end{pmatrix} = \underline{\mathbf{T}}(\xi) \begin{pmatrix} |0(\xi)\rangle \\ |1(\xi)\rangle \end{pmatrix}. \quad (4.17)$$

The transformation matrix  $\underline{\mathbf{T}}(\xi)$  is chosen in a way to absorb the dependence on the nuclear coordinates  $\xi$ . In Fig. 4.2 the adiabatic and diabatic states are shown. Whereas adiabatic states localize or not localize depending on the nuclear geometry, diabatic states are always localized. They are defined in one reference nuclear configuration<sup>4</sup>,  $\xi_0$ , and so do not carry any dependence on the nuclear coordinates anymore, hence their matrix elements with the non-adiabicity operator vanish:

$$\langle X|\hat{\Theta}|Y\rangle = 0 \text{ with } X, Y \in \{A, B\}. \quad (4.18)$$

They are no longer eigenstates of the electronic Hamiltonian, except at  $\xi_0$ :

$$\hat{H}_{\text{el}}(\xi_0)|X\rangle = E_{\text{el}}^X|X\rangle, \text{ with } X \in \{A, B\}. \quad (4.19)$$

In the thus defined *diabatic basis* the Hamiltonian reads:

$$\mathcal{H}^{AB} = \hat{H}_{\text{nuc}}^A(\xi)|A\rangle\langle A| + \hat{H}_{\text{nuc}}^B(\xi)|B\rangle\langle B| + J_{AB}(|A\rangle\langle B| + |B\rangle\langle A|). \quad (4.20)$$

As all terms containing the non-adiabicity operator vanish, electronic coupling between the diabatic states is introduced via:

$$J_{AB}(\xi) = \langle A|\hat{H}_{\text{el}}(\xi)|B\rangle. \quad (4.21)$$

If the system is in one of the diabatic states  $|A\rangle$  or  $|B\rangle$ , the nuclear dynamics are described by the following Hamiltonian:

$$\hat{H}_{\text{nuc}}^{A/B} = \hat{T}_{\text{nuc}} + \underbrace{\hat{V}_{\text{nuc-nuc}} + J_{AA/BB}(\xi) + E_{\text{el}}^{A/B}}_{=U^{A/B}(\xi)} \quad (4.22)$$

In Fig. 4.2 the diabatic energy surfaces cross at  $\xi^*$ . This is necessary as diabatic states are localized, i.e., for certain molecular configurations ( $\xi > \xi^*$  state  $|B\rangle$  is energetically more optimal than  $|A\rangle$ ). Adiabatic states/surfaces exhibit an avoided crossing at  $\xi^*$ , as they cannot cross because an adiabatic state is always defined

<sup>4</sup>Basically you pick a molecular arrangement  $\xi_0$ , calculate the adiabatic states, then mix these states to get states, which are completely localized on  $A$  or on  $B$  and use these states as basis for all molecular configurations  $\xi$

with respect to its energy, i.e. the ground state adiabatic state is defined as the lowest energy state. Instead the adiabatic state changes character from being more localized on  $A$  to being more localized on  $B$ .

How to calculate  $J_{AB}$  for excitons will in detail be described in Chapter 6.

Using the diabatic basis, we proceed by calculating the rate expression  $\omega_{A \rightarrow B}$ . As the excitation is localized  $J_{AB}$  is small and can be treated as a perturbation [104, 105]. Using Fermi's golden rule yields:

$$\omega_{A \rightarrow B} = \frac{2\pi}{\hbar} |J_{AB}|^2 \int d\xi f(\xi) \delta(U_A(\xi) - U_B(\xi)), \quad (4.23)$$

with the integration over all configuration  $\xi$  weighted by the Boltzmann factor  $f(\xi) \propto \exp(-U_A(\xi)/k_B T)$ . The delta-function enforces energy-conservation, as a transition can only happen at the crossing point  $\xi^*$ , where  $U_A(\xi^*) = U_B(\xi^*)$ . We also neglect the dependency of  $J_{AB}$  on  $\xi$  as in the *Condon approximation*.

If the diabatic PESs  $U_A(\xi)$  and  $U_B(\xi)$  are known the rate equation eq. 4.23 can be solved. For most systems the computational cost of calculating the PES is too large and so the PESs have to be approximated. The first simplification is the introduction of the reaction coordinate  $\xi$ . If we go back one step and look at a general PES  $U(\mathbf{R})$ , with some minimum at  $\mathbf{R}^0$ , we can expand it to second order around that minimum:

$$U(\mathbf{R}) = U^0 + \sum_{ij} h_{ij} (R_i - R_i^0)(R_j - R_j^0) = U^0 + \sum_a \omega_a (Q_a - Q_a^0)^2 = U(\mathbf{Q}), \quad (4.24)$$

where  $Q_a$  are mass weighted normal mode coordinates with eigenfrequencies  $\omega_a$ , obtained by diagonalizing the Hessian matrix  $h_{ij}$ . The excitation transfer reaction is typically triggered by a subset of these eigenmodes. Often the nuclear motion can be described as a linear combination of these eigenmodes, yielding the reaction coordinate,  $\xi$ , with its eigenfrequency  $\omega_\xi$  and conjugate momentum operator  $\hat{P}_\xi$ . The corresponding nuclear Hamiltonian then reads:

$$\hat{H}_{\text{nuc}} = \frac{1}{2} \hat{P}_\xi^2 + U^0 + \frac{1}{2} \omega_\xi (\xi - \xi^0)^2. \quad (4.25)$$

Treating the oscillations along  $\xi$ , i.e. the promoting mode, classically we arrive at the Marcus rate equation [104, 105]:

$$\omega_{A \rightarrow B} = \frac{2\pi}{\hbar} \frac{|J_{AB}|^2}{\sqrt{4\pi\lambda k_B T}} \exp\left[-\frac{(U_{AB} - \lambda)^2}{4\lambda k_B T}\right]. \quad (4.26)$$

Here  $\lambda$  denotes the classical reorganization energy, which describes the molecular rearrangement necessary for the excitation transfer to happen

$$\lambda = \frac{1}{2}\omega_{\xi}(\xi_A - \xi_B)^2. \quad (4.27)$$

If the dimer complex is surrounded by other molecules environmental reorganization effects may also contribute. These can be described by an additional harmonic mode  $\tilde{\xi}$ , yielding the outer sphere reorganization energy:

$$\lambda^{\text{out}} = \frac{1}{2}\omega_{\tilde{\xi}}(\tilde{\xi}_A - \tilde{\xi}_B)^2. \quad (4.28)$$

$U_{AB}$  in eq. 4.26 is the energy difference:

$$U_{AB} = U_A(\xi_A) - U_B(\xi_B) \quad (4.29)$$

The Marcus rate has been used to great success to describe charge transfer in solution and solids [106]. The classical treatment of the promoting modes  $\xi, \tilde{\xi}$  is only justified if  $k_B T \gg \omega_{\xi}, \omega_{\tilde{\xi}}$ . This is rarely the case in organic electronics, as intra molecular vibrations have zero-point energies of around 0.1 eV, which is roughly four times the thermal energy at room temperature. Yet, the Marcus theory has been shown to give good results even at the limits of its validity [34, 92, 107]. Other rate expression like, Marcus-Levich-Jortner rates, which treat the promoting mode quantum mechanically or Weiss-Dorsey rates [108, 109], which treat the whole system quantum mechanically, extend the formal applicability of transfer rate theories. Unfortunately, these rates require additional input parameters to describe the PES, which can only be obtained at substantial computational cost.

Computational cost is already a major concern, as diabatic states, defined via eq. 4.18, are very difficult or even impossible to calculate [110]. Practically, the diabatic states have to be approximated. As the diabatic state  $|A\rangle$  resembles an excited monomer  $A$  and a ground state molecule  $B$ , the following simplification is used:

$$|A\rangle \approx |1_a\rangle \otimes |0_b\rangle. \quad (4.30)$$

The diabatic state is approximately the product of the adiabatic excited state of the isolated monomer  $A$ ,  $|1_a\rangle$  and the ground state of the isolated monomer  $B$ ,  $|0_b\rangle$ . This product ansatz reduces the number of states, that have to be calculated for  $N$  molecules, from  $\frac{1}{2}N(N-1)$  to  $N$ . All energetic contributions separate into monomer contributions as well, i.e.,

$$\begin{aligned}
 U_{AB} &= U_A(\xi_A) - U_B(\xi_B) \approx U_a^1(\xi_a^1) + U_b^0(\xi_b^0) - (U_a^0(\xi_a^0) + U_b^1(\xi_b^1)) \\
 &= \underbrace{(U_a^1(\xi_a^1) - U_a^0(\xi_a^0))}_{\Delta E_a} - \underbrace{(U_b^1(\xi_b^1) - U_b^0(\xi_b^0))}_{\Delta E_b} = \Delta E_{ab},
 \end{aligned}
 \tag{4.31}$$

where  $\Delta E_{ab}$  is the site energy difference between the molecules and  $\xi_{a/b}^{0/1}$  are the molecular configuration of monomer  $A/B$  in state  $0/1$ .

So for a system of  $N$  molecules  $N$  site energies,  $N$  reorganization energies and  $N(N-1)/2$  electronic couplings have to be calculated.

## 4.2.2 Partitioning of the system

Before the exciton dynamics can be calculated using rate models, a given morphology has to be divided into sites, on which excitations localize. This requires knowledge of the localization of the electronic states, as each site should preferably contain a single diabatic state of the complete system. In detail knowledge of the localization requires electronic structure calculations of the whole system, which are not feasible for larger systems. Instead the partitioning into segments can only be justified a posteriori by assessing the magnitude of the electronic coupling between segments. In many systems chemical intuition allows to define partitioning, which satisfies this test retrospectively, e.g., in most organic electronic systems a conjugated system (see Chapter 2) is a good minimal guess. As shown in Fig. 4.3 all atoms belonging to a single site are collectively referred to as a conjugate segment.

In small molecule systems each molecule is typically chosen as a single conjugated segment, because electronic structure calculations typically show complete delocalization of electronic states over the individual molecules. In polymeric systems this simple approach may fail, as torsion of the backbone and electron-phonon interaction may lead to localization on polymeric subunits instead of delocalization over the whole polymer chain. In these cases quantum mechanical calculations of the whole chain are necessary to determine localization sites [90, 111, 112].

After the system is partitioned into segments, these segments are additionally separated into rigid fragments, as depicted in Fig. 4.3. These fragments are typically insensitive to thermal fluctuations, e.g., a thiophene or benzene ring stays planar even at elevated temperatures. Although the fragment definitions are theoretically

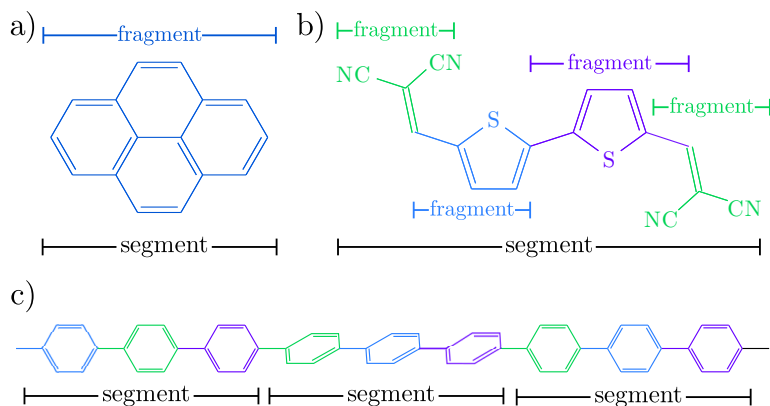


Figure 4.3: Partitioning scheme as employed in VOTCA. a) For small, inflexible molecules, the whole molecule is replaced by a rigid fragment. b) For larger molecules, more fragments are used to allow for some flexibility for the slower degrees of freedom. The whole molecule is still one segment. c) For a polymer, the chain is cut into segments, using input from quantum mechanical studies. Each segment may also contain more than one rigid fragment.

not necessary for the calculation of rates, the molecular dynamics configurations of the rigid fragments are often replaced with quantum mechanically optimized rigid fragments in order to “integrate out” fast degrees of freedom, e.g., the promoting modes, which are already described in the rate models. This has the additional benefit of removing some of the mismatch between quantum mechanically obtained geometries and molecular dynamics results.

### 4.2.3 Site energies

The site energy,  $\Delta E_a$ , of a molecule  $a$  is basically defined via eq. 4.31. Although this is a simple definition it is frayed with computational difficulties as the energy  $U_a$  not only depends on the isolated molecule but also the chemical environment it is located in. As discussed before, the electronic state also must be sufficiently localized on the molecule to even make the definition of a site energy valid. Sufficient localization entails weaker coupling to the surrounding, allowing us to treat the chemical environment as a small perturbation to the electronic state.

Although there are exchange, dispersion, and electrostatic interactions between

molecules, we focus only on the last, electrostatic interaction. There are a couple of reasons for this approximation. Firstly, we are not really interested in the absolute values of site energies but in differences between different electronic states, i.e.,  $\Delta E_a = U_a^1 - U_a^0$ . Consequently, all interactions which influence both states nearly equally, e.g. dispersion interaction, cancel out [113, 114]. Secondly, electrostatic interaction is very directional, thus it is very sensitive to changes in the charge distribution on the molecules. Thirdly, and most importantly, it is typically the strongest interaction present due to its slow decay with distance. So the site energy of a molecule  $a$  in state  $i$  is decomposed into the energy from the internal degrees of freedom  $E_{\text{int}}$  and the electrostatic contribution from the environment  $E_{\text{estat}}$ :

$$U_a^i(\xi_a^i) \approx E_{\text{int}}^i + E_{\text{estat}}^i. \quad (4.32)$$

The internal site energy difference  $\Delta E_{\text{int}} = E_{\text{int}}^1 - E_{\text{int}}^0$  can be calculated from the vacuum PES of the single molecule via:

$$\Delta E_{\text{int}} = U_{\text{vac}}^1(\xi_a^1) - U_{\text{vac}}^0(\xi_a^0). \quad (4.33)$$

Theoretically  $\Delta E_a$  is an adiabatic excitation energy calculated from the respective geometries for the ground and excited state. Depending on the electronic excitation (electron, hole, exciton) and the system at hand, slow (compared to the timescale of hopping) vibrational modes may seriously change the local excitation energy by distorting molecular geometries. These distortions lead to disorder in the internal site energies. Using vacuum optimized geometries may not be a good approximation, as they optimize out this dynamic, but on the time scale of electronic motion, frozen disorder. In practice geometries from molecular dynamics simulations are used for the ground and excited states, using the mapping procedure described earlier to account for the geometry reorganization upon excitation in the site energies (see Chapter 7).

As mentioned above, the electrostatic contribution to the site energy of a molecule  $E_{\text{estat}}^i$  depends on the surrounding. The question is how to treat this effect. A fully quantum mechanical treatment of the whole system is impossible. Instead the interaction between the quantum mechanical excitation and the environment can be modeled on different levels (see Fig. 4.4). Starting with the quantum mechanical excitation in vacuum, Fig. 4.4(a), either the electrostatic potential of the surrounding molecules can be fully added to the Hamiltonian operator of the quantum mechanical region Fig. 4.4(c). Instead the interaction can be described as classically interacting charge densities, Fig. 4.4(b), which will be described in the next



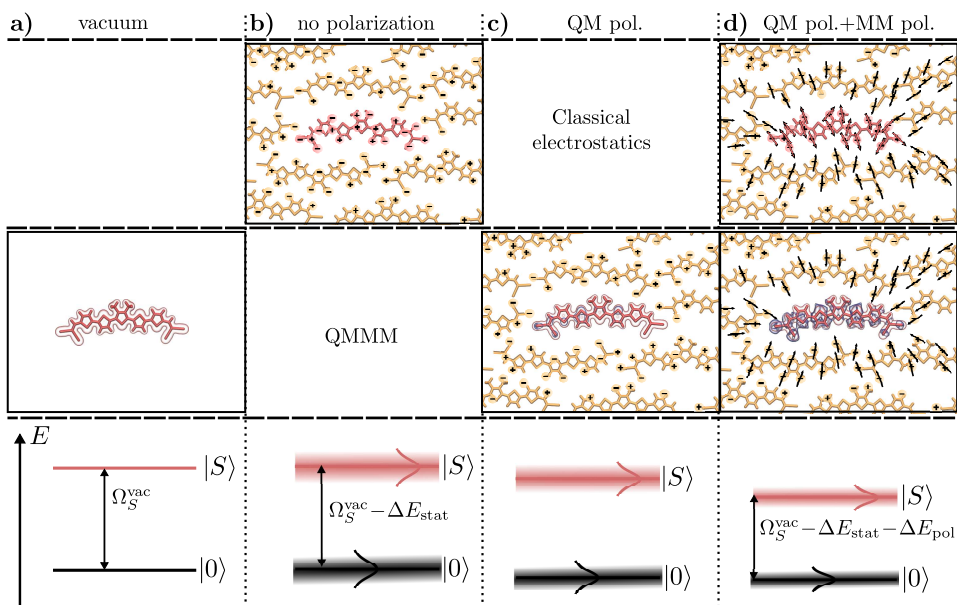


Figure 4.4: Overview of the site energy calculation options in the VOTCA suite using either a perturbative classical approach or a coupled QM/MM approach. For the classical approach the initial starting point is a vacuum QM calculation, yielding the ground state and excited state energies in vacuum (a). Adding purely classical electrostatics leads to different environments for every molecule and thus a spread of the HOMO and LUMO energies (b). (d) Adding classical polarization (indicated by black arrows) on neighboring molecules allows the system to relax and reduce the energetic disorder. Likewise the QM/MM treatment inserts a fully quantum mechanical description of the molecule surrounded by classical charges (c) or as in the classical model a full polarization response of the environment (d). The difference being, that a the polarization response of the molecule in question is more flexible in the QM/MM treatment, as charge can flow over the whole molecule.

paragraphs. The effects of polarization contributions, Fig. 4.4(d), which allow the environment to react to excitations will be described later.

Focusing on one molecule, the electrostatic contribution of the environment to its Hamiltonian reads:

$$\hat{H}_{\text{ext}} = \int d^3\mathbf{r} \hat{\rho}(\mathbf{r}) \varphi(\mathbf{r}), \quad (4.34)$$

where  $\hat{\rho}(\mathbf{r})$  is the molecule's charge density operator and  $\varphi(\mathbf{r})$  is the external electrostatic potential due to the environment. It can be written as:

$$\varphi(\mathbf{r}) = \sum_K \int d^3\mathbf{r}' \frac{\rho_K(\mathbf{r}')}{|\mathbf{r}' - \mathbf{r}|}, \quad (4.35)$$

where  $K$  runs over all molecules in the environment and  $\rho_K(\mathbf{r}')$  is the molecular charge density belonging to molecule  $K$ . Here, we modeled the neighboring molecules as classical entities by replacing their charge density operator with the respective classical charge densities.

Calculating the external potential, eq. 4.35, requires an integration over the charge densities of the adjacent molecules, which although possible is computationally very demanding for large systems. Instead a distributed multipole expansion is used to calculate the external potential. In a distributed multipole expansion, the molecular charge density  $\rho(\mathbf{r})$  is not expanded via multipoles centered around a single point. Instead the molecule is divided into regions, which are described by their own multipole moments. A region typically comprises a single atom, with the origin located at the atom. The potential of a single region of molecule can be expanded as

$$\varphi(\mathbf{r})^{\text{el}} = T(\mathbf{r})q - T_\alpha(\mathbf{r})d_\alpha + \frac{1}{3}T_{\alpha\beta}(\mathbf{r})\Theta_{\alpha\beta} - \dots + \frac{(-1)^n}{(2n-1)!!}T_{\alpha\beta\dots\nu}^{(n)}(\mathbf{r})\zeta_{\alpha\beta\dots\nu}^{(n)}, \quad (4.36)$$

with  $q$  being the charge of that region,  $d$  the dipole moment,  $\Theta_{\alpha\beta}$  the cartesian quadrupole tensor and  $\zeta_{\alpha\beta\dots\nu}^{(n)}$  the corresponding higher moments. The cartesian interaction tensor  $T_{\alpha\beta\dots\nu}^{(n)}$  is defined as:

$$T_{\alpha\beta\dots\nu}^{(n)}(\mathbf{r}) = \nabla_\alpha \nabla_\beta \dots \nabla_\nu \frac{1}{|\mathbf{r}|}. \quad (4.37)$$

Finally,  $\varphi(\mathbf{r})$  reduces to a sum over all regions  $r(K)$  of all adjacent molecules  $K$ :

$$\varphi(\mathbf{r}) = \sum_K \sum_{r(K)} \varphi(\mathbf{r})_{K,r(K)}^{\text{single}}. \quad (4.38)$$

The resulting potential can then be inserted into eq. 4.34 and in conjunction with the *ab initio* methods from Chapter 3 the excited and ground state energy can be calculated. This corresponds to the first QM/MM approach in Fig. 4.4, where the quantum mechanical charge density reacts to the static environment. This approach still has two drawbacks. Firstly, performing an *ab initio* calculation for every molecule in a large system can be computationally infeasible. Secondly, so

far we have assumed that the environment does not react to the excitation. In reality, the environment tries to lower the total energy by screening the excitation, i.e., the environment polarizes. The polarization response of the environment in turn will lead to a polarization of the center molecule. This feedback loop requires a self-consistent treatment, regardless of whether the central molecule is described classically or quantum mechanically.

To address the first problem, we simply substitute the quantum mechanical treatment of the center molecule by a classical description via distributed multipole moments. The electrostatic interaction  $V_{\text{elstatic}}^{AB}$  between two molecules  $A$  and  $B$  then reduces to

$$V_{\text{elstatic}}^{AB} = \sum_{a \in A} \sum_{b \in B} \left[ T^{ab} q^a q^b + T_{\alpha}^{ab} (q^a d_{\alpha}^b - d_{\alpha}^a q^b) + T_{\alpha\beta}^{ab} \left( \frac{1}{3} q^a \Theta_{\alpha\beta}^b - d_{\alpha}^a d_{\beta}^b + \frac{1}{3} \Theta_{\alpha\beta}^a q^b \right) + \dots \right] \quad (4.39)$$

with  $T^{ab} = T(\mathbf{r}_a - \mathbf{r}_b)$ .

The electrostatic contribution to the site energy of molecule  $A$  in state  $i$  then reads:

$$E_{\text{estat}}^i = \sum_B V_{\text{elstatic}}^{AB}(a^i), \quad (4.40)$$

where  $(a^i)$  denotes that the multipoles belonging to the state  $i$  should be used.  $B$  runs over all other molecules, with their respective ground state multipoles. The classical environment correction for a transition from the ground state to  $n$ -th excited state then be  $\Delta E = E_{\text{estat}}^0 - E_{\text{estat}}^n$ .

The second problem of how to incorporate the polarization response of the environment requires an extension of the distributed multipole model. Every atom  $a$  of a molecule is also assigned a polarization tensor  $\alpha_{\alpha\beta}^a$ . An external field  $F_{\alpha}^a$  will lead to an induced dipole moment on site  $a$ . The induced dipoles are not only caused by the external field originating from the by static multipoles on other atoms but also by the fields originating from induced dipole moments on other atoms. The total field at  $a$  thus is a combination of the static external field  $F_{\alpha}^a$  as well as the induced fields from the induced dipoles on all other atoms. The induced dipole on  $a$  is

$$\Delta d_{\gamma}^a = \alpha_{\alpha\beta}^a \left( F_{\alpha}^a + \sum_{b \neq a} T_{\alpha\beta}^{ab} \Delta d_{\beta}^b \right). \quad (4.41)$$

The assignment of atomic polarizabilities is called the Applequist model [115]. Here, the polarizations are only correlated via the fields they generate (see eq. 4.41)

and cannot model the flow of charges across the whole molecule. For molecules with large conjugated systems, which can displace charges over larger distances, necessitating more advanced polarization models [116, 117] or a full quantum mechanical treatment are necessary (see Fig. 4.4 and sec. 5.4). The system of equations, eq. 4.41, has to be solved self-consistently or via matrix inversion, which both increase the computational cost approximately by one order of magnitude in comparison to a static approach.

Letting the environment react to the excitation on the center molecule explicitly couples the QM and MM system to each other. So energy differences cannot be calculated for the embedded molecule but instead total energies have to be subtracted. For example, the first excitation energy  $\Omega_1$  has to be calculated via

$$\Omega_1 = [GS(BG[\Omega_1]) + \Omega_1(BG[\Omega_1])] - GS(BG[GS]), \quad (4.42)$$

with  $GS(BG[\Omega_1])$  being the ground state energy, in a background/environment polarized for the first excited state. As a result, for each site energy the excited state in its polarization environment as well as the ground state in its polarization environment have to be calculated, further increasing the computational cost in comparison to a simple static approach.

Finally, the induced-induced interaction of the Applequist model leads to a polarization catastrophe at short distances. This is an artifact of the point-dipole description of polarization, as in reality the polarization response is smeared out. An empirical fix, called Thole damping [118], avoids this overpolarization by introducing a smeared out charge density  $\rho(u)$  with  $u = r/S_{ab}$  and  $S_{ab} = (\alpha_a\alpha_b)^{1/6}$ , which modifies the dipole-dipole interaction between atoms  $a$  and  $b$  with mean polarizabilities  $\alpha_a, \alpha_b$  as follows

$$\tilde{T}_{\alpha\beta}^{ab} = \frac{f_e R^2 \delta_{\alpha\beta} - 3f_t R_\alpha R_\beta}{R^5}. \quad (4.43)$$

Here  $f_e$  and  $f_t$  are the corresponding damping functions, which depend on the form of the smeared out charge density. We use the smeared density from the AMOEBA force field [119]:

$$\rho(u) = \frac{3a}{4\pi} \exp(-au^3). \quad (4.44)$$

This leads to  $f_e = 1 - \exp(-\lambda u^3)$  and  $f_t = 1 - (1 + \lambda u^3) \exp(-\lambda u^3)$ . In this work we use  $\lambda = 0.37$ . The atomic polarizabilities  $\alpha$  were taken from a generic set of element-based polarizabilities ( $\alpha_C = 1.334\text{\AA}^3$ ,  $\alpha_H = 0.496\text{\AA}^3$ ,  $\alpha_N = 1.073\text{\AA}^3$ ,  $\alpha_O = 0.873\text{\AA}^3$ ,  $\alpha_S = 2.929\text{\AA}^3$ ). These are sufficient to reproduce the molecular polarizability of

many organic compounds. However,  $\pi$ -conjugated molecules with their delocalized  $\pi$ -orbitals have higher polarizabilities which cannot be reproduced with the generic atomic polarizabilities. In this case the atomic polarizabilities are scaled to match the molecular polarizabilities from ab-initio calculations for the respective compounds [113, 120].

A technical difficulty that may even arise from the simple electrostatic summation in eq. 4.39 is the question of how many neighboring molecules have to be considered. Traditionally a cut-off based approach is used, taking all molecules within a certain distance into account. This is problematic because the electrostatic interaction does not converge with increasing cutoff size. Although this is ameliorated by the fact, that most systems are not charged and thus the charge-charge interaction cancels out, even charge-quadrupole interaction is only conditionally convergent. Depending on the dimensionality of the system and the excitation of interest more advanced methods like *long-range aperiodic embedding* [121] have to be used.

This finally leaves the question of how to reduce the molecular density  $\rho(\mathbf{r})$  to a set of multipole moments located on the atoms  $\{Q_{\alpha\beta}^i\}$ . There is a number of different methods to arrive at atom-centered multipoles, from Mulliken charges [122] over NBO [123] charges to GDMA [124] multipoles. We will briefly outline the CHELPG (CHarges from ELectrostatic Potential, Grid-base) method [125], which, although it does not produce chemically intuitive charges, is designed to reproduce the electrostatic potential outside the molecule optimally via point charges. The point charges derived from molecular charge densities are typically referred to as partial charges.

CHELPG partial charges  $\{q_i\}$  are derived by calculating the electrostatic potential  $\phi_{el}(\mathbf{r})$  from the electron density  $\rho(\mathbf{r})$  at a large number of grid points outside the molecule  $\{\mathbf{g}_j\}$  and then adjusting the partial charges to reproduce the potential in a least square sense as optimally as possible, e.g., by minimizing:

$$\min = \left( \sum_{j=0}^K \phi_{el}(\mathbf{g}_j) - \sum_{i=0}^N \frac{q_i}{|\mathbf{r}_i - \mathbf{g}_j|} \right)^2 - \lambda \left( q_{\text{mol}} - \sum_{i=0}^N q_i \right), \quad (4.45)$$

where  $j$  runs over all grid points,  $\phi_{el}(\mathbf{g}_j)$  is the respective potential at that grid point and  $N$  is the number of atomic sites.  $\lambda$  is a Lagrange multiplier to constrain the optimization to the desired total charge of the molecule  $q_{\text{mol}}$ .

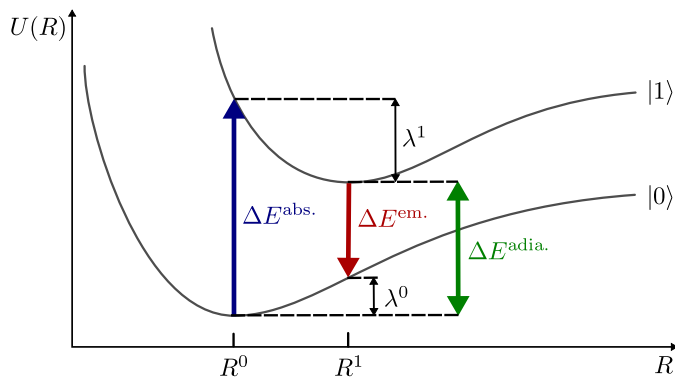


Figure 4.5: Absorption and emission inside a molecule.

#### 4.2.4 Reorganization energies

In Marcus theory, the nuclear rearrangement on excitation and deexcitation of a molecule are expressed in the two reorganization energies:

$$\lambda_{A \rightarrow B} = U_B(\xi_A) - U_B(\xi_B) \quad (4.46)$$

$$\lambda_{B \rightarrow A} = U_A(\xi_B) - U_A(\xi_A). \quad (4.47)$$

Using the approximation that the diabatic state can be written as a product of monomer states (eq. 4.30) the energy of a diabatic state  $U_B(\xi_A)$  splits into a sum of monomer contributions:

$$\begin{aligned} \lambda_{A \rightarrow B} &= U_b^1(\xi_b^0) + U_a^0(\xi_a^1) - (U_b^1(\xi_b^1) + U_a^0(\xi_a^0)) \\ \lambda_{B \rightarrow A} &= U_a^1(\xi_a^0) + U_b^0(\xi_b^1) - (U_a^1(\xi_a^1) + U_b^0(\xi_b^0)). \end{aligned} \quad (4.48)$$

$U_b^1(\xi_b^0)$  is the energy of monomer  $B$ , in its first excited state, evaluated at the nuclear coordinates  $\xi_b^0$  of the ground state of  $B$ . Consequently, within this approximation the reorganization energy for a pair of molecules can be calculated from monomer properties of the individual molecules.

A better understanding of the reorganization energy can be gained if we first avoid the dimer problem and look at the single molecule problem of light absorption and emission in a single molecule as depicted in Fig. 4.5. Upon absorption of a photon with energy  $\Delta E^{\text{abs.}}$  the molecule transitions from the electronic ground state  $|0(R^0)\rangle$ , where  $R^0$  is the minimum of the ground state PES, to an excited

state,  $|1(R^0)\rangle$ . Here it is assumed, that during the absorption the geometry does not change. This is again the Condon approximation. After absorption the molecule then releases the energy  $\lambda^1$  thermally, reaching the minimum of the excited state PES,  $|1(R^0)\rangle$ . Afterwards the molecule emits a photon of energy  $\Delta E^{\text{em}}$ , returning to the electronic ground state  $|0(R^1)\rangle$ , but at an excited geometry. Through thermalisation of the energy  $\lambda^0$  the molecule finally “descends” to  $|0(R^0)\rangle$ . If we look at exciton transfer reactions between two molecules, the transfer can be conceptualized as the emission of a photon on one molecule and adsorption on the other. Assigning the emission and, thus,  $\lambda^0$  to molecule  $A$  and  $\lambda^1$  to molecule  $B$ , we also arrive at equation eq. 4.48. Figure 4.5 also shows that  $\Delta E^{\text{em}}$  is always smaller than  $\Delta E^{\text{abs}}$ . The difference between the two is called the *Stokes-shift* and can be experimentally determined from spectroscopic measurements. Measurements of the Stokes-Shift allow us to compare theoretical reorganization energies with experimental values. As mentioned before in the derivation of the Marcus rates, for excitation transfer to happen  $\Delta E_B^{\text{abs}}$  must equal  $\Delta E_A^{\text{em}}$  to conserve energy. An energy quantum, corresponding to the Stokes shift, has to be provided by thermal fluctuations.

The calculation of  $U^1(\xi^1)$  requires a geometry optimization to find the nuclear configuration with the lowest energy. Especially for excited states, these geometry optimizations are extremely costly. As a further approximation the reorganization is assumed to be independent of the molecular environment. In doing so, the value  $\lambda$  only has to be calculated once for each molecular species in the system at hand, instead of for every molecule.

### 4.2.5 Directed graphs

After calculating all rates between the segments we have reduced the real system of molecules to a discrete irregular lattice of sites<sup>5</sup>, which are connected (see Fig. 4.6). These connections are also called edges. The combination of vertices and edges is called a graph. The graph that results from transfer rate theory is weighted, as the edges connecting vertices  $A$  and  $B$  have different rates for each pair, and also directed as the weights differ in both directions:

$$\omega_{A \rightarrow B} \neq \omega_{B \rightarrow A}. \quad (4.49)$$

<sup>5</sup>In most texts about graphs these sites are referred to as vertices

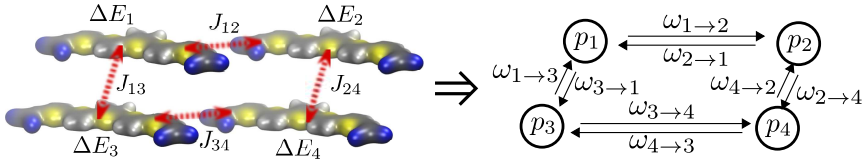


Figure 4.6: Molecular structure and the resulting directed graph. The rates calculated from the molecular properties reduce the molecular structure allow us to build a directed and weighted graph, with edges weighted by the appropriate rates and vertices carrying occupation probabilities.

As we assume that the excitation hops from site to site and that hopping is a rather rare event, the excitation resides on the site long enough for the thermal vibration to dissipate the information of where the excitation came from. The transport is said to be incoherent, meaning the excitation has lost its memory and the next hop of the excitation is independent of the last hop. Such a process is called *Markovian*. It allows us to formulate an equation of how the occupation probabilities of each vertex  $p_A$  evolve in time is:

$$\frac{\partial}{\partial t} p_A(t) = \sum_B p_B(t) \omega_{B \rightarrow A} - p_A(t) \omega_{A \rightarrow B}. \quad (4.50)$$

This continuity equation simply states that change in occupation of site  $A$  is equal to the probability current flowing in minus the current flowing out and so conserves the total probability. It is also referred to as the Master Equation. In this formulation it only describes the motion of a single excitation, as it does not account for interaction between excitations. Although there are ways to incorporate interaction between excitations into eq. 4.50, we will first deal with its solution. The master equation is simply a system of linear differential equations and can be solved using standard numerical methods. Although this has approach has its merits, we instead choose a very different option using the *kinetic Monte Carlo* or KMC method, because it allows us to easily add excitation interaction, excitation decay and conversion from one species to another. Furthermore, KMC is better suited for very large systems, in which explicitly setting up a large rate matrix is prohibitively expensive, and for systems with widely varying rates, as solvers otherwise run into numerical difficulties.

In KMC, we explicitly simulate the hopping of individual excitations. Using a variable step size method, we promote time and at each time step we randomly choose



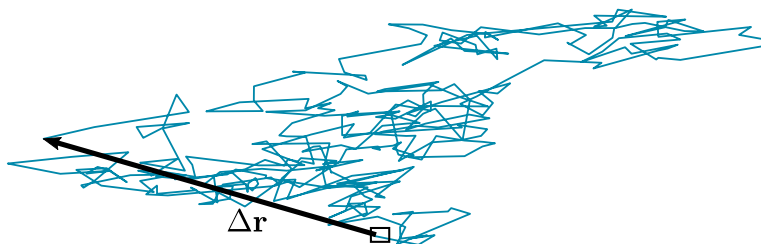


Figure 4.7: KMC trajectory of an exciton.  $\Delta \mathbf{r}$  denotes the end-end distance of the trajectory. The small box indicates the initial simulation box. Diffusion coefficients can be calculated from averaging over trajectories.

an excitation and its next hopping destination [126]. The probability of choosing a hopping destination is weighted by the rate assigned to that transition. As these rates can vary by orders of magnitude we do not increment time by a fixed amount but instead use the variable step size method (VSSM) [127].

From the resulting ensemble of trajectories (see Fig. 4.7) the diffusion coefficient  $D_{\alpha\beta}$  can be calculated via:

$$6D_{\alpha\beta}t = \langle \Delta r_{\alpha} \Delta r_{\beta} \rangle. \quad (4.51)$$

Here  $t$  is the temporal length of the trajectories,  $\Delta \mathbf{r}$  denotes the distance vector between initial and last site and  $\langle \dots \rangle$  denotes an average over the ensemble of trajectories.

With the calculation of the diffusion constant conceptually the bridge between *ab-initio* input and macroscopic transport properties has been build. So using the molecular dynamics approach we are able to simulate morphologies of organic semiconductors and then reintroduce electronic dynamics via rate models. This workflow relies on electronic structure theories to solve the electronic Hamiltonian as introduced in Chapter 3. The actual implementation of these concepts for ground and excited state and the integration of classical environments for, e.g., the calculation of site energies is discussed in the next chapter.



## Chapter 5

# Numerical implementation of DFT/*GW*-BSE and quantum-classical approaches in VOTCA

The theoretical concepts outlined in the previous chapters are implemented in the VOTCA (versatile object-oriented toolkit for coarse-graining and energy-transport applications) suite of tools<sup>1</sup>. VOTCA is an open source software and available for download at [github.com/votca](https://github.com/votca).

The VOTCA suite consists of five subparts, namely TOOLS, CSG, MOO, CTP, XTP and KMC (see Fig. 5.1). TOOLS is a low level library, which contains linear algebra and other convenience functions. CSG is a library which adds coarse graining routines for molecular dynamics simulations [128]. MOO is an library used for the calculation of electronic couplings for electrons and holes in the ZINDO formalism [129]. CTP implements electrostatic and electronic coupling calculations for

---

<sup>1</sup>This chapter is mostly based on Jens Wehner, Lothar Brombacher, Joshua Brown, Christoph Jung-hans, Onur Çaylak, Yuriy Khalak, Pranav Madhikar, Gianluca Tirimbò and Björn Baumeier. "Electronic Excitations in Complex Molecular Environments: Many-Body Green's Functions Theory in VOTCA-XTP" *J. Chem. Theory. Comput.* 14 (12) (2018), pp 6253–6268

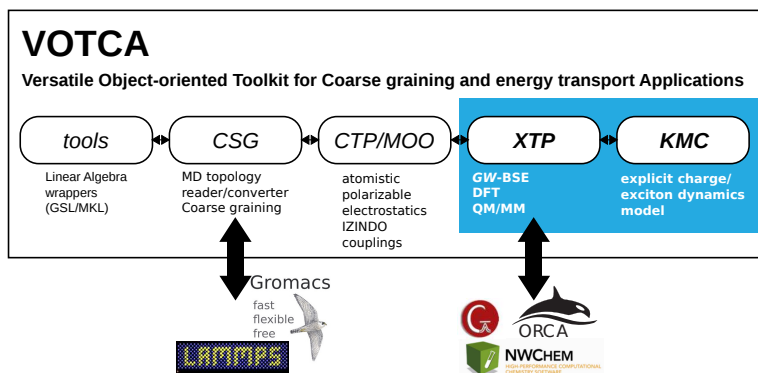


Figure 5.1: Overview of the VOTCA suite of packages. Interfaces to MD packages are implemented via CSG and DFT code interfaces are implemented via XTP. The blue box are the packages in which the majority of the implementation happened.

charge carriers and implements the rate theory formalism [92]. XTP extends this formalism for excitations, including a DFT and *GW*-BSE implementation, capable of QM/MM calculations using CTP electrostatics. Finally the KMC module solves the master equation, eq. 4.50, via kinetic Monte-Carlo simulations.

In this chapter we will only look at the implementation and results of the quantum mechanical methods provided by XTP.

As the software package VOTCA-XTP grew and contributions of different developers came in. Modern software practices had to be adopted to ensure that the code has as little bugs as possible and maintain that state, despite modifications, as well as increase the user friendliness. So in the following I will briefly outline the design choices for VOTCA and the adaptation of recent software development best practices.

## 5.1 Developing for VOTCA

As mentioned above VOTCA consists of five subparts, which are developed by groups in Germany, the United States, and the Netherlands. The complete set of libraries is hosted on Github as part of the VOTCA organization. Github, which necessitates the use of Git as version control tool, allows for decentralized devel-

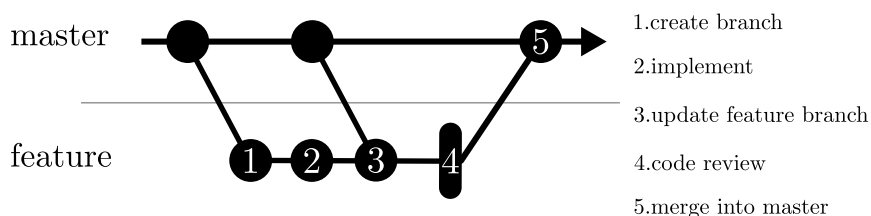


Figure 5.2: Software development workflow in VOTCA using the Git. Feature development happens on feature branches, which can only be merged into the master branch after code review. This guarantees, that the master branch can always compile.

opment and stringent version control. The basic idea revolves around saving each major change of the source code including the documentation as a *commit*. A string of these commits is referred to as a branch. Fortunately, version control was already set up for the CSG library, on which XTP is build. We rely heavily on the branch idea of Git. The *master* branch is the current fully working version, from which people can establish their own branches to work on specific features. For XTP we established code review practices, so that code from feature branches cannot be simply merged into the *master* branch, without at least another pair of eyes checking and reviewing it. The complete workflow is outlined in Fig. 5.2.

In parallel the master branch CSG and XTP and all branches which want to merge into it are build on external servers, to check if compilation succeeds. Additionally, each function and class has to have unit tests which guarantee that the behavior of that function remains stable under code changes. These tests are also run on any code, that is to be merged into the master branch. To guarantee that individual classes work together correctly, we also created a set of larger scale integration tests, which also double as a tutorial for novice users of the library.

As the CSG library was implemented in the C++ programming language, XTP could capitalize on that, as C++ is among the top 3 programming languages in raw performance, which is advantageous for running the expensive quantum chemistry calculations. Besides the efforts in testing, code review and version control, XTP has upgraded the C++ standard from C++98 to C++11 to use more abstract and powerful language features, especially for memory management. Furthermore, XTP now heavily relies on the Eigen3 library for linear algebra[130], which offers a modern and efficient interface to vector and matrix operations. It allows to write abstract, vectorizable code. For even higher performance we link the linear algebra against the Intel MKL library, which is a highly optimized BLAS/LAPACK library for

intel chipsets. Finally, to take advantage of thread parallelism in modern CPU architectures, we employ the OpenMP library to distribute calculations over multiple threads in a shared memory environment [131].

## 5.2 Density functional theory in a Gaussian basis

To provide a starting point for *GW*-BSE calculations XTP provides, next to the interfaces to standard quantum-mechanical packages, a native implementation of density functional theory. Next to development purposes, the native implementation provides additional functionality, such as the inclusion of point dipole and quadrupole potentials, required for coupled quantum-classical calculations using the distributed multipole expansion for environment molecules. The Kohn-Sham implementation uses Gaussian basis functions, as the code is primarily used for molecular systems. As these systems are finite, also the Kohn-Sham orbitals can be represented as real quantities. At the moment, explicit spin dependence is not implemented and only closed shell systems can be treated.

Various parametrization for exchange correlation functionals are provided by the *LibXC* library [132]. Currently, XTP supports the LDA, GGA, and hybrid functionals. To evaluate the contributions of the exchange correlation functional to the Hamiltonian matrix, as well as the total energy, numerical integration is performed using a superposition of atom-centered spherical Lebedev and radial Euler-Maclaurin grids, as used in NWChem [133]. Besides integration of the exchange functional, the grids can also be used to numerically integrate external potentials, e.g., the long-range embedding potential [121].

To start the self-consistency cycle discussed in Chapter 3.2, two initial guess algorithms are available. Either non-interacting electrons can be chosen, in which case eq. 3.20 is simply diagonalized. The non-interacting orbitals are typically much too localized, as no electron-electron repulsion pushes them apart. So many iterations are required to reach convergence. A better guess is the superposition of atomic densities, where one atomic DFT calculation is performed for each element separately and the resulting densities are added up [134].

To speed up the convergence of the SCF iteration procedure the density matrix resulting from the new coefficients is not simply inserted into the next iteration, instead a linear combination of Hamiltonians from previous iterations is used instead. The coefficients are either chosen to reduce an approximate energy func-

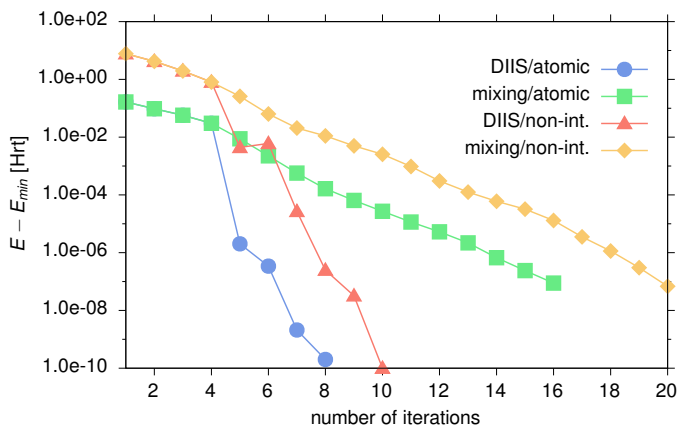


Figure 5.3: Convergence of the DFT total energy with the number of self-consistency iterations in methane for different initial guesses using PBE/def2-svp. The initial guess is either *atomic*, which refers to the superposition of atomic densities, or non-interacting electrons. Convergence acceleration is provided by DIIS algorithms and simple mixing.

tional, ADIIS [135], or the commutator of the Fock and density matrix, DIIS [136, 137].

The advantage of these methods can be seen in Fig. 5.3. The total energy at each iteration is shown for CH<sub>4</sub> using an all-electron calculation with the def2-svp basis set [72]. The non-interacting starting guess requires 20% more iterations to reach convergence than the atomic superposition. The use of the DIIS method halves the amount of steps till convergence compared to mixing of density matrices, e.g.  $\underline{\mathbf{D}}^{n+1} = \alpha \underline{\mathbf{D}}^n + (1 - \alpha) \underline{\mathbf{D}}^{n-1}$ , with  $\alpha = 0.3$  typically.

The usage of Gaussian basis functions introduces a number of integrals over said functions. Most prominently the electron-electron interaction integrals between

basis functions  $\chi_i$  and  $\chi_j$  have to be calculated according to eq. 3.50:

$$\langle \chi_i | \hat{V}_H | \chi_j \rangle = \iint d\mathbf{r} d\mathbf{r}' \chi_i(\mathbf{r}) \chi_j(\mathbf{r}) \frac{1}{|\mathbf{r} - \mathbf{r}'|} \rho(\mathbf{r}') \quad (5.1)$$

$$= \iint d\mathbf{r} d\mathbf{r}' \sum_{kl} \underline{\mathbf{D}}_{kl} \frac{\chi_l(\mathbf{r}') \chi_k(\mathbf{r}') \chi_i(\mathbf{r}) \chi_j(\mathbf{r})}{|\mathbf{r} - \mathbf{r}'|} \quad (5.2)$$

$$= \sum_{kl} \underline{\mathbf{D}}_{kl} \iint d\mathbf{r} d\mathbf{r}' \frac{\chi_i(\mathbf{r}) \chi_j(\mathbf{r}) \chi_k(\mathbf{r}') \chi_l(\mathbf{r}')}{|\mathbf{r} - \mathbf{r}'|} \quad (5.3)$$

$$= \sum_{kl} \underline{\mathbf{D}}_{kl} (ij|kl), \quad (5.4)$$

where we used eq. 3.63 in the second line and defined:

$$(ij|kl) = \iint d\mathbf{r} d\mathbf{r}' \frac{\chi_i(\mathbf{r}) \chi_j(\mathbf{r}) \chi_k(\mathbf{r}') \chi_l(\mathbf{r}')}{|\mathbf{r} - \mathbf{r}'|}. \quad (5.5)$$

These are also called 4-center integrals. Similar integrals also appear in the matrix elements for the exchange interaction eq. 3.35. The evaluation of these integrals is the costliest part of the DFT calculation and requires  $N^4$  calculations, if  $N$  is the number of basis functions. In VOTCA-XTP these integrals over Gaussian basis functions are evaluated using the modified recursive algorithms by Obara [71, 138]. In total VOTCA-XTP can compute these integrals for contracted gaussian basis functions with up to  $l = 4$ .

In order to reduce the scaling, we make use of the fact that the set of product functions  $\chi_i(\mathbf{r}) \chi_j(\mathbf{r})$  contains  $N^2$  distinct functions. This space of products of basis functions is highly linearly dependent and can thus be well approximated by a smaller space of auxiliary basis functions  $\xi_v$ , which contains only  $(3-5)N$  functions. This approximation, also known as density-fitting, reduces the scaling from  $N^4$  to  $N^3$ . The 4-center integrals can be written as a combination of 3-center and 2-center repulsion integrals [139]:

$$(ij|kl) \approx \sum_{v,\mu} (ij|v) (v|\mu)^{-1} (\mu|kl), \quad (5.6)$$

where  $(v|\mu)^{-1}$  is the inverse of the 2-center repulsion matrix

$$(v|\mu) = \iint d^3\mathbf{r}_1 d^3\mathbf{r}_2 \xi_v(\mathbf{r}_1) \frac{1}{|\mathbf{r}_1 - \mathbf{r}_2|} \xi_\mu(\mathbf{r}_2) \quad (5.7)$$

and  $(ij|v)$  is the 3-center repulsion matrix

$$(ij|v) = \iint d^3\mathbf{r}_1 d^3\mathbf{r}_2 \chi_i(\mathbf{r}_1) \chi_j(\mathbf{r}_1) \frac{1}{|\mathbf{r}_1 - \mathbf{r}_2|} \xi_v(\mathbf{r}_2). \quad (5.8)$$



Formally, eq. 5.6 appears like the insertion of a resolution of the identity with metric  $(\nu|\mu)^{-1}$ . As the 2-center repulsion matrix  $(\nu|\mu)$  is often also abbreviated as  $V_{\nu\mu}$ , this method is also known as *RI-V*. This method is implemented in VOTCA-XTP to use for larger systems. The error due to the RI-approximation is of the order of  $1 \mu\text{Ha}/\text{atom}$  and can be improved upon by choosing a larger auxiliary basis set [140]. Currently, VOTCA-XTP precalculates all integrals at the start of the calculation and stores them in memory. For larger systems VOTCA-XTP has to use the RI approximation, as using explicit 4-center integrals as in eq. 5.5 would exceed the available memory.

Apart from the typical 2-, 3- and 4-center integrals, VOTCA-XTP has the option to calculate electrostatic interaction integrals with dipoles,  $\mathbf{d}$ , or quadrupoles,  $\Theta$ , located at  $\mathbf{C}$  outside the molecule.

$$(i|\mathbf{d}_\alpha|j) = \int d\mathbf{r} \chi_i(\mathbf{r}) \frac{\mathbf{r}_\alpha - \mathbf{C}_\alpha}{|\mathbf{r} - \mathbf{C}|^3} \chi_j(\mathbf{r}); \quad (\alpha = x, y, z) \quad (5.9)$$

$$(i|\Theta_{\alpha\beta}|j) = \int d\mathbf{r} \chi_i(\mathbf{r}) \frac{(\mathbf{r}_\alpha - \mathbf{C}_\alpha)(\mathbf{r}_\beta - \mathbf{C}_\beta)}{|\mathbf{r} - \mathbf{C}|^5} \chi_j(\mathbf{r}) \quad (\alpha, \beta = x, y, z). \quad (5.10)$$

This allows for more accurate representations of external electrostatic potentials, which is useful in QM/MM calculations. Especially dipole integrals are useful to accurately model the effect of classical induced dipoles as outlined in the last section of this chapter.

To further reduce the computational cost, VOTCA-XTP allows for the usage of pseudo potentials, eliminating the core electron and thus reducing the number of basis functions [141, 142].

The complete workflow of a DFT calculation is depicted in Fig. 5.4. First the overlap matrix,  $\underline{\mathbf{S}}$  and the sum of independent particle hamiltonians,  $\underline{\mathbf{H}}_0$ , are calculated and stored in memory. Additionally, the 3-center repulsion integrals are stored and kept in memory. The memory requirement of these integrals at the moment defines the accessible system size. Direct approaches, which only calculate the 3-center matrix elements when needed, are not implemented yet. Afterwards an initial guess is produced and the resulting density matrix constructed. From the density matrix the first exchange correlation matrix and electron repulsion matrices are constructed, which yields the first Fock matrix. In later iterations this Fock matrix is then linearly combined with older Fock matrices to optimize the next iteration in the DIIS procedure. The resulting KS-orbitals are then used to calculate a new density matrix. The iterative procedure is stopped, when the change in energy falls below a specified input and the final energies and KS-orbitals are written out.

Table 5.1: Total energies in Hartree for methane ( $\text{CH}_4$ ), DCV2T and DCV5T, calculated with three different DFT implementations, XTP-DFT engine, Gaussian09 and ORCA, using PBE as the exchange correlation functional [59]. ECP denotes pseudo-potential calculations using ubecppol as the basis set and Stuttgart-Köln effective core-potentials [148]. For the all-electron calculations the def2-svp basis set was used. RI denotes density fitting used.

$\text{CH}_4$	SVP	SVP-RI	ECP	ECP-RI
g09	-40.4141862	-40.4142835	-8.0692929	-8.0720562
ORCA	-40.4142150	-40.4143118	-8.0732375	-8.0732566
XTP	-40.4141995	-40.4142963	-8.0720495	-8.0720620
DCV2T	SVP	SVP-RI	ECP	ECP-RI
g09	-1626.37096	-1626.3715863	-154.554602	-154.5506801
ORCA	-1626.3717225	-1626.3723483	-154.5926740	-154.5933087
XTP	-	-1626.3721822	-	-154.5507288
DCV5T	SVP	SVP-RI	ECP	ECP-RI
g09	-3358.5602481	-3358.5614893	-270.7297088	-270.730097
ORCA	-3358.5617132	-3358.5629540	-270.8209578	-270.822384
XTP	-	-3358.5623371	-	-271.086210

In table Tab. 5.1 a comparison of VOTCA-XTP results with two popular DFT codes, ORCA [143] and Gaussian09 [144], is shown for methane, DCV2T and DCV5T-Me(3,3). DCV2T and DCV5T-Me(3,3) are dicyanovinyl end-capped oligothiophenes used as donor material in state-of-the-art organic solar cells [145–147]. The chemical structures can be found in app. A. The VOTCA-XTP DFT implementation yields very similar results for all molecules. Slight deviations between the values arise because each code uses slightly different numerical grids for the exchange correlation functional, as well as different cut-off and numerical stabilization procedures for matrix inversion.

In summary the DFT implementation of VOTCA-XTP allows to calculate accurate Kohn-Sham energies and orbitals in a localized gaussian basis for finite systems. The algorithms can be coupled to classical electrostatics in QM/MM calculations and also used as input for excited state calculations via *GW*-BSE as described below.

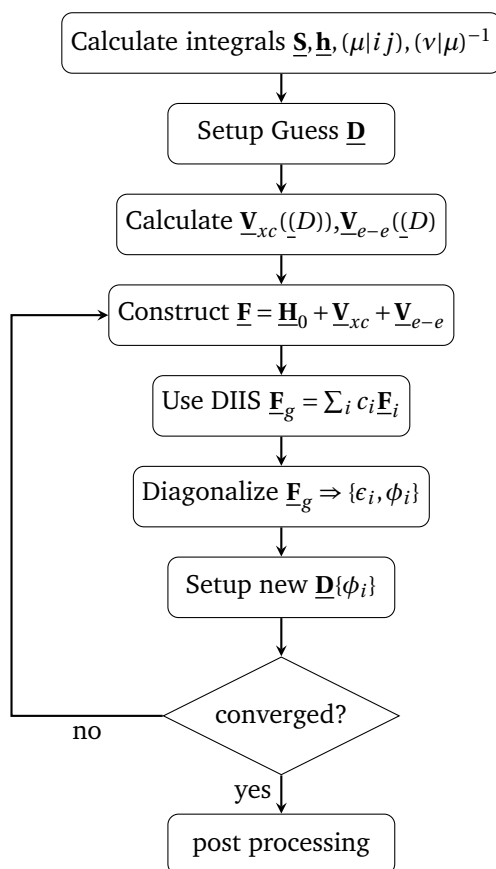


Figure 5.4: DFT workflow as implemented in VOTCA-XTP. The self-consistency circle ends if the change of the total energy and the commutator of Fock and density matrix are smaller than a specified amount.

### 5.3 GW-BSE in a Gaussian basis

The GW-BSE implementation in VOTCA-XTP uses a preceding DFT-calculation as a starting point, which are either calculated in XTP itself or in an external DFT implementation. VOTCA-XTP possesses interfaces to Gaussian versions 03 or 09 [144, 149], NWChem [133], and ORCA [143] to run and retrieve the Kohn-Sham states, as stated in Chapter 3. The exchange correlation functional matrix elements needed for the evaluation of the self-energy (eq. 3.106) is obtained from the XTP-DFT implementation.

The Kohn-Sham orbitals,  $\phi_i^{\text{KS}}(\mathbf{r})$ , from the preceding calculation are not only used as a starting point but also as the basis functions, in which all quasi-particle states and later electron-hole states are expressed. Additionally we use the already introduced auxiliary basis with functions  $\xi_\mu$  and their orthogonalized versions  $\xi'_{\mu'} = \sum_\mu \mathbf{S}_{\mu'\mu}^{-1/2} \xi_\mu$ , where  $\mathbf{S}$  is the overlap matrix of auxiliary basis functions.

The polarizability, which in the GW approximation is calculated as the convolution of the initial Green's function eq. 3.103, is written as:

$$P(\mathbf{r}_1, \mathbf{r}_2, \omega) = 2 \sum_{m,l} \frac{\phi_l^{\text{KS}}(\mathbf{r}_1) \phi_l^{\text{KS}}(\mathbf{r}_2) \phi_m^{\text{KS}}(\mathbf{r}_1) \phi_m^{\text{KS}}(\mathbf{r}_2)}{\omega - (\epsilon_m^{\text{KS}} - \epsilon_l^{\text{KS}}) + i\eta} - \frac{\phi_l^{\text{KS}}(\mathbf{r}_1) \phi_l^{\text{KS}}(\mathbf{r}_2) \phi_m^{\text{KS}}(\mathbf{r}_1) \phi_m^{\text{KS}}(\mathbf{r}_2)}{\omega + \epsilon_m^{\text{KS}} - \epsilon_l^{\text{KS}} - i\eta}, \quad (5.11)$$

where  $m$  runs over unoccupied and  $l$  over occupied KS functions. The factor 2 accounts for the fact that in a closed shell system, each level is occupied by two electrons. As will be apparent later, it is numerically beneficial to introduce the symmetrized Coulomb interaction  $\tilde{v}(\mathbf{r}_1, \mathbf{r}_2) = \pi^{-3/2} / |\mathbf{r}_1 - \mathbf{r}_2|^2$ , leading to:

$$\tilde{\epsilon}(1,2) = \delta(1,2) - \iint d^3 \mathbf{r}_3 4 \tilde{v}(1,3) P(3,4) \tilde{v}(4,2) \quad (5.12)$$

for the symmetric dielectric function. The symmetrized Coulomb interaction convoluted with itself results in the full Coulomb interaction, i.e.,

$$v(\mathbf{r}_1, \mathbf{r}_2) = \int d^3 \mathbf{r}_3 \tilde{v}(\mathbf{r}_1, \mathbf{r}_3) \tilde{v}(\mathbf{r}_3, \mathbf{r}_2) \quad (5.13)$$

or, symbolically,  $v = \tilde{v}\tilde{v}$ . Consequently the symmetric dielectric function is related to the conventional dielectric function according to  $\tilde{\epsilon} = \tilde{v}^{-1}\epsilon\tilde{v}$ . The screened Coulomb interaction  $W$  is then obtained via  $W = \tilde{v}\tilde{\epsilon}^{-1}\tilde{v}$ . Inserting eq. 5.11 into this equation and making use of resolution of identity, we can write  $\tilde{\epsilon}_{\tilde{v}\tilde{v}}$  in the basis of orthogo-

normalized auxiliary basis functions.

$$\tilde{\epsilon}_{\mu'\nu'}(\omega) = \delta_{\mu'\nu'} - 2 \sum_{m,l} I_{\mu'}^{ml} I_{\nu'}^{ml} \left[ \frac{1}{\omega - (\epsilon_m^{\text{KS}} - \epsilon_l^{\text{KS}}) + i\eta} - \frac{1}{\omega + (\epsilon_m^{\text{KS}} - \epsilon_l^{\text{KS}}) - i\eta} \right], \quad (5.14)$$

where  $l$  runs over occupied and  $m$  over unoccupied levels,  $I_{\nu'}^{mn}$  is:

$$I_{\nu'}^{ml} = \sum_{\mu} V_{\nu'\mu}^{l-1/2} M_{\mu}^{ml}, \quad (5.15)$$

with  $\underline{V}^{l-1/2} = (\underline{\mathbf{S}}^{-1/2} \underline{\mathbf{V}} \underline{\mathbf{S}}^{-1/2})^{-1/2} \underline{\mathbf{S}}^{-1/2}$ ,  $\underline{V}_{\nu\mu} = (v|\mu)$  as in eq. 5.7, and  $M_{\mu}^{nm}$  are:

$$M_{\mu}^{ml} = \iint d^3 \mathbf{r}_1 d^3 \mathbf{r}_2 \phi_m^{\text{KS}}(\mathbf{r}_1) \phi_l^{\text{KS}}(\mathbf{r}_1) \frac{1}{|\mathbf{r}_1 - \mathbf{r}_2|} \xi_{\mu}(\mathbf{r}_2). \quad (5.16)$$

$\xi_{\mu}(\mathbf{r}_2)$  is an auxiliary basis function and the 3-center integral can be decomposed into integrals over basis functions using eq. 3.60 and eq. 5.8:

$$M_{\mu}^{ml} = \sum_{i,j} X_{im} X_{jl} (ij|\mu). \quad (5.17)$$

Using the matrix inverse of  $\tilde{\epsilon}_{\mu'\nu'}$  and using eq. 3.91, we arrive at the following expression for the self-energy  $\Sigma(E)$ :

$$\langle \phi_n^{\text{KS}} | \Sigma(E) | \phi_m^{\text{KS}} \rangle = \sum_{\mu',\nu'} \sum_l I_{\mu'}^{ml} I_{\nu'}^{nl} \frac{i}{2\pi} \int d\omega \exp(i\omega\theta) \frac{\tilde{\epsilon}_{\mu'\nu'}^{-1}(\omega)}{E + \omega - \epsilon_l^{\text{KS}} \pm i\eta}, \quad (5.18)$$

where the plus sign in the denominator is used if  $\phi_l$  is occupied and the minus sign otherwise. Using the symmetrized version of the Coulomb interaction in combination with the RI-V approximation thus allows us to collect all terms containing integrals over basis functions into the three center terms  $M_{\mu}^{ml}$ , which can be stored in memory.

A number of ways to perform the frequency integration in eq. 5.18 exist. First the integral can be solved analytically by diagonalizing the Hamiltonian of the RPA equation (eq. 5.14) and then transforming it to its spectral representation [150, 151]. Although this is the most accurate version, it requires the most computational resources due to the diagonalization, which scales as  $N^6$  for  $N$  the number of basis functions.

Otherwise the frequency dependence can be analytically integrated [152], which requires some care due to poles of the denominator on the real axis. Instead the

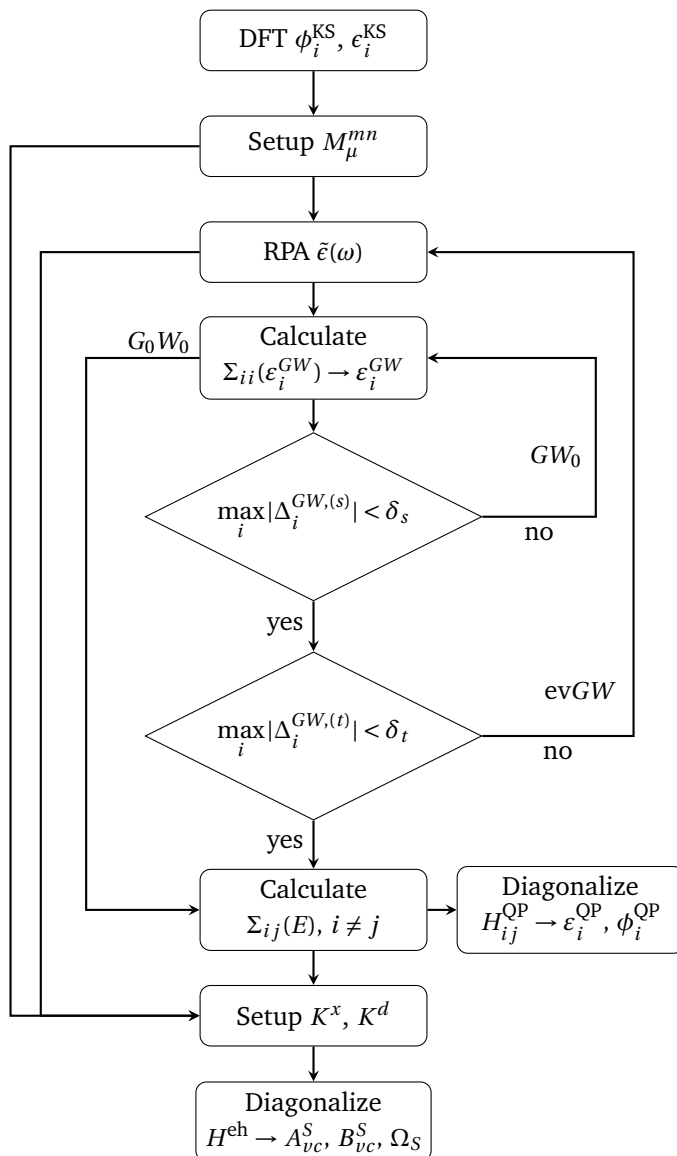


Figure 5.5: GW-BSE workflow as implemented in VOTCA-XTP. The inner self-consistency loop corresponds to the  $GW_0$  algorithm, the outer convergence loop, which requires the recalculation of the RPA is the evGW.

frequency can be analytically continued to the complex domain and integrated along the imaginary axis, where the integrand is smoother [153]. VOTCA-XTP employs a generalized plasmon pole model (PPM) as outlined in Ref. [154] to perform the frequency integration. This model allows for a quick evaluation of the integral in eq. 5.18, but at the same time turns the self-energy into a real operator [155]. The PPM was chosen with the application to complex molecular systems of considerable size, e.g., with relevance to organic electronics such as polymer-fullerene clusters, in mind. The particular model used in this work has been successfully applied to determine quasiparticle and optical excitations in bulk semiconductor and insulator crystals [156, 157], their surfaces [154, 158], defect levels [159], inorganic clusters [155], polymers [81, 160, 161], as well as inorganic and organic molecules [73, 75, 80, 162–164]. Explicit integration of the complex integral using (partially) analytic techniques [150, 152, 153, 165] is planned for future versions.

The steps of the GW-BSE calculation are in more detail depicted in Fig. 5.5. First an initial DFT calculation is performed to access the Kohn-Sham orbitals and energies ( $\phi_i^{\text{KS}}, \epsilon_i^{\text{KS}}$ ). Then the 3-center integrals ( $ij|\mu$ ) are calculated and multiplied with the Kohn-Sham expansion coefficients and the square root of the inverse of the 2-center repulsion matrix to yield  $I_v^{mn}$  via eq. 5.17 and eq. 5.15.

The dielectric function in the RPA approximation (eq. 5.14) is evaluated at two points in frequency space, from which via the plasmon pole model a complete inverse dielectric function is constructed. Then the diagonal elements of the self-energy are evaluated at the energies  $\epsilon_i^{\text{KS}}$  (eq. 5.18). This yields GW corrected Kohn-Sham energies  $\epsilon_i^{\text{GW}}$  according to (eq. 3.106). These can be directly fed back into (eq. 5.18) until convergence is reached, which is denoted  $GW_0$ . After convergence the resulting energies can be used to calculate a new RPA with  $\epsilon_i^{\text{GW}}$  instead of  $\epsilon_i^{\text{KS}}$ . This self-consistency scheme is called *evGW*. Not using any self-consistency scheme is typically denoted  $G_0W_0$ . Afterwards the off-diagonal elements of  $\Sigma$  are calculated and if requested the quasiparticle Hamiltonian can be diagonalized to yield  $\phi_i^{\text{QP}}, \epsilon_i^{\text{QP}}$  energies. Afterwards the BSE-Hamiltonian is set up according to eq. 3.139 and eq. 3.136 and  $W(\omega = 0)$  is used. The resulting BSE-Hamiltonian is then diagonalized yielding the corresponding electron-hole amplitudes ( $A_{vc}^S, B_{vc}^S$ ) and excitation energies  $\Sigma_S$ .

The influence of the self-consistency on the starting point can be seen in Fig. 5.6, where the ground state for benzene was calculated using a local density functional (LDA), a GGA (PBE) and a hybrid functional (PBE0). Whereas the resulting HOMO-LUMO gap in DFT differs strongly from the local functionals LDA/PBE vs

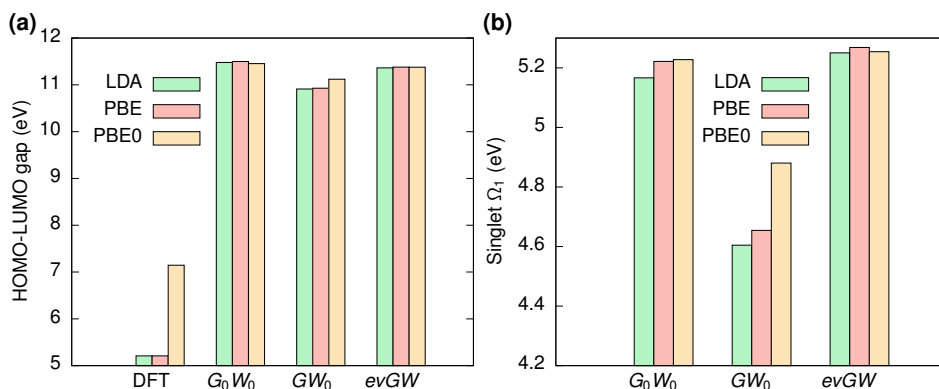


Figure 5.6: Influence of the self-consistency approach on HOMO-LUMO gaps (a) and exciton-excitation energies (b) in benzene using the ubecppol/ECP combination. Three different functionals LDA, PBE(GGA) and PBE0(hybrid) are used.

the non-local hybrid functional, the *GW* method opens up the HOMO-LUMO gap and show more similar results for all functionals, which is a result of the inclusion of exchange effects in the self energy operator. In comparison to the  $G_0W_0$  approach and evGW approach, the  $GW_0$  approach still shows the largest deviations in HOMO-LUMO gap and singlet excitation energies. This is a result of the unequal treatment of the *G* and *W*. The partial self-consistency in evGW results reduces the influence of the starting functional even further, but comes at a much higher computational cost. As a final note, both graphs together also explain why density functional theory is often wrongly used to explain excitation spectra. The DFT HOMO-LUMO gap is for PBE and LDA roughly 5.2 eV, which is very close to the excitation energy  $\Omega_1$  of the first singlet in the evGW and  $G_0W_0$  results. This agreement is completely coincidental, as KS-DFT does not capture any of the excited state effects.

As discussed before, *GW*-BSE is a non-standard quantum-chemical approach (compared to TDDFT, or wave function based theories such as Configuration Interaction or Coupled Cluster) to determine electronically excited states of molecules. In recent years, a few groups have started systematically evaluating the suitability of this beyond-DFT methodology with respect to (i) different technical implementations (e.g., numerical orbitals vs GTO, use of RI etc.) [76, 80, 166–170] and (ii) different application scenarios [73, 75, 77, 80, 82, 155, 171, 172].



With this work's application target of studying the static and dynamic properties of electronically excited states *in complex molecular environments relevant* in mind, it is important to demonstrate the viability of the methodology itself but also the implementation as described in the previous chapters. In particular, several essential questions need to be addressed:

1. How accurate is the combination of methodology/implementation in application to single molecules?
2. What is the convergence behavior of the methodology/implementation with respect to computational parameters, such as basis sets dependence, size of the active space (i.e., the size of the single-particle product function space used to expand the electron-hole wave functions), or the level used in the Bethe-Salpeter Equation (i.e., full BSE compared to TDA)?
3. What are the computational costs of the computations? What are the resulting limitations and can computational parameters be *optimized* to make application to relevant molecular systems (composition, sizes) tractable?
4. Can one efficiently use GW-BSE in hybrid quantum-classical setups?

In order to answer questions 1-3, the following section deals with the application of the VOTCA-XTP's GW-BSE implementation to a small molecule test set, also known as the *Thiel set*, used as a standard benchmark for method development in excited state electronic structure theory. After that, we consider as a prototypical complex molecular system double-stranded DNA in sec. 5.4 with specific focus on the effects of local-electric fields and environment polarization on charge transfer excitations.

### 5.3.1 Single molecule data: Thiel set

The Thiel set for the benchmarking of our implementation of the GW-BSE formalism contains 28 small molecules of different types shown in app. A: unsaturated aliphatic hydrocarbons, aldehydes, ketones, amides, aromatic hydrocarbons and heterocycles, as well as four nucleobases. While the size of these molecules is much smaller than that of the typical molecules relevant for organic electronics (the largest ones, naphthalene and octatetraene, contain 18 atoms), the set offers reference data from both experiment and high-order wave function techniques for a representative variety of types of excitations. The benchmark set covers  $\pi \rightarrow \pi^*$

(e.g., ethene),  $n \rightarrow \pi^*$  (e.g., pyrazine), and  $\sigma \rightarrow \pi^*$  (e.g., cyclopropene) excitations. These different excitations also cover a wide range of energies from 2 eV to 8 eV.

For the benchmarking the following procedure has been used. First, the ground state geometries of the molecules have been optimized using DFT at three different levels of theory, including all-electron (AE) calculations with the aug-cc-pVTZ and cc-pVTZ basis sets [72], respectively, as well as calculations making use of effective core potentials and an associated basis set, [148] that has been augmented by a single shell of polarization functions taken from the 6-311G\*\* basis [173]. Due to the significantly reduced computational requirements, the latter case can be considered a *minimal setup* and is further referred to as ubecppol. All DFT calculations have been performed using the hybrid PBE0 functional [62], and optimized auxiliary basis sets [140].

Optimized auxiliary basis sets for (aug-)cc-pVTZ [140, 174] taken from the Basis Set Exchange [175] have been used in the resolution-of-identity steps. For the ubecppol basis, we constructed an auxiliary basis using the technique employed in the SAPT code [176–178]. For all cases, we have compared the obtained results to those from calculations using large auxiliary bases created with the AutoAux functionality [179] available in Orca [143], and found agreement within a few 10 meV.

For the optimized geometries, excited state energies are determined within the *GW*-BSE formalism making use of the full BSE (eq. 3.128) on top of *evGW* self-consistent quasi-particle energies using the procedure outlined in sec. 3.3, in which all *GW* energies are converged to  $10^{-5}$  Hartree. Transitions between all occupied and empty states, with their total number determined by the respective basis set sizes as in Tab. B.1, are taken into account in the calculation of the dielectric screening in the RPA. This choice is conservatively large, since including about 10 times as many empty as occupied states has typically shown to be sufficient to yield converged low energy excitations, as shown in Fig. 5.7. Similarly, quasi-particle corrections are determined for all available states, which are then used to construct the basis of product states for the expansion of the electron-hole wave functions in the BSE. For example in the smallest system, ethene, our calculations with the aug-cc-pVTZ basis include 8 occupied and 130 empty states, leading to 1040 transitions in the RPA and for the BSE product basis. For naphthalene, inclusion of 34 occupied and 610 empty states amount to 20740 RPA transitions/BSE product functions.

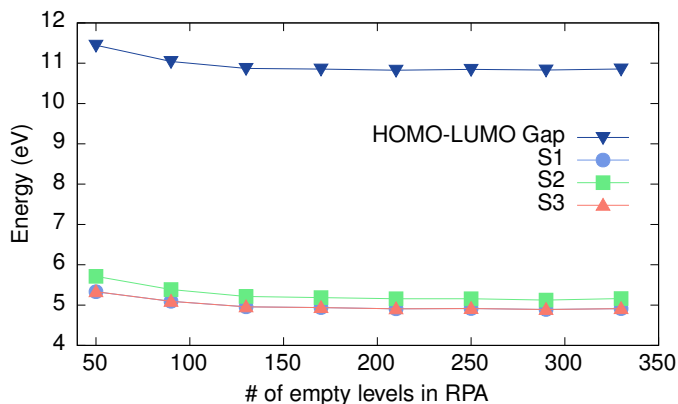


Figure 5.7: Convergence of the quasi-particle HOMO-LUMO gap and the three lowest-energy singlet excitations of pyridine with respect to the number of empty states in the evaluation of the microscopic dielectric function in the RPA. Quasiparticle corrections are determined for the lowest 42 (21 occupied, 21 empty) states, and 441 product basis functions are used for the BSE.

### 5.3.2 Comparison to experiment

From the resulting set of excitations for the respective molecules, the excitations with optical activity are identified and their energies are compared to the ones obtained from experiment, as summarized in Fig. 5.8. The four different categories of small molecules are represented by differently colored symbols (see caption for details). For the aug-cc-pVTZ basis set that contains additional diffuse functions the results depicted in Fig. 5.8(a) indicate a very good agreement with the reference data with a RMSD of 0.24 eV. The largest deviation is found for cyclopropene, whose excitation is reported to be at 7.19 eV in experiment compared to 6.38 eV in our GW-BSE calculation. Such a deviation is, however, not unique to our implementation. In Ref. [167], a GW-BSE excitation energy of 6.14 eV was reported, which is very close to the value of 6.18 eV obtained by TDDFT with the PBE0 functional. Even the *Theoretical Best Estimate* based on high-order wave function methods of 6.65 eV shows a similar deviation. We note that the difference of some of our GW-BSE results from those in Ref. [167] is likely an effect of the different treatment of the frequency dependence of the dielectric functions (PPM vs. complex contour integration). Overall we find a mean absolute error of 0.14 eV between our PPM approach and the literature results. For the moderately-sized

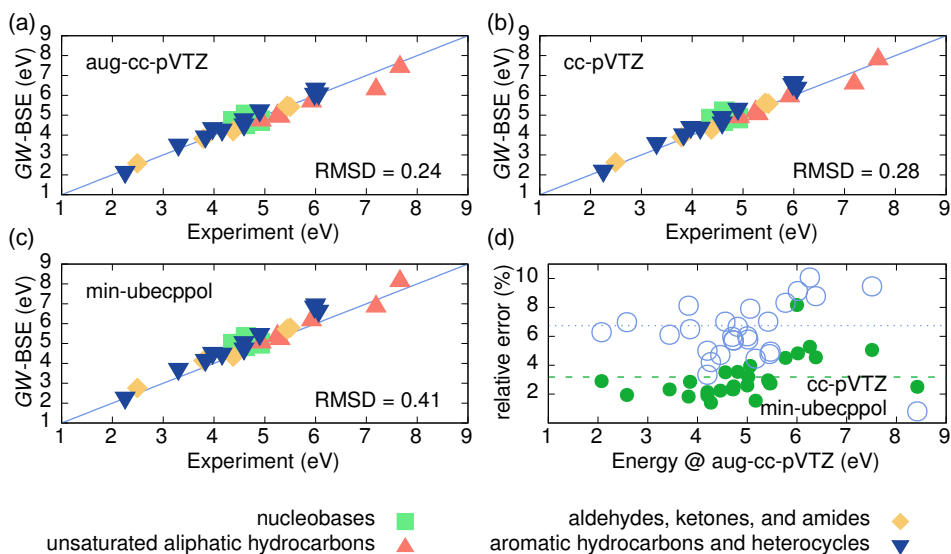


Figure 5.8: Comparison of calculated lowest singlet excitation energies with experimental data (in eV) for the 28 small molecules in Thiel's set. Ground state DFT calculations including geometry optimizations have been performed on all-electron (AE) level with the (a) aug-cc-pVTZ and (b) cc-pVTZ basis sets, as well as (c) employing effective core potentials and the ubecppol basis set, respectively. The same fitting auxiliary basis functions have been used for both DFT and *GW*-BSE stages. Data for nucleobases is given by green squares, for unsaturated aliphatic hydrocarbons by red up-triangles, formaldehydes, ketones, and amides by other diamonds, and for aromatic hydrocarbons by blue down-triangles. Panel (d) shows the relative error between the smaller AE/cc-pVTZ (green filled circles) and ECP/ubecppol (open blue circles) calculations as compared to the more complete AE/aug-cc-pVTZ as a function of energy. The green dashed (blue dotted) lines indicate the mean error of  $(3.2 \pm 1.0)\%$  and  $(6.7 \pm 2.0)\%$ , respectively.

nucleobases, for which one would expect the PPM to be a better approximation, this error is as small as 0.03 eV. Such an error is negligible compared to the effects of the molecular environment on the excitation energies, which can be on the order of 1 eV (see sec. 5.4). Smaller deviations could also be attributed to more subtle variations in the computational protocol, such as in the stabilization of near linear dependencies in the basis sets and auxiliary basis sets. In general, a more direct comparison between the various theoretical approaches is made somewhat difficult by the fact that molecular geometries have been optimized at different levels of theory and therefore can distort the picture slightly. Using diffuse basis functions in quantum-chemical calculations is typically associated with significant computational costs due to increased number of functions not only in the basis set itself but also the auxiliary basis sets for RI. Concomitantly, one occasionally encounters problems with linear dependencies in the basis sets that require careful treatment. In this situation, it is desirable to avoid such diffuse functions, especially in applications to larger molecules. In Fig. 5.8(b), the GW-BSE results obtained with the cc-pVTZ basis set show overall an excellent agreement with the experimental reference. On average, the RMSD of 0.28 eV is as expected larger than that for the aug-cc-pVTZ basis. This is illustrated in Fig. 5.8(d), in which the relative deviation of the excitation energies (in %, indicated by green filled circles) obtained with cc-pVTZ from those obtained with the more complete aug-cc-pVTZ basis sets are shown depending on the absolute aug-cc-pVTZ energies. It can clearly be seen that on the energy range covered by the test set, the relative deviation varies between 1% and 9%, yielding a mean relative error of 3.2% with standard deviation of 1.0%. More importantly, however, the average run time is reduced to  $(25.2 \pm 6.5)\%$ .

To scrutinize whether our results are affected by the choice of functional in the underlying ground state DFT calculation, we have computed the respective excitation energies also with the gradient-corrected PBE [59] functional instead of its hybrid variant PBE0. The full data for both  $G_0W_0$  and evGW variants are given in Tab. 5.2. Inclusion of quasi-particle energy self-consistency reduces the mean-absolute error between the PBE0 and PBE functionals from  $0.087 \pm 0.053$  eV to  $0.052 \pm 0.028$  eV. The largest difference on  $G_0W_0$  level is 0.18 eV for formaldehyde, compared to only 0.02 eV with evGW. Overall, we note only a very weak starting point dependence, in particular for evGW.

While neglecting diffuse functions already massively reduces computational costs with only minimal loss of overall accuracy and reliability, all-electron calculations explicitly include the typically inert core electrons, such as the two electrons in the

Table 5.2: Comparison between singlet excitation energies (in eV) for self-consistent  $evGW$  and one-shot  $G_0W_0$  using the PBE0 and PBE functionals, respectively, with aug-cc-pVTZ basis set.  $\Delta(G_0W_0)$  and  $\Delta(evGW)$  are the differences between PBE0 and PBE based energies for the two approaches.

	PBE0		PBE		$\Delta(G_0W_0)$	$\Delta(evGW)$	
	$evGW$	$G_0W_0$	$evGW$	$G_0W_0$			
<b>NUCLEOBASES</b>							
cytosine	4.56	4.62	4.51	4.64	-0.02	+0.05	
thymine	4.73	4.73	4.72	4.75	-0.02	+0.01	
uracil	4.70	4.70	4.69	4.71	-0.01	+0.01	
adenine	5.02	5.03	4.95	5.00	+0.03	+0.07	
<b>UNSATURATED ALIPHATIC HYDROCARBONS</b>							
ethene	7.51	7.69	7.48	7.83	-0.14	+0.03	
butadiene	5.77	5.96	5.72	6.06	-0.10	+0.05	
hexatriene	4.81	5.01	4.76	5.11	-0.10	+0.05	
cyclopropene	6.38	6.56	6.34	6.66	-0.10	+0.04	
cyclopentadiene	5.00	5.22	4.93	5.34	-0.12	+0.07	
norbornadiene	5.06	5.25	4.98	5.32	-0.07	+0.08	
<b>ALDEHYDES, KETONES, and AMIDES</b>							
formaldehyde	3.82	3.94	3.84	4.12	-0.18	-0.02	
acetone	4.20	4.27	4.19	4.44	-0.17	+0.01	
benzoquinone	2.58	2.71	2.48	2.76	-0.05	+0.10	
formamide	5.42	5.48	5.45	5.63	-0.15	-0.03	
acetamide	5.45	5.41	5.45	5.57	-0.16	+0.00	
propanamide	5.47	5.43	5.47	5.58	-0.15	+0.00	
<b>AROMATIC HYDROCARBONS and HETEROCYCLES</b>							
benzene	5.17	5.35	5.11	5.43	-0.08	+0.06	
naphthalene	4.27	4.45	4.19	4.51	-0.06	+0.08	
furan	6.02	6.24	5.94	6.39	-0.15	+0.08	
pyrrole	6.00	6.14	5.95	6.17	-0.03	+0.05	
imidazole	6.26	6.40	6.19	6.44	-0.04	+0.07	
pyridine	4.72	4.79	4.65	4.83	-0.04	+0.07	
pyrazine	3.85	3.97	3.77	4.06	-0.09	+0.08	
pyrimidine	4.20	4.25	4.13	4.31	-0.06	+0.07	
pyridazine	3.44	3.57	3.35	3.63	-0.06	+0.09	
triazine	4.46	4.46	4.41	4.48	-0.02	+0.05	
tetrazine	2.07	2.29	2.00	2.45	-0.16	+0.07	
					MAE	0.087	0.052
					$\sigma$ (MAE)	0.053	0.028

1s shell of carbon. It is therefore possible to simply exclude them from the active space of product functions. However, the presence of such explicit core electrons requires the use of normal and auxiliary basis sets with strongly localized functions in the DFT ground state calculation underlying the *GW*-BSE formalism.

To avoid the expensive calculation of these core states altogether, effective core potentials can be used in combination with the *ubecppol* basis set. In Fig. 5.8(c), the obtained excitation energies are shown compared to the experimental reference. The overall RMSD of 0.42 eV, while slightly larger than that recorded for *aug-cc-pVTZ* and *cc-pVTZ*, respectively, is still very good. One can observe a general tendency for the ECP/*ubecppol* combination to overestimate the measured data. This is also apparent considering the relative deviations from *aug-cc-pVTZ* shown as open circles in Fig. 5.8(d). Interestingly, the relative deviation varies between 1% and 10%, only slightly larger than for *cc-pVTZ*. However the mean error is larger and amounts to  $(6.7 \pm 2.0)\%$ , which can be considered acceptable, in particular when one takes into account that the computational cost is reduced to as much as  $(6.3 \pm 3.1)\%$  as compared to *aug-cc-pVTZ*. These numbers highlight that the use of the minimal ECP/*ubecppol* variant offers a great compromise between accuracy and computational cost, which make it particularly attractive for the application to large, relevant molecular systems.

For completeness, a comparison of the electronic excitation energies obtained with *GW*-BSE to the Theoretical Best Estimate (TBE), Fig. 5.9 clearly reveals that all three basis set variants considered in this work exhibit a very satisfying agreement with the high-order reference. A table with all relevant values is also available in table Tab. B.2 in the appendix.

### 5.3.3 Optimal strategies for large-scale applications

Molecules typically used in organic electronic devices, such as fullerenes or oligo-*hiophenes*, are significantly larger than the molecules included in the Thiel set. While it could be convincingly demonstrated in the previous discussion that *GW*-BSE is a powerful and accurate approach for the investigation of electronically excited states in molecular systems, one of the biggest challenges one faces lies in guaranteeing the practicality of application to larger systems.

To this end, the identification of a minimal reliable basis set in the form of the ECP/*ubecppol* combination is an important step. Besides this, there are more

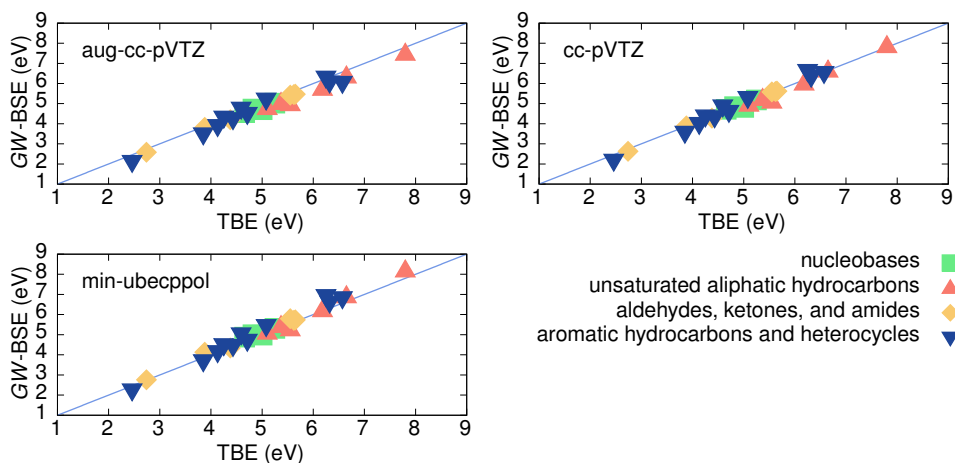


Figure 5.9: Comparison of calculated lowest singlet excitation energies with the Theoretical Best Estimate (TBE, in eV) for the 28 small molecules in Thiel's set. Symbols and labels identical to the ones used in Fig. 5.8.

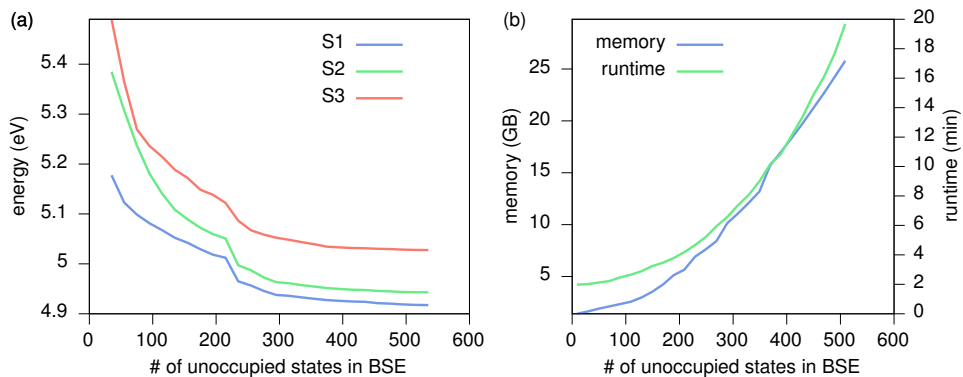


Figure 5.10: (a) Convergence of three lowest singlet excitation energies in adenine as a function of the number of unoccupied levels taken into account in the BSE on top of an AE/aug-cc-pVTZ DFT calculation. At this level, about 350 unoccupied levels are required to obtain results that are converged to within 0.01 eV. (b) Memory consumption and run time using four OpenMP threads on a i7-4770 CPU @3.40 GHz.



calculational parameters that can be varied. To illustrate this point, we show in Fig. 5.10(a) the convergence of the three lowest excitation energies in adenine with respect to the number of unoccupied states taken into account when constructing the product functions for the expansion of the electron-hole wave functions, cf. Eq. eq. 3.129. The calculations have been performed at all-electron level with the aug-cc-pVTZ basis set. Since the dimension (size) of the matrix form of the BSE is  $2N_{\text{occ}} \cdot N_{\text{unocc}}$  ( $4(N_{\text{occ}} \cdot N_{\text{unocc}})^2$ ), the choice of  $N_{\text{unocc}}$  has an extreme impact on the required numerical effort. In the example of adenine at AE/aug-cc-pVTZ level,  $N_{\text{occ}} = 35$  is fixed but  $N_{\text{unocc}}$  can range up to 540 (defined by the size of the DFT basis set), in which case the full BSE matrix is  $37800 \times 37800$ .

From the convergence behavior in Fig. 5.10(a) it becomes evident that taking all unoccupied levels into account is not necessary to find converged solutions to the low-lying excitations. Instead, for this particular system, the choice of  $N_{\text{unocc}} = 350$  is sufficient. The graphs in Fig. 5.10(b) show that with this choice, significant reductions in runtime from about 20 min to about 6 min can be achieved, as well as a remarkable reduction in memory consumption. It should be noted at this point, however, that the extreme memory consumption of up to 25 GB as seen here is a direct consequence of building the full BSE Hamiltonian explicitly. Eigenproblem solvers, which do not require the full matrix but only a the product of the matrix with a given test vector, can reduce this bottleneck [180].

It is also worth emphasizing that the combination of the ECP/ubecppol variant with optimized  $N_{\text{occ}}$  brings down execution times of the GW-BSE step to just about one minute using four OpenMP threads on a i7-4770 CPU @3.40 GHz.

Additional savings can in principle be achieved by resorting to the Tamm-Dancoff Approximation (TDA), in which as explained in sec. 3.3.2 the resonant-antiresonant coupling terms  $K$  (eq. 3.130) are neglected in the Bethe Salpeter Equation. Thereby the dimension of the matrix system is reduced by a factor of two which directly translates into significant numerical gains. It is known from previous studies [87] that resonant-antiresonant coupling influences the energies of singlet  $\pi \rightarrow \pi^*$  excitations. This omission of the corresponding coupling terms in the BSE can reduce the associated energies by several 0.1 eV, depending on the size of the  $\pi$ -conjugated system. The smaller the  $\pi$ -system, the stronger the effect. For the relatively small molecules in the Thiel test set, it is therefore expected that the TDA deviations will be noticeable.

In Fig. 5.11, the excitation energies obtained with the three basis sets discussed above as resulting from full BSE calculations and TDA are compared, respectively.

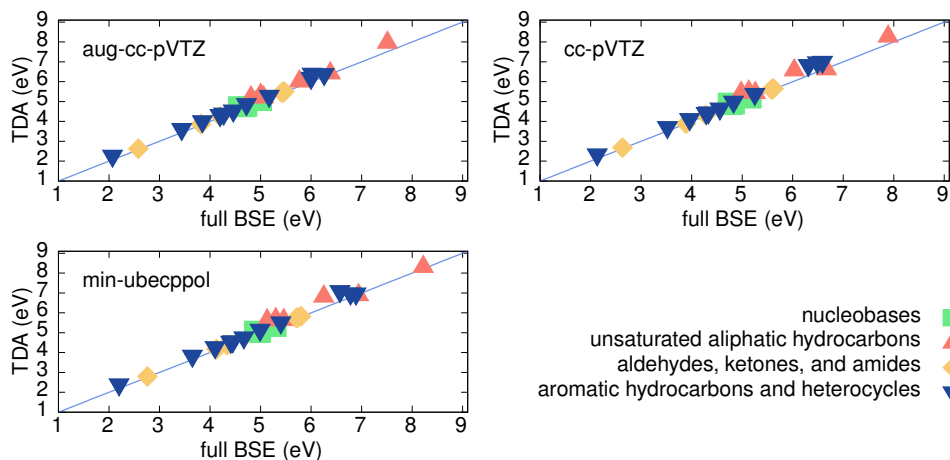


Figure 5.11: Comparison of calculated lowest singlet excitation energies (in eV) within the Tamm-Dancoff Approximation (TDA) versus the full BSE formalism for the 28 small molecules in Thiel's set. Symbols and labels identical to the ones used in Fig. 5.8.

As expected, the TDA energies are typically larger than those from the full BSE. Also the size dependence is clearly visible. The strongest effects can be seen for ethene ( $C_2H_4$ ), the molecule with the smallest  $\pi$  system. For the aug-cc-pVTZ basis, TDA yields an excitation energy of 8.04 eV as compared to 7.51 eV obtained by the full BSE formalism. Resonant-antiresonant coupling accounts for as much as 0.53 eV. In contrast, for a larger molecule such as adenine, the effect is reduced to just 0.02 eV. These results illustrate that the TDA can be a useful approximation depending on the specific system of interest and should therefore be carefully evaluated.

In summary, after the careful analysis of the performance of VOTCA-XTP's *GW*-BSE implementation with respect to accuracy and computational cost, we can conclude that

1. The combination of methodology/implementation in application to small single molecules from a benchmark test set shows a high accuracy, comparable to that of state of the art high order wave function methods.
2. The *GW*-BSE results show a non-negligible dependence on the choice of the basis set, the size of the product function space, and the variant of the Bethe Salpeter equation employed. The exact size of the effects depends on the

particular system and need to be checked diligently, as in any other computational approach. Analysis and understanding of the different contributing factors allows one to extrapolate rough guidelines for the application to larger systems.

3. It is found that the inclusion of diffuse functions in augmented basis sets cause a considerable computational cost compared to not-augmented variants. At the same time, the effect on calculated excitation energies is smaller so that in most cases, diffuse functions can be neglected. For (very) large systems, the use of effective core potentials and minimal basis sets can be a viable strategy showing a good compromise between accuracy and computational cost, as can be the use of the TDA.

With these promising conclusions regarding the application to single small molecule systems at hand, the following section will focus on the integration of *GW*-BSE in coupled quantum-classical QM/MM setups for complex molecular environments.

## 5.4 Quantum-classical QM/MM simulations

Electronic excitations in complex molecular systems are typically not solely defined by the properties of isolated substructures, e.g., single monomers. Instead, the nature of excited states is in general a result of an intricate interplay between the intrinsic quantum-mechanical properties of the constituent units and the local and global morphology of the large-scale molecular system. Such effects can include, for instance, static and/or dynamic conformational properties, such as backbone torsions in conjugated polymers, or the global ordering in bulk or thin-film structures on the order of nm.

In order to accurately predict the static and dynamic properties of electronic excitations in these cases, it is paramount to take the available information of the full, in extreme cases mesoscopic system into account. It is evident that a full quantum-mechanical treatment of such a complex system and its typical length (and time) scales is practically impossible. This problem is further exacerbated for high-level methods such as *GW*-BSE, even when using the optimized strategies introduced in the previous section.

In such situations, the use of hybrid methods, which combine multiple different techniques adequate for the different scales involved, is indispensable. Such multi

scale and multi method setups that marry a quantum-mechanical treatment of a part of the full system with a classical model for its environment are known as QM/MM methods. Here, we will first describe the implementation of such a QM/MM approach for the evaluation of electronic excitation energies in VOTCA-XTP. Its unique features are the use of *GW*-BSE as the quantum technique, and its coupling to a multilayer atomistic environment that can include polarization effects. After that, the capabilities of this setup will be demonstrated in application to optical absorption and charge transfer excitations in a prototypical DNA system.

### 5.4.1 Workflow and implementation

The assumption that underlies the QM/MM setup used in this work is that it must be possible to adequately partition the full system into two distinct regions which are only weakly coupled as described in Chapter 4. Often, the assignment of quantum and classical (MM) regions is determined by the nature of the full supramolecular assembly and the type of excitation of interest. For instance, if one aims to study the optically active Frenkel excitons in small-molecule organic semiconductors, the QM part typically contains a single unit while the remaining molecules are part of the classical region. In macromolecules, such as conjugated polymers or biomolecules, the situation is more complex as one needs a priori information – or at least an informed guess – about the regions in which electronic states are localized and partition the macrosystem accordingly. This step then typically involves the truncation of a covalent bond (typically single bonds), saturation of the dangling bonds by hydrogen or methyl, and careful adjustment of the previously connecting atoms in the now classical region to avoid double-counting, prevent too close contacts, and maintain charge-conservation. As an alternative, it has been suggested in the literature to construct special pseudo-potentials (see sec. 3.2.3) with valence configurations for bridging atoms that do not require saturation [181].

Fig. 5.12 illustrates this idea for the case of a DNA double strand solvated in water. A single nucleobase is chosen as the QM region, while the rest of the system that is within a certain distance to this region is assigned to the MM region. To be more precise, we differentiate between two distinct MM regions, here referred to MM0 and MM1, according to the way these interact with each other and the QM region.

In case of weak coupling, it is assumed that the classical region affects the quantum one (and vice versa) via electrostatic interactions only. *Static local-fields* are associ-

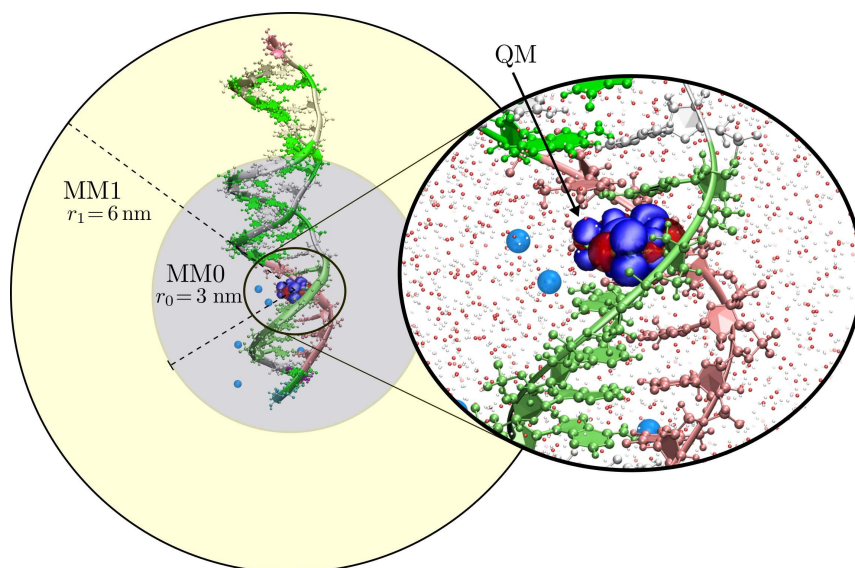


Figure 5.12: Schematic representation of the DNA solvated in water and separation into MM0 and MM1 for an adenine nucleobase. The QM region is magnified in the small inset.

ated with the distribution of static partial point charges (or, more generally, static point multipoles) in the MM region. These multipoles remain unchanged during the QM/MM calculation and can either be taken from classical force fields used in the molecular dynamics simulations or fitted to ab-initio vacuum calculations.

In addition to these static local-field effects, the electron density of the QM region redistributes upon excitation and accordingly its electrostatic potential affecting the MM region is modified. Such modifications are typically strongest for charged excitations, or excitations involving large changes of molecular dipole moments. Depending on the specific case these modifications of the electrostatic potential cause a significant response of the atoms in the vicinity of the QM region. Then these *polarization effects* are not negligible. We model them in our QM/MM approach with the distributed polarizable dipole model introduced in Chapter 4. This polarization model is used in the MM0 region indicated in Fig. 5.12, while the MM1 region has no polarization response and uses only static multipole moments.

Figure 5.13 shows the practical workflow of our QM/MM setup. After partitioning

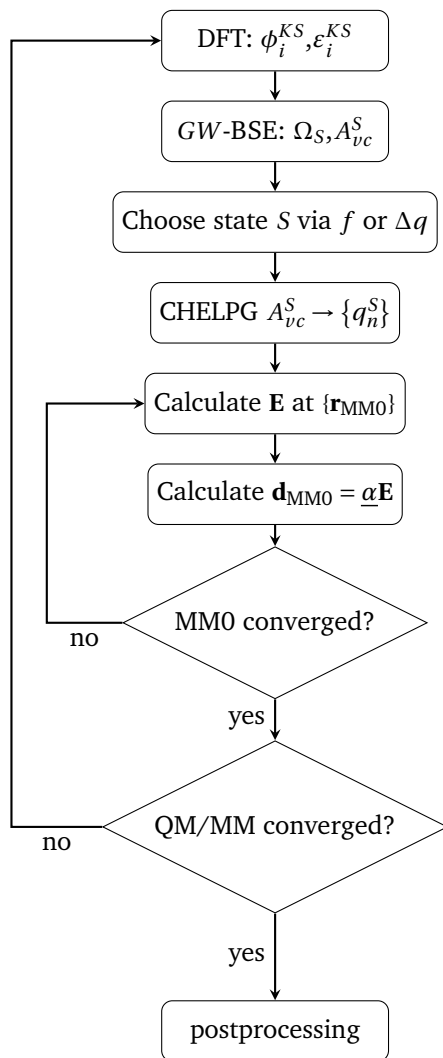


Figure 5.13: QM/MM workflow as implemented in the VOTCA-XTP package.

the system as described above, first a QM calculation on DFT and, depending on the state of interest, *GW*-BSE level is performed. The QM electron density is determined and then reduced to a set of classical atomic point charges  $\{q_n^S\}$  via the CHELPG algorithm (see sec. 4.2.3).

In a first step using the  $\{q_n^S\}$  of the QM region and all classical charges in the MM region the electric field  $\mathbf{E}$  inside the MM region is calculated. As a response to these fields, polarization induced dipoles  $\mathbf{d}_{\text{MM1}}$  are formed in the MM0 region. Those induced dipoles cause, in turn, a change in the electric field  $\mathbf{E}$ . As described in Chapter 4, the sequence of steps of this classical polarization model within the MM0 region needs to be iterated until the electrostatic energy and the  $\mathbf{d}_{\text{MM0}}$  converge. We use the implementation of the Thole model from the VOTCA-CTP library [92]. After this classical polarization model in MM0 is converged to a self-consistent solution, the total electric field acting on the QM region, determined from the static moments in both MM0 and MM1 and the induced dipoles in MM0, is updated. Within this new external potential the next DFT and *GW*-BSE calculation are performed. This sequence is also iterated until self-consistency, until the charges and energies in both the QM and MM region change less than a specified amount.

Note that as was discussed in Chapter 4, the inclusion of explicit polarization effects makes the QM/MM Hamiltonian depend on the electronic state of interest. Excitation energies hence must be determined as total energy differences as in eq. 4.42.

The explicit state dependence of the coupled QM/MM system introduces another difficulty, in particular when excited states via *GW*-BSE are calculated. The solution of the BSE yields a spectrum of excitations, which are ordered according to their energy. These states can be energetically separated or very close, depending on the specific system. As a consequence, the index of a specific excitation of interest can vary for different external potentials at the individual steps of the QM/MM self-consistency procedure. It is therefore important to be able to identify the electronically excited state of interest during the calculation. In practice, a filtering of the total spectrum is employed which selects states according to some predefined property. Currently, the selectable properties are the oscillator strength  $f$  for optically active excitations and the amount of charge transferred ( $\Delta q$ ) from one fragment to another for charge transfer states. For such filtering criteria to be applicable, it is implicitly assumed that the overall characteristics of the excited states do not change significantly during the QM/MM calculation.

If only static interactions are taken into account, no difficulties arise, as the QM/MM Hamiltonian is no longer state-dependent.

## 5.4.2 Charge transfer excitations in aqueous DNA

To demonstrate the application of the above-mentioned QM/MM techniques, we will in the following focus on a water-solvated DNA double-strand, as a prototypical system. Since the basic DNA nucleobases are part of the Thiel set used in section sec. 5.3.1, this constitutes an ideal scenario which connects the single molecule study to an investigation of a more complex molecular environment.

Besides these practical considerations, there is also a relevant scientific motivation for this choice of system. Photophysical processes triggered by the absorption of ultraviolet solar radiation can cause damage and subsequent mutations in DNA [182]. Due to the complexity of such biological systems, gaining an understanding of the processes involving excited states is extremely challenging. Bimolecular charge transfer (CT) excitations between base pairs are considered to play an important role in the excited-state dynamics of DNA, which as part of more complicated processes lead to structural or chemical decay and, eventually, gene mutations [183, 184]. One of the proposed processes is the rapid decay of an initially photoexcited  $\pi \rightarrow \pi^*$  state to a longer-lived CT state, which can induce structural modifications or chemical oxidation/reduction reactions [185, 186]. Such an initial decay process is very close in concept to the conversion of localized Frenkel excitons to CT excitons at the donor-acceptor interface of an organic solar cell, as discussed in Chapter 2, though the structural/morphological details are fundamentally different.

As a first step to gain further insight into the exact conditions under which dynamical excited state processes of this kind can occur in DNA, a detailed understanding of the CT state energies is vital. While it is suggested from experiment on water-solvated single-strands of 20 adenine bases ( $A_{20}$ ) that CT states cause a faint UV absorption at energies below the energy of the UV active  $\pi \rightarrow \pi^*$  transition at approximately 5 eV [187], a high-level second-order approximate coupled-cluster method yields CT excitations far above that for an isolated  $A_2$  dimer in the gas phase [188, 189]. Due to the long-range electron-hole interaction, CT energies are typically very sensitive of the arrangement of the constituent monomers of the base pair. Optimized gas-phase structures are likely to exhibit different stacking distances and even motifs compared to a real single-strand, and lack the effect of the aqueous environment not only on the structure but also on the electrostatic environment entirely.

Based on the experimental evidence, one should expect a redshift on the order of



1 eV for CT energies in aqueous DNA as compared to a vacuum situation. Inclusion of a polarizable environment using a Polarizable Continuum Model (PCM) on top of TDDFT [188, 189] fail to reproduce this observation, with the redshift being reported to be as small as 0.1 eV. The use of model structures and notorious difficulties of TDDFT to accurately describe CT excitons are likely origins of this discrepancy. To reliably distinguish the different effects of the aqueous environment and to quantify how they affect the character of CT excitations and how they contribute to the observed redshift, it is important to consider a realistic morphology of aqueous DNA and treat it with an accurate set of techniques. The *GW*-BSE formalism has been reported to yield very accurate predictions of CT excitation energies in prototypical small-molecule dimers. Subsequently, Yin et al. [164] studied small complexes of adenine dimers and water ( $A_2-(H_2O)_m$ ). Geometries of the complex were obtained from Classical Molecular Dynamics, while *GW*-BSE was used to evaluate the excitation energies. It was found that CT energies are strongly affected by the dipole electric fields in the first hydration shell around the  $A_2$ , giving rise to an overall energetic shift to below that of the  $\pi \rightarrow \pi^*$  transition in single adenine, much more in line with the experimental observation.

Inspired by these results, we will use *GW*-BSE within the QM/MM framework discussed above on aqueous DNA. We go beyond the model used by Yin et al and instead of a single hydrated adenine dimer, we consider a full double-strand of DNA solvated in explicit water. This will allow us to study, among other things, the effects of a realistic stacking, the differences between intra- and inter-strand charge transfer excitations, and the explicit effect of the DNA backbone. Given the sensitivity of the CT excitations to water hydration, inclusion of these structural parameters can have a substantial influence since the electrostatic environment will be vastly different from the idealized situation of a hydrated dimer. We will also be able to study dimers formed by different types of nucleobases on an equal footing. Considering different embedding variants (vacuum (or gas phase), QM/MM with static interactions only, and QM/MM with polarizable interactions), allows us to disentangle the effects of the geometric structure of the dimer, of local electric fields, of the structure of the environment, and of electronic polarization.

To obtain the atomistic structural information, an exemplary DNA double strand with 23 base pairs in the sequence shown in Fig. 5.14 was prepared. This double strand was solvated by 42216 water molecules and 44 sodium counter ions. For this system, in the following referred to as aqDNA, classical molecular dynamics simulations were performed using the AMBER99 forcefield [190] for DNA and

GGGGCGGCGGGCGTTTTTGG  
 CCGCCGCGCGCCGAAAAACC

Figure 5.14: DNA double strand sequence used in QM/MM simulation. G:guanine, C:cytosine, A:adenine and T:thymine. Compare with Fig. 5.12. The respective chemical structures are given in app. A.

sodium, and the SPC/E water model [191]. Geometric mixing rules [ $\sigma_{ij} = \sqrt{\sigma_{ii}\sigma_{jj}}$  and  $\epsilon_{ij} = \sqrt{\epsilon_{ii}\epsilon_{jj}}$ ] for Lennard-Jones (LJ) diameters ( $\sigma$ ) and LJ energies ( $\epsilon$ ) were used for atoms of different species [192–194]. Non-bonded interactions between atom pairs within a molecule separated by one or two bonds were excluded. Interaction was reduced by a factor of 1/2 for atoms separated by three bonds and more. Simulations were run using GROMACS version 5 [195]. A 0.9 nm cutoff was employed for the real space part of electrostatics and Lennard-Jones interactions. The long-range electrostatics was calculated using particle-mesh Ewald (PME) [196, 197] with the reciprocal-space interactions evaluated on a 0.16 grid with cubic interpolation of order 4. First, the system was energy minimized using the steepest descents algorithm. Then, 10 ns simulations in constant particle number, volume and temperature (NVT) ensemble at 300 K were performed using the stochastic velocity rescaling thermostat [96] with time constant 0.1 ps. The velocity-Verlet algorithm [93] was employed to integrate the equations of motions with 2 fs time step. The simulation box size was  $(12 \times 12 \times 8) \text{ nm}^3$ . Simulations were then continued in constant particle number, pressure and temperature (NpT) ensemble at 300 K and 1 bar controlled by Parrinello-Rahman [100] barostat with a coupling time constant of 2.0 ps. Molecular visualizations were rendered using Visual Molecular Dynamics (VMD) software [198].

For the parametrization of the polarizable model used in the coupled QM/MM calculations, atomic partial charges and molecular polarizability tensors were determined for the nucleobases and for water based on DFT calculations using the PBE0 functional and the cc-pVTZ basis set. Classical atomic polarizabilities were then optimized to reproduce the molecular polarizable volume of the DFT reference calculation. For the DNA backbone, partial charges were taken from the force field used in the MD simulation and default atomic polarizabilities from the AMOEBA forcefield [119]. Either a single nucleobase or a pair of nucleobases is chosen as QM region in the QM/MM setup. As this region is covalently bonded to the MM region, the bond to the frontier atom was truncated saturated with a hydrogen atom as described above. All residues inside a 4.3 nm closest contact to the molecules

defining the QM region were assigned to the MM region. When polarized QM/MM calculations were performed, polarization effects were included for all residues within a closest contact distance of 2.0 nm from the QM region.

From the simulated DNA structure, neighboring nucleobases with separation less than 1 nm were defined as pairs (yielding 59 pairs in total) between which CT excitations are calculated. These include both intra- and interstrand excitations. Due to the presence of the four nucleobases adenine (A), guanine (G), cytosine (C) and thymine (T) (see chemical structures in app. A) in the present system of aqDNA, 10 different types of dimers can be formed.

First, we compare the results obtained using QM calculation of gas-phase dimers with those obtained using QM/MM with only static classical interactions. Figure 5.15 shows the distribution of CT exciton energies for both cases. We refer to these distributions and their Gaussian broadened guide-to-the-eye as CT Density of States (DOS). CT DOS for dimers in vacuum is represented by blue bars, while the DOS of QM/MM dimers embedded in a static background of point charges is indicated by red bars. The inset labels state both the type of combination and in brackets the total number of CT states found in vacuum and static QM/MM. In all cases, an excitation was labeled as a CT state if the charge transfer between the two nucleobases in the pair exceeded 0.5 e.

A general observation is that the total number of CT states found in the covered energy region of 5 eV to 9 eV is always larger in the QM/MM case. This observation can be attributed to two effects. First, some of CT states that fall outside of the energy interval in the gas-phase calculation get pushed down in energy to values below 9 eV in static QM/MM. Second, some of the CT states change their character by embedding in the static background.

A more detailed analysis of the changes in distributions, in particular in the low energy regions, show no universal behavior. In some cases such as for the adenine dimers (A-A) some individual excitations lie at lower energies in static QM/MM than in the gas-phase. While not resolved in Fig. 5.15, the lowest energy CT excitation, at about 5.35 eV, is an intra-stand adenine dimer of the kind previously discussed by Yin et al. in a more idealized structure. We will scrutinize the properties of this particular excitation in more detail below.

Very much in contrast to this behavior, dimers formed from two cytosine bases exhibit CT excitons at higher energy than in the respective gas-phase calculation, irrespective of whether it is a intra- or interstrand excitation, see Fig. 5.15.

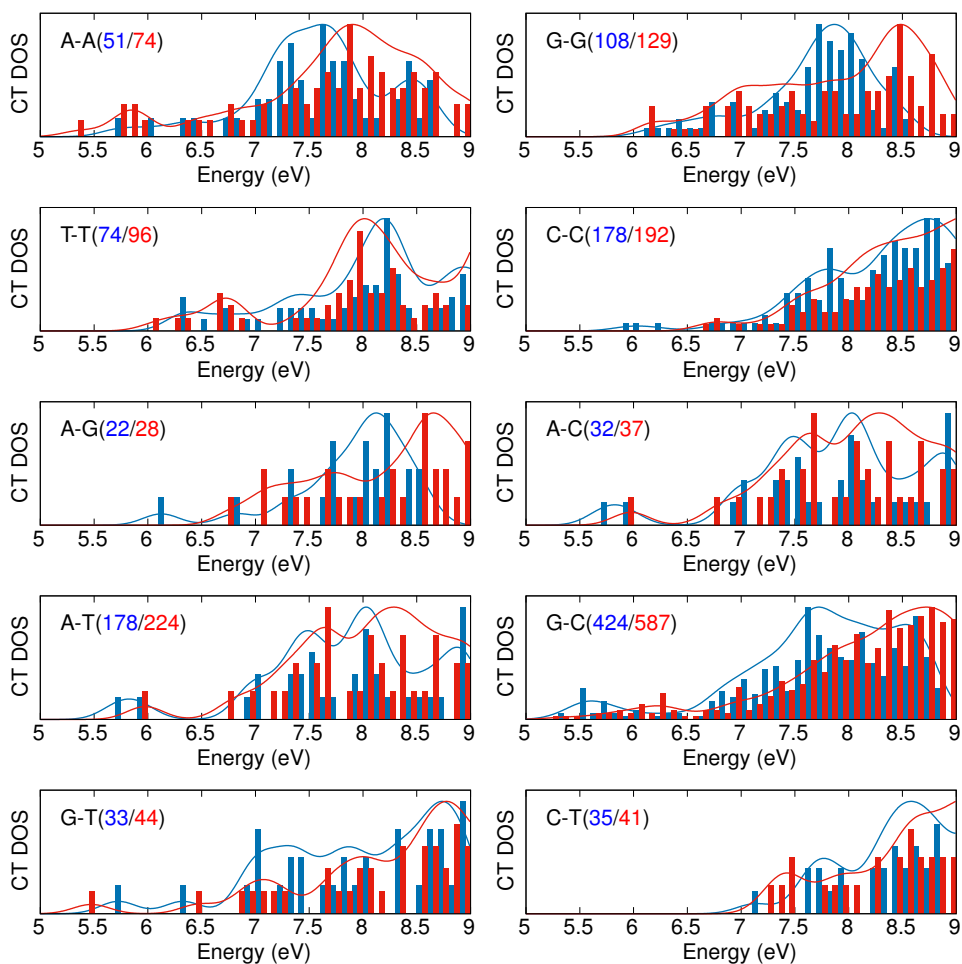


Figure 5.15: Density of states (DOS) for charge transfer (CT) excitations in aqDNA as obtained from dimers in vacuum (blue bars) and QM/MM embedded in a static background of point charges (red bars), respectively. The individual panels show different base pair combinations, in which neighboring nucleobases within a closest contact distance of less than 1 nm are considered as pairs. Due to the specific sequence of the model strand used in this work, different numbers of pairs are found for each combination. The inset labels indicate both the type of combination and in brackets the total number of CT states found in vacuum and static QM/MM. A cutoff of 4.3 nm was used for the atomistic electrostatic embedding.

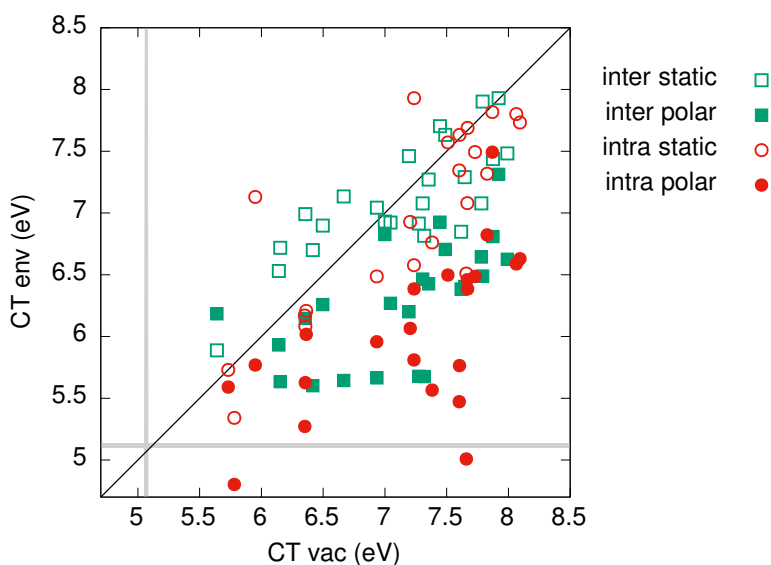


Figure 5.16: Comparison of CT excitation energies (in eV) calculated in static (open symbols) and polarizable (filled symbols) QM/MM setups with vacuum QM results. Interstrand (intrastrand) excitations are represented by green squares (red circles). The gray shaded areas indicate the range of single nucleobase UV absorption energies of adenine.

Given the non-universal behavior observed upon the inclusion of a static atomistic environment, we limit the following discussion to only the lowest energy CT excitation in each of the 59 pairs. The aim is to understand the influence of environment polarization in the QM/MM calculations. In Fig. 5.16 CT excitation energies resulting from both static (open symbols) and polarized (closed symbols) QM/MM calculations are shown against the respective vacuum energy. Here, also the differences between intrastrand (circles) and interstrand (squares) excitations are resolved. First, the data obtained for the static case reflects what has already been discussed above. No general trend can be discerned. CT excitation energies are both lowered and increased due to the presence of the environment. There appears to be a tendency that the lower-energy interstrand CTs up to an energy of 7 eV are all resulting at about 0.5 eV higher energies in the static case.

Taking polarization effects into account within the QM/MM approach universally lowers the energy, not only with respect to the static QM/MM results, but most

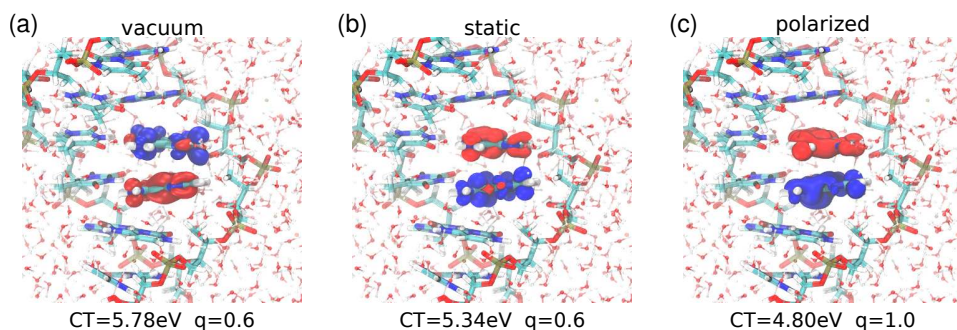


Figure 5.17: Isosurfaces ( $\pm 2 \times 10^{-3} e/\text{\AA}^3$ ) of excitation electron densities of the lowest energy adenine dimer resulting from (a) a gas-phase (vacuum) calculation, (b) a QM/MM calculation with static environment, and (c) a QM/MM calculation with polarizable environment. Red color corresponds to negative values (hole density) and blue color corresponds to positive values (electron density).

importantly also with respect to the vacuum calculation. On average, we observe a redshift of the interstrand CT energies by  $(-0.83 \pm 0.5) \text{ eV}$ , while intrastrand CTs are red shifted by  $(-1.15 \pm 0.6) \text{ eV}$ , compared to respective vacuum results. Notably, these redshifts are on the order of the redshift observed in experiment. Also, the CT excitation with the lowest energy of 4.81 eV is found for a  $A_2$  dimer in the chain.

In addition to the individual CT energies, the gray shaded areas in Fig. 5.16 indicate the energy range in which single adenine nucleobases absorb UV light, according to gas-phase and QM/MM calculations. While not shown here explicitly, the inclusion of a polarizable environment does not affect the energetic properties of these localized Frenkel excitons perceptively, with absorption predicted to be in the range  $(5.12 \pm 0.02) \text{ eV}$ . The lowest energies of CT excitations found in our dataset are approximately 0.3 eV below this absorption energy, indicating that the decay of the UV excitation to a CT excited state is energetically possible, as speculated.

Due to this energetic situation, it is worthwhile to analyze the  $A_2$  CT exciton in further detail and to illustrate how the atomistic environment not only affect its energy but also its electron-hole wave function. To this end, we show in Figure 5.17 the distributions of electron and hole densities on the  $A_2$  dimer for (a) vacuum QM, (b) static QM/MM, and (c) polarized QM/MM, respectively. The associated excitation energy and the effective charge transfer are shown below. As discussed before, for the vacuum case the CT energy is of 5.78 eV is several 0.1 eV above the

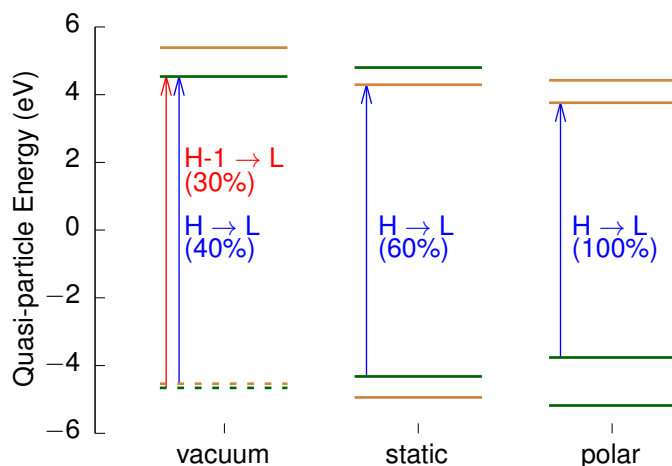


Figure 5.18: Quasi-particle energy levels (eV) for HOMO-1, HOMO, LUMO, and LUMO+1 resulting from (a) a gas-phase (vacuum) calculation, (b) a QM/MM calculation with static environment, and (c) a QM/MM calculation with polarizable environment. The color of horizontal lines indicates the localization of the quasi-particle states on either of the two nucleobases. Brown (dark green) represents localization on  $A_U$  ( $A_L$ ). For HOMO-1 and HOMO in the vacuum case, the quasi-particle states are distributed over the whole base pair, which is noted as a dashed line. Vertical arrows show the dominant transitions forming the CT excitation.

energy of the UV active excitation. The amount of charge transferred in the CT state is not integer but only  $0.6e$ , with the hole contribution on the lower nucleobase ( $A_L$ ) and the electron contribution on the upper one ( $A_U$ ). Upon inclusion of the static environment, the energy of this excitation is lowered by  $0.44\text{ eV}$  to  $5.34\text{ eV}$ . While the amount of charge transferred between the two adenines remains at  $0.6e$ . Despite this similarity, the characteristic of the excitation is changed significantly, as can be seen in Fig. 5.17(b). The localization of electron and hole contribution in the excitation is inverted. The electronic part is now localized on the lower adenine molecule, while the hole part can be found on the upper one. Including polarization effects, the general character of the CT excitation remains unaffected, i.e., the hole is localized on  $A_U$  and the electron on  $A_L$ . Most notably, however, the excitation exhibits integer charge transfer character in this situation.

The observation that the nature of the CT excitation can be affected dramatically by

the complex molecular environment can be attributed to a combination of a shift of energy levels and changed composition of transitions, as we discuss in detail below. To this end, we analyze in particular the quasi-particle energy levels obtained at the *GW* step of the respective calculations. Fig. 5.18 shows the energies of two highest occupied and two lowest empty quasi-particle levels for vacuum, static, and polarized calculations. Note that for an easier comparison, the zero of the energy scale has been set to the center of the HOMO-LUMO gap in all individual cases. The spatial distribution of all quasi-particle wave functions has been inspected and is indicated by the horizontal lines' color. Brown (dark green) lines indicate states that are localized on  $A_L$  ( $A_U$ ). In addition, the vertical lines show the contributions of the quasi-particle transitions to the respective CT excitations in Fig. 5.19, with the weights given as inset.

In the case of the vacuum calculation on the adenine dimer taken from the MD snapshot, it turns out that the two occupied levels cannot be uniquely assigned to either of the two nucleobases. Instead, the quasi-particle states delocalize over the dimer, however not at equal distribution. Note, though, that they are only separated by 0.13 eV in energy. To make this also visually clear, the two levels are shown as dashed lines in Fig. 5.18. As can be seen from the two arrows, the CT excitation in this environment-free QM calculation is composed of HOMO-1  $\rightarrow$  LUMO and HOMO  $\rightarrow$  LUMO transitions with nearly equal weight. The fact that the combined weight is only 70 % emphasizes that even more quasi-particle transitions play a significant role here. It is likely that this is directly linked to the delocalized nature of the occupied states. Taken as a whole, the hole contribution of the CT, arising in large parts from the HOMO and HOMO-1 states, is consequently localized on  $A_L$ . For the two unoccupied levels shown here, no strong delocalization over the dimer can be identified. Since the LUMO is localized on  $A_U$ , also the electron density in the CT state is found on this nucleobase.

Turning now towards the results obtained from calculation performed in the static QM/MM setup, one can spot significant changes as compare to the vacuum only calculation. First, all quasi-particle states around the HOMO-LUMO gap are localized on either of the two nucleobases of the excimer. In the occupied manifold, one can now assign the HOMO to be uniquely localized on  $A_U$  and HOMO-1 on  $A_L$ . As a consequence the energetic separation is more pronounced, amounting to 0.62 eV. At the same time also the two unoccupied states change character. While also localized on either of the two nucleobases in the vacuum calculation, one finds that the specific localization site is switched. The LUMO is now localized on



$A_L$ , and LUMO+1 on  $A_U$ . Combined with the fact that the dominant transition in the CT excitation is a HOMO to LUMO transition from  $A_U$  to  $A_L$  with a weight of approximately 60 %, see Fig. 5.18, the localization behavior of hole and electron densities is inverted as compared to the vacuum case. The total transferred charge is however still at 0.6 eV only, which can be attributed to the additional transitions that collectively contribute to 40 % of the excited state.

We note in passing that the HOMO-LUMO gap is also slightly reduced by the embedding in a static molecular environment, namely from 9.07 eV to 8.64 eV. A word of caution: The fact that the reduction by 0.43 eV of this gap is numerically similar to the lowering of the CT excitation energy by 0.44 eV is likely coincidental. Typically, a change in localization of the contribution quasi-particle states leads to a very different composition of the effective electron-hole interaction that determines the exciton binding energy and, concomitantly, the excitation energy.

From the quasi-particle levels in the polarized QM/MM calculation as shown on the right-hand side of Fig. 5.18, one can see that the environment polarization response modifies this picture even more. First of all, the shown two occupied states are localized on the upper adenine nucleobase, and the two unoccupied ones are localized on the lower one. The HOMO-LUMO gap is further reduced to 7.52 eV, and the energetic separation of the occupied and unoccupied levels is increased. Most remarkably, the CT excitation is in this case given as a pure HOMO to LUMO transition, with the hole contribution being exclusively localized on  $A_U$  and the electron contribution exclusively localized on  $A_L$ , yielding an integer charge transfer.

The above detailed analysis of the characteristics of the quasi-particle and CT excited states for the minimum energy CT found in our data set clearly reveals that the resulting excitation energies in complex molecular environments obtained from QM/MM calculations are a result of an intricate interplay of several effects. In particular modifications on the nature of the quasi-particle states are highly significant since their localization/delocalization characteristic have a profound and direct effect on the two-particle excitations. This interplay goes beyond a simple perturbative energy correction due to the environment that can simply be applied to a vacuum QM calculation.

To scrutinize whether the change of effective charge transfer in the CT excitation observed for the intra-strand adenine dimer observed above is a more general effect of embedding into a static and/or polarizable molecular environment, we show in Fig. 5.19 the calculated amount of transferred charge as a function of center-of-

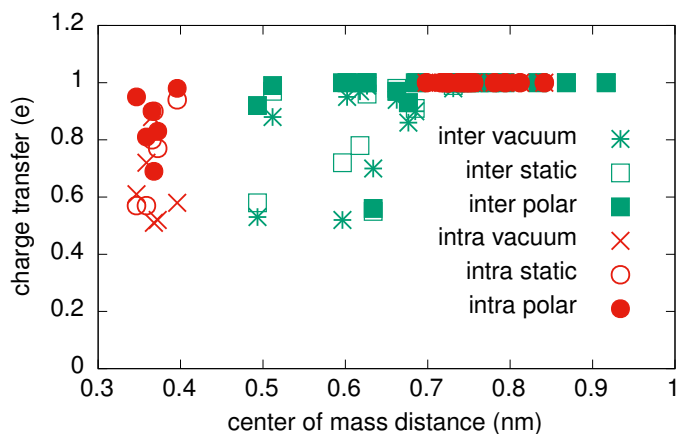


Figure 5.19: Effective charge transfer character (in  $e$ ) in the CT excitations as a function of center-of-mass distance of the involved monomers (in nm). Results for intra- and interstrand excitations are compared for the three different calculation setups: vacuum, static QM/MM, and polarized QM/MM.

mass distance for the various calculation setups. We differentiate also between intra- and inter-strand excitations.

It can be seen that for the excimers with the closest intermolecular separation between  $3 \text{ \AA}$  and  $4 \text{ \AA}$ , which are exclusively intra-strand excitations, vacuum calculations yield only partial charge transfer upon excitation between  $0.5 e$  and  $0.9 e$ . The same holds for inter-strand dimers with distances of  $5 \text{ \AA}$  and  $6 \text{ \AA}$ . All these short distance dimers are essentially neighboring molecules whose electron density can spatially overlap and the associated interaction yielding (partially) delocalized quasi-particle states. For all dimers with separation larger than  $0.7 \text{ nm}$  center-of-mass distance, i.e., second-nearest neighbors, such a direct interaction is not possible. In case of intra-strand excitations, it means that in a stack of three bases (base trimer), only the outer two nucleobases are treated quantum-mechanically, while the center one is part of the polarizable MM region. This is strictly speaking a fairly strong approximation. When base stacking interactions are strong, the purely classical treatment cannot cover possible effects of forming delocalized states and the associated partial charge transfer. Also, such explicit base pair interactions might affect the CT excitation energies directly. A possible pathway to cover such effects is to treat the full base trimer quantum-mechanically and embed this in a classical environment. However, this case goes beyond the scope of this thesis and is left for

future studies.

We focus in the following on the short-distance excimers. When the molecular environment is taken account, the static-only interactions (open symbols in Fig. 5.19) affect the amount of effectively transferred charge roughly in the same fashion as observed for the  $A_2$  system with minimal CT excitation energy discussed above. In some cases, one can note a change of this effective charge by up to 0.3 eV. However, at least for the first shell of intra- and inter-strand dimers, there is no observable integer charge transfer state.

Only upon adding environment polarization effects (filled symbols in Fig. 5.19), most of the CT states are approaching such an integer CT character. It stands to reason that remnant delocalization for quasi-particle states is responsible for that.

In summary, the study of electronic excitations in prototypical aqDNA using the QM/MM approach based on *GW*-BSE developed in this thesis has revealed that charge transfer excitations are extremely sensitive to the specific atomistically resolved environment. For the lowest energy CT excitations in an intrastrand adenine dimer, the approach predicts energies below that of the UV active single nucleobase excitation. This has a large impact on the possibility of an initial (fast) decay of such an UV excited state into a bi-nucleobase CT exciton, which is considered one of the pathways for UV-induced DNA damage. The calculated redshift of the CT excitation energy compared to a nucleobase dimer treated only in vacuum is of the order of 1 eV, which matches expectations from experimental data. As shown above, the QM/MM methodology used here allows to gain very detailed insight into the mechanisms leading to the observed energies. It is possible to disentangle the effects of the different levels of the explicit molecular environment on single-particle and two-particle excitations. Incorporating *GW*-BSE into the presented QM/MM setup is therefore an extremely powerful tool to study a wide range of types of electronic excitations in complex molecular environments.



## Chapter 6

# Transfer integrals for exciton transport

This chapter deals with the electronic couplings  $J_{AB}$ , which we introduced in Chapter 4, eq. 4.21<sup>1</sup>. Here, we focus solely on exciton electronic coupling, as electronic coupling for electrons and holes is already a quite well-established topic [129, 199, 200].

Although eq. 4.21 formally defines the electronic coupling, due to the intrinsic two-particle nature of excitons more than one pathway for transfer between two monomers  $A$  and  $B$  is possible, as depicted in Fig. 6.1. The electronic coupling is also sensitive to the molecular arrangement, i.e, the distance and relative orientation between monomers, which will be explored in this chapter.

In this chapter a dimer projection (DIPRO) method for exciton coupling based on many-body Green's functions theory (see Chapter 3 and Chapter 5) is presented. Monomer electron-hole wave functions serve as pseudo diabatic states and a projection method is employed to express these functions in the basis of products of single-particle functions used to determine the  $GW$ -BSE Hamiltonian in a *supramolecular* calculation. This dimer projection procedure allows for an efficient evaluation of the direct excitonic transfer integral  $J_{AB}$  using linear algebra

---

<sup>1</sup>The content of this chapter is based on: Jens Wehner and Björn Baumeier. „Intermolecular Singlet and Triplet Exciton Transfer Integrals from Many-Body Green's Functions Theory“. In: *J. Chem. Theory. Comput.* 13.4 (2017), pp. 1584–1594.

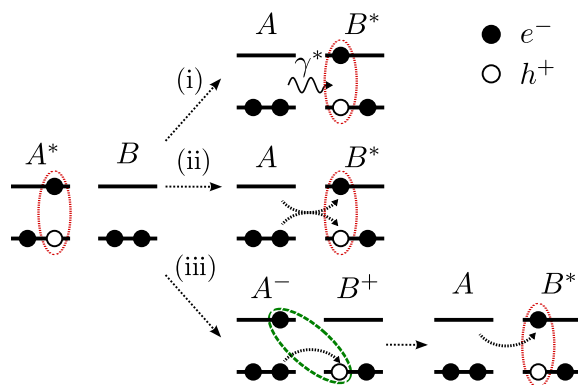


Figure 6.1: Illustration of the different pathways for exciton transfer between chromophores A and B. (i) Förster type energy transfer via exchange of a virtual photon. (ii) Dexter (charge) transfer via simultaneous hop of the electron-hole pair. (iii) CT mediated Dexter transfer via sequential hop of electron and hole.

methods.

*GW*-BSE, providing an accurate representation of long-range Coulomb and short-range exchange interactions, is of particular relevance for describing the wide range of possible excitonic coupling mechanisms, depending on the type of excitation and the involved length scales. Singlets can exhibit significant coupling even for distances exceeding 1 nm, typically estimated in the Förster picture from the interaction of the transition dipoles of the two chromophores involved in the transfer [201], see Fig. 6.1(i). On shorter length scales, higher order multipole terms in the Coulomb coupling [202] and short-range exchange effects can significantly influence the distance and orientation dependence of singlet couplings. Triplets couple exclusively via exchange interaction, which decays exponentially with chromophore distance, and are therefore restricted to next-neighbor transfers [36, 203]. For the exchange based contributions to singlet and triplet coupling, two distinctly different pathways need to be considered. The electron-hole pair can transfer either as an entity (Fig. 6.1(ii)) or via intermediate CT states [204] (see Fig. 6.1(iii)). Inclusion of the CT mediated processes into an effective coupling is particularly important since they can, at short chromophore distances, contribute equally or even more than the direct process, depending on the details of the CT wave function and its energy relative to those of the localized excitons. Approximate CT wave functions have previously been constructed using, e.g., constrained

DFT to study their coupling to localized excitations derived from TDDFT [205]. *GW*-BSE allows to derive both from the same Hamiltonian, and to this end, intermolecular CT excitations of types  $A^-B^+$  and  $A^+B^-$  are constructed within *GW*-BSE-DIPRO as product states from the respective monomer single-particle orbitals. All the couplings between the CT excitations, as well as, to the localized monomer excitons are calculated. From these, an effective coupling  $J_{AB}^{\text{eff}}$  is determined via a reduction technique, which maps the complete multi-state system onto two effective states. Unlike previous approaches based on first-order perturbation theory, this reduction technique method is also applicable to cases with energetic resonances of CT and localized excitons.

In the following, *GW*-BSE-DIPRO is first applied to model configurations of pyrene dimers at various distances and orientations. As small-molecule prototype systems, these allow for a detailed analysis of the quality of the approach in application to bright and dark singlet, as well as triplet excitons. Particular emphasis is placed on the convergence of the results with respect to the number of included CT excitations as well as the differences between the perturbation and reduction techniques. After assessing the choice of the exchange-correlation functional in the density-functional theory (DFT) calculations that underlie *GW*-BSE, optimizations of computational parameters are evaluated. Later we use DCV5T-Me<sub>3</sub>, a dicyanovinyl end-capped oligothiophene used as donor material in state-of-the-art organic solar cells, for defining a benchmark for the application of *GW*-BSE-DIPRO to large-scale morphologies of technologically relevant materials. For the molecular structure see app. A.

## 6.1 Excitonic coupling elements via *GW*-BSE-DIPRO

In the following, diabatic states  $|A\rangle$  and  $|B\rangle$  are approximated by TDA monomer electron-hole wave functions,  $|\Phi^A\rangle$  and  $|\Phi^B\rangle$ , as defined in eq. 3.131, because an exact diabatization is for most systems difficult or even impossible as mentioned in Chapter 4. With the BSE Hamiltonian of the dimer formed by the chromophores,  $\hat{H}^D$ , one can setup an effective ( $2 \times 2$ ) generalized eigenvalue problem

$$\underline{\mathbf{H}}^D \mathbf{c}_i = \underline{\mathbf{S}} \mathbf{c}_i \epsilon_i \quad (6.1)$$

with

$$\underline{\mathbf{H}}^D = \begin{pmatrix} \langle \Phi^A | \hat{H}^D | \Phi^A \rangle & \langle \Phi^A | \hat{H}^D | \Phi^B \rangle \\ \langle \Phi^B | \hat{H}^D | \Phi^A \rangle & \langle \Phi^B | \hat{H}^D | \Phi^B \rangle \end{pmatrix} \quad (6.2)$$

and

$$\underline{\mathbf{S}} = \begin{pmatrix} 1 & \langle \Phi^A | \Phi^B \rangle \\ \langle \Phi^B | \Phi^A \rangle & 1 \end{pmatrix}. \quad (6.3)$$

$\mathbf{c}_i$  is the  $i$ -th eigenvector and  $\epsilon_i$  the corresponding eigenvalue. Because the normalized monomer states are only approximations to the diabatic states, they are not necessarily orthogonal,  $\underline{\mathbf{S}} \neq \underline{\mathbf{1}}$ , and  $J_{AB}$  cannot be directly identified with the off-diagonal elements of  $\underline{\mathbf{H}}^D$ . Instead, following the idea successfully established by Valeev *et al.* for electronic coupling [199, 200], the generalized eigenvalue problem in eq. 6.1 first needs to be transformed into a standard eigenvalue problem

$$\tilde{\underline{\mathbf{H}}}^D \tilde{\mathbf{c}}_i = \tilde{\epsilon}_i \tilde{\mathbf{c}}_i, \quad (6.4)$$

via a Löwdin orthogonalization [206]. The choice for this technique is motivated by the fact that unlike, e.g., the Schmidt orthogonalization, it treats both wave functions on an equal footing and the resulting symmetrically orthogonalized functions are the least distant in the Hilbert space from the original functions. With the orthonormalized states  $|\tilde{\Phi}^{A(B)}\rangle$ , the diagonal and off-diagonal elements of  $\tilde{\underline{\mathbf{H}}}^D$  can be identified with the excitation energies  $\epsilon_{A(B)}$  and exciton coupling elements  $J_{AB}$ , respectively. It should be noted that this construction of approximate diabatic dimer states starting from monomer functions as above can be considered complementary to the approximate diabatization of adiabatic dimer states via the Boys or Mulliken-Hush scheme [207–209]. While such an approach is also feasible, it comes at a higher computational cost in particular due to the fact that solutions to the BSE equation eq. 3.130 for the dimer system are required. This time-consuming step for dimers of larger molecules can be avoided using the approximation adopted here, as will be outlined in the following.

With the orthonormalized states  $|\tilde{\Phi}^{A(B)}\rangle$ , the diagonal and off-diagonal elements of  $\tilde{\underline{\mathbf{H}}}^D$  can be identified with the excitation energies  $\epsilon_{A(B)}$  and exciton coupling elements  $J_{AB}$ , respectively.

What remains is to calculate the elements of  $\underline{\mathbf{H}}^D$  and  $\underline{\mathbf{S}}$ . They can be written as  $\langle \Phi_i | \hat{O} | \Phi_j \rangle$  with  $i \in A, B$  and  $\hat{O} = \{\hat{H}^D, 1\}$ . In the following,  $|\nu\rangle, |\alpha\rangle, |\beta\rangle$  ( $|c\rangle, |\alpha'\rangle, |\beta'\rangle$ ) are occupied (empty) single-particle orbitals of the dimer, monomer  $A$ , and monomer  $B$ , respectively. With this, the electron-hole wave functions for the localized



monomer excitations (eq. 3.131) can be written as

$$|\Phi_A\rangle = \sum_{\alpha\alpha'} A_{\alpha\alpha'} |\alpha\alpha'\rangle \quad (6.5)$$

$$|\Phi_B\rangle = \sum_{\beta\beta'} B_{\beta\beta'} |\beta\beta'\rangle. \quad (6.6)$$

Inserting the identity  $\mathbf{I} = \sum_{\nu c} |\nu c\rangle\langle \nu c|$  twice into the expression for the off-diagonal matrix elements of eq. 6.2, and using the above definitions of  $|\Phi_A\rangle$  and  $|\Phi_B\rangle$  from eq. 6.6 yields:

$$\begin{aligned} \langle \Phi_A | \hat{O} | \Phi_B \rangle &= \sum_{\nu c} \sum_{\nu' c'} \sum_{\alpha\alpha'} A_{\alpha\alpha'} \langle \alpha\alpha' | \nu c \rangle \langle \nu c | \hat{O} | \nu' c' \rangle \sum_{\beta\beta'} B_{\beta\beta'} \langle \nu' c' | \beta\beta' \rangle \\ &= \sum_{\nu c} \sum_{\nu' c'} \kappa_{\nu c}^A \langle \nu c | \hat{O} | \nu' c' \rangle \kappa_{\nu' c'}^B \end{aligned} \quad (6.7)$$

In practical calculations,  $\hat{O} = \hat{H}^D$  is setup directly in terms of  $|\nu c\rangle$ , so  $\langle \nu c | \hat{H}^D | \nu' c' \rangle = H_{\nu c, \nu' c'}^{\text{BSE}}$  is readily available. For  $\hat{O} = 1$  it holds that  $\langle \nu c | \nu' c' \rangle = \delta_{\nu\nu'} \delta_{cc'}$  yielding

$$\begin{aligned} \langle \Phi^A | \hat{H}^D | \Phi^B \rangle &= \sum_{\nu c} \sum_{\nu' c'} \kappa_{\nu c}^A H_{\nu c, \nu' c'}^{\text{BSE}} \kappa_{\nu' c'}^B = \boldsymbol{\kappa}^A \underline{\mathbf{H}}^{\text{BSE}} \boldsymbol{\kappa}^B \\ \langle \Phi^A | \Phi^B \rangle &= \sum_{\nu c} \kappa_{\nu c}^A \kappa_{\nu c}^B = \boldsymbol{\kappa}^A \boldsymbol{\kappa}^B. \end{aligned} \quad (6.8)$$

The quantities  $\boldsymbol{\kappa}^{A(B)}$  are projections of the monomer electron-hole wave functions, expressed in monomer single-particles functions, onto dimer single-particle orbitals, e.g.:

$$\kappa_{\nu c}^A = \sum_{\alpha\alpha'} A_{\alpha\alpha'} \langle \alpha\alpha' | \nu c \rangle. \quad (6.9)$$

These projections are evaluated by inserting the expansion of the respective single-particle orbitals in terms of the atomic orbital basis. When dimer and monomer calculations share the same basis set of atomic functions  $\{|\chi_\mu\rangle\}$ , it holds that

$$|\nu\rangle = \sum_{\mu} d_{\nu, \mu} |\chi_\mu\rangle \quad |c\rangle = \sum_{\mu} d_{c, \mu} |\chi_\mu\rangle \quad (6.10)$$

$$|\alpha\rangle = \sum_{\mu} d_{\alpha, \mu} |\chi_\mu\rangle \quad |\beta\rangle = \sum_{\mu} d_{\beta, \mu} |\chi_\mu\rangle. \quad (6.11)$$

Thus the terms of type  $\langle \alpha\alpha' | \nu c \rangle$  occurring in eq. 6.9 can be rewritten as:

$$\begin{aligned} \langle \alpha\alpha' | \nu c \rangle &= \langle \alpha | \nu \rangle \langle \alpha' | c \rangle = \sum_{\mu\mu'} d_{\alpha, \mu} d_{\nu, \mu'} \langle \chi_\mu | \chi_{\mu'} \rangle \sum_{\nu\nu'} d_{\alpha', \nu} d_{c, \nu'} \langle \chi_\nu | \chi_{\nu'} \rangle \\ &= (\mathbf{d}_\alpha^T \mathcal{S} \mathbf{d}_\nu) (\mathbf{d}_{\alpha'}^T \mathcal{S} \mathbf{d}_c), \end{aligned} \quad (6.12)$$

where  $\mathcal{S}$  is the overlap matrix of the atomic orbitals.

## 6.2 Influence of intermolecular CT states

While the projection technique as presented above captures the coupling mechanisms depicted in Fig. 6.1(i) and (ii), the charge transfer state mediated mechanism (iii) is not accounted for. The aim is to include these effects, which are CT inherent and whose interactions are contained in the BSE Hamiltonian, but which are not represented by the subspace spanned by  $|\tilde{\Phi}^{A(B)}\rangle$ .

Intermolecular CT excitons are approximated as product states of two single-particle orbitals localized on different monomers, i.e.

$$\begin{aligned} |CT\rangle_{(i,j)}^{-+} &= |A_i^- B_j^+\rangle = |\alpha'_{L+i}\rangle |\beta_{H-j}\rangle \\ |CT\rangle_{(i,j)}^{+-} &= |A_i^+ B_j^-\rangle = |\alpha_{H-i}\rangle |\beta'_{L+j}\rangle, \end{aligned} \quad (6.13)$$

where  $\alpha_H$  ( $\beta_H$ ) is the highest occupied molecular orbital (HOMO) and  $\alpha_L$  ( $\beta_L$ ) is the lowest unoccupied molecular orbital (LUMO) of chromophore A(B), respectively, and  $i, j = 0, \dots, M$ .  $M$  is the number of additional orbitals below (above) the HOMO (LUMO) taken into account<sup>2</sup>. In total, a set  $\{|CT_i\rangle\}$  comprising  $N_{CT} = 2(M+1)^2$  CT excitations is generated according to eq. 6.13.

As these approximate CT states are not orthogonal to the orthonormalized localized states after eq. 6.4, each  $|CT_i\rangle$  is first individually orthogonalized with respect to  $|\tilde{\Phi}^{A(B)}\rangle$

$$|CT'_i\rangle = |CT_i\rangle - \langle CT_i | \tilde{\Phi}^A \rangle |\tilde{\Phi}^A\rangle - \langle CT_i | \tilde{\Phi}^B \rangle |\tilde{\Phi}^B\rangle \quad (6.14)$$

and then normalized via  $|\overline{CT}_i\rangle = |CT'_i\rangle / \sqrt{\langle CT'_i | CT'_i \rangle}$ .

Equation 6.4 then turns into a  $([2 + N_{CT}] \times [2 + N_{CT}])$  eigenvalue problem with block structure of the augmented Hamiltonian:

$$\begin{pmatrix} \underline{\mathbf{H}}^{\text{FE}} & \underline{\mathbf{H}}^{\text{FE-CT}} \\ \underline{\mathbf{H}}^{\text{CT-FE}} & \underline{\mathbf{H}}^{\text{CT}} \end{pmatrix} \mathbf{C}_i = \epsilon_i \begin{pmatrix} \underline{\mathbf{1}}^{\text{FE}} & \mathbf{0} \\ \mathbf{0} & \underline{\mathbf{S}}^{\text{CT}} \end{pmatrix} \mathbf{C}_i, \quad (6.15)$$

where  $\underline{\mathbf{H}}^{\text{FE}} = \tilde{\mathbf{H}}^D$ . In a final step, the subspace of CT states in eq. 6.15 is diagonalized, i.e., solving

$$\underline{\mathbf{H}}^{\text{CT}} \mathbf{C}_i^{\text{CT}} = \Omega_i^{\text{CT}} \underline{\mathbf{S}}^{\text{CT}} \mathbf{C}_i^{\text{CT}}. \quad (6.16)$$

<sup>2</sup>For the sake of a compact presentation,  $M$  is chosen to be the same for both occupied and unoccupied levels of both molecules forming the dimer. In the actual implementation, these numbers can be chosen independently to account for potentially different densities of state.

The eigenfunctions  $|\widetilde{CT}_i\rangle = \sum_j C_j^{(i)} |\overline{CT}_j\rangle$  and energies  $\Omega_i^{\text{CT}}$  are used to transform eq. 6.15 into an ordinary eigenvalue problem:

$$\begin{pmatrix} \widetilde{\mathbf{H}}^{\text{FE}} & \widetilde{\mathbf{H}}^{\text{FE-CT}} \\ \widetilde{\mathbf{H}}^{\text{CT-FE}} & \widetilde{\mathbf{H}}^{\text{CT}} \end{pmatrix} \widetilde{\mathbf{C}}_i = \tilde{\epsilon}_i \widetilde{\mathbf{C}}_i, \quad (6.17)$$

with  $\widetilde{\mathbf{H}}^{\text{CT}} = \text{diag}(\Omega_i^{\text{CT}})$ . For the special case of  $M = 0$ , i.e., construction of two CT like excitations from the respective HOMO and LUMO single-particle orbitals, these corresponds to the  $(2+2) \times (2+2)$  system

$$\left( \begin{array}{cc|cc} \epsilon_A & J_{AB} & J_{A,1} & J_{A,2} \\ J_{BA} & \epsilon_B & J_{B,1} & J_{B,2} \\ \hline J_{1,A} & J_{1,B} & \Omega_1 & 0 \\ J_{2,A} & J_{2,B} & 0 & \Omega_2 \end{array} \right) \widetilde{\mathbf{C}}_i = \tilde{\epsilon}_i \widetilde{\mathbf{C}}_i \quad (6.18)$$

### 6.2.1 Perturbation theory

To obtain an effective excitonic coupling element  $J_{AB}^{\text{eff}}$  between  $|\widetilde{\Phi}^A\rangle$  and  $|\widetilde{\Phi}^B\rangle$ , that includes effects from coupling via intermediate CT excitations, the influence of the latter on the localized states has to be evaluated. Within first order perturbation theory, the corrections  $|\delta\widetilde{\Phi}^{A(B)}\rangle$  to  $|\widetilde{\Phi}^{A(B)}\rangle$  due to the  $|\widetilde{CT}_i\rangle$  can be expressed as [107, 204]:

$$|\delta\widetilde{\Phi}^{A(B)}\rangle = \frac{1}{2} \sum_i \frac{\langle \widetilde{CT}_i | \hat{H} | \widetilde{\Phi}^{A(B)} \rangle}{E_i^{\text{CT}} - E^{A(B)}} |\widetilde{CT}_i\rangle. \quad (6.19)$$

The modified coupling is then obtained to first order in  $|\delta\widetilde{\Phi}^{A(B)}\rangle$  as:

$$\begin{aligned} J_{AB}^{\text{eff}} &= \langle \widetilde{\Phi}^A + \delta\widetilde{\Phi}^A | \hat{H} | \widetilde{\Phi}^B + \delta\widetilde{\Phi}^B \rangle \\ &\approx \langle \widetilde{\Phi}^A | \hat{H} | \widetilde{\Phi}^B \rangle + \langle \delta\widetilde{\Phi}^A | \hat{H} | \widetilde{\Phi}^B \rangle + \langle \widetilde{\Phi}^A | \hat{H} | \delta\widetilde{\Phi}^B \rangle \\ &= \langle \widetilde{\Phi}^A | \hat{H} | \widetilde{\Phi}^B \rangle + \\ &\quad \frac{1}{2} \sum_i \langle \widetilde{\Phi}^A | \hat{H} | \widetilde{CT}_i \rangle \langle \widetilde{CT}_i | \hat{H} | \widetilde{\Phi}^B \rangle \left[ \frac{1}{E_i^{\text{CT}} - E^A} + \frac{1}{E_i^{\text{CT}} - E^B} \right]. \end{aligned} \quad (6.20)$$

All terms required to evaluate eq. 6.20 can be identified with elements of the Hamiltonian in eq. 6.17:  $\langle \widetilde{\Phi}^A | \hat{H} | \widetilde{\Phi}^B \rangle$  is the off-diagonal element of  $\widetilde{\mathbf{H}}^{\text{FE}}$  (i.e., the unperturbed excitonic coupling),  $\langle \widetilde{\Phi}^A | \hat{H} | \widetilde{CT}_i \rangle$  are elements of  $\widetilde{\mathbf{H}}^{\text{FE-CT}}$ , and the energies occurring in the denominator are the diagonal elements of  $\widetilde{\mathbf{H}}^{\text{FE}}$  and  $\widetilde{\mathbf{H}}^{\text{CT}}$ ,

respectively. For the example of the  $M = 0$  case as in eq. 6.18, the expression for the effective excitonic coupling element explicitly reads:

$$J_{AB}^{\text{eff}} = J_{AB} + \frac{1}{2} \sum_{i=1,2} J_{A,i} J_{i,B} \left[ \frac{1}{\Omega_i - \epsilon_A} + \frac{1}{\Omega_i - \epsilon_B} \right]. \quad (6.21)$$

## 6.2.2 Reduction method

From the structure of eq. 6.20, it is apparent that the perturbative approach to account for the influence of CT excitations on excitonic coupling is not readily applicable to situations in which a CT excitation is energetically in, or close to, resonance with the localized excitations. Instead of going to even higher orders of perturbation theory, an alternative technique that starts from the augmented Hamiltonian of eq. 6.17 is proposed.

The main idea is to reduce the augmented  $(2 + N_{\text{CT}}) \times (2 + N_{\text{CT}})$  system to an effective  $(2 \times 2)$  system. In spirit similar to perturbation theory, the states forming this reduced system are expected to be close to the original states  $|\tilde{\Phi}^{A(B)}\rangle$ , and consequently the effects of the intermediate CT states is mapped onto a coupling between those states. To achieve this, first eq. 6.17 is diagonalized, yielding the eigenenergies  $\tilde{\epsilon}_i$  and the set of corresponding eigenvectors  $\tilde{\mathbf{C}}_i$ .

From this, two elements  $\tilde{\mathbf{C}}_{a(b)}$  are chosen according to having the maximum overlap with the states  $\tilde{\Phi}_A$  and  $\tilde{\Phi}_B$ , respectively. Projecting  $\tilde{\mathbf{C}}_{a(b)}$  onto the subspace spanned by  $\tilde{\Phi}_A$  and  $\tilde{\Phi}_B$ , followed by a Löwdin transformation, yields new orthonormalized vectors  $\mathbf{C}_{a(b)}^*$ .

The diagonal  $(2 \times 2)$  matrix  $\epsilon^*$  formed with the energies  $\tilde{\epsilon}_{a/b}$  can be transformed to its non-diagonal form using the transformation matrix  $\mathbf{U} = (\mathbf{C}_a^* \mathbf{C}_b^*)$ . Resulting in a reduced, effective system

$$\mathbf{H}_{\text{eff}} = \mathbf{U} \cdot \epsilon^* \cdot \mathbf{U}^T, \quad (6.22)$$

which allows to read-off the effective excitonic coupling  $J_{AB}^{\text{eff}}$  as its offdiagonal elements.

To illustrate the differences and similarities between obtaining the effective coupling according to this reduction method (RM) and the perturbation theory (PT), it is convenient to consider a simplified model of the minimal system introduced in eq. 6.18. Specifically, a symmetric system is assumed with  $\epsilon_A = \epsilon_B = \epsilon$ ,  $\Omega_1 = \Omega_2 = \Omega$ ,

and  $J_{A(B),1(2)} = J_{CT}$ . Using perturbation theory, the effective coupling reads with  $\Delta\epsilon = \Omega - \epsilon$

$$J_{AB}^{\text{eff,PT}} = J_{AB} + \frac{2J_{CT}^2}{\Delta\epsilon}, \quad (6.23)$$

with the obvious resonance for  $\Delta\epsilon = 0$ . Using the reduction method yields an analytical solution

$$J_{AB}^{\text{eff,RM}} = \frac{1}{4} \left[ 3J_{AB} - \Delta\epsilon + \sqrt{(J_{AB} + \Delta\epsilon)^2 + 16J_{CT}^2} \right]. \quad (6.24)$$

In the limit of  $\Delta\epsilon \rightarrow 0$ ,  $J_{AB}^{\text{eff,RM}}$  remains finite. Away from the energetic resonance, i.e.  $\Delta\epsilon \gg J_{AB}, J_{CT}$ , it holds that

$$\begin{aligned} J_{AB}^{\text{eff,RM}} &= \frac{1}{4} \left[ 3J_{AB} - \Delta\epsilon + (J_{AB} + \Delta\epsilon) \sqrt{1 + \frac{16J_{CT}^2}{(J_{AB} + \Delta\epsilon)^2}} \right] \\ &\approx \frac{1}{4} \left[ 3J_{AB} - \Delta\epsilon + (J_{AB} + \Delta\epsilon) \left( 1 + \frac{16J_{CT}^2}{2(J_{AB} + \Delta\epsilon)^2} \right) \right] \\ &= J_{AB} + \frac{2J_{CT}^2}{J_{AB} + \Delta\epsilon} \approx J_{AB} + \frac{2J_{CT}^2}{\Delta\epsilon} = J_{AB}^{\text{eff,PT}} \end{aligned} \quad (6.25)$$

For more complex systems with less symmetry or  $M > 0$ , no closed form analytical expressions for  $J_{AB}^{\text{eff,RM}}$  can be obtained. Therefore, the method is in the following employed and assessed in practical application to realistic molecular systems.

## 6.3 Results

To assess the quality of the procedures outlined in the previous section, model configurations of pyrene dimers at various distances and orientations are considered. Within the TDA of *GW*-BSE, pyrene exhibits energetically well separated optically inactive ( $S_1$ ) and active ( $S_2$ ) singlet as well as triplet ( $T_1$ ) excitations. Analysis of the excitonic couplings for these different types of excitations allows scrutiny of how well the different pathways, see Fig. 6.1, are accounted for. The convergence of the results with respect to the number of included CT excitations, the differences between the perturbation and reduction techniques, basis set dependence, as well as the influence of the choice of the exchange-correlation functional in the density-functional theory (DFT) calculations that underlie the *GW*-BSE steps

are evaluated. Later, optimizations of computational parameters are devised using DCV5T, defining a benchmark for the application of *GW*-BSE-DIPRO to large-scale morphologies of technologically relevant materials.

For the practical calculations in this chapter the starting Kohn-Sham calculations were performed using the Gaussian03 package [149], Stuttgart/Dresden effective core potentials [148] and the associated basis sets that are augmented by additional polarization functions [173] of *d* symmetry. The auxiliary basis sets used to represent the polarization include orbitals of *s*, *p*, and *d* symmetry with the decay constants  $\alpha$  (in a.u.) 0.20, 0.67, and 3.0 for N and S, 0.25, 0.90, 3.0 for C, and 0.4 and 1.5 for H atoms, yielding converged excitation energies.

### 6.3.1 Model pyrene dimers

The geometry of a single pyrene molecule was optimized on DFT level using the PBE functional [59] with the 6-311G(d,p) basis set. From this geometry, ideal  $\pi$ -stacked dimers with intermolecular distances ranging from 2.7 Å to 7 Å are constructed. *GW*-BSE calculations are performed for the monomers, as well as the dimer configuration (only setup of  $\underline{\mathbf{H}}^{\text{BSE}}$ ), and coupling elements determined according to the projection method.

In this configuration the molecules forming the dimer are related by a symmetry transformation and the energetic states of the monomers are well separated, it is also possible to obtain the effective excitonic coupling via  $2J^{\text{eff}} = \Delta\Omega^D$ , where  $\Delta\Omega^D$  is the Davydov splitting of the respective monomer excitation in the dimer. To facilitate this comparison, full *GW*-BSE-TDA calculation for the dimer configuration were performed and the splitting from the resulting spectrum extracted.

Figure 6.2 shows the distance dependence of  $|J|$  for (a)  $S_1$ , (b)  $S_2$ , and (c)  $T_1$  excitations obtained via *GW*-BSE-DIPRO with the reduction method. For all excitations large deviations from the Davydov splitting are found when no intermediate CT states ( $N_{\text{CT}} = 0$ ) are included. At the typical  $\pi$ - $\pi$  stacking distance of 3.5 Å, these deviations can be on the order of 1-2 orders of magnitude. For the two singlet states, the observed underestimation decreases exponentially with distance, typical for an exchange based coupling mechanism as the one mediated by charge transfer. Inclusion of CT excitations ameliorates this situation. For  $S_2$  and  $T_1$ , taking only two CT excitations between the respective HOMO and LUMO states ( $M = 0$ ,  $N_{\text{CT}} = 2$ ) into account practically recovers the split results. In contrast, no

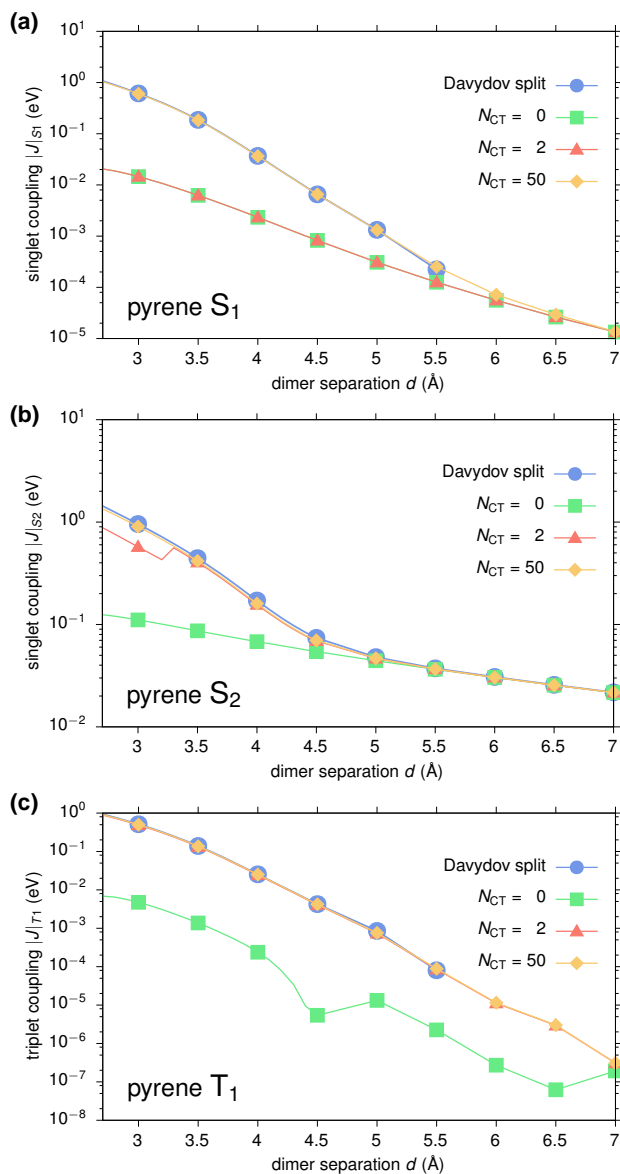


Figure 6.2: Distance dependence of excitonic couplings for (a)  $S_1$ , (b)  $S_2$ , and (c)  $T_1$  excitations in an ideally  $\pi$ -stacked pyrene dimer. Results obtained via  $GW$ -BSE-DIPRO with the reduction method for increasing numbers of included CT excitations are compared to the reference determined from the Davydov splitting in a full supermolecular calculation.

effect can be registered for  $S_1$ . Here, an agreement with the Davydov split estimate can only be achieved for  $M = 1$ , i.e., by construction of additional CT excitations based on HOMO-1 and LUMO+1, respectively. This is due to the fact that, unlike  $S_2$  and  $T_1$ , which have the main contribution from a HOMO→LUMO transition, the first singlet excitation in single pyrene is formed by a linear combination of HOMO-1→LUMO and HOMO→LUMO+1, and the choice of  $M$  in the reduction method needs to reflect the composition of the various localized excited states. In all cases, converged exciton couplings are achieved including  $N_{CT} = 50$  CT excitations ( $M = 4$ ). Note that for distances  $\geq 6\text{\AA}$ , the coupling in  $S_1$  and  $T_1$  becomes so small that the split estimate becomes numerically inaccurate.

From the converged results and the Davydov splittings it can be seen that the excitonic couplings based on *GW*-BSE simultaneously exhibit characteristics of short-range exchange and long-range Coulomb coupling, depending on the type of excitation. For  $S_1$  (with a negligibly small transition dipole) and  $T_1$ ,  $|J|$  decays proportional to  $\exp(-\alpha d)$  with  $\alpha(S_1) \approx 3.2\text{\AA}^{-1}$  and  $\alpha(T_1) \approx 3.4\text{\AA}^{-1}$ , respectively. In contrast, the optically active  $S_2$  shows an exponential decay for distances in the range of 3-4.5  $\text{\AA}$  ( $\alpha(S_2) \approx 1.7\text{\AA}^{-1}$ ), before the effective coupling is dominated by slowly-decaying Coulomb contributions.

To ascertain the quality of excitonic coupling elements obtained from *GW*-BSE, they are in the following compared to ones obtained from standard methods of similar complexity: time-dependent Hartree-Fock (TDHF), TDDFT/B3LYP, and configuration-interaction singles (CIS). Since the projection technique as used in *GW*-BSE-DIPRO is not available for those, the comparison is performed for the Davydov splittings in the ideally  $\pi$ -stacked dimer configurations, using the same ECP and basis set. The respective results are listed in Tab. 6.1 for dimer separations of  $d = 3.0 - 6.0\text{\AA}$ . At all separations, *GW*-BSE, TDHF, and CIS agree well for the dark  $S_1$  state. Same holds for the optically active  $S_2$ . Here, the data from all four methods practically agree at short and long distances, while in the intermediate region TDDFT appears to decay slightly faster. All in all, a good agreement between all four methods can be noted for singlets. For the  $T_1$  state all methods show approximately the same decay of the coupling with separation. Note however, that TDHF calculations suffered from triplet instabilities yielding negative excitation energies, which led to the results being discarded [210, 211].

In many realistic molecular aggregates, chromophores do not arrange in an ideal  $\pi$ -stack as assumed in the previous section. Instead, they assume relative positions and orientations characterized by shifts and rotations which are not compatible



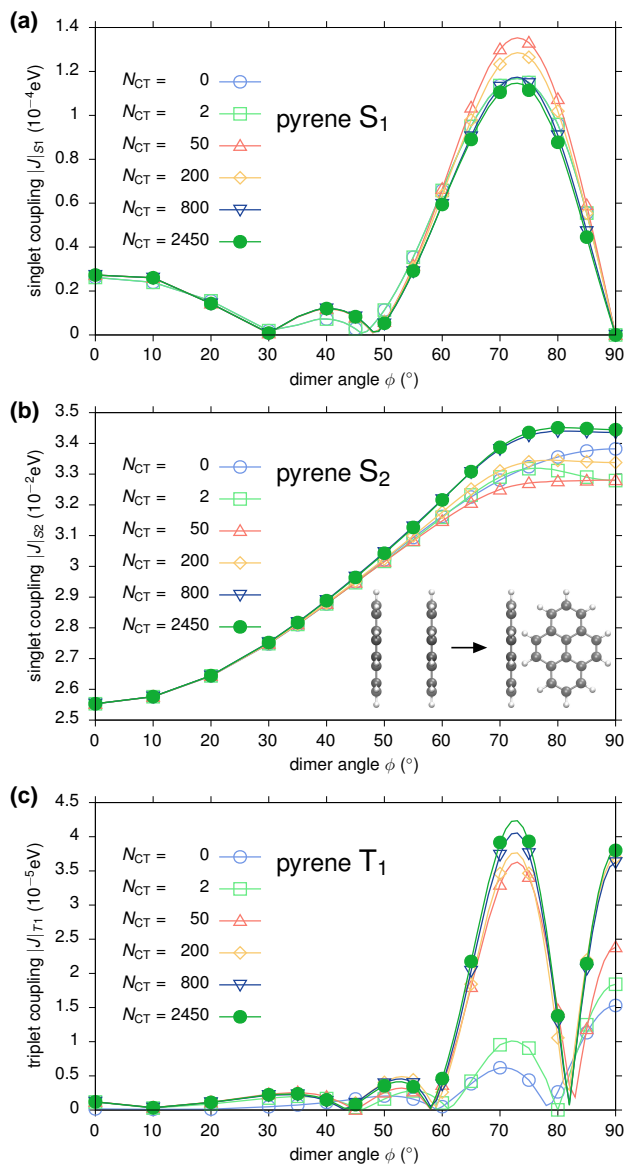


Figure 6.3: Rotational dependence of excitonic couplings for (a)  $S_1$ , (b)  $S_2$ , and (c)  $T_1$  excitations in a pyrene dimer. The configuration at  $\phi = 0^\circ$  corresponds to an ideal  $\pi$ -stacking at a distance of  $6.5 \text{ \AA}$ . Results obtained via  $GW$ -BSE-DIPRO with the reduction method for increasing numbers of included CT excitations.

Table 6.1: Excitonic coupling elements  $|J|$  from Davydov splitting (in eV) for  $S_1$ ,  $S_2$ , and  $T_1$  excitations in an ideally  $\pi$ -stacked pyrene dimer with varying distance  $d$ , as obtained by  $GW$ -BSE, TDHF, TDDFT/B3LYP, and CIS, respectively. For  $d = 6.0\text{\AA}$  the coupling in  $S_1$  and  $T_1$  becomes so small that the split estimate becomes numerically inaccurate and is therefore omitted.

type	$d = 3.0\text{\AA}$	$d = 4.0\text{\AA}$	$d = 5.0\text{\AA}$	$d = 6.0\text{\AA}$
<b>Davydov split <math>S_1</math></b>				
$GW$ -BSE	$6.13 \cdot 10^{-1}$	$3.70 \cdot 10^{-2}$	$1.53 \cdot 10^{-3}$	
TDHF	$6.24 \cdot 10^{-1}$	$4.94 \cdot 10^{-2}$	$2.50 \cdot 10^{-3}$	
TDDFT	$6.81 \cdot 10^{-1}$	$1.08 \cdot 10^{-1}$	$8.35 \cdot 10^{-3}$	
CIS	$6.41 \cdot 10^{-1}$	$4.77 \cdot 10^{-2}$	$2.50 \cdot 10^{-3}$	
<b>Davydov split <math>S_2</math></b>				
$GW$ -BSE	$9.57 \cdot 10^{-1}$	$1.71 \cdot 10^{-1}$	$4.80 \cdot 10^{-2}$	$2.18 \cdot 10^{-2}$
TDHF	$8.38 \cdot 10^{-1}$	$1.40 \cdot 10^{-1}$	$5.11 \cdot 10^{-2}$	$3.22 \cdot 10^{-2}$
TDDFT	$6.74 \cdot 10^{-1}$	$7.36 \cdot 10^{-2}$	$3.45 \cdot 10^{-2}$	$2.87 \cdot 10^{-2}$
CIS	$8.87 \cdot 10^{-1}$	$1.55 \cdot 10^{-1}$	$5.60 \cdot 10^{-2}$	$3.56 \cdot 10^{-2}$
<b>Davydov split <math>T_1</math></b>				
$GW$ -BSE	$5.12 \cdot 10^{-1}$	$2.54 \cdot 10^{-2}$	$8.51 \cdot 10^{-4}$	
TDDFT	$5.26 \cdot 10^{-1}$	$3.83 \cdot 10^{-2}$	$1.55 \cdot 10^{-3}$	
CIS	$3.97 \cdot 10^{-1}$	$2.33 \cdot 10^{-2}$	$1.70 \cdot 10^{-3}$	

with the basic symmetry operations. Due to the asymmetry in the geometry an estimation of coupling elements from Davydov splits is inaccurate and the use of techniques such as  $GW$ -BSE-DIPRO is indispensable. To assess the procedure for such a case, starting from the ideal  $\pi$ -stacking configuration with an intermolecular distance of  $6.5\text{\AA}$  one molecule is rotated along its long axis from  $0^\circ$  to  $90^\circ$  (see, cf. inset in Fig. 6.3(b)). As for the distance dependence, the convergence of the excitonic coupling elements with respect to the number of included CT states is investigated for  $S_1$ ,  $S_2$ , and  $T_1$ . The results shown in Fig. 6.3 generally exhibit more structure compared to the distance dependence in Fig. 6.2 as a consequence of intricate interactions between the two  $\pi$  systems upon rotation. It is also evident that for rotation angles of up to approximately  $50^\circ$ , converged results are obtained for  $N_{CT} = 50$  for all excitations. At larger rotations, strong couplings are found for

$S_1$  and  $T_1$  in particular. In this region, the convergence is much slower and up to 2450 ( $M = 34$ ) intermediate CT states are required. This is probably a result of the stronger and asymmetric polarization of the dimer states with respect to the monomer calculations. It should be emphasized, however, that the two chromophores approach each other very closely for those angles. At the perpendicular configuration, the minimal distance is reduced to only 3.1 Å and concomitantly strong effects and mixing of single-particle functions can be expected.

To highlight the differences and similarities, distance and rotational dependence of singlet and triplet excitonic transfer integrals as obtained by the reduction method presented in this work and the perturbation theory are compared for the model pyrene configurations. In all cases, 50 CT states are included in the distance dependence, and 2450 in the rotational dependence. As is apparent from Fig. 6.4(a), the distance dependence of the coupling constants for  $S_1$  and  $T_1$  shows good agreement between the approaches. Only at distances smaller than 3.5 Å perturbation theory slightly overestimates the RM results, which agree with the Davydov split estimates, cf. Fig. 6.2. For the optically active  $S_2$  state, however, significant deviations can be observed. For an intermolecular separation of 3.5 Å, a characteristic resonance structure is found, representing a massive overestimation of the transfer integral by nearly two orders of magnitude. Deviations are noticeable around this typical  $\pi$ -stacking distance in many molecular semiconductors up to a distance of 4.5 Å. For the rotated systems, see Fig. 6.4(b), both approaches yield qualitatively similar behavior with some quantitative deviations up to a factor of 2 for the close contact structures at large rotation angles. All in all, the reduction method compares favorably with the perturbation theory approach.

The basis set used in this work is optimized for the use with the effective core potentials [148], which will be referred to as `ubecp` in the following. All results presented to this point have been obtained from calculations, in which (d,p) polarization functions of the 6-311G basis set [173], have been added to form the basis `ubecppol`. To further gauge the convergence of the reported values for the singlet and triplet exciton coupling elements with respect to the basis set choice, two basis sets with diffuse functions (`ubecppol+`,  $s$  shells, decay constant 0.0438 a.u. for C, and 0.102741 a.u. for H) and (`ubecppol++`, additional  $p$  shell, decay constant 0.0691 a.u. for C) have been prepared as well. Three representative configurations of the pyrene dimers have been chosen: ideal  $\pi$ -stack geometries with distances 3.5 Å and 7.0 Å, respectively, and one at  $d = 5.5$  Å with an additional rotation by 45°. For the latter no results could be obtained using the `ubecppol++` because of

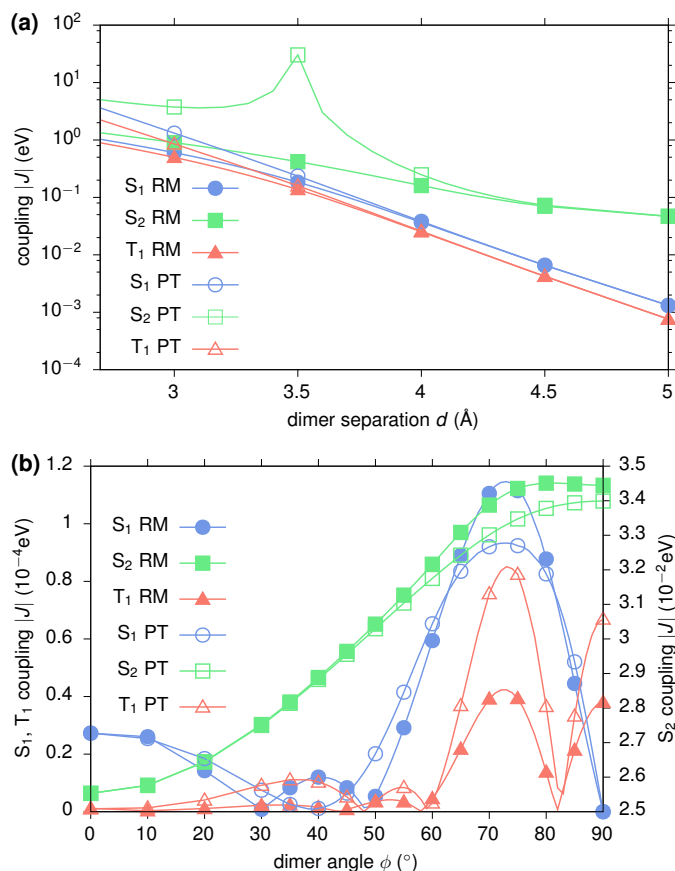


Figure 6.4: Comparison of the (a) distance and (b) rotation dependence of effective excitonic couplings in the pyrene model dimers, obtained with reduction method (RM) and via perturbation theory (PT), respectively. The distance dependence of both approaches as seen in (a) is nearly identical for S<sub>1</sub> and T<sub>1</sub> with the exception of short intermolecular distances. For the S<sub>2</sub> couplings, large deviations are observed due to energetic resonance of localized and intermediate CT excitons. For the rotated structures (b) both approaches show similar qualitative behavior.

Table 6.2: Basis set dependence of the calculated transfer integrals  $|J|$  (in eV) for  $S_1$ ,  $S_2$ , and  $T_1$  states in representative configurations of pyrene dimers. The average timings for the different calculations relative to the one with the smallest ubecp set are given at the bottom.

type	ubecp	ubecppol	ubecppol+	ubecppol++
<b>ideal <math>\pi</math>-stack, <math>d = 3.5\text{\AA}</math></b>				
$S_1$	$1.90 \cdot 10^{-1}$	$1.85 \cdot 10^{-1}$	$1.87 \cdot 10^{-1}$	$1.95 \cdot 10^{-1}$
$S_2$	$4.59 \cdot 10^{-1}$	$4.20 \cdot 10^{-1}$	$4.31 \cdot 10^{-1}$	$4.53 \cdot 10^{-1}$
$T_1$	$1.42 \cdot 10^{-1}$	$1.37 \cdot 10^{-1}$	$1.39 \cdot 10^{-1}$	$1.46 \cdot 10^{-1}$
<b>ideal <math>\pi</math>-stack, <math>d = 7.0\text{\AA}</math></b>				
$S_1$	$1.86 \cdot 10^{-5}$	$1.35 \cdot 10^{-5}$	$1.33 \cdot 10^{-5}$	$1.32 \cdot 10^{-5}$
$S_2$	$2.52 \cdot 10^{-2}$	$2.16 \cdot 10^{-2}$	$2.19 \cdot 10^{-2}$	$2.29 \cdot 10^{-2}$
$T_1$	$4.18 \cdot 10^{-7}$	$3.08 \cdot 10^{-7}$	$2.47 \cdot 10^{-7}$	$1.62 \cdot 10^{-7}$
<b>rotation <math>\phi = 45^\circ</math>, <math>d = 5.5\text{\AA}</math></b>				
$S_1$	$3.44 \cdot 10^{-4}$	$4.18 \cdot 10^{-4}$	$4.31 \cdot 10^{-4}$	
$S_2$	$5.91 \cdot 10^{-2}$	$4.88 \cdot 10^{-2}$	$5.06 \cdot 10^{-2}$	
$T_1$	$3.97 \cdot 10^{-5}$	$5.04 \cdot 10^{-5}$	$6.63 \cdot 10^{-5}$	
Timings	1.00	1.26	1.50	2.20

convergence issues in the underlying DFT calculation. The obtained couplings for  $S_1$ ,  $S_2$ , and  $T_1$  excitons for these configurations are listed in Tab. 6.2. It is clear that the results are fairly independent of the choice of the basis set. Even the use of the standard ubecp without additional polarization or diffuse functions yields excitonic transfer integrals in reasonable agreement with the ones obtained by extended basis sets. This is of great significance for the computational costs listed at the bottom of Tab. 6.2. It is obvious that the addition of diffuse functions in particular increases the calculation time dramatically. The control of the computation time with the choice of basis set gains more importance for molecules bigger than pyrene and will be further discussed below.

Until this point, the discussion of the *GW*-BSE-DIPRO approach has been limited to results obtained via *GW*-BSE based on DFT calculations using the semi-local PBE functional. It is known from literature that this technique can be marred by a starting point dependence, i.e., that the computed excited states depend on

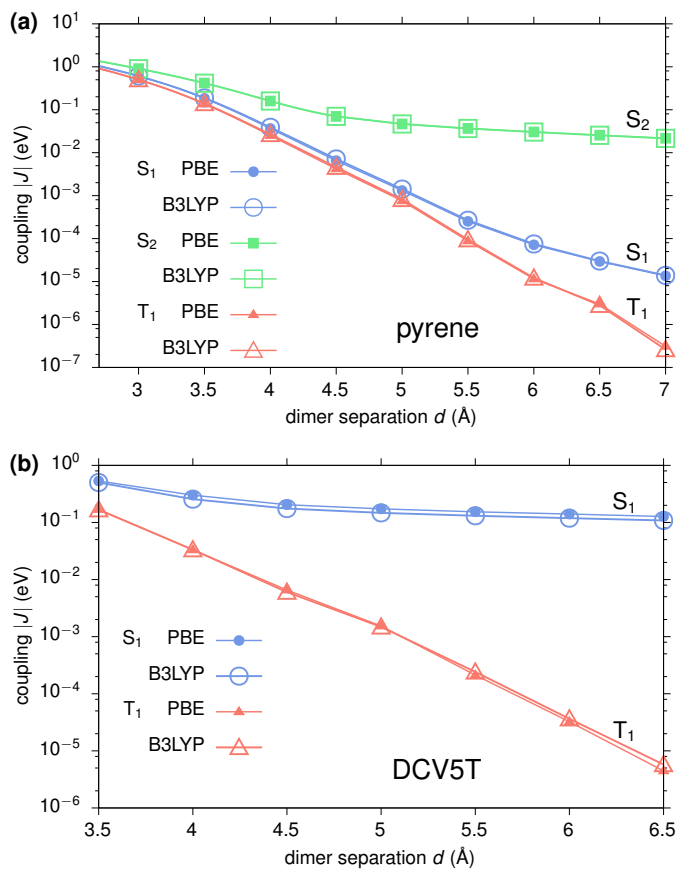


Figure 6.5: Comparison of the distance dependence of exciton transfer integrals in ideally  $\pi$ -stacked dimers of (a) pyrene and (b) DCV5T, obtained starting from DFT calculations using PBE and B3LYP functionals, respectively. 50 CT states have been taken into account using the reduction method.

the quality of the underlying ground-state calculation [212]. In particular, one-shot  $G_0W_0$  techniques are affected by this. As a result of the iterative procedures regarding the refinement of quasi-particle energies as described in Chapter 5 for the  $GW$ -BSE implementation used here, this problem is alleviated. To confirm this, the distance dependence of the exciton transfer integrals has been recalculated using DFT with the B3LYP hybrid functional for the pyrene dimer. The comparison to the results based on PBE as shown in Fig. 6.5(a) reveals practical independence on the DFT starting point for all three types of excitations considered.

### 6.3.2 Optimizations for application to large scale morphologies

In the following, the focus shifts to the evaluation of  $GW$ -BSE-DIPRO to chromophores of sizes typical and relevant for application in organic devices. To this end, exciton transfer integrals in an ideal stack of DCV5T molecules are investigated for the lowest energy singlet ( $S_1$ , optically active) and triplet excitons ( $T_1$ ), respectively.

The obtained distance dependence is shown in Fig. 6.5(b), with the  $GW$ -BSE calculations being based on PBE and B3LYP DFT ground states. As for the pyrene dimer, different behavior is observed for the two excitations. The coupling of the optically active singlet states is dominated by long-range Coulomb interactions, representing Förster type coupling. In contrast,  $T_1$  shows an exponential distance dependence, as expected for a Dexter type exchange coupling. Results for the two functionals are practically identical, with a shift to slightly larger  $S_1$  couplings noticeable for PBE compared to B3LYP. This is a consequence of an approximately 9% bigger transition dipole moment from the PBE calculation.

The above confirms that the  $GW$ -BSE-DIPRO method used in this work is well applicable to complex molecular systems of relevant size. However, the investigation of, e.g., exciton diffusion in realistic large-scale morphologies requires the calculation of tens of thousands excitonic transfer integrals. It is therefore highly desirable to devise optimizations of the involved computational procedures. To this end, approximations on DFT,  $GW$ -BSE, and  $GW$ -BSE-DIPRO levels to decrease computation times are evaluated.

On the DFT level, it has been shown for the calculation of charge transfer integrals that it is computationally advantageous to use an initial guess for the dimer calculation formed by merging the involved densities of the monomer fragments [200].

Table 6.3: Effect of different computational parameters for DFT and *GW*-BSE calculations on run times and exciton transfer integrals for  $S_1$  and  $T_1$  in a DCV5T dimer separated by 3.5 Å. Calculations were performed using 4 threads on a i5-4690 CPU @3.50 GHz. The value of 0.22 Ryd for the fixed shift runs was taken from the result of the iterative procedure at 3 Å.

DFT@PBE	<i>GW</i> -BSE	Time [min:s]	$ J _{S_1}$ [eV]	$ J _{T_1}$ [eV]
SCF	iterate	44:50	0.5354	0.1709
SCF	fixed	40:28	0.5355	0.1710
noSCF	iterate	37:51	0.5277	0.1721
noSCF	fixed	33:40	0.5278	0.1721

This also allows to perform only a single SCF step on the dimer, instead of obtaining a fully self-consistent solution.

A possible simplification of the *GW*-BSE run concerns the iterative procedure used to scissor shift the Kohn-Sham spectrum before calculating  $W$ . Instead of iterating this shift for each dimer configuration a fixed value can be predetermined, e.g., from a single representative configuration or averaging over a couple.

In Tab. 6.3 the run times and exciton transfer integrals for  $S_1$  and  $T_1$  in a DCV5T dimer separated by 3.5 Å are compared for different combinations of computational procedures. Using a fixed shift in *GW*-BSE saves on average 3-4 iterations, which for this system translates to reducing the runtime by approximately 4 min. The effect on the exciton couplings is negligible. Similarly, using the noSCF procedure in the DFT part has a slightly bigger effect decreasing the singlet coupling by about 1.5%. Combining both approximations cuts computation time by about 25%.

Additionally, the distance dependence of triplet and singlet couplings in DCV5T has been calculated for all four options given in Tab. 6.3. The results shown in Fig. 6.6 underline that the choice of noSCF and fixed shift does not lead to larger deviations even at greater intermolecular separations. Even though this choice reduces the computational time by 25% compared to using fully self-consistent procedures on all levels, the remaining absolute time is still substantial. In particular, the slow distance decay of couplings for optically active singlets implies the necessity to determine transfer integrals for a number of chromophore dimers that is intractable for any first-principles based technique such as *GW*-BSE-DIPRO.

The setup of the dimer *GW*-BSE Hamiltonian matrix takes up a significant amount



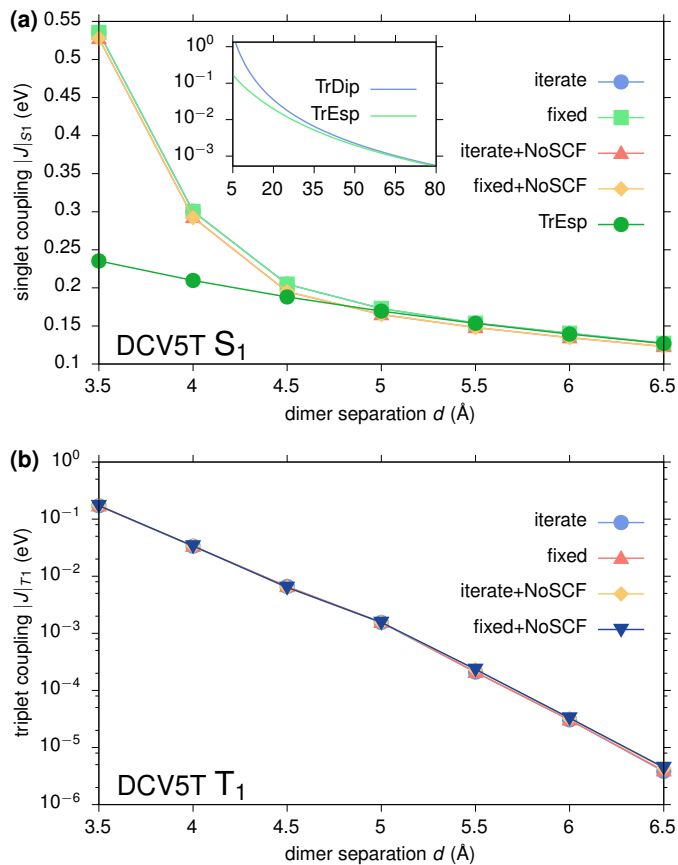


Figure 6.6: Comparison of the effect of different approximations on the distance dependence of triplet (a) and singlet (b) couplings in DCV5T. Inset in (a) shows additionally estimates from transition partial charges and transition dipole interactions for very long distances.

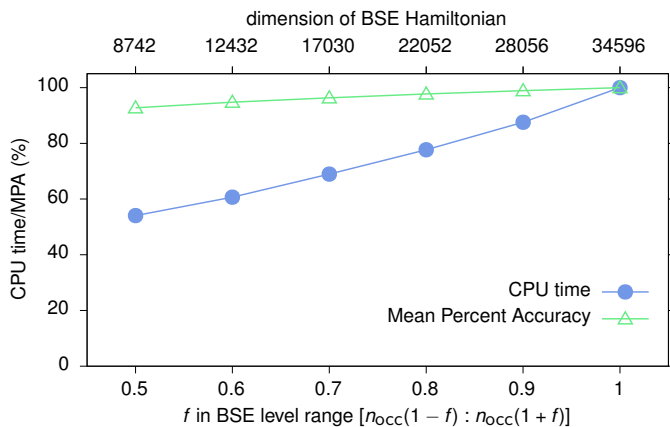


Figure 6.7: Relative reduction of computation time of the *GW*-BSE calculation (excluding the DFT part) for the DCV5T singlet coupling. Couplings were calculated for 5 distances and the relative errors with respect to the high dimension BSE result averaged.

of the total computer time when applied to larger molecules. All calculations in this chapter used all  $n_{\text{occ}}$  occupied and as many virtual single-particle levels in the construction of the product basis for the dimer. With  $n_{\text{occ}} = 186$  for DCV5T, this corresponds to a matrix of dimension 34569. Naturally, calculations can be accelerated by reducing the number of single particle states taken into account in this step. Using several values of the factor  $f$  to set the range single particle states considered to  $[n_{\text{occ}}(1-f) : n_{\text{occ}}(1+f)]$ , the relative reduction in computational time and relative deviation of singlet couplings is evaluated. As depicted in Fig. 6.7, reducing  $f$  to 0.5 approximately halves the computational cost, while only a 8% decrease in accuracy is observed.

Furthermore, it can be assumed, that beyond some distance, the long-ranged couplings are given as classical Coulomb interactions of transitions densities of the constituent chromophores. It is convenient to map the full transition density to a set of atomic partial charges that reproduce its electrostatic potential [213, 214] via e.g. the CHELPG method described in sec. 4.2.3. Such a classical model allows the computation of many thousands excitonic transfer integrals per minute using:

$$J_{AB}^{\text{TrEsp}} = \sum_{a \in A} \sum_{b \in B} \frac{q_a q_b}{|\mathbf{r}_a - \mathbf{r}_b|}, \quad (6.26)$$

where  $J_{AB}^{\text{TrEsp}}$  is the coupling between molecule  $A$  and  $B$  and  $\{q_a\}$  and  $\{q_b\}$  are the respective sets of atomic partial charges for the transition densities. As can be seen in Fig. 6.6(b) the results from this TrESP approach agree well with the  $GW$ -BSE-DIPRO couplings beyond a separation of  $5 \text{ \AA}$ , a typical distance at which intermolecular exchange effects can be expected to be negligible relative to the Coulomb interactions of large transition densities. The inset shows a comparison between classical interactions of transition charges with those of transition dipoles (TrDip), a coarser and often employed representation of transition densities. At a distance of  $5 \text{ \AA}$ , the dipole coupling overestimates the TrESP and  $GW$ -BSE-DIPRO results by one order of magnitude. Practical agreement can only be observed for separations larger than  $60 \text{ \AA}$ , casting doubts about the use of the TrDip approximation for intermediate distances.

## 6.4 Summary

In this chapter we derived a general approach to determine orientation and distance-dependent effective intermolecular exciton transfer integrals from quantum many-body Green's functions theory within the  $GW$  approximation and the Bethe-Salpeter Equation (BSE). A projection technique is employed to obtain the excitonic coupling by forming the expectation value of a supramolecular BSE Hamiltonian with electron-hole wave functions for excitations localized on two separated chromophores. Within this approach effects of coupling mediated by intermolecular charge transfer (CT) excitations are accounted for via a reduction technique that proves to be applicable to situation in which conventional perturbative approaches break down.

Application to model dimers reveals an accurate description of short-range exchange and long-range Coulomb interactions for the coupling of singlet and triplet excitons by this  $GW$ -BSE-DIPRO technique. An optimal strategy for simulations of full large-scale morphologies includes a combination of loosening of self-consistency parameters, reduction of the active space in  $GW$ -BSE, and, for optically active singlets, a change to classical transition density-based interaction models at larger distances. The strategies to evaluate the electronic couplings will be used to calculate couplings in a large scale morphology.



# Chapter 7

## Exciton dynamics in DCV5T

In this chapter we will investigate the singlet and triplet exciton dynamics in an organic crystal as a prototypical example of exciton transport. The material investigated is DCV5T-Me(3,3), a dicyanovinyl end-capped oligothiophene used as donor material in state-of-the-art organic solar cells [147]. To simulate exciton trajectories we will use the rate approach outlined in Chapter 4 with parameters calculated from *GW*-BSE calculations. As explained in Chapter 2, the diffusion of excitons towards the donor-acceptor heterojunction is the first step in the generation of free charge carriers in an organic solar cell. A better understanding of exciton diffusion and decay is paramount for the design of more efficient organic solar cells. The efficiency of triplet vs singlet transport is still debated, as singlets due to the long-ranged coupling move much faster but also decay quickly to the ground state via radiative recombination, limiting their diffusion length [13, 215].

Rate based models for exciton transport have already been studied by various groups [33, 34, 107, 215]. Most studies have focused on singlet transport, as electronic couplings can be approximated by transition dipole coupling [201]. In Chapter 6 we showed, however, that Dexter transfer, which is not captured by transition dipole coupling, increases the coupling by more than a factor of two at short separations. Such a strong singlet coupling can also lead to a breakdown of the assumptions underlying the Marcus rate. In our multiscale framework we explore if the strong coupling and the breakdown of the Marcus rate have a meaningful impact on the obtained diffusion lengths.

Furthermore, rate models had so far only been used for excitons on relatively small (400 molecule) [34, 107] systems, which limits the distance over which singlet excitons can be transferred. In contrast, the system studied in this chapter is four times as large and allows us to evaluate the importance of long-ranged singlet couplings compared to next-neighbor interaction for singlet diffusion lengths.

Next to the increase in computing power, the increase in system size was possible due to the usage of an efficient *GW*-BSE implementation, which allows us to treat singlet and triplet couplings on an identical footing and compare their diffusion lengths, to use larger basis sets than formerly used<sup>1</sup>, and use only one method for the calculation of all relevant values.

Finally, we explore the influence of energetic disorder due to internal vibrations and chemical environment on the exciton diffusion length and discuss the proper protocol for its inclusion in the rate equations.

Before we answer these questions, we detail the multiscale workflow, that was already sketched in Chapter 4, and present the intermediate results, which enter the rate equations.

## 7.1 Multiscale workflow

The workflow of the calculation is outlined in Fig. 7.1. Using crystal structure data, initial morphologies are generated from classical molecular dynamics (MD) simulations. The ensemble of molecules is then partitioned into segments. To establish which segments are within a certain distance from to each other, a neighbor search for each segment is performed and the resulting pairs are stored.

For triplets this is analogous to the procedure for charge transport [92], as the electronic coupling decays exponentially with distance, as described in the previous chapter. Singlets due to their long-ranged coupling can hop to more distant molecules, requiring larger cutoffs and consequently a lot more excitonic couplings have to be evaluated (see Fig. 7.2). As the coupling beyond the first neighbor shell is dominated by Förster like transition density coupling, we use a split approach, calculating the short ranged couplings explicitly using the *GW*-BSE-DIPRO method explained in Chapter 6 and the long ranged singlet couplings using the

---

<sup>1</sup>now: ubecppol+pseudo potentials,962 functions for DCV5T for 186 valence electrons vs before: def2-SVP,646 basis function for 304 electrons

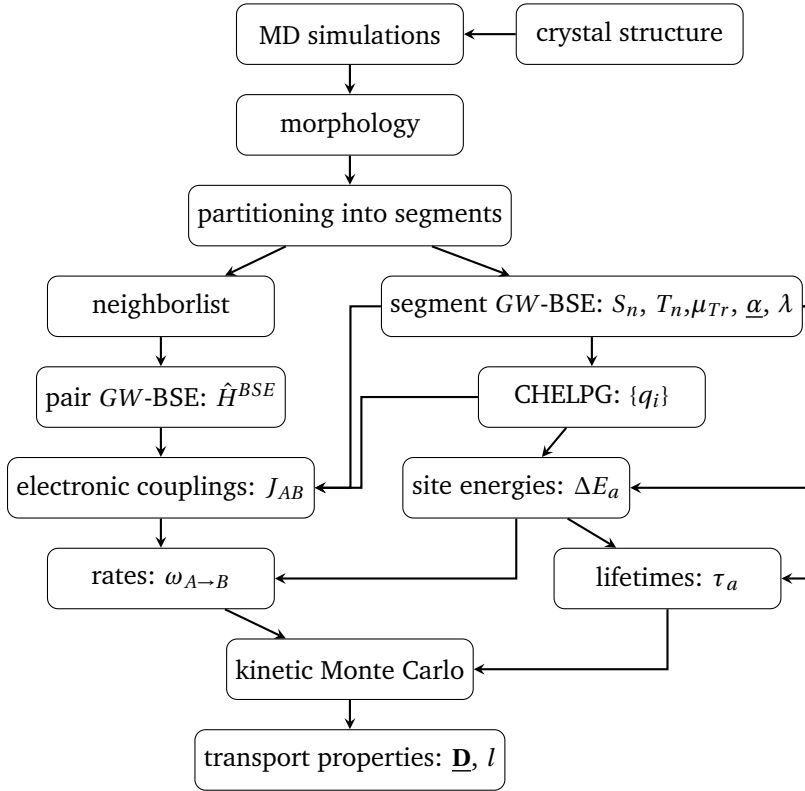


Figure 7.1: Exciton diffusion workflow as implemented in the VOTCA-XTP package.

TrEsp method [216, 217] with CHELPG [218] derived partial charges  $\{q_i\}$  from *GW*-BSE transition densities.

For each segment a *GW*-BSE calculation is performed, from which the excitation energies  $\Omega_{S_1}, \Omega_{T_1}$ , the partial charges  $\{q_i\}$  for TrEsp and the monomer orbitals for *GW*-BSE-DIPRO are used. For each pair within the first shell in Fig. 7.2 then another *GW*-BSE calculation has to be performed to obtain the dimer Hamiltonian  $\hat{H}^D$ . As each dimer calculation has roughly  $2N$  basis functions with  $N$  the number of basis functions of a monomer, the dimer calculations take  $(2N)^4 = 16$  times longer<sup>2</sup>, making the calculation of  $J_{AB}$  the bottleneck of these computations. The

<sup>2</sup>It scales only  $(2N)^4$  and not as  $(2N)^5$ , as  $\hat{H}^D$  only has to be constructed and not diagonalized, so the  $N^4$  scaling of the RPA in *GW* is the most expensive part.

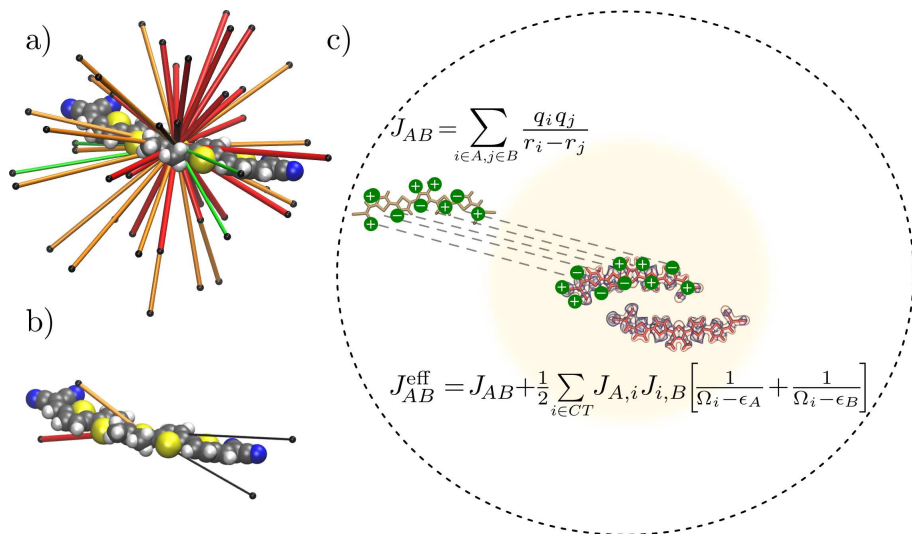


Figure 7.2: Exciton coupling for (a) singlets and (b) triplets. In both cases couplings with  $|J_{AB}| > 10^{-4}$  eV are represented as tubes. (c) Schematic representation of the double cutoff used in VOTCA-XTP. For short ranged couplings the quantum mechanical *GW-BSE-DIPRO* method is used. Long distance couplings are approximated using the *TrEsp* method.

evaluation of one dimer coupling takes roughly 40 min on a 4 core CPU as has been shown in Tab. 6.3 of Chapter 6. The same computation time is more than enough to evaluate all 370000 long-ranged couplings on one core.

The polarizability tensor  $\underline{\alpha}$  and the reorganization energy  $\lambda$  are only calculated once for an optimized geometry and assumed to be valid for all molecules. From the polarizabilities and partial charges the site energies  $\Delta E_a$  are calculated using classical cutoff or aperiodic embedding techniques [121].

From the electronic couplings  $J_{AB}$ , the site energies and the reorganization energies, the Marcus rates  $\omega_{A \rightarrow B}$  are calculated via eq. 4.26. Finally kinetic Monte Carlo (KMC) simulations are performed from which the macroscopic diffusion tensor can be extracted. For the case of singlet dynamics this poses two challenges. Firstly, due to the long range nature of the coupling, the connected graph is very dense. It will need a large amount of KMC runs to adequately sample all possible transition pathways to obtain converged results. Secondly, singlets can undergo fluorescent decay into the ground state and may decay quickly, even before the diffusive regime



of transport has been reached. The radiative decay time  $\tau_{\text{rad}}$  for a singlet state  $S$ , is given by Einstein's formula for spontaneous emission [219]:

$$\tau_{\text{rad}}^{-1} = \sqrt{\varepsilon} \frac{4\alpha\Omega_S^3}{3c^2\hbar^3} \mu_{Tr}^2, \quad (7.1)$$

where  $\varepsilon$  is the dielectric constant of the material,  $\alpha$  the fine structure constant,  $\Omega_S$  the excitation energy, and  $\mu_{Tr}$  the transition dipole moment of the transition. Therefore we can also define a decay rate  $\omega_{\text{decay}} \approx \tau_{\text{rad}}^{-1}$  and explicitly include exciton decay in the KMC simulations, allowing us to extract the distance excitons travel before decaying. Although we neglect non-radiative decay, due to the difficulties of calculating electron-phonon interaction, the radiative decay serves as a lower bound for the full decay rate:

$$\tau_{\text{decay}}^{-1} = \tau_{\text{rad}}^{-1} + \tau_{\text{nonrad}}^{-1} > \tau_{\text{rad}}^{-1}. \quad (7.2)$$

## 7.2 Morphology

For a demonstration of multiscale exciton transport simulations, a crystalline structure of DCV5T-Me<sub>3</sub> was chosen, which is a donor material in highly efficient (at some point record-holding) organic solar cells [146, 147]. From experimentally available X-ray data [146] a super cell containing 1568 DCV5T-Me(3,3) molecules was created as an initial structure. Different views on an orthogonal unit cell, containing 4 molecules can be seen in Fig. 7.3. To introduce thermal disorder to the morphology, MD simulations were performed with the force field taken from *Schrader et al* [145] at 300 K and 1 bar using a stochastic velocity rescaling thermostat [96] and a Berendsen barostat and run for 1.5 ns. For the electronic structure simulations six snapshots in 20 ps intervals were taken beginning at 1.320 ns, which we will refer to as snapshots 1 to 6.

For the rate-based model, each DCV5T molecule was mapped onto a single segment, resulting in 1568 segments. In order to generate pairs for the electronic coupling calculations, a neighbor search was performed, in which all molecules with a minimal separation of 0.6 nm or less are included as quantum mechanically interacting pairs. This resulted in about 6000 couplings per snapshot and roughly  $6000 \cdot 2 / 1568 \approx 8$  neighbors per molecule. For the singlet couplings, as depicted in Fig. 7.2, a second neighbor search with a cutoff of 3.5 nm was performed, yielding approximately 366000 long ranged couplings. On average each singlet has

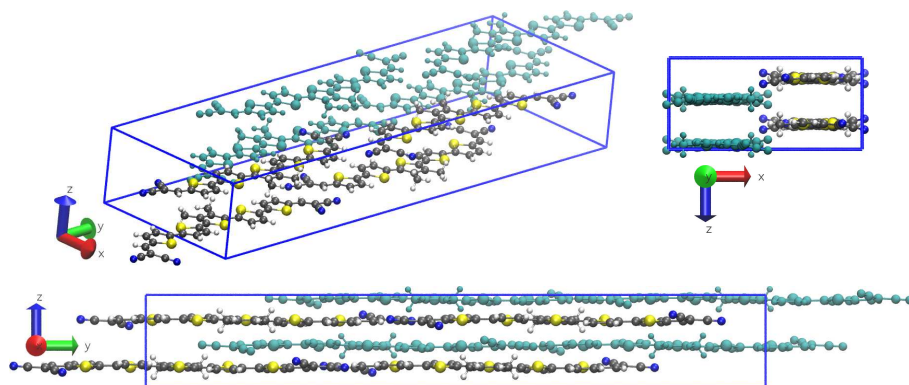


Figure 7.3: Crystal structure of DCV5T-Me(3,3), taken from [146].

about  $372000 \cdot 2 / 1568 \approx 470$  other segments to hop to. Although even at a separation of 3.5 nm the couplings for an optimal molecular alignment are at  $J_{AB} = 5 \cdot 10^{-2}$  eV, see inset in Fig. 6.6(b) of Chapter 6, but any larger cutoff would have exceeded the super cell dimensions.

### 7.3 Reorganization energies and polarization

The reorganization energies for the  $T_1$  and  $S_1$  were obtained from structural optimizations using *evGW*-BSE on PBE/*ubecppol* DFT ground state calculations. As currently analytic gradients are not available in VOTCA-XTP, numerical gradients in conjunction with a BFGS trust-region optimizer in cartesian coordinates was used [220]. To keep the number of numerical gradient evaluations tractable, geometries were pre-optimized on TDDFT level using the same basis set and functional with the Gaussian package [221]. The reorganization energies were evaluated using equation eq. 4.48 yielding  $\lambda_S = 0.37$  eV for singlets and  $\lambda_T = 0.77$  eV for triplets. Noticeable is the large reorganization energy for the triplet, in comparison to the hole reorganization energy  $\lambda_e = 0.22$  eV [222]. Stehr and Lunkenheimer reported similar high reorganization energies for other organic compounds, e.g.,  $\lambda_S = 0.351$  eV for the  $S_1$  state of naphthalene (SCS-CC2@cc-pVDZ) [91] and  $\lambda_T = 0.748$  eV for the  $T_1$  state of Alq<sub>3</sub> (ADC(2)@SVP) [107].

Electronic polarizabilities, needed for the inclusion of environment polarization ef-

Table 7.1: Polarizability tensors  $\underline{\alpha}$  for the ground state  $N$ , first singlet state  $S_1$  and first triplet state  $T_1$  for the DCV5T-Me(3,3) molecule (see app. A. The  $y$  coordinate runs along the backbone of segments and the  $z$ -direction is normal to the plane of the molecule.

[Å <sup>3</sup> ]	$xx$	$yy$	$zz$	$xy$	$xz$	$yz$
$N$	76	293	34	0	0	-1
$S_1$	74	1022	27	-5	-3	1
$T_1$	70	646	33	-2	-2	-7

fects in the site energy evaluations, were computed using the same evGW-BSE on PBE/ubecppol combination on the respective optimized geometries. The results are given in Tab. 7.1 for the ground state  $N$ , and the excited states  $S_1$  and  $T_1$ , respectively. As in the case of the geometry optimization, numerical gradients were used to calculate polarizabilities for excited and ground state<sup>3</sup>. Compared to the ground state, both excited states have approximately the same polarizability perpendicular to the backbone of the molecule and much elevated polarizabilities along the conjugated backbone. Partial charges for the classical treatment of the electrostatic interaction were calculated from the optimized geometries using CHELPG [218].

## 7.4 Site energies and lifetimes

Electrostatic site energy contributions,  $\Delta E_S$ , were obtained from a cut-off based scheme [92] using 3 nm and 6 nm for MM0 and MM1 respectively (see Fig. 5.12 in Chapter 5). For the electrostatics, cutoffs in excess of half the box dimension are allowed because the outer non polarizable sphere mostly exists to balance the polarizable volume and the influence of individual distant molecules is diluted by the large amount of molecules.

A second contribution to the site energies can arise from internal, quantum mechanical details of the molecules, i.e., the adiabatic excitation energy which reads  $\Delta E_{\text{int},a} = U_a^1(\xi_1) - U_a^0(\xi_0)$  (compare eq. 4.33). This quantity is in charge transport simulations typically assumed to be much smaller than the electrostatic disor-

<sup>3</sup>The numerical ground state polarizabilities were checked against analytically obtained results to check for convergence

Table 7.2: Standard deviation  $\sigma$  for electrostatic site energies  $\Delta E_{\text{el}}$  and internal site energy  $\Delta E_{\text{int}}$  for singlets and triplets in eV for all snapshots

	$\sigma(\Delta E_{\text{el}}^S)$	$\sigma(\Delta E_{\text{int}}^S)$	$\sigma(\Delta E_{\text{el}}^S + \Delta E_{\text{int}}^S)$	$\sigma(\Delta E_{\text{el}}^T)$	$\sigma(\Delta E_{\text{int}}^T)$	$\sigma(\Delta E_{\text{el}}^T + \Delta E_{\text{int}}^T)$
1	0.077	0.109	0.133	0.045	0.114	0.122
2	0.076	0.106	0.133	0.044	0.116	0.127
3	0.074	0.109	0.131	0.043	0.116	0.124
4	0.076	0.108	0.131	0.044	0.117	0.127
5	0.079	0.108	0.131	0.046	0.116	0.125
6	0.076	0.112	0.139	0.044	0.118	0.129

der [92]. An exact treatment is computationally extremely demanding, as it requires an excited state geometry optimization to obtain  $U_a^1(\xi_1)$  for each molecule  $a$  in its respective, unique molecular environment.

Instead, in the following we make a few simplifying assumptions: First, since the system under study only contains a single molecular species, we are not interested in evaluating the adiabatic energies on an absolute scale, but only the differences between two molecules  $a$  and  $b$ , i.e.,  $\Delta(\Delta E_{\text{int}})_{ab}$ . Furthermore, the adiabatic excitation energy of molecule  $a$  is related to the vertical excitation energy by the reorganization energy, i.e.,  $U_a^1(\xi_1^a) - U_a^0(\xi_0^a) = U_a^1(\xi_0^a) - \lambda_a - U_a^0(\xi_0^a)$ . We adopt the same approximation as in the previous section, and set the reorganization energy to be identical for all molecules. With this, we obtain:

$$\begin{aligned}
 \Delta(\Delta E_{\text{int}})_{ab} &= U_a^1(\xi_1^a) - U_a^0(\xi_0^a) - (U_b^1(\xi_1^b) - U_b^0(\xi_0^b)) \\
 &\approx U_a^1(\xi_0^a) - U_a^0(\xi_0^a) - \lambda - (U_b^1(\xi_0^b) - U_b^0(\xi_0^b) - \lambda) \\
 &= U_a^1(\xi_0^a) - U_a^0(\xi_0^a) - (U_b^0(\xi_1^b) - U_b^0(\xi_0^b)) = \Omega_a^1 - \Omega_b^1.
 \end{aligned} \tag{7.3}$$

The standard deviations of the site energy distributions and their individual contributions for all six evaluated snapshots are given in Tab. 7.2. The electrostatic site energy distributions show a considerably smaller disorder for singlets,  $\langle \Delta E_{\text{el}}^S \rangle = 0.076$  eV and triplets  $\langle \Delta E_{\text{el}}^T \rangle = 0.044$  eV, compared to 0.1 eV for electrons and holes [120]. This is not surprising, as the excitons are uncharged excitations. The difference between the electrostatic disorder can be partially rationalized by looking at the dipole moments:  $d^{S1} = 0.27$  e · nm vs  $d^{T1} = 0.25$  e · nm. Additionally, the  $S_1$  state has a 20% larger quadrupole moment ( $\Theta_{S1}^{yy} = 1.45$  e · nm<sup>2</sup> vs  $\Theta_{T1}^{yy} = 1.20$  e · nm<sup>2</sup>).

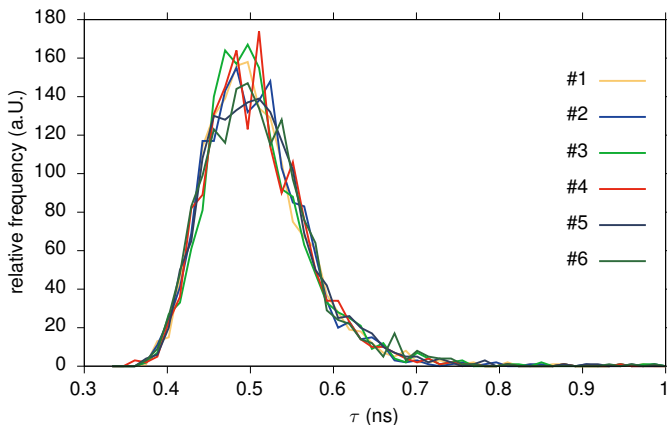


Figure 7.4: Distribution of decay times for singlet excitons in DCV5T

These effects cannot be fully compensated by the larger polarizability of the  $S_1$  state (see Tab. 7.1). In comparison to the electrostatic contribution, the internal site energy distribution is substantially wider for both singlets  $\langle \Delta E_{\text{int}}^S \rangle = 0.109 \text{ eV}$  and triplets  $\langle \Delta E_{\text{int}}^T \rangle = 0.116 \text{ eV}$ . Furthermore, the two individual contributions are mostly uncorrelated, as  $\sigma(\Delta E_{\text{el}} + \Delta E_{\text{int}}) \approx \sqrt{\sigma(\Delta E_{\text{el}})^2 + \sigma(\Delta E_{\text{int}})^2}$ . The corresponding histograms can be found in appendix A.

As mentioned before, in electron or hole transport simulations, the internal site energy contribution can typically be neglected [222], as electrostatic disorder is larger for charged excitations. The breakdown of this assumption is problematic for exciton transfer, as the concept of the rate based models assumes that a distinction between slow degrees, responsible for the static disorder, and fast degrees of freedom, responsible for exciton transfer, can be made. Although the earlier mentioned mapping procedure should eliminate the fast degrees of freedom, parts of residual fast degrees could be responsible for the large internal site energies. A more in-depth study of these problems is outside the scope of this thesis. We so choose to run KMC simulation once with and without internal site energy contributions, as a lower and upper bound on the expected result.

For the calculation of singlet decay rates via eq. 7.1,  $\mu_S$  and  $\Omega_S$  were obtained from individual monomer  $GW$ -BSE calculations, which were required for the  $GW$ -BSE-DIPRO couplings (compare Chapter 6) to be discussed in the following section. Apart from the excitation energy and transition dipole, the lifetimes also depend

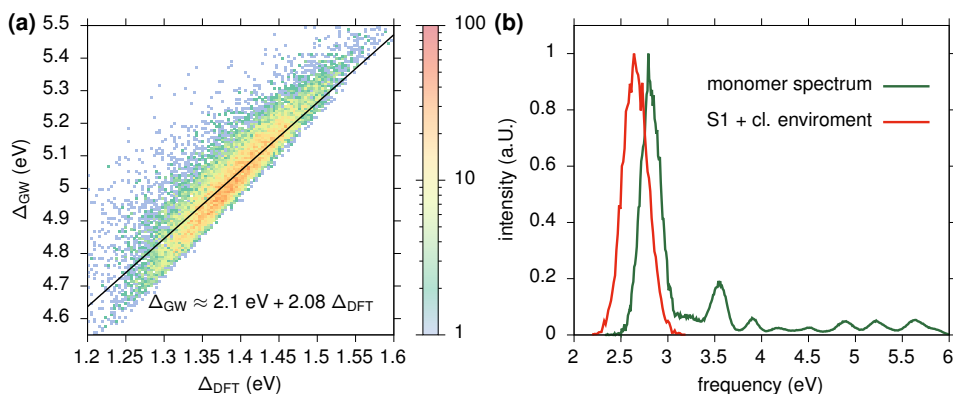


Figure 7.5: (a) Correlation between DFT and GW corrected HOMO-LUMO gaps for all 1568 DCV5T molecules in all different snapshots. The black line defines a linear fit. (b) Corresponding spectrum for singlets. Each frequency was weighted by the respective oscillator strength. The red curve indicates the S1 peak, which was corrected by the respective electrostatic and polarization interaction, analogous to Fig. 4.4(d)

on the relative dielectric constant of the material. As the exact dielectric constant of DCV5T has not been measured to our knowledge, we assume  $\epsilon \approx 3$ , which is a typical value for organic materials [23]. Note that we have included electrostatic corrections to the excitation energies. The obtained singlet lifetimes are shown in Fig. 7.4. Its average is nearly constant for all snapshots with  $\tau_{\text{rad}} = 0.5\text{ ns}$ . To our knowledge there are no singlet lifetime measurement on DCV5T, but our value is comparable to other reported singlet exciton lifetimes<sup>4</sup> [13, 28].

The results of these monomer *GW*-BSE-DIPRO calculations can additionally be analyzed in different contexts. In figure 7.5(a), we show the analysis of the influence of the *GW* approximation on the HOMO-LUMO gap. As stated in previous chapters, the *GW* approximation opens the gap in a non-trivial manner. Larger DFT HOMO-LUMO gaps are opened further due to the smaller RPA screening response (eq. 5.14), leading to a larger self-energy operator  $\Sigma$  (eq. 5.18). Figure 7.5(b) shows in more detail the distribution of absorption energies as superposition of individual vacuum monomer spectra (green curve) and only the main peak after inclusion of environment effects (red curve) as defined by eq. 4.40. The resulting redshift of

<sup>4</sup>2,5-dihexyl-3,6-bis[4-(5-hexylthiophene-2-yl)phenyl]-pyrrolo[3,4-c]-pyrrole-1,4-dione: 0.4 ns 2,5-dihexyl-3,6-bis[4-(5-hexyl-2,2'-bithiophene-5-yl)-phenyl]pyrrolo[3,4-c]-pyrrole-1,4-dione: 2.0 ns

the  $S_1$  peak amounts to 0.15 eV.

## 7.5 Electronic couplings

Electronic couplings were calculated using the perturbation method outlined in the previous chapter. Short ranged couplings were computed with the *GW*-BSE-DIPRO method, whereas the long ranged couplings were evaluated via TrEsp, with partial charges obtained from *GW*-BSE calculations on individual segments.

Figure 7.6(a) shows the distribution of singlet couplings. The distributions for different snapshots show nearly perfect agreement with each other. In Fig. 7.6(b) the distribution of couplings for the first snapshot is displayed separately for *GW*-BSE-DIPRO and TrEsp couplings. The *GW*-BSE-DIPRO couplings show a median of  $\langle J \rangle = 0.044$  eV, which is significantly smaller than the reorganization energy  $\lambda_S = 0.37$  eV. Thus, in general, a hopping-like transport mechanism seems valid a posteriori. However, there are also a number of couplings, which exceed this value significantly. Their effect on the exciton dynamics will be discussed later.

It is noteworthy that, on average, the singlet coupling elements are 2-3 orders of magnitude higher than electron or hole ones [145], which is a result of the long ranged exchange interaction. This can also be seen from Fig. 7.6(d), which spatially resolves the distribution of couplings. The red “islands”, marking high concentrations of couplings corresponding to different crystal directions and distances, clearly show a non-exponential decay as would be characteristic for exchange interaction. The influence of thermal fluctuations can also be clearly seen from the size of the islands, as in a perfect crystal all couplings would collapse towards the centers of the islands.

Triplet couplings, depicted in Fig. 7.6(e) exhibit larger fluctuations, which is a result of the geometrically more sensitive short ranged transfer, which relies on molecular overlap. Consequently, the median coupling  $\langle J \rangle = 7.4 \cdot 10^{-5}$  eV is lower and much smaller than the reorganization energy  $\lambda_T = 0.77$  eV. Figure 7.6(f) shows the distance resolved distribution of triplet couplings. The quick decay of the couplings with distance is in good agreement with the results from Fig. 6.6(a) in Chapter 6.

As discussed in the previous chapter, electronic coupling elements can be significantly influenced by the nature of intermediate CT states, which can in certain molecular configurations lie energetically very close to the localized FE states.

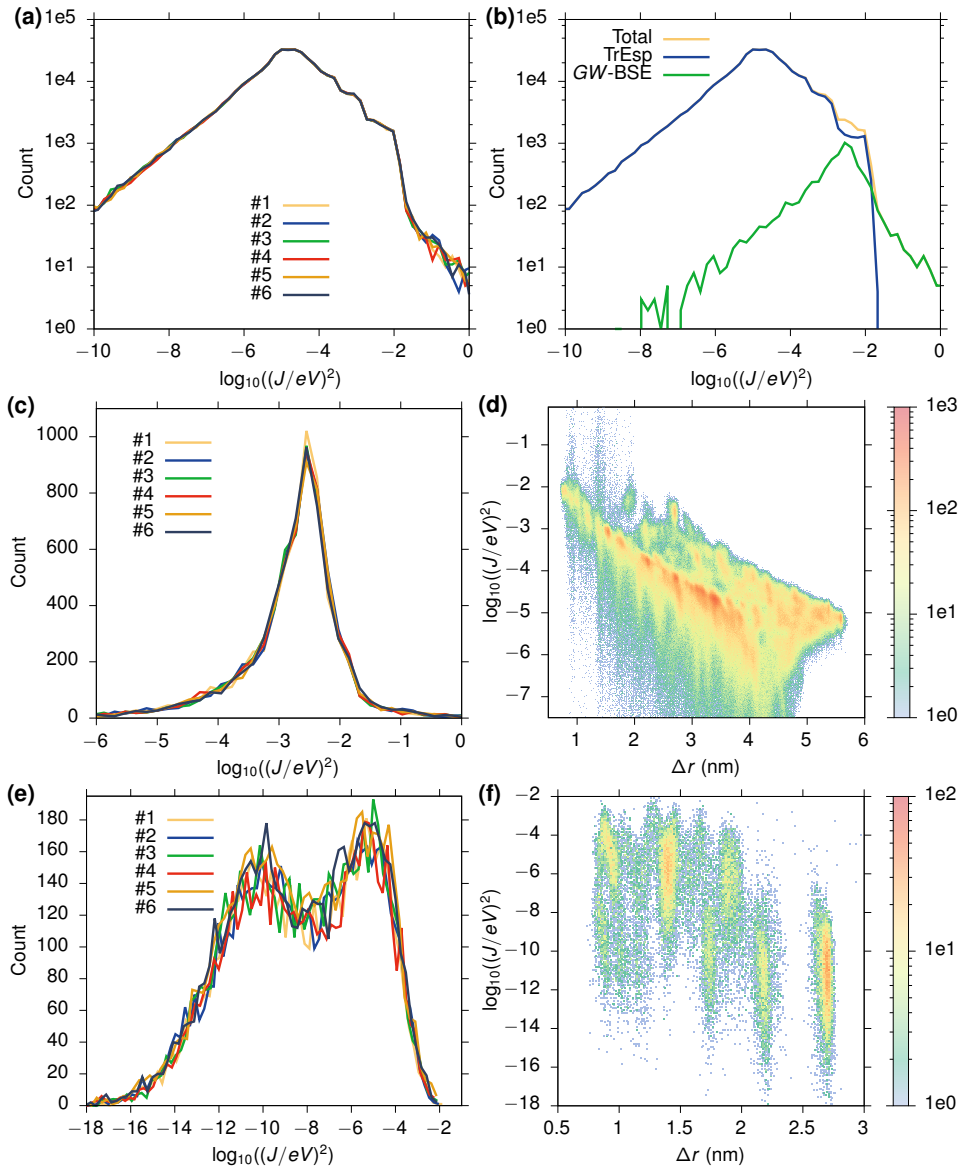


Figure 7.6: (a) Distributions of singlet couplings. (b) Separation in short ranged GW-BSE-DIPRO and long ranged TrEsp couplings for first snapshot. (c) Distributions of GW-BSE-DIPRO couplings for singlets. (d) Distribution of singlet couplings, depending on pair distance including all snapshots. (e) Distributions of triplet couplings. (f) Distribution of triplet couplings, depending on pair distance including all snapshots.



Closer inspection of the results discussed above reveals that the a situation like this is present for a small number of states.

The projection method corrects for this situation by splitting the CT-contribution symmetrically among both FE states via the Löwdin orthogonalization. The same problem arises in perturbation theory, if the effective FE state is expanded to higher orders than the first (eq. 6.19), which creates non-orthogonal pseudo diabatic states. It then requires an orthogonalization equivalent to the projection method.

Additionally, the perturbative approach faces a problem with low lying CT-states close to the FE states, as the denominator in eq. 6.20 approaches zero. Resulting 'resonant' couplings larger than 0.2 eV were found for about 1 – 2% of the singlet transfers calculated via *GW*-BSE-DIPRO (see Fig. 7.6(b)). Lower lying triplet states were not affected, as only singlet states with their higher excitation energies come close to the respective CT-state energies.

The resulting high couplings indicate that the assumption of single molecule localized excitons might not always be strictly valid. Instead in these configurations, an exciton is likely to delocalize over the dimer and, consequently, rather the whole dimer should be regarded as one segment. At the moment this is however beyond the capabilities of our model. The resulting large coupling constants were taken at face value and their effect on singlet transport properties are later shown to be within the errors of the method.

If only singlet properties are of interest, a further possible approximation comprises replacing *GW*-BSE-DIPRO by TrEsp couplings even for next-neighbor couplings. Figure 7.7(a) shows the coupling distributions of both approaches. The *GW*-BSE-DIPRO approach yields significantly more couplings above 0.1 eV, while the major peak position is in good agreement for both variants. The correlation plot in Fig. 7.7(b) shows that the majority of couplings agree well. The systematic slight underestimate along the diagonal is probably a result the multipole expansion of the transition density in the TrEsp method and the neglect of overlap effects. The outliers result from the short ranged overlap effects, which can, depending on the value of the FE-CT coupling, give a positive or negative contribution (see eq. 6.20). To assess the influence of replacing *GW*-BSE-DIPRO singlet couplings with TrEsp couplings kinetic Monte-Carlo simulations were performed, which are discussed in the next section.

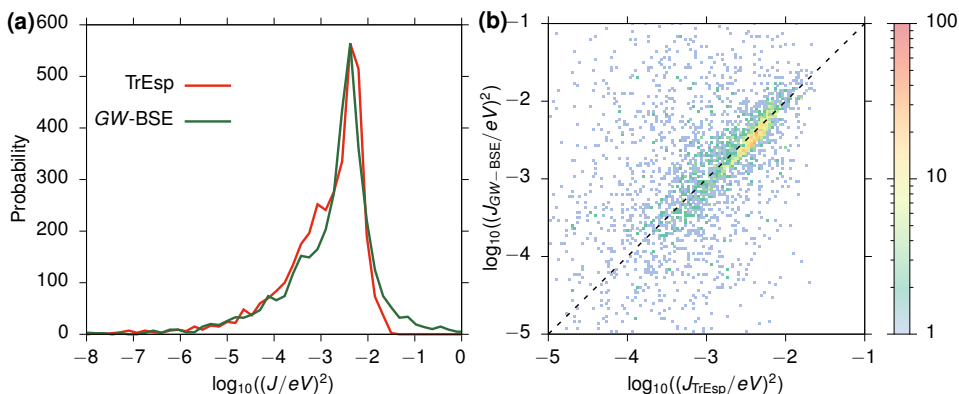


Figure 7.7: (a) Distribution of singlet couplings for the GW-BSE-DIPRO and TrEsp methods for one snapshot. (b) Correlation plot of both methods. The dashed line indicates a 1:1 agreement.

## 7.6 Kinetic Monte-Carlo simulations

In order to solve the Master equation eq. 4.50 for singlets and triplets, we use kinetic Monte-Carlo simulations. In the case of triplets, 20 Monte Carlo simulations were run for each snapshot, with on average  $9 \cdot 10^{11}$  steps, equating to around 700 s of simulation time. The diffusion tensor is calculated via eq. 4.51 and the corresponding results are displayed in Tab. 7.3 and Tab. 7.4 for the simulations without internal site energies and with internal site energies, respectively.

For the case without internal site energies, the diffusion tensor exhibits strong anisotropy with diffusion along the  $y$ -axis (molecule axis) one order of magnitude larger than along the  $z$  (stacking direction) and two orders of magnitude larger than diffusion along the  $x$  axis. As here the energetic disorder is comparatively small (see Tab. 7.2) and reorganization energies are assumed to be all identical for all molecules, the transport properties are governed by the electronic couplings. Comparing with Fig. 7.2(b) and Fig. 7.3 illustrates that the strongest coupling between molecules is present in the  $y-z$  plane with  $z$  being the stacking direction. Due to shift of neighboring molecules along the  $y$ -axis, the displacement for each jump is about three times larger along the  $y$ -axis than the  $z$ -axis ( $\langle \Delta y \rangle = 1.18$  nm vs  $\langle \Delta z \rangle = 0.37$  nm). To arrive at a rough estimate for the diffusion length we assume that the triplet lifetime is roughly  $\tau_T \approx 1 \cdot 10^{-3}$  s, as triplet lifetimes typically six magnitudes larger than the respective singlet lifetimes[13]. The diffusion length is

Table 7.3: Elements of the triplet diffusion tensors for all snapshots, obtained from kinetic Monte-Carlo simulations. Units are  $10^{-9} \text{ cm}^2/\text{s}$ . The last row gives the averages over all snapshots and runs.

#	$D_{xx}$	$D_{xy}$	$D_{xz}$	$D_{yy}$	$D_{yz}$	$D_{zz}$
1	$0.23 \pm 0.04$	$-0.17 \pm 0.83$	$0.04 \pm 0.23$	$79.52 \pm 29.67$	$-1.54 \pm 5.10$	$6.36 \pm 1.60$
2	$0.23 \pm 0.01$	$-0.39 \pm 0.51$	$0.04 \pm 0.15$	$35.88 \pm 7.65$	$0.63 \pm 1.43$	$3.02 \pm 0.40$
3	$1.33 \pm 0.14$	$-2.50 \pm 1.52$	$0.62 \pm 0.41$	$67.19 \pm 20.18$	$-1.13 \pm 2.66$	$4.38 \pm 0.75$
4	$0.54 \pm 0.06$	$1.07 \pm 0.92$	$0.24 \pm 0.37$	$48.57 \pm 12.37$	$-1.36 \pm 4.19$	$6.66 \pm 1.11$
5	$1.43 \pm 0.10$	$-0.56 \pm 1.49$	$0.20 \pm 0.51$	$41.98 \pm 6.88$	$-2.54 \pm 2.47$	$4.50 \pm 0.93$
6	$1.26 \pm 0.11$	$-0.04 \pm 1.51$	$0.09 \pm 0.58$	$52.39 \pm 16.01$	$4.81 \pm 4.08$	$6.72 \pm 1.15$
$\langle . \rangle$	$0.84 \pm 0.01$	$-0.43 \pm 0.05$	$0.21 \pm 0.02$	$54.26 \pm 0.66$	$-0.19 \pm 0.13$	$5.27 \pm 0.04$

Table 7.4: Elements of the triplet diffusion coefficients for all snapshots, obtained from kinetic Monte-Carlo simulations. Units are  $10^{-12} \text{ cm}^2/\text{s}$ . The last row gives the averages over all snapshots and runs. This results use external and internal site energies.

#	$D_{xx}$	$D_{xy}$	$D_{xz}$	$D_{yy}$	$D_{yz}$	$D_{zz}$
1	$0.76 \pm 0.09$	$7.26 \pm 1.27$	$5.97 \pm 0.46$	$101.6 \pm 22.8$	$57.96 \pm 9.19$	$55.35 \pm 4.49$
2	$7.94 \pm 0.18$	$-7.44 \pm 2.56$	$-1.35 \pm 0.38$	$26.98 \pm 6.95$	$2.80 \pm 0.91$	$0.76 \pm 0.14$
3	$0.62 \pm 0.10$	$-1.51 \pm 0.70$	$-0.51 \pm 0.24$	$27.14 \pm 5.31$	$1.27 \pm 1.87$	$2.88 \pm 0.53$
4	$6.81 \pm 0.18$	$18.63 \pm 1.80$	$16.36 \pm 0.33$	$59.92 \pm 10.72$	$44.03 \pm 3.70$	$40.40 \pm 1.87$
5	$7.75 \pm 0.33$	$-7.56 \pm 2.14$	$12.59 \pm 0.69$	$21.62 \pm 5.09$	$-12.77 \pm 3.64$	$21.13 \pm 1.61$
6	$0.05 \pm 0.00$	$-0.02 \pm 0.03$	$0.05 \pm 0.01$	$0.60 \pm 0.15$	$0.01 \pm 0.05$	$0.09 \pm 0.02$
$\langle . \rangle$	$3.99 \pm 0.03$	$1.56 \pm 0.10$	$5.52 \pm 0.06$	$39.64 \pm 0.49$	$15.55 \pm 0.27$	$20.10 \pm 0.19$

then for a system without (with) internal site energies:

$$l_T = \sqrt{\frac{1}{3} \text{Tr } \underline{\mathbf{D}} \cdot \tau_T} \approx 45 \text{ nm} (1.46 \text{ nm}), \quad (7.4)$$

with  $l_{T,x} \approx 9 \text{ nm} (0.63 \text{ nm})$ ,  $l_{T,y} \approx 74 \text{ nm} (1.99 \text{ nm})$  and  $l_{T,z} \approx 23 \text{ nm} (1.42 \text{ nm})$ . The large energetic disorder due to the inclusion of internal disorder leads to more than a tenfold decrease in diffusion length, while the anisotropy is preserved. This is not surprising, as the anisotropy is mostly governed by the couplings, which are independent of the energetic disorder.

Table 7.5: Singlet diffusion lengths, obtained from kinetic Monte-Carlo simulations using only the short-ranged couplings from *GW*-BSE-DIPRO and TrEsp method. For each configuration  $10^4$  singlet insertions are performed. Diffusion lengths are given in nm.

	$l_x$	$l_y$	$l_z$
<i>GW</i> -BSE-DIPRO	$5.95 \pm 0.06$	$37.14 \pm 0.38$	$2.82 \pm 0.03$
TrEsp	$6.18 \pm 0.06$	$38.84 \pm 0.39$	$2.20 \pm 0.02$

For singlet excitons the diffusion length was calculated without reference to the diffusion tensor by explicitly taking exciton decay into account. At each kinetic Monte-Carlo step the exciton can either hop or decay. Whenever an exciton decays, its traveled distance, as well as the site on which it decayed are recorded. Then a new exciton is randomly inserted onto a site.

First, the influence of the small number of nonphysically high couplings has to be addressed, which results from resonances between CT and Frenkel states in eq. 6.21. In order to assess the influence of these states, KMC simulations for singlets are performed using only the short ranged couplings. One set of simulations is run using couplings from eq. 6.21 and one set using TrEsp couplings. The resulting diffusion lengths are given in Tab. 7.5. All simulations for the evaluation of the couplings were performed using only the electrostatic site energies, as the lower disorder improves the convergence rate of the kinetic Monte-Carlo simulations.

The differences between both methods are below 5%, without taking the influence of the majority of long distance couplings into account. To study the influence of the long ranged coupling and the influence of the large short ranged elements, we calculated singlet diffusion lengths for four different configurations:

1. *GW*-BSE-DIPRO for the short-ranged couplings and TrEsp for the long-ranged coupling
2. TrEsp couplings for short and long ranged couplings
3. *GW*-BSE-DIPRO for short range with large coupling elements  $|J| > \lambda$  set to zero and TrEsp long ranged couplings.
4. Short ranged *GW*-BSE-DIPRO with long ranged TrEsp couplings screened by the dielectric constant  $J_{\text{scr.}} = J/\epsilon$ .  $\epsilon = 3$  is assumed to be consistent with the calculation of the exciton lifetimes (sec. 7.4).

Table 7.6: Singlet diffusion lengths, obtained from kinetic Monte-Carlo simulations using different versions of couplings from *GW-BSE-DIPRO* and *TrEsp* method. For each configuration  $10^4$  singlet insertions are performed. Diffusion lengths are given in nm. (sr and lr denote short range and long range, respectively)

	$l_x$	$l_y$	$l_z$
DIPRO(sr) + TrEsp(lr)	$46.55 \pm 0.48$	$89.65 \pm 0.91$	$39.84 \pm 0.40$
TrEsp(sr+lr)	$46.69 \pm 0.47$	$91.62 \pm 0.92$	$40.21 \pm 0.40$
DIPRO $_{ J >\lambda=0}$ (sr) + TrEsp(lr)	$46.87 \pm 0.46$	$87.56 \pm 0.88$	$40.48 \pm 0.40$
DIPRO(sr) + TrEsp $_{\epsilon}$ (lr)	$17.10 \pm 0.17$	$51.67 \pm 0.51$	$13.97 \pm 0.14$

The results displayed in Tab. 7.6 clearly show that the effect of the large couplings is irrelevant for the singlet diffusion. The long ranged couplings are critical to an accurate description of singlet diffusion, as the longer jumps contribute about 60% to the exciton diffusion length. Furthermore the long ranged couplings are responsible for a more isotropic transport, as they allow jumps into more directions (see Fig. 7.2(a)). Even the crude approximate screening of this long ranged couplings analogous to Stehr et al. [35] by division with the macroscopic dielectric constant leads to large reduction of the diffusion length. More sophisticated screening models exist, but so far rely on an energetic gap between the active material and screening environment as in the case of chromophores solvated in water [217]. This is not the case for a chemically homogeneous organic semiconductor such as DCV5T.

Finally to understand the influence of molecular motion on the exciton diffusion length, we ran KMC simulations on each snapshot. As variations now only arise due to the slightly different displacements of molecules and the changed distribution of site energies and couplings, we ran  $2 \cdot 10^6$  insertions for every snapshot. The results are displayed in Tab. 7.7 and Tab. 7.8 for the simulations without and with internal site energies, respectively.

The difference between diffusion lengths between the two approaches is roughly a factor of 4. The singlet diffusion is less affected by the energetic disorder than triplet diffusion, as each singlet has a much larger number of other sites it can jump to. Nonetheless, the deviations between individual snapshots are much more pronounced in the system with internal site energies taken into account. Only the third snapshot without internal site energies yielded starkly different results, which will be discussed in the following.

Table 7.7: Singlet diffusion lengths without internal site energies, obtained from kinetic Monte-Carlo simulations using short ranged *GW*-BSE-DIPRO and long ranged TrEsp method for all snapshots. For each snapshot a minimum of  $2 \cdot 10^6$  singlet insertions are performed. Diffusion lengths are given in nm. The last row contains the average value of the exciton diffusion length averaged over all snapshots.

#	$l_x$	$l_y$	$l_z$
1	$46.84 \pm 0.01$	$89.03 \pm 0.02$	$40.09 \pm 0.01$
2	$46.07 \pm 0.03$	$74.18 \pm 0.05$	$41.83 \pm 0.03$
3	$36.62 \pm 0.00$	$70.07 \pm 0.01$	$32.00 \pm 0.00$
4	$48.65 \pm 0.00$	$91.07 \pm 0.01$	$43.01 \pm 0.00$
5	$44.09 \pm 0.01$	$84.76 \pm 0.02$	$38.40 \pm 0.01$
6	$44.42 \pm 0.00$	$83.39 \pm 0.01$	$40.15 \pm 0.00$
$\langle \cdot \rangle$	$44.45 \pm 3.82$	$82.08 \pm 7.58$	$39.25 \pm 3.55$

Table 7.8: Singlet diffusion lengths with internal site energies, obtained from kinetic Monte-Carlo simulations using short ranged *GW*-BSE-DIPRO and long ranged TrEsp method for all snapshots. For each snapshot  $2 \cdot 10^6$  singlet insertions are performed. Diffusion lengths are given in nm. The last row contains the average value of the exciton diffusion length averaged over all snapshots.

#	$l_x$	$l_y$	$l_z$
1	$9.853 \pm 0.002$	$16.348 \pm 0.003$	$7.924 \pm 0.001$
2	$22.854 \pm 0.004$	$39.650 \pm 0.007$	$20.769 \pm 0.004$
3	$14.034 \pm 0.002$	$28.513 \pm 0.005$	$13.710 \pm 0.002$
4	$8.464 \pm 0.001$	$14.719 \pm 0.002$	$7.035 \pm 0.001$
5	$16.989 \pm 0.003$	$28.929 \pm 0.005$	$14.327 \pm 0.002$
6	$8.030 \pm 0.001$	$14.185 \pm 0.002$	$7.771 \pm 0.001$
$\langle \cdot \rangle$	$13.37 \pm 5.30$	$23.72 \pm 9.40$	$11.92 \pm 4.90$

In all snapshots, the histograms for decay times (Fig. 7.4), site energies (Fig. C.1), and electronic couplings (Fig. 7.6) show no relevant differences, which could explain this deviation.

Considering the simulated lifetimes of each individual singlet as in Fig. 7.8, we

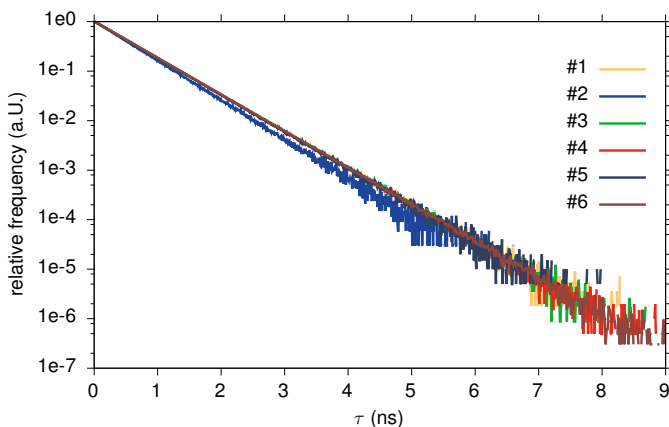


Figure 7.8: Distribution of lifetimes for singlet exciton in DCV5T for the system without internal site energies. The scale is logarithmic.

notice that they are nearly perfectly exponentially distributed for all snapshots, as they form straight lines in the logarithmic plot. This observation is quite surprising given the distribution of decay times in Fig. 7.4. A possible explanation is that the decay does not happen homogeneously on all sites but occurs on only a few of them. To gain a better understanding of this process, we recorded, for all simulations, the site on which the exciton decayed. The resulting normalized decay probability, as well as the decay times and site energies are given *per site* in Fig. 7.9. Note that the sites are indexed in increasing order of decay probability.

It is apparent that the decay probability (blue line) exhibits a nearly exponential increase. Most excitons decay on only a very small subset of sites which, as indicated by the green line, are sites with very low energies. The yellow line, indicating the *intrinsic* decay time  $\tau_i$  on each site, shows actually a modest increase in decay time, i.e., excitons live longer on these sites. Exciton diffusion length in this case thus does not appear to be limited by sites with short decay times, where excitons nearly instantaneously decay. A better measure is the relative decay probability  $\tilde{\tau}_i^{-1}$ , defined as:

$$\tilde{\tau}_i^{-1} = \frac{\tau_i^{-1}}{\sum_j \omega_{ij} + \tau_i^{-1}}, \quad (7.5)$$

where  $\omega_{ij}$  is the rate of jumping from site  $i$  to site  $j$ . The relative decay probability is the likelihood of an exciton decaying in the next KMC step instead of hopping to another site. For most snapshots  $\tilde{\tau}^{-1}$  increases clearly, indicating that excitons

Table 7.9: Computational cost of Marcus rate input parameters for a system with  $N$  sites and each site having  $N_{nn}$  nearest neighbors. The computation time is measured for DCV5T molecule using the ubecppol basis set, the aux-ubecppol\_0.2 auxiliary basis set and the PBE exchange correlation functional for the  $GW$ -BSE calculation. The evaluation of the TrEsp coupling from atomic partial charges according to eq. 6.26 is negligible.

paramter	comp. time	# of calculations
reorganization energy	7 days	1
DFT+ $GW$ -BSE-DIPRO monomer	52 min	$N$
DFT+ $GW$ -BSE-DIPRO dimer	300 min	$N \cdot N_{nn}/2$
site energy	4 min	$N$
TrEsp CHELPG	1 min	$N$

get trapped in certain states with low site energies, from which they cannot escape. From Fig. 7.9(c) it becomes clear why the exciton diffusion length in the third snapshot is lowest of all. In this snapshot the majority of excitons decay on one single site, which has the lowest site energies of all sites in all snapshots with -0.43 eV. Not all important sites have a high relative decay probability. Consequently, these sites must be visited extremely often to account for the high number of decays.

A similar relation can be seen for the system with internal site energies taken into account. Snapshots 1, 4, and 6 show exactly the same pattern when compared to Tab. 7.8 with Fig. 7.10. Singlet exciton diffusion is thus largely governed by the lowest lying energy levels, as singlets due to their long ranged coupling can jump into the trap from far away. Thus for an accurate simulation of singlet diffusion, large enough systems are required to adequately sample the real energy landscape.

Finally, compared to the expectation of an exciton diffusion length of around 10 nm from experimental observations for nearly all organic materials [13, 28], the results obtained from our simulations are larger. This can be rationalized by the fact that we simulated a nearly defect free crystalline material with only thermal disorder. Even in this near perfect system, the large influence of a single trap site on the exciton diffusion length became evident.

Before we close this chapter, we briefly have to address the topic of computational cost. In Tab. 7.9 the computation time for each parameter of the Marcus rate is given for DCV5T, assuming a single threaded execution. Under the assumption,



that the reorganization energy  $\lambda$  is the same for all chemically identical molecules, the DIPRO dimer calculation is the bottleneck. If only singlet diffusion is of interest, using TrEsp couplings instead of *GW*-BSE-DIPRO couplings reduces the computational expense to around 60 min per site. For a system of 1600 sites this roughly equals 4 days on one 16 core cluster node.

In summary we developed a workflow to simulate exciton diffusion in organic materials. Using DCV5T, an organic semiconductor, we used kinetic Monte-Carlo simulations parametrized from *ab-initio* simulations to simulate singlet and triplet excitons. We compared *GW*-BSE-DIPRO and TrEsp couplings for singlets and showed, that the difference is negligible even at close ranges. This is certainly not a general result, as the relative importance of short and long ranged couplings depends on the morphology and the transition dipole strength of the state and molecule of interest. We included TrEsp long range couplings and showed that long ranged jumps significantly contribute to the diffusion process. Furthermore, we included radiative singlet exciton decay as a lower bound on lifetime. Additionally, we showed the impact of low energy sites on the diffusion of singlet excitons, as they get trapped on these sites. The major open question, that remains is the separation of internal static and dynamic disorder. Hopefully, better mapping procedures might help to alleviate this problem.

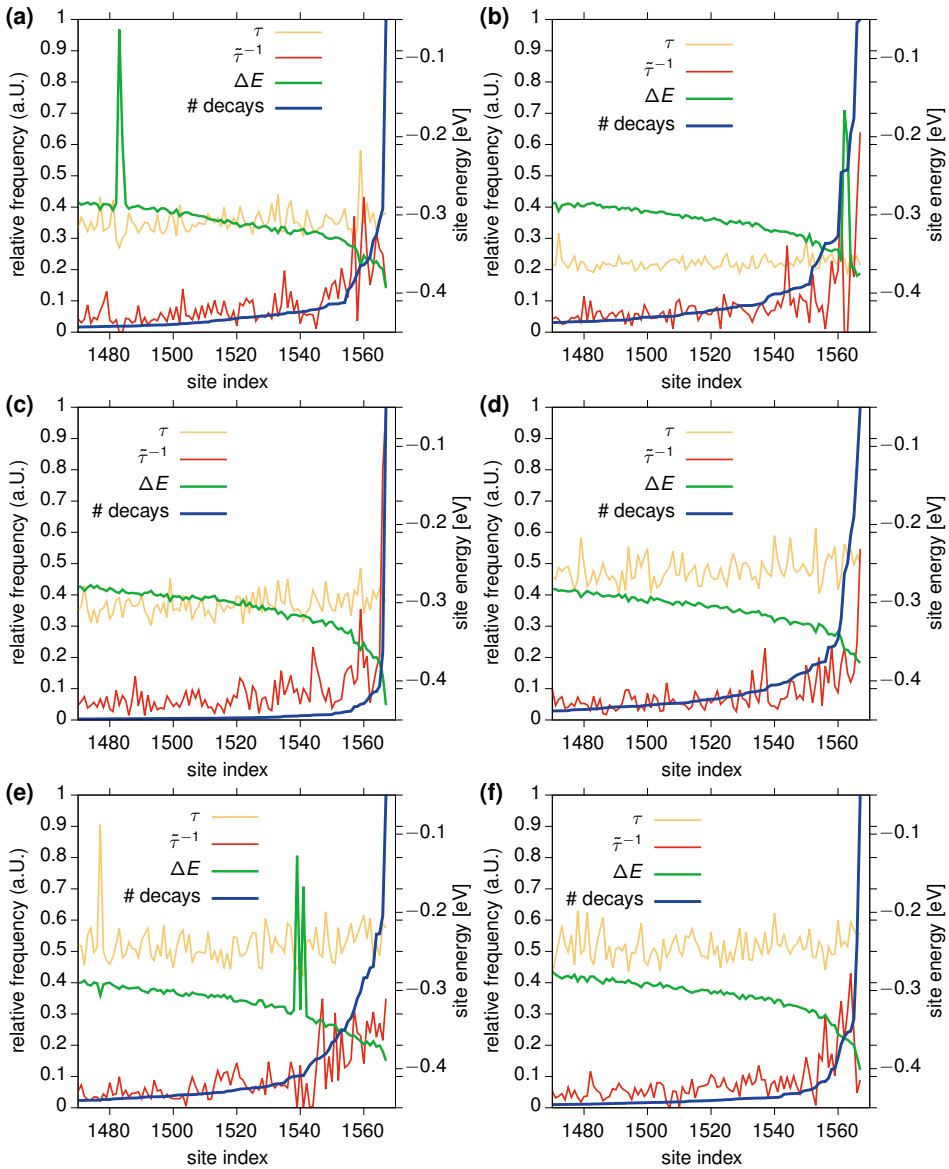


Figure 7.9: Frequency of exciton decay plotted over the sites, sorted from lowest to largest probability (blue line). In each plot only the 100 most likely sites are plotted. The normalized decay time for each segment is shown (yellow line) for comparison. The green line indicates the site energies of the respective sites (without internal site energies).

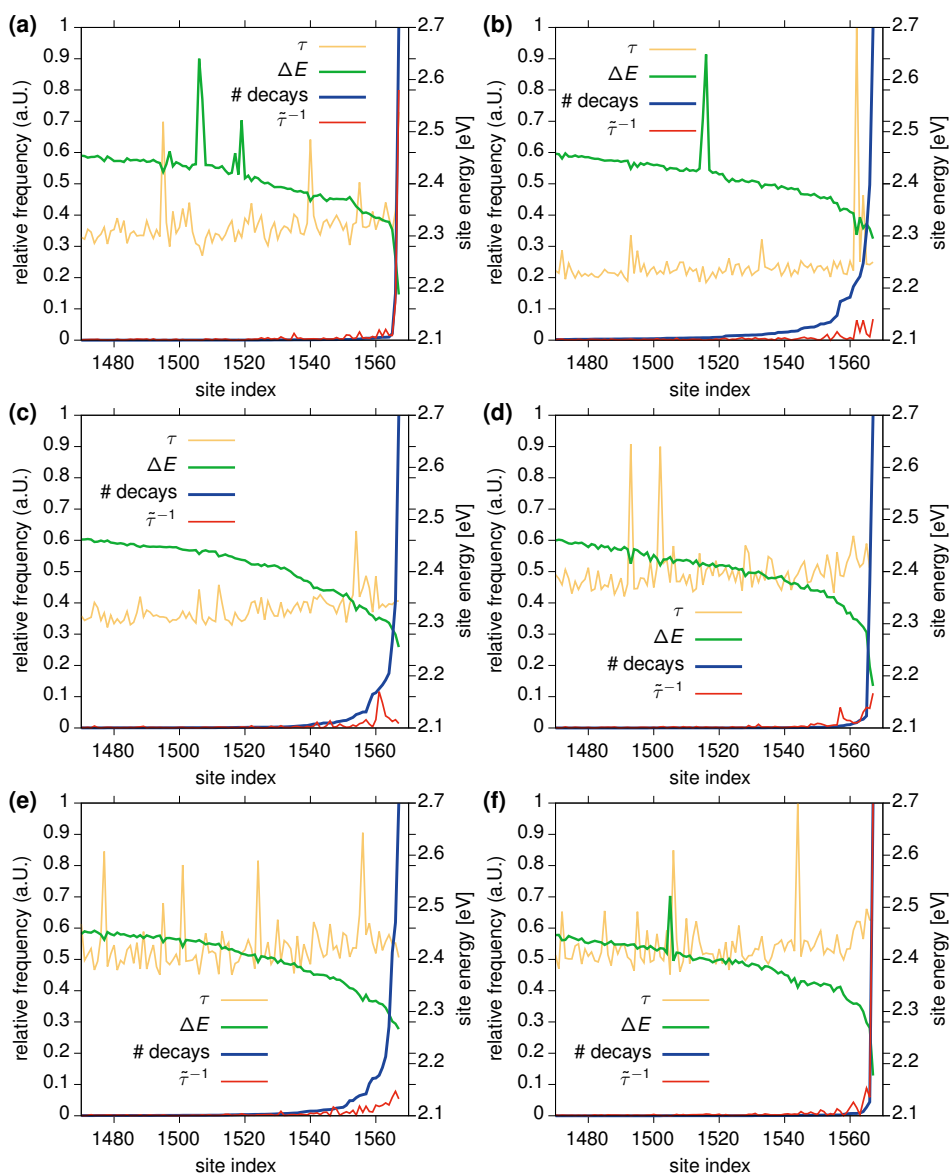


Figure 7.10: Frequency of exciton decay plotted over the sites, sorted from lowest to largest probability (blue line). In each plot only the 100 most likely sites are plotted. The normalized decay time for each segment is shown (yellow line) for comparison. The green line indicates the site energies of the respective sites (with internal site energies)



## Chapter 8

# Conclusion and outlook

The present thesis aimed at exploring the properties of excitons created by light absorption inside an organic solar cell. The model paradigm was to relate chemical properties of constituent molecules and molecular packing to experimentally measurable quantities, for instance, diffusion lengths.

To this end we implemented a multi scale model consisting of five steps: Generation of a morphology via molecular dynamics simulations, definition of hopping sites, the calculation of rate parameters, the evaluation of exciton transfer rates, and the simulation of exciton dynamics. The penultimate two steps were here linked by excitation transfer rates, which in the limit of high-temperature adiabatic exciton transfer, are described via the Marcus rate equation. For the evaluation of these rates site energies, the electronic coupling elements and the reorganization energies had to be calculated from *ab initio* methods, supplemented by classical electrostatics.

To accurately parameterize rate equations for larger, industrially relevant molecules a quantum mechanical approach is required, which is both accurate and efficient. To this end we implemented and scrutinized the *GW*-BSE method in the VOTCA-XTP package, which explicitly describes single particle excited states (*GW*) and the interaction between them (BSE). To correctly simulate QM/MM environments, including higher order multipoles and numeric potentials, we also developed our own DFT implementation to provide accurate starting points for the *GW*-BSE calculations. The benchmarks of our DFT implementation against other commercial and

non-commercial DFT packages showed excellent agreement. For the more involved *GW*-BSE approach we compared our results with high level quantum chemistry results and experimental values for a set of 28 small molecules and achieved good agreement with the reference results. With the aim of reducing the computational footprint we explored the application of pseudo potentials in lieu of all-electron calculations, which allow for smaller basis sets.

As the excitations in individual molecules can drastically vary from excitations in solution or the bulk material, we used the QM/MM setup of VOTCA to analyze the energetics of charge transfer states in a double strand of DNA solvated in water. We found, that the inclusion of a classical, polarizable environment leads to a stabilization of charge transfer states in comparison to calculations on dimers in vacuum, accompanied by a pronunciation of the charge transfer character. These low energy CT states may be intermediaries in the UV-degradation of DNA and are thus of considerable interest.

CT states also play a vital role in the exciton transfer reaction, where they serve as intermediate states, through which a localized Frenkel exciton moves from one molecule to another. In the framework of *GW*-BSE we developed an algorithm to calculate effective electronic couplings for singlet and triplet excitons. We benchmarked this approach against quantum chemical methods for the pyrene and DCV5T-Me(3,3) molecule. It was found that depending on the character of the excitation the inclusion of several CT states was necessary to achieve correct results. To accelerate the computation of electronic couplings for large-scale morphologies we explored the influence of self-consistency on the DFT and *GW*-BSE level and the reduction of the active space in the BSE-Hamiltonian.

For the calculation of exciton dynamics the three aforementioned methods together with new kinetic Monte-Carlo implementation for singlets were combined into a multi-scale model. Singlet and triplet exciton dynamics were simulated for a DCV5T-Me(3,3) crystal. For singlet dynamics we explicitly incorporated radiative decay and approximate long-ranged exchange coupling. We explored the influence of long-ranged couplings on exciton transport and investigated the impact of energetic disorder on the exciton diffusion length. We found a strong dependency on the energetic disorder, as especially singlets due to their long-ranged coupling would preferably jump into these traps, limiting their diffusion length.

While the multi scale model offers the chance to bridge multiple length and time scales, the distinction between fast degrees of motion, which trigger the transfer reaction and slow degrees of freedom, which lead to basically static disorder on the

timescales cannot be automatically made. Better mapping procedures to transfer quantum mechanically obtained geometries onto molecular dynamics geometries would be highly welcome. Additionally, the efficient calculation of analytical forces on the *GW*-BSE level would allow more insight into the vibrational spectra of excited states. This would also allow the usage of more advanced rate equations beyond the Marcus rate approach, e.g., Weiss-Dorsey rates[108, 109], but also open a pathway to better mapping procedures.

To gain a more complete understanding of the elementary processes inside a solar cell, additional reactions, like the conversion of FE states into CT states, or singlet-triplet conversion have to be included in rate models. In the former case this requires QM/MM approaches, as preliminary results (see Fig. 8.1) indicate that the polarization response is critical in lowering CT energies. By stabilizing the CT state with respect to localized Frenkel excitons, conversion of FE into CT by thermal activation alone might be possible. However, to properly describe the energetics around the heterojunction long ranged electrostatics and polarization effects have to be included into quantum mechanical QM/MM calculations. The latter case of singlet-triplet conversion requires the explicit inclusion of spin degrees of freedom as well as spin-orbit coupling into the *GW*-BSE framework.

With a workflow for exciton dynamics in place, it may also be possible to study

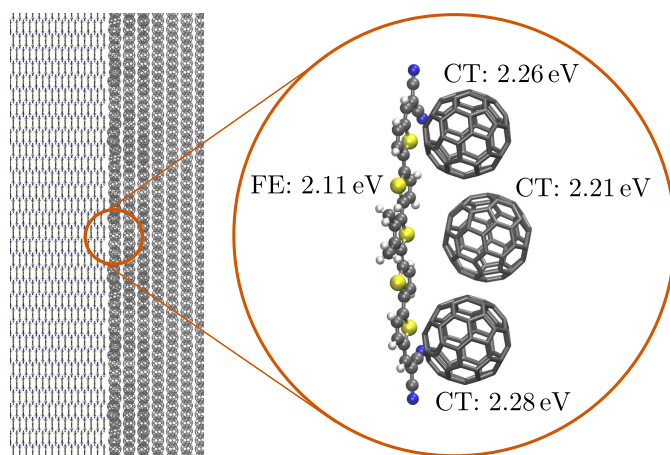


Figure 8.1: CT and FE state energies at the DCV5T:C60 interface from *GW*-BSE calculations in a polarizable QM/MM environment.

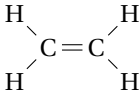
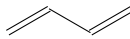

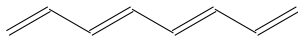


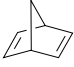
the influence of defects on exciton dynamics. The identification of structural defect configurations and its relation to molecular arrangement and chemical structure could facilitate the design of more efficient solar cells.



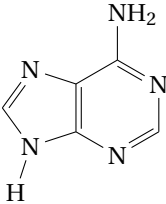
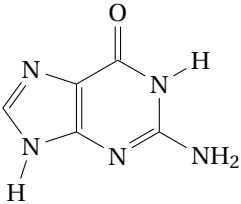
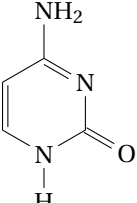
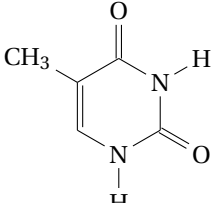
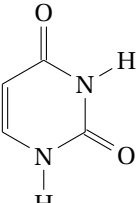
# Appendix A

## Chemical structures

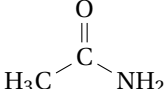
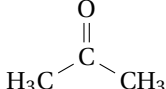
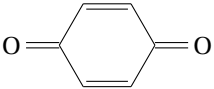
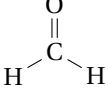
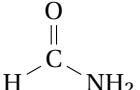
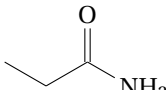
Thiel set: unsaturated, aliphatic hydrocarbons

<b>name</b>	<b>structure</b>	<b>name</b>	<b>structure</b>
ethene		butadiene	
hexatriene		octatetraene	
cyclopropene		cyclopentadiene	
norbornadiene			

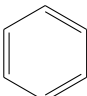
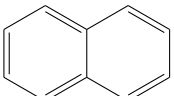
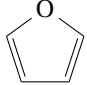
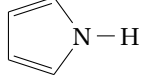
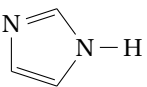
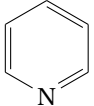
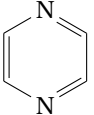
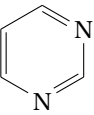
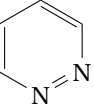
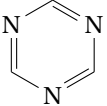
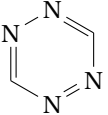
## Thiel set: nucleobases

name	structure	name	structure
adenine		guanine	
cytosine		thymine	
uracil			

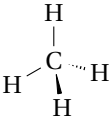
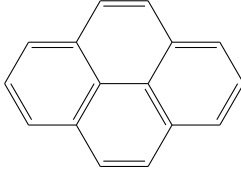

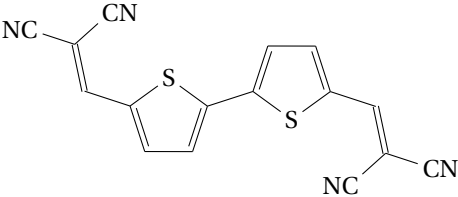
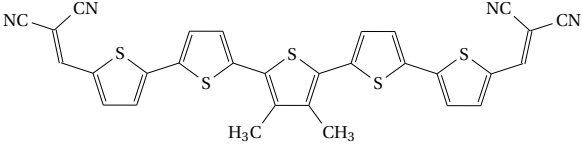
## Thiel set: aldehydes, ketones, amides

name	structure	name	structure
acetamide		acetone	
benzoquinone		formaldehyde	
formamide		propanamide	

## Thiel set: aromatic hydrocarbons, heterocycles

<b>name</b>	<b>structure</b>	<b>name</b>	<b>structure</b>
benzene		naphthalene	
furan		pyrrole	
imidazole		pyridine	
pyrazine		pyrimidine	
pyridazine		triazine	
tetrazine			

## Organic electronics

name	structure
methane	
pyrene	
C <sub>60</sub>	
DCV2T	
DCV5T- Me(3,3)	

## **Appendix B**

### **Thiel set data**

Table B.1: Number of basis functions in the atomic orbital basis for the molecular orbitals (MO) and the associated auxiliary basis (RI) used for the resolution-of-identity, respectively, for all molecules in the Thiel set. See Chapter 5 for the definition of ubecppol basis.

	cc-pVTZ		aug-cc-pVTZ		ubecppol	
	MO	RI	MO	RI	MO	RI
<b>NUCLEOBASES</b>						
cytosine	310	798	483	1078	211	1013
thymine	354	909	552	1230	243	1152
uracil	296	768	460	1032	206	992
adenine	370	960	575	1290	250	1215
<b>UNSATURATED ALIPHATIC HYDROCARBONS</b>						
ethene	116	282	184	396	74	320
butadiene	204	504	322	700	132	578
hexatriene	292	726	460	1004	190	836
cyclopropene	146	363	230	502	95	418
cyclopentadiene	234	585	368	806	153	676
norbornadiene	322	807	506	1110	211	934
<b>ALDEHYDES, KETONES, and AMIDES</b>						
formaldehyde	88	222	138	304	61	284
acetone	204	504	322	700	135	604
benzoquinone	296	768	460	1032	206	960
formamide	132	333	207	456	90	429
acetamide	190	474	299	654	127	589
propanamide	248	615	391	852	164	749
<b>AROMATIC HYDROCARBONS and HETEROCYCLES</b>						
benzene	264	666	414	912	174	774
naphthalene	412	1050	644	1428	274	1228
furan	206	525	322	714	140	640
pyrrole	220	555	345	760	145	661
imidazole	206	525	322	714	137	646
pyridine	250	636	391	866	166	759
pyrazine	236	606	368	820	158	744
pyrimidine	236	606	368	820	158	744
pyridazine	236	606	368	820	158	744
triazine	222	576	345	774	150	729
tetrazine	208	546	322	728	142	714

Table B.2: Calculated lowest singlet excitation energies (in eV) performed using PBE0 on all-electron (AE) level with the aug-cc-pVTZ and cc-pVTZ basis sets as well as employing effective core potentials and the ubecppol basis set with TD-PBE0 [167],PBE0 [167], TBE-2 [223] and experimental data (from Ref. [224] and references therein). Our results are obtained as solutions of both the full BSE and the Tamm-Dancoff Approximation (TDA), respectively. Mean absolute errors are given on the difference of our *GW* results using a Plasmon-Pole Model for the frequency dependence of the dielectric function and the ones obtained in Ref. [167] using complex integration.

	TD-PBE0	Ref. [167]/ PBE0	TBE-2	Exp	cc-pVTZ		aug-cc-pVTZ		ubecppol		
					full	TDA	full	TDA	full	TDA	
<b>NUCLEOBASES</b>											
cytosine	4.71	4.57	4.66	4.6	4.72	4.93	4.56	4.75	4.88	5.09	
thymine	4.76	4.72	4.82	4.9	4.85	4.88	4.73	4.76	5.00	5.02	
uracil	4.70	4.70	5.00	4.38	4.81	4.84	4.70	4.73	4.98	5.00	
adenine	5.04	4.93	5.25	4.63	5.18	5.17	5.02	5.04	5.31	5.31	
<b>UNSATURATED ALIPHATIC HYDROCARBONS</b>											
ethene	7.48	7.32	7.80	7.66	7.89	8.35	7.51	8.04	8.22	8.39	
butadiene	5.65	5.71	6.18	5.92	6.03	6.65	5.77	6.09	6.25	6.90	
hexatriene	4.68	4.79	5.10	4.93	4.98	5.52	4.81	5.29	5.13	5.70	
cyclopropene	6.18	6.14	6.65	7.19	6.67	6.70	6.38	6.50	6.94	6.97	
cyclopentadiene	5.02	4.88	5.55	5.30	5.13	5.58	5.00	5.42	5.30	5.77	
norbornadiene	4.81	4.89	5.37	5.25	5.26	5.51	5.06	5.29	5.46	5.72	
<b>ALDEHYDES, KETONES, and AMIDES</b>											
formaldehyde	3.85	3.61	3.88	3.79	3.89	3.89	3.82	3.87	4.13	4.17	
acetone	4.35	3.97	4.38	4.38	4.28	4.32	4.20	4.25	4.34	4.38	
benzoquinone	2.48	2.67	2.74	2.49	2.63	2.68	2.58	2.63	2.76	2.80	
formamide	5.64	5.59	5.55	5.5	5.58	5.61	5.42	5.45	5.80	5.83	
acetamine	5.65	5.56	5.62	5.44	5.60	5.63	5.45	5.48	5.71	5.74	
propanamide	5.67	5.55	5.65	5.44	5.62	5.65	5.47	5.50	5.74	5.77	
<b>AROMATIC HYDROCARBONS and HETEROCYCLES</b>											
benzene	5.45	5.04	5.08	4.90	5.25	5.30	5.17	5.21	5.40	5.44	
naphthalene	4.38	4.20	4.25	3.97	4.33	4.37	4.27	4.31	4.45	4.49	
furan	6.02	5.78	6.32	6.06	6.31	6.76	6.02	6.32	6.57	7.01	
pyrrole	6.65	6.67	6.57	5.98	6.49	6.89	6.00	6.11	6.78	6.89	
imidazole	6.27	5.96	6.25	6.00	6.59	6.92	6.26	6.30	6.89	6.89	
pyridine	4.83	4.79	4.59	4.59	4.83	4.91	4.72	4.79	4.99	5.07	
pyrazine	3.96	3.90	4.13	3.83	3.96	4.04	3.85	3.93	4.10	4.19	
pyrimidine	4.31	4.26	4.43	4.16	4.29	4.34	4.20	4.24	4.41	4.46	
pyridazine	3.65	3.57	3.85	3.3	3.52	3.63	3.44	3.54	3.65	3.76	
triazine	4.62	4.66	4.71	4.59	4.56	4.57	4.46	4.47	4.67	4.68	
tetrazine	2.29	2.19	2.46	2.25	2.13	2.26	2.07	2.19	2.20	2.32	
	MAE(all)						0.14				
	MAE(nucleobases)						0.03				
	MAE(unsat. aliphatic hydrocarbons)						0.13				
	MAE(aldehydes, ketones, amides)						0.15				
	MAE(aromatic hydrocarbons and heterocycles)						0.19				

## **Appendix C**

### **DCV5T site energies**



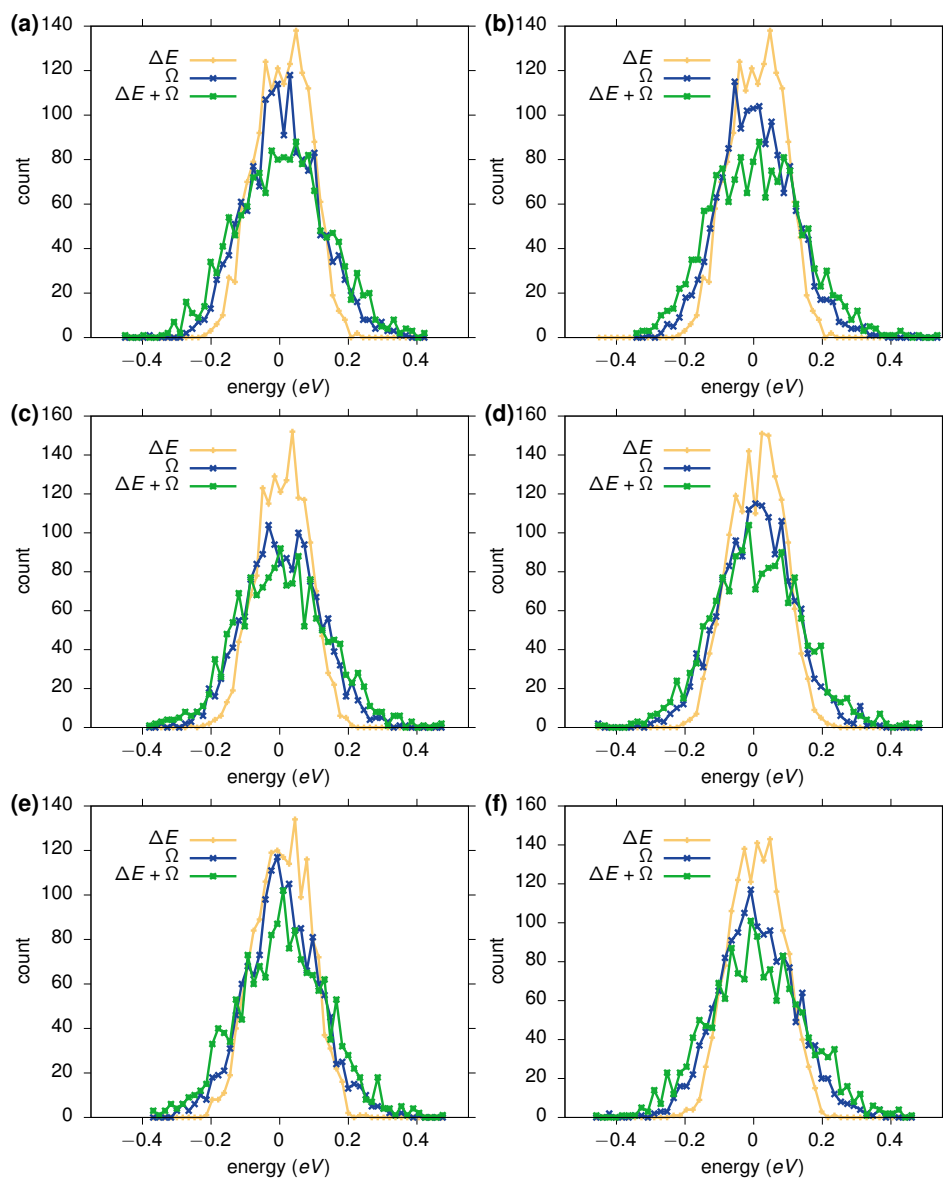


Figure C.1: Singlet site energy distributions including excitation energies for the first six snapshots. The mean of each distribution is normalized to zero.  $\Omega$  is the internal site energy and  $\Delta E$  the electrostatic site energy.

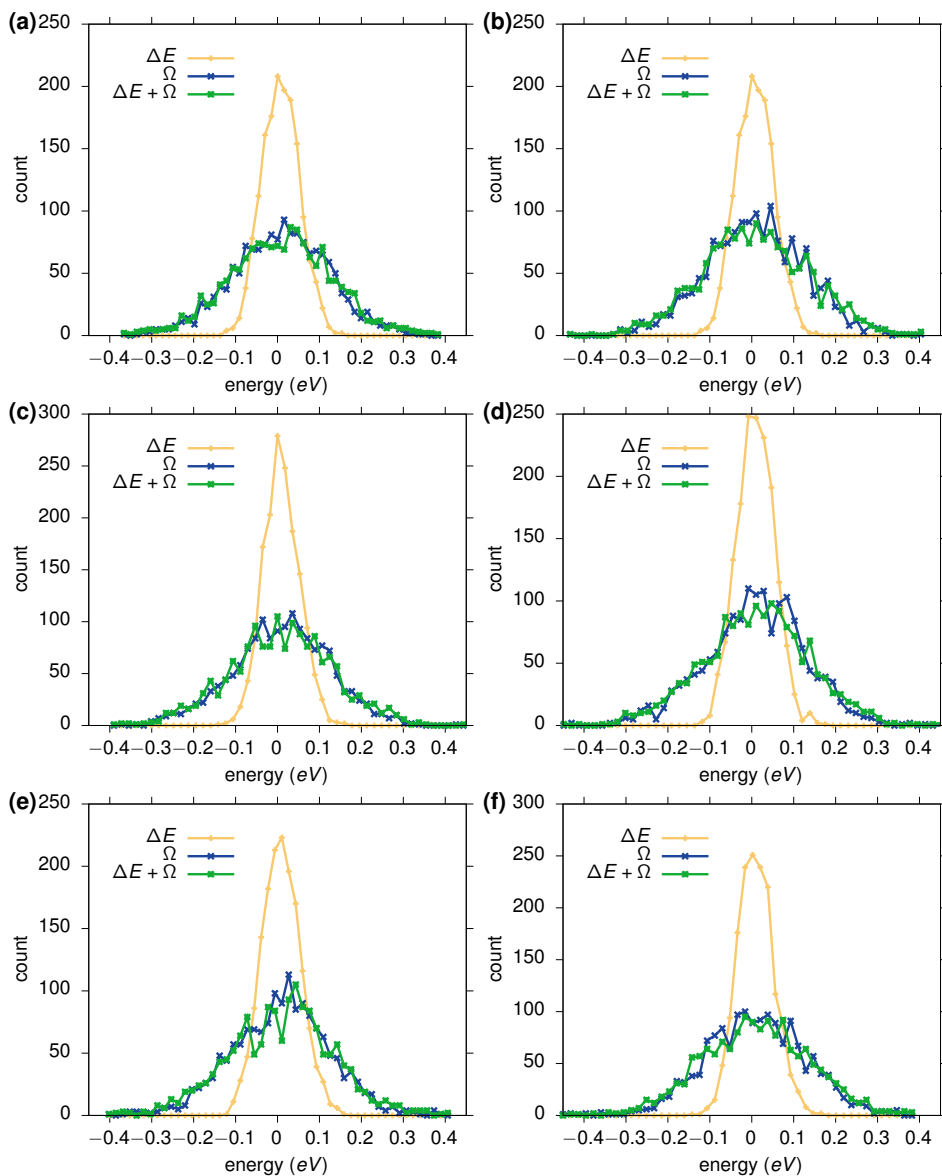


Figure C.2: Triplet site energy distributions including excitation energies for the first six snapshots. The mean of each distribution is normalized to zero.  $\Omega$  is the internal site energy and  $\Delta E$  the electrostatic site energy.

# Bibliography

- [1] W. Shockley and H. J. Queisser. “Detailed Balance Limit of Efficiency of P-n Junction Solar Cells”. In: *J. Appl. Phys.* 32.3 (1961), pp. 510–519 (cit. on p. 2).
- [2] W. S. Yang et al. “Iodide Management in Formamidinium Lead Halide Based Perovskite Layers for Efficient Solar Cells”. In: *Science* 356.6345 (2017), pp. 1376–1379 (cit. on p. 2).
- [3] A. Babayigit et al. *Toxicity of Organometal Halide Perovskite Solar Cells*. 2016. URL: <https://www.nature.com/articles/nmat4572> (visited on 07/28/2018) (cit. on p. 2).
- [4] D. Bryant et al. “Light and Oxygen Induced Degradation Limits the Operational Stability of Methylammonium Lead Triiodide Perovskite Solar Cells”. In: *Energy & Environmental Science* 9.5 (2016), pp. 1655–1660 (cit. on p. 2).
- [5] T. D. Lee and A. U. Ebong. “A Review of Thin Film Solar Cell Technologies and Challenges”. In: *Ren. Sus. Ene. Rev.* 70 (2017), pp. 1286–1297 (cit. on p. 2).
- [6] *New World Record for Solar Cell Efficiency at 46% - Fraunhofer ISE*. URL: <https://www.ise.fraunhofer.de/en/press-media/press-releases/2014/new-world-record-for-solar-cell-efficiency-at-46-percent.html> (visited on 07/28/2018) (cit. on p. 2).
- [7] J. Kalowekamo and E. Baker. “Estimating the Manufacturing Cost of Purely Organic Solar Cells”. In: *Sol. Ene.* 83.8 (2009), pp. 1224–1231 (cit. on p. 3).

- [8] M. C. Barr et al. “Direct Monolithic Integration of Organic Photovoltaic Circuits on Unmodified Paper”. In: *Adv. Mater.* 23.31 (2011), pp. 3500–3505 (cit. on p. 3).
- [9] F. C. Krebs et al. “25th Anniversary Article: Rise to Power – OPV-Based Solar Parks”. In: *Adv. Mater.* 26.1 (2013), pp. 29–39 (cit. on p. 3).
- [10] M. Hösel et al. “Failure Modes and Fast Repair Procedures in High Voltage Organic Solar Cell Installations”. In: *Adv. Ene. Mat.* 4.7 (), p. 1301625 (cit. on p. 3).
- [11] *Photovoltaic Lifetime Project | Photovoltaic Research | NREL*. URL: [www.nrel.gov/pv/lifetime.html](http://www.nrel.gov/pv/lifetime.html) (visited on 07/15/2018) (cit. on p. 3).
- [12] J. Yuan et al. “Single-Junction Organic Solar Cell with over 15% Efficiency Using Fused-Ring Acceptor with Electron-Deficient Core”. In: *Joule* 0.0 (2019) (cit. on pp. 3, 7).
- [13] O. V. Mikhnenko, P. W. M. Blom, and T.-Q. Nguyen. “Exciton Diffusion in Organic Semiconductors”. In: *Ene. Env. Sci.* 8.7 (2015), pp. 1867–1888 (cit. on pp. 4, 12, 20, 155, 164, 168, 174).
- [14] J. J. Kranz and M. Elstner. “Simulation of Singlet Exciton Diffusion in Bulk Organic Materials”. In: *J. Chem. Theory. Comput.* 12.9 (2016), pp. 4209–4221 (cit. on pp. 4, 20).
- [15] *Press Release: The 2000 Nobel Prize in Chemistry*. URL: [www.nobelprize.org/nobel\\_prizes/chemistry/laureates/2000/press.html](http://www.nobelprize.org/nobel_prizes/chemistry/laureates/2000/press.html) (visited on 12/29/2017) (cit. on p. 7).
- [16] A. Facchetti. “Organic Semiconductors: Made to Order”. In: *Nat. Mater.* 12.7 (2013), p. 598 (cit. on p. 7).
- [17] H. Sirringhaus et al. “Two-Dimensional Charge Transport in Self-Organized, High-Mobility Conjugated Polymers”. In: *Nature* 401.6754 (1999), p. 685 (cit. on p. 8).
- [18] H. Kang et al. “Determining the Role of Polymer Molecular Weight for High-Performance All-Polymer Solar Cells: Its Effect on Polymer Aggregation and Phase Separation”. In: *J. Am. Chem. Soc.* 137.6 (2015), pp. 2359–2365 (cit. on p. 8).
- [19] Y. Diao et al. “Morphology Control Strategies for Solution-Processed Organic Semiconductor Thin Films”. In: *Ene. Env. Sci.* 7.7 (2014), pp. 2145–2159 (cit. on p. 8).

- [20] T. Moench et al. "Influence of Meso and Nanoscale Structure on the Properties of Highly Efficient Small Molecule Solar Cells". In: *Adv. Ene. Mat.* 6.4 (2016) (cit. on p. 8).
- [21] D. Z. Garbuzov et al. "Photoluminescence Efficiency and Absorption of Aluminum-Tris-Quinolate (Alq3) Thin Films". In: *Chem. Phys. Lett.* 249.5-6 (1996), pp. 433–437 (cit. on p. 8).
- [22] M. Baldo et al. "Organic Vapor Phase Deposition". In: *Adv. Mater.* 10.18 (1998), pp. 1505–1514 (cit. on p. 8).
- [23] J. Nelson. "Polymer:Fullerene Bulk Heterojunction Solar Cells". In: *Mat. Tod.* 14.10 (2011), pp. 462–470 (cit. on pp. 9, 15, 164).
- [24] C. Ambrosch-Draxl et al. "The Role of Polymorphism in Organic Thin Films: Oligoacenes Investigated from First Principles". In: *New J. Phys.* 11.12 (2009), p. 125010 (cit. on p. 10).
- [25] C. W. Tang. "Two-layer Organic Photovoltaic Cell". In: *Appl. Phys. Lett.* 48.2 (1986), pp. 183–185 (cit. on p. 11).
- [26] J. Lee et al. "Charge Transfer State Versus Hot Exciton Dissociation in Polymer-Fullerene Blended Solar Cells". In: *J. Am. Chem. Soc.* 132.34 (2010), pp. 11878–11880 (cit. on p. 12).
- [27] G. Grancini et al. "Hot Exciton Dissociation in Polymer Solar Cells". In: *Nat. Mater.* 12.1 (2013), p. 29 (cit. on p. 12).
- [28] O. V. Mikhnenko et al. "Trap-Limited Exciton Diffusion in Organic Semiconductors". In: *Adv. Mater.* 26.12 (2014), pp. 1912–1917 (cit. on pp. 12, 164, 174).
- [29] S. M. Menke, W. A. Luhman, and R. J. Holmes. "Tailored Exciton Diffusion in Organic Photovoltaic Cells for Enhanced Power Conversion Efficiency". In: *Nat. Mater.* 12.2 (2013), p. 152 (cit. on p. 12).
- [30] V. S. Inc. "General Properties of Si, Ge, SiGe, SiO<sub>2</sub> and Si<sub>3</sub>N<sub>4</sub>". In: (2012) (cit. on p. 15).
- [31] A. L. Fetter and J. D. Walecka. *Quantum Theory of Many-Particle Systems*. Courier Corporation, 2003 (cit. on p. 17).
- [32] *The Perrin - Jablonski Diagram | TikZ Example*. URL: [www.texample.net/tikz/examples/the-perrin-jablonski-diagram/](http://www.texample.net/tikz/examples/the-perrin-jablonski-diagram/) (visited on 01/30/2018) (cit. on p. 20).

- [33] M. C. Heiber and A. Dhinojwala. “Dynamic Monte Carlo Modeling of Exciton Dissociation in Organic Donor-Acceptor Solar Cells”. In: *J. Chem. Phys.* 137.1 (2012), p. 014903 (cit. on pp. 20, 155).
- [34] V. Stehr et al. “Singlet Exciton Diffusion in Organic Crystals Based on Marcus Transfer Rates”. In: *J. Chem. Theory. Comput.* 10.3 (2014), pp. 1242–1255 (cit. on pp. 20, 75, 155, 156).
- [35] V. Stehr et al. “Anisotropy of Singlet Exciton Diffusion in Organic Semiconductor Crystals from Ab Initio Approaches”. In: *J. Chem. Phys.* 140.2 (2014), p. 024503 (cit. on pp. 20, 171).
- [36] D. L. Dexter. “A Theory of Sensitized Luminescence in Solids”. In: *J. Chem. Phys.* 21.5 (1953), pp. 836–850 (cit. on pp. 20, 132).
- [37] G. D. Scholes. “Long-Range Resonance Energy Transfer in Molecular Systems”. In: *Anu. Rev. Phy. Chem.* 54.1 (2003), pp. 57–87 (cit. on p. 20).
- [38] W. A. Luhman and R. J. Holmes. “Investigation of Energy Transfer in Organic Photovoltaic Cells and Impact on Exciton Diffusion Length Measurements”. In: *Adv. Funct. Mater.* 21.4 (2011), pp. 764–771 (cit. on p. 20).
- [39] R. Koeppe and N. S. Sariciftci. “Photoinduced Charge and Energy Transfer Involving Fullerene Derivatives”. In: *Photochem. Photobio. Sci.* 5.12 (2006), pp. 1122–1131 (cit. on p. 20).
- [40] *Press Release: The 1998 Nobel Prize in Chemistry*. URL: [www.nobelprize.org/nobel\\_prizes/chemistry/laureates/1998/press.html](http://www.nobelprize.org/nobel_prizes/chemistry/laureates/1998/press.html) (visited on 12/29/2017) (cit. on p. 23).
- [41] J. P. Perdew. “Density Functional Theory and the Band Gap Problem”. In: *Int. J. Quantum Chem.* 28.S19 (1985), pp. 497–523 (cit. on p. 24).
- [42] *Essentials of Computational Chemistry: Theories and Models*. 2 edition. Chichester, West Sussex, England ; Hoboken, NJ: Wiley, 2004 (cit. on p. 24).
- [43] D. Marx and J. Hutter. “Ab initio molecular dynamics: Theory and implementation”. In: *Modern methods and algorithms of quantum chemistry*. 2000, pp. 329–477 (cit. on pp. 24, 64, 70).
- [44] C. Faber. “Electronic, Excitonic and Polaronic Properties of Organic Systems within the Many-Body GW and Bethe-Salpeter Formalisms: Towards Organic Photovoltaics”. PhD Thesis. Université Grenoble Alpes, 2014 (cit. on p. 24).

- [45] L. Hedin. “New Method for Calculating the One-Particle Green’s Function with Application to the Electron-Gas Problem”. In: *Phys. Rev.* 139.3A (1965), A796–A823 (cit. on pp. 24, 50).
- [46] *Quantum Theory of Many-Particle Systems*. Mineola, N.Y: Dover Publications, 2003 (cit. on pp. 24, 60).
- [47] J. Gräfenstein and D. Cremer. “Can Density Functional Theory Describe Multi-Reference Systems? Investigation of Carbenes and Organic Biradicals”. In: *Phys. Chem. Chem. Phys.* 2.10 (2000), pp. 2091–2103 (cit. on p. 33).
- [48] M. Huix-Rotllant et al. “Assessment of Density Functional Theory for Describing the Correlation Effects on the Ground and Excited State Potential Energy Surfaces of a Retinal Chromophore Model”. In: *J. Chem. Theory. Comput.* 9.9 (2013), pp. 3917–3932 (cit. on p. 33).
- [49] F. Bernardi et al. “MCSCF Gradient Calculation of Transition Structures in Organic Reactions”. In: *Far. Symp. Chem. Soc.* 19.0 (1984), pp. 137–147 (cit. on p. 33).
- [50] D. I. Lyakh et al. “Multireference Nature of Chemistry: The Coupled-Cluster View”. In: *Chem. Rev.* 112.1 (2012), pp. 182–243 (cit. on p. 33).
- [51] C. David Sherrill and H. F. Schaefer. “The Configuration Interaction Method: Advances in Highly Correlated Approaches”. In: *Adv. Qua. Chem.* 34 (1999), pp. 143–269 (cit. on p. 33).
- [52] C. Møller and M. S. Plesset. “Note on an Approximation Treatment for Many-Electron Systems”. In: *Phys. Rev.* 46.7 (1934), pp. 618–622 (cit. on p. 33).
- [53] P. Hohenberg and W. Kohn. “Inhomogeneous Electron Gas”. In: *Phys. Rev.* 136.3B (1964), B864–B871 (cit. on p. 34).
- [54] L. H. Thomas. “The Calculation of Atomic Fields”. In: *Mat. Pro. Cambridge. Phi. Soc.* 23.5 (1927), pp. 542–548 (cit. on p. 35).
- [55] C. Huang and E. A. Carter. “Toward an Orbital-Free Density Functional Theory of Transition Metals Based on an Electron Density Decomposition”. In: *Phys. Rev. B* 85.4 (2012) (cit. on p. 35).
- [56] W. Kohn and L. J. Sham. “Self-Consistent Equations Including Exchange and Correlation Effects”. In: *Phys. Rev.* 140.4A (1965), A1133–A1138 (cit. on p. 35).

- [57] A. D. Becke. “Density-functional Thermochemistry. III. The Role of Exact Exchange”. In: *J. Chem. Phys.* 98.7 (1993), pp. 5648–5652 (cit. on p. 39).
- [58] P. J. Stephens et al. “Ab Initio Calculation of Vibrational Absorption and Circular Dichroism Spectra Using Density Functional Force Fields”. In: *J. Phys. Chem.* 98.45 (1994), pp. 11623–11627 (cit. on p. 39).
- [59] J. P. Perdew, K. Burke, and M. Ernzerhof. “Generalized Gradient Approximation Made Simple”. In: *Phys. Rev. Lett.* 77.18 (1996), pp. 3865–3868 (cit. on pp. 39, 96, 107, 140).
- [60] M. Steinmetz and S. Grimme. “Benchmark Study of the Performance of Density Functional Theory for Bond Activations with (Ni,Pd)-Based Transition Metal Catalysts”. In: *Chem. Open* 2.3 (2013), pp. 115–124 (cit. on p. 39).
- [61] J. P. Perdew, M. Ernzerhof, and K. Burke. “Rationale for Mixing Exact Exchange with Density Functional Approximations”. In: *J. Chem. Phys.* 105.22 (1996), pp. 9982–9985 (cit. on p. 39).
- [62] C. Adamo and V. Barone. “Toward Reliable Density Functional Methods without Adjustable Parameters: The PBE0 Model”. In: *J. Chem. Phys.* 110.13 (1999), pp. 6158–6170 (cit. on pp. 39, 104).
- [63] A. Dreuw and M. Head-Gordon. “Failure of Time-Dependent Density Functional Theory for Long-Range Charge-Transfer Excited States: The Zinobacteriochlorin-Bacteriochlorin and Bacteriochlorophyll-Spheroidene Complexes”. In: *J. Am. Chem. Soc.* 126.12 (2004), pp. 4007–4016 (cit. on p. 39).
- [64] D. Nazarian, P. Ganesh, and D. S. Sholl. “Benchmarking Density Functional Theory Predictions of Framework Structures and Properties in a Chemically Diverse Test Set of Metal–Organic Frameworks”. In: *J. Mat. Chem. A* 3.44 (2015), pp. 22432–22440 (cit. on p. 40).
- [65] S. Grimme. “Density Functional Theory with London Dispersion Corrections”. In: *Wiley Interdisciplinary Reviews: Computational Molecular Science* 1.2 (2011), pp. 211–228 (cit. on p. 40).
- [66] T. Schwabe and S. Grimme. “Double-Hybrid Density Functionals with Long-Range Dispersion Corrections: Higher Accuracy and Extended Applicability”. In: *Phys. Chem. Chem. Phys.* 9.26 (2007), pp. 3397–3406 (cit. on p. 40).



- [67] T. Schwabe and S. Grimme. “Towards Chemical Accuracy for the Thermodynamics of Large Molecules: New Hybrid Density Functionals Including Non-Local Correlation Effects”. In: *Phys. Chem. Chem. Phys.* 8.38 (2006), pp. 4398–4401 (cit. on p. 40).
- [68] K. Lejaeghere et al. “Error Estimates for Solid-State Density-Functional Theory Predictions: An Overview by Means of the Ground-State Elemental Crystals”. In: *Crit. Rev. Sol. State Mat. Sci.* 39.1 (2014), pp. 1–24 (cit. on p. 40).
- [69] L. Goerigk and S. Grimme. “A Thorough Benchmark of Density Functional Methods for General Main Group Thermochemistry, Kinetics, and Noncovalent Interactions”. In: *Phys. Chem. Chem. Phys.* 13.14 (2011), pp. 6670–6688 (cit. on p. 40).
- [70] G. Onida, L. Reining, and A. Rubio. “Electronic Excitations: Density-Functional versus Many-Body Green’s-Function Approaches”. In: *Rev. Mod. Phys.* 74.2 (2002), pp. 601–659 (cit. on p. 40).
- [71] S. Obara and A. Saika. “Efficient Recursive Computation of Molecular Integrals over Cartesian Gaussian Functions”. In: *J. Chem. Phys.* 84.7 (1986), p. 3963 (cit. on pp. 42, 94).
- [72] F. Weigend and R. Ahlrichs. “Balanced Basis Sets of Split Valence, Triple Zeta Valence and Quadruple Zeta Valence Quality for H to Rn: Design and Assessment of Accuracy”. In: *Phys. Chem. Chem. Phys.* 7.18 (2005), pp. 3297–3305 (cit. on pp. 43, 93, 104).
- [73] Y. Ma, M. Rohlfing, and C. Molteni. “Excited States of Biological Chromophores Studied Using Many-Body Perturbation Theory: Effects of Resonant-Antiresonant Coupling and Dynamical Screening”. In: *Phys. Rev. B* 80.24 (2009), p. 241405 (cit. on pp. 46, 101, 102).
- [74] X. Blase, C. Attaccalite, and V. Olevano. “First-Principles GW Calculations for Fullerenes, Porphyrins, Phtalocyanine, and Other Molecules of Interest for Organic Photovoltaic Applications”. In: *Phys. Rev. B* 83.11 (2011), p. 115103 (cit. on p. 46).
- [75] B. Baumeier, D. Andrienko, and M. Rohlfing. “Frenkel and Charge Transfer Excitations in Donor-Acceptor Complexes from Many-Body Green’s Functions Theory”. In: *J. Chem. Theory. Comput.* 8.8 (2012), pp. 2790–2795 (cit. on pp. 46, 101, 102).

- [76] N. Marom et al. “Benchmark of GW Methods for Azabenzenes”. In: *Phys. Rev. B* 86.24 (2012), p. 245127 (cit. on pp. 46, 102).
- [77] X. Blase and C. Attaccalite. “Charge-Transfer Excitations in Molecular Donor-Acceptor Complexes within the Many-Body Bethe-Salpeter Approach”. In: *Appl. Phys. Lett.* 99.17 (2011), p. 171909 (cit. on pp. 46, 102).
- [78] S. Sharifzadeh et al. “Low-Energy Charge-Transfer Excitons in Organic Solids from First-Principles: The Case of Pentacene”. In: *J. Phys. Chem. Lett.* 4.13 (2013), pp. 2197–2201 (cit. on p. 46).
- [79] C. Faber et al. “Excited States Properties of Organic Molecules: From Density Functional Theory to the GW and Bethe-Salpeter Green’s Function Formalisms”. In: *Phil. Trans. Roy. Soc. London A: Mat., Phy. and Eng. Sci.* 372.2011 (2014), p. 20130271 (cit. on p. 46).
- [80] B. Baumeier, M. Rohlfing, and D. Andrienko. “Electronic Excitations in Push-Pull Oligomers and Their Complexes with Fullerene from Many-Body Green’s Functions Theory with Polarizable Embedding”. In: *J. Chem. Theory. Comput.* 10.8 (2014), pp. 3104–3110 (cit. on pp. 46, 101, 102).
- [81] B. Bagheri, M. Karttunen, and B. Baumeier. “Solvent Effects on Optical Excitations of Poly Para Phenylene Ethynylene Studied by QM/MM Simulations Based on Many-Body Green’s Functions Theory”. In: *Euro. Phys. J. Spe. Top.* 225.8-9 (2016), pp. 1743–1756 (cit. on pp. 46, 101).
- [82] F. Kaplan et al. “Quasi-Particle Self-Consistent GW for Molecules”. In: *J. Chem. Theory. Comput.* 12.6 (2016), pp. 2528–2541 (cit. on pp. 55, 102).
- [83] S. V. Faleev, M. van Schilfgaarde, and T. Kotani. “All-Electron Self-Consistent GW Approximation: Application to Si, MnO, and NiO”. In: *Phys. Rev. Lett.* 93.12 (2004), p. 126406 (cit. on p. 55).
- [84] M. Shishkin, M. Marsman, and G. Kresse. “Accurate Quasiparticle Spectra from Self-Consistent GW Calculations with Vertex Corrections”. In: *Phys. Rev. Lett.* 99.24 (2007), p. 246403 (cit. on p. 56).
- [85] A. Schindlmayr and R. W. Godby. “Systematic Vertex Corrections through Iterative Solution of Hedin’s Equations Beyond the GW Approximation”. In: *Phys. Rev. Lett.* 80.8 (1998), pp. 1702–1705 (cit. on p. 56).
- [86] T. Rangel et al. “An Assessment of Low-Lying Excitation Energies and Triplet Instabilities of Organic Molecules with an Ab Initio Bethe-Salpeter Equation Approach and the Tamm-Dancoff Approximation”. In: *J. Chem. Phys.* 146.19 (2017), p. 194108 (cit. on p. 60).

- [87] P. Puschnig, C. Meisenbichler, and C. Draxl. “Excited State Properties of Organic Semiconductors: Breakdown of the Tamm-Dancoff Approximation”. In: *arXiv:1306.3790* (2013) (cit. on pp. 60, 111).
- [88] S. Mohr et al. “Accurate and Efficient Linear Scaling DFT Calculations with Universal Applicability”. In: *Phys. Chem. Chem. Phys.* 17.47 (2015), pp. 31360–31370 (cit. on p. 63).
- [89] A. Troisi. “Charge Transport in High Mobility Molecular Semiconductors: Classical Models and New Theories”. In: *Chem. Soc. Rev.* 40.5 (2011), pp. 2347–2358 (cit. on p. 64).
- [90] W. Barford et al. “Exciton Localization in Disordered Poly(3-Hexyl Thiophene)”. In: *J. Chem. Phys.* 133.4 (2010), p. 044504 (cit. on pp. 64, 76).
- [91] V. Stehr. “Prediction of Charge and Energy Transport in Organic Crystals with Quantum Chemical Protocols Employing the Hopping Model”. PhD Thesis. Würzburg, 2015 (cit. on pp. 64, 160).
- [92] V. Rühle et al. “Microscopic Simulations of Charge Transport in Disordered Organic Semiconductors”. In: *J. Chem. Theory. Comput.* 7.10 (2011), pp. 3335–3345 (cit. on pp. 64, 75, 90, 117, 156, 161, 162).
- [93] L. Verlet. “Computer “Experiments” on Classical Fluids. I. Thermodynamical Properties of Lennard-Jones Molecules”. In: *Phys. Rev.* 159.1 (1967), pp. 98–103 (cit. on pp. 68, 120).
- [94] P. J. Channell and C. Scovel. “Symplectic Integration of Hamiltonian Systems”. In: *Nonlinearity* 3.2 (1990), p. 231 (cit. on p. 69).
- [95] K. Nakamoto, M. Margoshes, and R. E. Rundle. “Stretching Frequencies as a Function of Distances in Hydrogen Bonds”. In: *J. Am. Chem. Soc.* 77.24 (1955), pp. 6480–6486 (cit. on p. 69).
- [96] G. Bussi, D. Donadio, and M. Parrinello. “Canonical Sampling through Velocity Rescaling”. In: *J. Chem. Phys.* 126.1 (2007), p. 14101 (cit. on pp. 69, 120, 159).
- [97] H. J. C. Berendsen et al. “Molecular Dynamics with Coupling to an External Bath”. In: *J. Chem. Phys.* 81.8 (1984), pp. 3684–3690 (cit. on pp. 69, 70).
- [98] W. Hoover. “Canonical Dynamics: Equilibrium Phase-Space Distributions”. In: *Phys. Rev. A: At., Mol., Opt. Phys.* 31 (1985), p. 1695 (cit. on p. 69).
- [99] P. H. Hünenberger. “Thermostat Algorithms for Molecular Dynamics Simulations”. In: *Adv. Comp. Sim. Advances in Polymer Science*. Springer, Berlin, Heidelberg, pp. 105–149 (cit. on p. 70).

- [100] M. Parrinello and A. Rahman. "Polymorphic Transitions in Single Crystals: A New Molecular Dynamics Method". In: *J. Appl. Phys.* 52.12 (1981), pp. 7182–7190 (cit. on pp. 70, 120).
- [101] R. Car and M. Parrinello. "Unified Approach for Molecular Dynamics and Density-Functional Theory". In: *Phys. Rev. Lett.* 55.22 (1985), pp. 2471–2474 (cit. on p. 70).
- [102] P. Kordt, T. Speck, and D. Andrienko. "Finite-Size Scaling of Charge Carrier Mobility in Disordered Organic Semiconductors". In: *Phys. Rev. B* 94.1 (2016), p. 014208 (cit. on p. 70).
- [103] W. L. Jorgensen and J. Tirado-Rives. "Monte Carlo vs Molecular Dynamics for Conformational Sampling". In: *J. Phys. Chem.* 100.34 (1996), pp. 14508–14513 (cit. on p. 70).
- [104] R. A. Marcus. "Electron Transfer Reactions in Chemistry. Theory and Experiment". In: *Rev. Mod. Phys.* 65.3 (1993), p. 599 (cit. on p. 74).
- [105] R. A. Marcus and N. Sutin. "Electron Transfers in Chemistry and Biology". In: (*BBA*) - *Rev. on Bioene.F* 811.3 (1985), pp. 265–322 (cit. on p. 74).
- [106] J. R. Miller, L. T. Calcaterra, and G. L. Closs. "Intramolecular Long-Distance Electron Transfer in Radical Anions. The Effects of Free Energy and Solvent on the Reaction Rates". In: *J. Am. Chem. Soc.* 106.10 (1984), pp. 3047–3049 (cit. on p. 75).
- [107] B. Lunkenheimer. "Simulationen Zur Exzitonendiffusion in Organischen Halbleitern". PhD Thesis. Universitätsbibliothek Mainz, 2014 (cit. on pp. 75, 137, 155, 156, 160).
- [108] M. P. Fisher and A. T. Dorsey. "Dissipative Quantum Tunneling in a Biased Double-Well System at Finite Temperatures". In: *Phys. Rev. Lett.* 54.15 (1985), p. 1609 (cit. on pp. 75, 181).
- [109] H. Grabert and U. Weiss. "Quantum Tunneling Rates for Asymmetric Double-Well Systems with Ohmic Dissipation". In: *Phys. Rev. Lett.* 54.15 (1985), pp. 1605–1608 (cit. on pp. 75, 181).
- [110] C. A. Mead and D. G. Truhlar. "Conditions for the Definition of a Strictly Diabatic Electronic Basis for Molecular Systems". In: *J. Chem. Phys.* 77.12 (1982), pp. 6090–6098 (cit. on p. 75).
- [111] W. J. D. Beenken and T. Pullerits. "Spectroscopic Units in Conjugated Polymers: A Quantum Chemically Founded Concept?" In: *J. Phys. Chem. B* 108.20 (2004), pp. 6164–6169 (cit. on p. 76).

- [112] A. Troisi and A. Shaw. “Very Large  $\pi$ -Conjugation Despite Strong Nonplanarity: A Path for Designing New Semiconducting Polymers”. In: *J. Phys. Chem. Lett.* 7.22 (2016), pp. 4689–4694 (cit. on p. 76).
- [113] C. R. Poelking. “The (Non-)Local Density of States of Electronic Excitations”. PhD Thesis. Universität Heidelberg (cit. on pp. 78, 83).
- [114] A. J. Stone. *The Theory of Intermolecular Forces*. Oxford: Clarendon Press, 1997 (cit. on p. 78).
- [115] J. Applequist, J. R. Carl, and K.-K. Fung. “Atom Dipole Interaction Model for Molecular Polarizability. Application to Polyatomic Molecules and Determination of Atom Polarizabilities”. In: *J. Am. Chem. Soc.* 94.9 (1972), pp. 2952–2960 (cit. on p. 81).
- [116] J. L. Banks et al. “Parametrizing a Polarizable Force Field from Ab Initio Data. I. The Fluctuating Point Charge Model”. In: *J. Chem. Phys.* 110.2 (1998), pp. 741–754 (cit. on p. 82).
- [117] H. A. Stern et al. “Fluctuating Charge, Polarizable Dipole, and Combined Models: Parameterization from Ab Initio Quantum Chemistry”. In: *J. Phys. Chem. B* 103.22 (1999), pp. 4730–4737 (cit. on p. 82).
- [118] P. T. van Duijnen and M. Swart. “Molecular and Atomic Polarizabilities: Thole’s Model Revisited”. In: *J. Phys. Chem. A* 102.14 (1998), pp. 2399–2407 (cit. on p. 82).
- [119] J. W. Ponder et al. “Current Status of the AMOEBA Polarizable Force Field”. In: *J. Phys. Chem. B* 114.8 (2010), pp. 2549–2564 (cit. on pp. 82, 120).
- [120] C. Poelking and D. Andrienko. “Design Rules for Organic Donor Acceptor Heterojunctions: Pathway for Charge Splitting and Detrapping”. In: *J. Am. Chem. Soc.* 137.19 (2015), pp. 6320–6326 (cit. on pp. 83, 162).
- [121] C. Poelking and D. Andrienko. “Long-Range Embedding of Molecular Ions and Excitations in a Polarizable Molecular Environment”. In: *J. Chem. Theory. Comput.* 12.9 (2016), pp. 4516–4523 (cit. on pp. 83, 92, 158).
- [122] R. S. Mulliken. “Electronic Population Analysis on LCAO–MO Molecular Wave Functions. I”. In: *J. Chem. Phys.* 23.10 (1955), pp. 1833–1840 (cit. on p. 83).
- [123] A. E. Reed, R. B. Weinstock, and F. Weinhold. “Natural Population Analysis”. In: *J. Chem. Phys.* 83.2 (1985), pp. 735–746 (cit. on p. 83).
- [124] A. J. Stone. “Distributed Multipole Analysis: Stability for Large Basis Sets”. In: *J. Chem. Theory. Comput.* 1.6 (2005), pp. 1128–1132 (cit. on p. 83).

- [125] L. E. Chirlian and M. M. Francl. “Atomic Charges Derived from Electrostatic Potentials: A Detailed Study”. In: *J. Comput. Chem.* 8.6 (1987), pp. 894–905 (cit. on p. 83).
- [126] K. Fichthorn and W. Weinberg. “Theoretical Foundations of Dynamic Monte-Carlo Simulations”. In: *J. Chem. Phys.* 95.2 (1991), pp. 1090–1096 (cit. on p. 87).
- [127] A. Jansen. “Monte-Carlo Simulations of Chemical-Reactions on a Surface with Time-Dependent Reaction-Rate Constants”. In: *Comp. Phys. Comm.* 86.1-2 (1995), pp. 1–12 (cit. on p. 87).
- [128] V. Rühle et al. “Versatile Object-Oriented Toolkit for Coarse-Graining Applications”. In: *J. Chem. Theory. Comput.* 5.12 (2009), pp. 3211–3223 (cit. on p. 89).
- [129] J. Kirkpatrick. “An Approximate Method for Calculating Transfer Integrals Based on the ZINDO Hamiltonian”. In: *Int. J. Quantum Chem.* 108.1 (2008), pp. 51–56 (cit. on pp. 89, 131).
- [130] *Eigen*. URL: [http://eigen.tuxfamily.org/index.php?title=Main\\_Page](http://eigen.tuxfamily.org/index.php?title=Main_Page) (visited on 02/06/2019) (cit. on p. 91).
- [131] L. Dagum and R. Menon. “OpenMP: An Industry Standard API for Shared-Memory Programming”. In: *Comp. Sci. Eng., IEEE* 5.1 (1998), pp. 46–55 (cit. on p. 92).
- [132] M. A. L. Marques, M. J. T. Oliveira, and T. Burnus. “Libxc: A Library of Exchange and Correlation Functionals for Density Functional Theory”. In: *Comp. Phys. Com.* 183.10 (2012), pp. 2272–2281 (cit. on p. 92).
- [133] M. Valiev et al. “NWChem: A Comprehensive and Scalable Open-Source Solution for Large Scale Molecular Simulations”. In: *Comp. Phys. Comm.* 181.9 (2010), pp. 1477–1489 (cit. on pp. 92, 98).
- [134] J. H. Van Lenthe et al. “Starting SCF Calculations by Superposition of Atomic Densities”. In: *J. Comput. Chem.* 27.8 (2006), pp. 926–932 (cit. on p. 92).
- [135] X. Hu and W. Yang. “Accelerating Self-Consistent Field Convergence with the Augmented Roothaan–Hall Energy Function”. In: *J. Chem. Phys.* 132.5 (2010), p. 054109 (cit. on p. 93).
- [136] P. Pulay. “Improved SCF Convergence Acceleration”. In: *J. Comput. Chem.* 3.4 (1982), pp. 556–560 (cit. on p. 93).

- [137] H. Sellers. “The C2-DIIS Convergence Acceleration Algorithm”. In: *Int. J. Quantum Chem.* 45.1 (1993), pp. 31–41 (cit. on p. 93).
- [138] S. Reine, T. Helgaker, and R. Lindh. “Multi-Electron Integrals”. In: *Wiley Interdis. Rev.: Comp. Mol. Sci.* 2.2 (2012), pp. 290–303 (cit. on p. 94).
- [139] K. Eichkorn et al. “Auxiliary Basis Sets to Approximate Coulomb Potentials (Chem. Phys. Letters 240 (1995) 283-290)”. In: *Chem. Phys. Lett.* 242.6 (1995), pp. 652–660 (cit. on p. 94).
- [140] F. Weigend. “A Fully Direct RI-HF Algorithm: Implementation, Optimised Auxiliary Basis Sets, Demonstration of Accuracy and Efficiency”. In: *Phys. Chem. Chem. Phys.* 4.18 (2002), pp. 4285–4291 (cit. on pp. 95, 104).
- [141] L. E. McMurchie and E. R. Davidson. “Calculation of Integrals over Ab Initio Pseudopotentials”. In: *J. Comput. Phys.* 44.2 (1981), pp. 289–301 (cit. on p. 95).
- [142] M. Dolg. “Relativistic Effective Core Potentials”. In: *Handbook of Rel. Quantum Chem.* (2017), pp. 449–478 (cit. on p. 95).
- [143] F. Neese. “The ORCA Program System”. In: *Wiley Interdis. Rev.: Comp. Mol. Sci.* 2.1 (2012), pp. 73–78 (cit. on pp. 96, 98, 104).
- [144] M. J. Frisch et al. *Gaussian 09 Revision E.01* (cit. on pp. 96, 98).
- [145] M. Schrader et al. “Comparative Study of Microscopic Charge Dynamics in Crystalline Acceptor-Substituted Oligothiophenes”. In: *J. Am. Chem. Soc.* 134.13 (2012), pp. 6052–6056 (cit. on pp. 96, 159, 165).
- [146] R. Fitzner et al. “Correlation of  $\pi$ -Conjugated Oligomer Structure with Film Morphology and Organic Solar Cell Performance”. In: *J. Am. Chem. Soc.* 134.27 (2012), pp. 11064–11067 (cit. on pp. 96, 159, 160).
- [147] R. Meerheim et al. “10.4% Efficient Triple Organic Solar Cells Containing near Infrared Absorbers”. In: *Appl. Phys. Lett.* 108.10 (2016), p. 103302 (cit. on pp. 96, 155, 159).
- [148] A. Bergner et al. “Ab Initio Energy-Adjusted Pseudopotentials for Elements of Groups 13–17”. In: *Mol. Phys.* 80 (1993), pp. 1431–1441 (cit. on pp. 96, 104, 140, 145).
- [149] M. J. Frisch et al. *Gaussian 03, Revision C.02*. 2004 (cit. on pp. 98, 140).
- [150] M. J. van Setten, F. Weigend, and F. Evers. “The GW-Method for Quantum Chemistry Applications: Theory and Implementation”. In: *J. Chem. Theory. Comput.* 9.1 (2013), pp. 232–246 (cit. on pp. 99, 101).

- [151] F. Bruneval. "Ionization Energy of Atoms Obtained from GW Self-Energy or from Random Phase Approximation Total Energies". In: *J. Chem. Phys.* 136.19 (2012), p. 194107 (cit. on p. 99).
- [152] F. Liu et al. "Numerical Integration for Ab Initio Many-Electron Self Energy Calculations within the GW Approximation". In: *J. Comput. Phys.* 286.Supplement C (2015), pp. 1–13 (cit. on pp. 99, 101).
- [153] H. N. Rojas, R. W. Godby, and R. J. Needs. "Space-Time Method for Ab Initio Calculations of Self-Energies and Dielectric Response Functions of Solids". In: *Phys. Rev. Lett.* 74.10 (1995), pp. 1827–1830 (cit. on p. 101).
- [154] M. Rohlfing, P. Krüger, and J. Pollmann. "Efficient Scheme for GW Quasiparticle Band-Structure Calculations with Applications to Bulk Si and to the Si(001)-(2x1) Surface". In: *Phys. Rev. B* 52.3 (1995), pp. 1905–1917 (cit. on p. 101).
- [155] M. Rohlfing and S. G. Louie. "Excitonic Effects and the Optical Absorption Spectrum of Hydrogenated Si Clusters". In: *Phys. Rev. Lett.* 80.15 (1998), p. 3320 (cit. on pp. 101, 102).
- [156] M. Rohlfing, P. Krüger, and J. Pollmann. "Quasiparticle Band Structure of CdS". In: *Phys. Rev. Lett.* 75.19 (1995), pp. 3489–3492 (cit. on p. 101).
- [157] M. Rohlfing and S. G. Louie. "Electron-Hole Excitations and Optical Spectra from First Principles". In: *Phys. Rev. B* 62.8 (2000), p. 4927 (cit. on p. 101).
- [158] N.-P. Wang et al. "Fast Initial Decay of Molecular Excitations at Insulator Surfaces". In: *Phys. Rev. Lett.* 92.21 (2004), p. 216805 (cit. on p. 101).
- [159] Y. Ma and M. Rohlfing. "Optical Excitation of Deep Defect Levels in Insulators within Many-Body Perturbation Theory: The F Center in Calcium Fluoride". In: *Phys. Rev. B* 77.11 (2008), p. 115118 (cit. on p. 101).
- [160] M. Rohlfing and S. G. Louie. "Optical Excitations in Conjugated Polymers". In: *Phys. Rev. Lett.* 82.9 (1999), p. 1959 (cit. on p. 101).
- [161] E. Artacho et al. "Structural Relaxations in Electronically Excited Poly (Paraphenylene)". In: *Phys. Rev. Lett.* 93.11 (2004), p. 116401 (cit. on p. 101).
- [162] M. Rohlfing. "Excited States of Molecules from Green's Function Perturbation Techniques". In: *Int. J. Quantum Chem.* 80.4-5 (2000), pp. 807–815 (cit. on p. 101).
- [163] Y. Ma, M. Rohlfing, and C. Molteni. "Modeling the Excited States of Biological Chromophores within Many-Body Green's Function Theory". In: *J. Chem. Theory Comput.* 6.1 (2010), pp. 257–265 (cit. on p. 101).



- [164] H. Yin et al. “Charge-Transfer Excited States in Aqueous DNA: Insights from Many-Body Green’s Function Theory”. In: *Phys. Rev. Lett.* 112.22 (2014), p. 228301 (cit. on pp. 101, 119).
- [165] F. Bruneval, S. M. Hamed, and J. B. Neaton. “A Systematic Benchmark of the Ab Initio Bethe-Salpeter Equation Approach for Low-Lying Optical Excitations of Small Organic Molecules”. In: *J. Chem. Phys.* 142.24 (2015), p. 244101 (cit. on p. 101).
- [166] D. Jacquemin et al. “Benchmark of Bethe-Salpeter for Triplet Excited-States”. In: *J. Chem. Theory. Comput.* 13.2 (2017), pp. 767–783 (cit. on p. 102).
- [167] D. Jacquemin, I. Duchemin, and X. Blase. “Benchmarking the Bethe–Salpeter Formalism on a Standard Organic Molecular Set”. In: *J. Chem. Theory. Comput.* 11.7 (2015), pp. 3290–3304 (cit. on pp. 102, 105, 189).
- [168] P. Koval, D. Foerster, and D. Sánchez-Portal. “Fully Self-Consistent GW and Quasiparticle Self-Consistent GW for Molecules”. In: *Phys. Rev. B* 89.15 (2014), p. 155417 (cit. on p. 102).
- [169] M. J. van Setten et al. “GW100: Benchmarking G0W0 for Molecular Systems”. In: *J. Chem. Theory. Comput.* 11.12 (2015), pp. 5665–5687 (cit. on p. 102).
- [170] D. Jacquemin et al. “Assessment of the Accuracy of the Bethe–Salpeter (BSE/GW) Oscillator Strengths”. In: *J. Chem. Theory. Comput.* 12.8 (2016), pp. 3969–3981 (cit. on p. 102).
- [171] P. Boulanger et al. “Fast and Accurate Electronic Excitations in Cyanines with the Many-Body Bethe–Salpeter Approach”. In: *J. Chem. Theory. Comput.* 10.3 (2014), pp. 1212–1218 (cit. on p. 102).
- [172] P. García-González and R. W. Godby. “GW Self-Energy Calculations for Surfaces and Interfaces”. In: *Comp. Phy. Com.* 137.1 (2001), pp. 108–122 (cit. on p. 102).
- [173] R. Krishnan et al. “Self-Consistent Molecular-Orbital Methods .20. Basis Set for Correlated Wave-Functions”. In: *Journal of Chemical Physics* 72.1 (1980), pp. 650–654 (cit. on pp. 104, 140, 145).
- [174] F. Weigend, A. Köhn, and C. Hättig. “Efficient Use of the Correlation Consistent Basis Sets in Resolution of the Identity MP2 Calculations”. In: *J. Chem. Phys.* 116.8 (2002), pp. 3175–3183 (cit. on p. 104).

- [175] K. L. Schuchardt et al. "Basis Set Exchange: A Community Database for Computational Sciences". In: *J. Chem. Inf. Model.* 47.3 (2007), pp. 1045–1052 (cit. on p. 104).
- [176] A. J. Misquitta et al. "Intermolecular Potentials Based on Symmetry Adapted Perturbation Theory with Dispersion Energies from Time-Dependent Density-Functional Calculations". In: *J. Chem. Phys.* 123.21 (2005), p. 214103 (cit. on p. 104).
- [177] A. Misquitta. "Ph.D. Thesis". PhD Thesis. Delaware: University of Delaware, 2004 (cit. on p. 104).
- [178] *Generation of Auxiliary Basis*. URL: [www.physics.udel.edu/~5Ctextasciitilde%7B%7Dszalewic/SAPT/sapt2012manualse22.html](http://www.physics.udel.edu/~5Ctextasciitilde%7B%7Dszalewic/SAPT/sapt2012manualse22.html) (cit. on p. 104).
- [179] G. L. Stoychev, A. A. Auer, and F. Neese. "Automatic Generation of Auxiliary Basis Sets". In: *J. Chem. Theory Comput.* 13.2 (2017), pp. 554–562 (cit. on p. 104).
- [180] E. R. Davidson. "The Iterative Calculation of a Few of the Lowest Eigenvalues and Corresponding Eigenvectors of Large Real-Symmetric Matrices". In: *J. Comput. Phys.* 17.1 (1975), pp. 87–94 (cit. on p. 111).
- [181] N. Reuter et al. "Frontier Bonds in QM/MM Methods: A Comparison of Different Approaches". In: *J. Phys. Chem. A* 104.8 (2000), pp. 1720–1735 (cit. on p. 114).
- [182] C. E. Crespo-Hernández et al. "Ultrafast Excited-State Dynamics in Nucleic Acids". In: *Chem. Rev.* 104.4 (2004), pp. 1977–2020 (cit. on p. 118).
- [183] S. Mouret et al. "UVA-Induced Cyclobutane Pyrimidine Dimers in DNA : A Direct Photochemical Mechanism?" In: *Orga. Biomol. Chem.* 8.7 (2010), pp. 1706–1711 (cit. on p. 118).
- [184] J. Cadet et al. "Sensitized Formation of Oxidatively Generated Damage to Cellular DNA by UVA Radiation". In: *Photochem. Photobio. Sci.* 8.7 (2009), pp. 903–911 (cit. on p. 118).
- [185] C. T. Middleton et al. "DNA Excited-State Dynamics: From Single Bases to the Double Helix". In: *Anu. Rev. Phy. Chem.* 60.1 (2009), pp. 217–239 (cit. on p. 118).
- [186] W.-M. Kwok, C. Ma, and D. L. Phillips. "Femtosecond Time- and Wavelength-Resolved Fluorescence and Absorption Spectroscopic Study of the Excited States of Adenosine and an Adenine Oligomer". In: *J. Am. Chem. Soc.* 128.36 (2006), pp. 11894–11905 (cit. on p. 118).

- [187] A. Banyasz et al. "Base Pairing Enhances Fluorescence and Favors Cyclobutane Dimer Formation Induced upon Absorption of UVA Radiation by DNA". In: *J. Am. Chem. Soc.* 133.14 (2011), pp. 5163–5165 (cit. on p. 118).
- [188] F. Santoro, V. Barone, and R. Improta. "Excited States Decay of the A-T DNA: A PCM/TD-DFT Study in Aqueous Solution of the (9-Methyl-Adenine) 2·(1-Methyl-Thymine)2 Stacked Tetramer". In: *J. Am. Chem. Soc.* 131.42 (2009), pp. 15232–15245 (cit. on pp. 118, 119).
- [189] A. W. Lange and J. M. Herbert. "Both Intra- and Interstrand Charge-Transfer Excited States in Aqueous B-DNA Are Present at Energies Comparable To, or Just Above, the  $1\pi\pi^*$  Excitonic Bright States". In: *J. Am. Chem. Soc.* 131.11 (2009), pp. 3913–3922 (cit. on pp. 118, 119).
- [190] J. Wang, P. Cieplak, and P. A. Kollman. "How Well Does a Restrained Electrostatic Potential (RESP) Model Perform in Calculating Conformational Energies of Organic and Biological Molecules?" In: *J. Comput. Chem.* 21.12 (2000), pp. 1049–1074 (cit. on p. 119).
- [191] H. J. C. Berendsen, J. R. Grigera, and T. P. Straatsma. "The Missing Term in Effective Pair Potentials". In: *J. Phys. Chem.* 91.24 (1987), pp. 6269–6271 (cit. on p. 120).
- [192] W. L. Jorgensen, J. D. Madura, and C. J. Swenson. "Optimized Intermolecular Potential Functions for Liquid Hydrocarbons". In: *J. Am. Chem. Soc.* 106.22 (1984), pp. 6638–6646 (cit. on p. 120).
- [193] W. L. Jorgensen, D. S. Maxwell, and J. Tirado-Rives. "Development and Testing of the OPLS All-Atom Force Field on Conformational Energetics and Properties of Organic Liquids". In: *J. Am. Chem. Soc.* 118.45 (1996), pp. 11225–11236 (cit. on p. 120).
- [194] E. K. Watkins and W. L. Jorgensen. "Perfluoroalkanes: Conformational Analysis and Liquid-State Properties from Ab Initio and Monte Carlo Calculations". In: *J. Phys. Chem. A* 105.16 (2001), pp. 4118–4125 (cit. on p. 120).
- [195] D. Van Der Spoel et al. "GROMACS: Fast, Flexible, and Free". In: *J. Comput. Chem.* 26.16 (2005), pp. 1701–1718 (cit. on p. 120).
- [196] T. Darden, D. York, and L. Pedersen. "Particle Mesh Ewald: An N-log(N) Method for Ewald Sums in Large Systems". In: *J. Chem. Phys.* 98.12 (1993), p. 10089 (cit. on p. 120).
- [197] U. Essmann et al. "A Smooth Particle Mesh Ewald Method". In: *J. Chem. Phys.* 103.19 (1995), p. 8577 (cit. on p. 120).

- [198] W. Humphrey, A. Dalke, and K. Schulten. "VMD: Visual Molecular Dynamics". In: *J. Mol. Graph.* 14.1 (1996), pp. 33–38 (cit. on p. 120).
- [199] E. F. Valeev et al. "Effect of Electronic Polarization on Charge-Transport Parameters in Molecular Organic Semiconductors". In: *J. Am. Chem. Soc.* 128.30 (2006), pp. 9882–9886 (cit. on pp. 131, 134).
- [200] B. Baumeier, J. Kirkpatrick, and D. Andrienko. "Density-Functional Based Determination of Intermolecular Charge Transfer Properties for Large Scale Morphologies". In: *Phys. Chem. Chem. Phys.* 12.36 (2010), pp. 11103–11113 (cit. on pp. 131, 134, 149).
- [201] T. Förster. "Zwischenmolekulare Energiewanderung Und Fluoreszenz". In: *Annalen der Physik* 437.1-2 (1948), pp. 55–75 (cit. on pp. 132, 155).
- [202] S. Athanasopoulos et al. "Trap Limited Exciton Transport in Conjugated Polymers". In: *J. Phys. Chem. C* 112.30 (2008), pp. 11532–11538 (cit. on p. 132).
- [203] Z.-Q. You and C.-P. Hsu. "The Fragment Spin Difference Scheme for Triplet-Triplet Energy Transfer Coupling". In: *J. Chem. Phys.* 133.7 (2010), p. 074105 (cit. on p. 132).
- [204] R. D. Harcourt, G. D. Scholes, and K. P. Ghiggino. "Rate Expressions for Excitation Transfer. II. Electronic Considerations of Direct and through Configuration Exciton Resonance Interactions". In: *J. Chem. Phys.* 101.12 (1994), p. 10521 (cit. on pp. 132, 137).
- [205] S. Difley and T. Van Voorhis. "Exciton/Charge-Transfer Electronic Couplings in Organic Semiconductors". In: *J. Chem. Theory. Comput.* 7.3 (2011), pp. 594–601 (cit. on p. 133).
- [206] P.-O. Löwdin. "On the Non-Orthogonality Problem Connected with the Use of Atomic Wave Functions in the Theory of Molecules and Crystals". In: *J. Chem. Phys.* 18.3 (1950), pp. 365–375 (cit. on p. 134).
- [207] C.-P. Hsu. "The Electronic Couplings in Electron Transfer and Excitation Energy Transfer". In: *Accounts Chem. Res.* 42.4 (2009), pp. 509–518 (cit. on p. 134).
- [208] C.-P. Hsu, Z.-Q. You, and H.-C. Chen. "Characterization of the Short-Range Couplings in Excitation Energy Transfer". In: *J. Phys. Chem. C* 112.4 (2008), pp. 1204–1212 (cit. on p. 134).

- [209] A. A. Voityuk. “Estimation of Electronic Coupling for Singlet Excitation Energy Transfer”. In: *J. Phys. Chem. C* 118.3 (2014), pp. 1478–1483 (cit. on p. 134).
- [210] F. Cordova et al. “Troubleshooting Time-Dependent Density-Functional Theory for Photochemical Applications: Oxirane”. In: *J. Chem. Phys.* (2007) (cit. on p. 142).
- [211] M. J. G. Peach, M. J. Williamson, and D. J. Tozer. “Influence of Triplet Instabilities in TDDFT”. In: *J. Chem. Theory. Comput.* 7.11 (2011), pp. 3578–3585 (cit. on p. 142).
- [212] F. Bruneval and M. A. L. Marques. “Benchmarking the Starting Points of the GW Approximation for Molecules”. In: *J. Chem. Theory. Comput.* 9.1 (2013), pp. 324–329 (cit. on p. 149).
- [213] J. C. Chang. “Monopole Effects on Electronic Excitation Interactions between Large Molecules. I. Application to Energy Transfer in Chlorophylls”. In: *J. Chem. Phys.* 67.9 (1977), pp. 3901–3909 (cit. on p. 152).
- [214] K. A. Kistler, F. C. Spano, and S. Matsika. “A Benchmark of Excitonic Couplings Derived from Atomic Transition Charges”. In: *J. Phys. Chem. B* 117.7 (2013), pp. 2032–2044 (cit. on p. 152).
- [215] S. R. Yost et al. “Triplet vs Singlet Energy Transfer in Organic Semiconductors: The Tortoise and the Hare”. In: *J. Phys. Chem. C* 116.33 (2012), pp. 17369–17377 (cit. on p. 155).
- [216] M. E. Madjet, A. Abdurahman, and T. Renger. “Intermolecular Coulomb Couplings from Ab Initio Electrostatic Potentials: Application to Optical Transitions of Strongly Coupled Pigments in Photosynthetic Antennae and Reaction Centers”. In: *J. Phys. Chem. B* 110.34 (2006), pp. 17268–17281 (cit. on p. 157).
- [217] T. Renger and F. Müh. “Theory of Excitonic Couplings in Dielectric Media”. In: *Photosyn. Res.* 111.1-2 (2011), pp. 47–52 (cit. on pp. 157, 171).
- [218] C. M. Breneman and K. B. Wiberg. “Determining Atom-Centered Monopoles from Molecular Electrostatic Potentials. The Need for High Sampling Density in Formamide Conformational Analysis”. In: *J. Comput. Chem.* 11.3 (1990), pp. 361–373 (cit. on pp. 157, 161).
- [219] J. van der Horst et al. “Predicting Polarizabilities and Lifetimes of Excitons on Conjugated Polymer Chains”. In: *Chem. Phys. Lett.* 334.4–6 (2001), pp. 303–308 (cit. on p. 159).

- [220] R. Fletcher. “A New Approach to Variable Metric Algorithms”. In: *The Comp. J.* 13.3 (1970), pp. 317–322 (cit. on p. 160).
- [221] A. Frisch. *Gaussian 09 User’s Reference* (cit. on p. 160).
- [222] M. Schrader. “Charge Transport in Organic Photovoltaic Cells”. PhD Thesis. Mainz, 2013 (cit. on pp. 160, 163).
- [223] M. R. Silva-Junior et al. “Benchmarks for Electronically Excited States: Time-Dependent Density Functional Theory and Density Functional Theory Based Multireference Configuration Interaction”. In: *J. Chem. Phys.* 129.10 (2008), p. 104103 (cit. on p. 189).
- [224] M. Schreiber et al. “Benchmarks for Electronically Excited States: CASPT2, CC2, CCSD, and CC3”. In: *J. Chem. Phys.* 128.13 (2008), p. 134110 (cit. on p. 189).
- [225] J. Wehner and B. Baumeier. “Intermolecular Singlet and Triplet Exciton Transfer Integrals from Many-Body Green’s Functions Theory”. In: *J. Chem. Theory. Comput.* 13.4 (2017), pp. 1584–1594 (cit. on p. 216).
- [226] J. Wehner et al. “Electronic Excitations in Complex Molecular Environments: Many-Body Green’s Functions Theory in VOTCA-XTP”. In: *J. Chem. Theory. Comput.* 14.12 (2018), pp. 6253–6268 (cit. on p. 216).

# Acknowledgments

This work would not have been possible without the advice and support of many people.

First, Björn Baumeier, now at TU/e Eindhoven, was my direct supervisor and basically taught me everything about the topic. He turned me into a critically thinking scientist and gave me the self-confidence to explore the topic at hand.

Secondly, I am very grateful to Barry Koren and Mark Peletier for the warm welcome in Eindhoven and the continuous support, as well as the opportunity to try out new things.

Thirdly, I am very grateful to Professor Kremer from MPIP Mainz, who was always very supportive.

My officemates from MPIP should not be missed on this list, some long gone, some still working. Xenbo Xiao, Pascal Kordt, Christoph Scherer and Svenja Wörner and of course the people from the kicker table, Roberto, Karsten, Kieran. Also the IT people, who were always helpful and supportive Harald Bopp, Robert Klein and Torsten Stühn.

At TU/e I also had the pleasure to work with young, bright and only sometimes frustrated colleagues. Special mentions to my CASA roommates Yuriy, Pranav, Behnaz, Gianluca, Onur, Wouter and Vivek. I am especially thankful to Wouter, who drove me to the edge of reason with his mathematical mind, but who also found tons of notational inconsistencies. Also on the list are the secretaries at ICMS and CASA Enna, Jolijn, Carla, Wendy and Cindy.

Speaking of secretaries, Doris Kirsch, you are an absolute gem. The emotional support, your warmth and nearly motherly care for us group members I cannot put

into words. You are precious to me and helped me through some gloomy days.

Of course, there is also my family, thank you Mama, Papa and Björn.

Finally, all my friends, who I feel carried me through this. I hopefully list you all. Sarah, thanks for all the Sushi and the talks. Caro for being the psychologist I always needed. Frank for not taking my frustration too serious. Anastasia for being the best Slammer and so supportive. Lutz for all the hosting and for driving me up the wall. Stefan for the mentoring and Susanne who pushed me to do science slams. Andreas for being a loyal friend, although I called too seldom. Sophie for the advice to take a break. Mia, Carsten, Minh, Johannes and Kat for the fun at KurzFormChaos. Finally Sandra for just being a really good friend and cook. Kristin for being a good dancer. Alex and Ana for being good neighbors and extremely talented software engineers/cocktail makers. :D

*ευχαριστω Πελαγια, μικρο μου γαιδουρακι, για την υπομονη και κατανοηση σου. θα προσπαθησω να επανορθωσω.*

Jens Wehner  
Eindhoven, May 2019



# Curriculum Vitae

Jens Wehner was born in Hannover, Germany, in 1987. He obtained his diploma in Materials Science from Technische Universität Darmstadt in Darmstadt, Germany, in 2013. In his diploma thesis he investigated the dynamics of ferroelectric crystals via coarse-grained finite-element methods. Later the same year he started his PhD at the Max Planck Institute for Polymer Research in Mainz, Germany. In 2018 he followed his supervisor, Björn Baumeier, to the Centre of Applied analysis, Scientific computing and Applications at the Department of Mathematics and Computer Science at Eindhoven University of Technology. The results of this research are presented in this dissertation.

## List of Publications

- J. Wehner and B. Baumeier. “Intermolecular Singlet and Triplet Exciton Transfer Integrals from Many-Body Green’s Functions Theory”. In: *J. Chem. Theory. Comput.* 13.4 (2017), pp. 1584–1594
- J. Wehner et al. “Electronic Excitations in Complex Molecular Environments: Many-Body Green’s Functions Theory in VOTCA-XTP”. in: *J. Chem. Theory. Comput.* 14.12 (2018), pp. 6253–6268